Cape Peninsula University of Technology

DESIGN AND IMPLEMENTATION OF A DC FAST CHARGING SYSTEM FOR ELECTRIC VEHICLES

by

AHMED TAHER AHMED ZENTANI

Thesis submitted in fulfilment of the requirements for the degree

Doctorate of Engineering: Electrical Engineering

in the Faculty of Engineering and the Built Environment

at the Cape Peninsula University of Technology

Supervisor: Dr AMA Almaktoof

Co-supervisor: Prof MTE Kahn

Bellville
May 2025

DECLARATION

I, Ahmed Taher Ahmed Zentani, declare that the contents of this dissertation/thesis represent my own unaided work, and that the dissertation/thesis has not previously been submitted for academic examination towards any qualification. Furthermore, it represents my own opinions and not necessarily those of the Cape Peninsula University of Technology.

Signed  **Date 27/05/2025**

ABSTRACT

The increasing penetration of electric vehicles (EVs) in the global transportation landscape has highlighted the importance of developing innovative charging infrastructure systems that meet the demands of modern EVs. Fast DC charging systems are key to reducing charging times and enhancing the user experience, particularly for EVs equipped with high-capacity batteries and extended driving ranges. This thesis presents a comprehensive study on the design and development of an off-board DC fast charging system that leverages renewable energy sources and advanced power electronics technologies to create a more sustainable and efficient charging solution. The integration of a photovoltaic (PV)-tied grid system as a primary supply source reflects a growing trend toward incorporating renewable energy in EV charging infrastructure. This approach not only reduces the load on traditional grid systems but also supports global efforts to minimize carbon emissions and transition to cleaner energy sources. At the core of the proposed system are the interconnection power electronics, consisting of bidirectional AC-DC and DC-DC converters. These converters are essential for managing the bidirectional power flow between the grid, the PV system, and the EV battery. By employing a Proportional Integral (PI) controller, the system can maintain a stable and efficient power transfer process, ensuring that the EV battery is charged quickly while avoiding unnecessary stress on the grid. The DC-DC step-up converter, which interfaces with the PV system, is designed with an advanced control algorithm based on Maximum Power Point Tracking (MPPT). The Perturb and Observe (P&O) MPPT method is chosen for its simplicity and effectiveness in optimizing energy extraction from the PV system, even under fluctuating environmental conditions. This ensures that the system operates at peak efficiency, maximizing the use of renewable energy while maintaining grid stability and power quality. Through rigorous testing and simulation in the MATLAB/Simulink environment, the study provides valuable insights into the performance and reliability of the proposed system under five case scenarios. These simulations not only validate the effectiveness of the control strategies but also offer practical guidelines for optimizing converter design, improvements in charging stability, reduced total harmonic distortion (<3%), efficient power transfer, and minimized current ripple, confirming the robustness of the proposed approach. The outcome of this research contributes to the growing body of knowledge on DC fast charging systems for EVs, offering practical solutions for enhancing charging efficiency, integrating renewable energy sources, and improving grid interaction. The findings also support the development of more robust, scalable, and energy-efficient EV charging infrastructures, addressing the evolving needs of the electric vehicle market.

Keywords: Fast Charging, Photovoltaic (PV)-Tied grid, DC-DC converter, Bidirectional converter, Electrical vehicles (EVs), PI controller, MATLAB/Simulink.

ACKNOWLEDGEMENTS

First and foremost, I extend my profound gratitude to ALLAH, whose guidance, blessings, and infinite wisdom have enabled me to acquire the knowledge, strength, and perseverance to successfully complete this degree.

I am deeply indebted to my supervisor, Dr. Ali Almaktoof, and my co-supervisor, Professor MTE Kahn, for their unwavering support, insightful guidance, and invaluable mentorship throughout the course of this research. Their dedication and encouragement have been pivotal in shaping the direction of this work, and I am truly thankful for their expertise and commitment.

I would like to express my sincere appreciation to all the members of the Faculty of Engineering, the staff at the Centre for Research in Power Systems (CRPS). and my friends for their constant encouragement, constructive suggestions, and continuous support. Their contributions have enriched this journey in ways that words can hardly convey.

A heartfelt thank you goes to my parents, my wife, my brothers and sisters, and my in-laws. Their love, patience, understanding, and sacrifices have been a source of strength and motivation. I am eternally grateful for their unwavering belief in me. May ALLAH bless them and grant them rewards both in this world and the Hereafter.

I would also like to acknowledge the support of the Libyan Embassy in Pretoria for their assistance during my studies.

To my friends and colleagues, I am deeply grateful for their moral support, encouragement, and camaraderie. Their presence has been a source of inspiration and strength.

Finally, I extend my appreciation to all those who contributed to this dissertation, either directly or indirectly. Your contributions, however big or small, have made a significant difference, and for that, I am truly thankful.

Ahmed Zentani 2025

DEDICATION

This thesis is dedicated to those who are dear to me, more particularly my parents, my wife Dr. Asma Alwakwak, my kids Yummna, Yussif, Yacob and Ayoub.

TABLE OF CONTENTS

LIST OF FIGURES

LIST OF TABLES

GLOSSARY

AFE	Active Front-End
AC	Alternative Current
ANNs	Artificial Neural Networks
BMS	Battery Management System
SoC	Battery's State of Charge
BSS	Battery Storage Systems
C	Capacitors
CLLC	Capacitor–Inductor–Inductor–Capacitor
CC	Constant Current
CCCV	Constant Current Constant Voltage
CV	Constant Voltage
CCS	Combined Charging System
CPT	Capacitive Power Transfer
DSPs	Digital Signal Processors
DC	Direct Current
DCFC	Direct Current Fast Charging
DESs	Distributed Energy Sources
DG	Distributed Generation
DS	Distribution Systems
DAB	Dual Active Bridge
D	Duty Cycle
EPRI	Electric Power Research Institute
EVs	Electric Vehicles
EMC	Electromagnetic Compatibility
EMI	Electro-Magnetic Interference
ESS	Energy Storage System
E-REVs	Extended-Range Electric Vehicles
FPGAs	Field-Programmable Gate Arrays
FCEVs	Fuel Cell Electric Vehicles
FLC	Fuzzy Logic Control
GaN	Gallium Nitride
HFT	High-Frequency Transformer
HVDC	High-Voltage Direct Current

HEVs	Hybrid Electric Vehicles
IC	Incremental conductance
IGBT	Insulated-Gate Bipolar Transistor
ISOP	Input-Series, Output-Parallel
IUT	Intelligent Universal Transformer
ILC	Interlinked Power Converter
IEC	International Electrotechnical Commission
IEA	International Energy Agency's
ISO	International Organization for Standardization
IPT	Inductive Power Transfer
IGBTs	Insulated Gate Bipolar Transistors
KM	Kilometres
kW	Kilo Watt
kWh	kilo Watt hour
L	Inductors
Li-ion	Lithium-Ion
LF	Loop Filter
LFT	Low-Frequency Transformer
LVDC	Low Voltage DC
MPPT	Maximum Power Point Tracking
MSE	Mean Squared Error
MVAC	Medium Voltage AC
MVDC	Medium Voltage DC
MVDCFC	Medium Voltage DC Fast Charger
MPC	Model Predictive Control
NPC	Neutral-Point-Clamped
OFF-BC	Off-Board Charging
ON-BC	On-Board Charger
OCPP	Open Charge Point Protocol
OCV	Open-Circuit Voltage
PSC	Partial Shading Conditions
PSO	Particle Swarm Optimization
P&O	Perturb and Observe
PD	Phase Detector
PLL	Phase-Locked Loop
PSFB	Phase-Shifted Full Bridge
PV	Photovoltaic

PEVs	Plug-in Electric Vehicles
PHEVs	Plug-in Hybrid Electric Vehicles
PCC	Point of Common Coupling
PFC	Power Factor Correction
PI	Proportional Integral
PWM	Pulse Width Modulation
RESs	Renewable Energy Sources
RMS	Root Mean Square
SiC	Silicon Carbide
SCRs	Silicon-Controlled Rectifiers
SPWM	Sinusoidal pulse width modulation
SWTs	Small Wind Turbines
SAE	Society of Automotive Engineers
SSTs	Solid-State Transformers
SVM	Space Vector Modulation
SFDR	Spurious-Free Dynamic Range
SoC	State of Charge
THD	Total Harmonic Distortion
UFC	Ultra-Fast Charging
V	Voltage
V2G	Vehicle to Grid
V2H	Vehicle-to-Home
VCO	Voltage-Controlled Oscillator
VSC	Voltage Source Converter
WBG	Wide Bandgap
ZVS	Zero Voltage Switching

CHAPTER ONE
INTRODUCTION

1.1 Introduction

With the rapid growth of energy consumption, large-scale utilization of new energy sources such as wind power, solar power, and fuel cells has emerged as a fundamental way to address human energy problems. Due to their randomness and volatility, large-scale renewable sources have caused significant fluctuations in power systems. Different approaches have been explored to charge Electric Vehicles (EVs) solely from carbon-free sources. During fast charging, extremely high power is required from the charging station, which negatively impacts the grid through voltage dips, power losses, and harmonics. This problem has been addressed by implementing hybrid (grid and renewables) charging stations [1]. As renewable energy sources, such as solar photovoltaic (PV) systems, are gaining popularity to reduce dependency on grid. To improve coordination between the power grid and the control framework, integrating EVs into a hybrid charging station offers a more effective interaction approach [2]. The control of the system is very complicated when the solar PV system is integrated with the DC bus [3],[4]. Hence, a suitable control algorithm is required to implement a hybrid charging station. Although the term “fast charging” is not strictly defined, the concept of fast battery charging implies that in an approximately 10-minute-long charging cycle, an EV’s battery gains enough energy to increase the car’s cruising range of about hundred kilometres (i.e., almost 15 kWh). Nevertheless, this charging type, which requires massive power densities in a low battery’s voltage range (400–800 V), makes power electronics involved in the charging system unique or even impractical for on-board implementation. Fast charging mainly refers to off-board dc charging stations with rated power equal to or higher than 50 kW [5].

In this perspective, fast DC charging provides a fascinating opportunity as it significantly reduces charging time. The off-board charger is made to interface directly to the EV battery pack without any further intermediate stage of an on-board charger [6]. Off-board chargers typically support multiple charging points, accommodating different charging standards. The off-board chargers are either a unidirectional or a bidirectional system with the grid support vehicle to grid vehicle-to-grid (V2G) capability [7]. The long charging time and the lack of adequate charging stations are two impediments to large-scale adoption of EVs. These issues are mainly addressed by the level 3 charging concept, which is also known as off-board direct current fast charging (DCFC). EV charging systems are typically classified into three levels based on power delivery and charging speed. Level 1 charging uses a standard 120V AC household outlet, offering slow charging typically suitable for overnight use at home [8]. Level

2 charging utilizes a 240V AC source and is common in residential garages and public charging stations, offering faster charging than Level 1 [9]. Level 3 charging, also known as DC fast charging, delivers high-voltage direct current (DC) directly to the EV battery, bypassing the onboard charger [10]. This enables rapid energy transfer and significantly reduces charging time, making it ideal for commercial and highway applications where quick turnaround is essential [11]. The Level 3, Off-board DC fast charging provides a fascinating opportunity and reduces charging time [12]. The off-board charger requires an ac-dc and/or dc-dc conversion system that directly connects to the EV battery pack without any further intermediate stage of an on-board charger [13]. The energy stored in the battery during low demand should discharge back to the grid when the renewable energies are not available. To realize the energy storage and bidirectional power transfer, exploring converters with the ability of two-way power transfer is a critical factor in the system. A bidirectional AC-DC converter is a fundamental requirement for the energy storage system and two-way power transfer between the EV and the grid. According to the application, different types of converters can be used [14]. A DC-DC step-up unit and a bidirectional DC-DC stage are also essential between the AC source and energy storage battery to provide additional voltage regulation. The development of EV makes it possible for lithium batteries to be widely used as an energy storage system. As a result, the grid-injected power can be stabilized. [15] investigated the use of batteries and supercapacitors to balance the output power of renewable energy sources, demonstrating improved dynamic performance in power stabilization. This study is highlighted here as an example of energy storage integration, while other related works are discussed in subsequent sections to provide a comprehensive overview.

This research presents the model of a DC fast electric vehicle charging station connected to the PV-tied grid system three-phase constant voltage source ensuring quality power transfer with reduced currents and voltage ripples. The charging station consists of a converter connecting grid to a DC bus where EVs get connected through battery chargers. An energy management strategy based on optimal power flow is also proposed by integrating a solar PV generation system with a charging station to alleviate the impact of DC fast charging on the grid. The combined system along with the power output of EV fleet batteries available at the charging station reduces the net energy provided by the grid, thereby decreasing the overall load on the grid as well as minimizing the conversion losses. The maximum power point of the PV system is tracked by using perturbation and observation method. Secondly, the EV lithium battery is connected to DC bus via a bidirectional DC-DC converter which use a Proportional Integral controller (PI). The last objective of this study is to develop simulation models of a high-performance DC fast charging station system for EVs in Simulink/MATLAB.

1.2 Statement of the research problem

The purpose of this research is to present the challenges of DC fast charging for electric vehicles (EVs) and to investigate their potential impacts on power quality. The rapid growth of the EV market, driven by rising fuel costs and environmental concerns, has created new and increasing load demands on the electrical grid. Long-distance driving and fast-charging capabilities can lead to sudden peaks in power demand, which may adversely affect the stability and reliability of the distribution system. DC fast charging of EVs can have detrimental effects on traditional power grids, including increased current and voltage ripples, harmonics in line currents, and DC offset. The nonlinear behavior of EV chargers, together with variations in charging rates, further impacts power quality. Daily fluctuations in EV fast charging power demand, as illustrated in Figure 1.1, also contribute to load variability and stress on the grid. These problems can reduce the performance and lifetime of distribution network equipment and significantly affect the reliability, security, efficiency, and economy of smart grids.

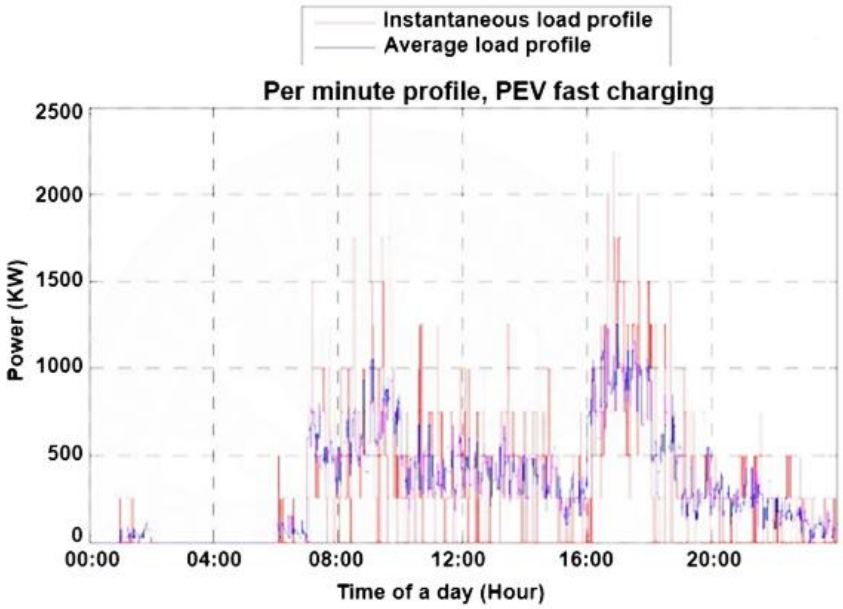

Figure 1.1: Change of the power electric vehicle fast charging in one day [16]**.**

Based on these observations, the main research problems addressed in this thesis can be summarized as follows:

- High load demand and peak power issues: Fast-charging EVs can create sudden peaks in power demand, especially during peak hours, which can overload the distribution system.
- Power quality degradation: DC fast charging introduces current and voltage ripples, harmonics, and DC offsets, which can compromise grid stability.

- Impact of AC-DC converters: The power quality issues caused by AC-DC converters used in EV chargers require careful investigation.
- Charging time optimization: The slow or uneven charging rates, particularly during peak periods, need strategies to mitigate grid stress.
- High ripples in charging current: These can reduce EV battery lifetime, decrease station efficiency, and impair overall system performance.
- Integration with smart grids: EV charging behavior can affect the reliability, efficiency, and economic operation of emerging smart grid systems.

Similar studies and projects, such as the ones developed by [17]–[19], have analyzed these issues to provide data and methodologies for modeling and mitigation strategies. This thesis builds on such work to investigate the interactions between fast-charging EVs and power quality, and to propose solutions that address the challenges outlined above.

1.3 Research significance

Several studies and projects have investigated DC fast charging for EVs and identified various challenges associated with off-board DC fast-charging stations. The main significance of this research is to demonstrate how developing an optimized DC fast-charging station can address key issues, including reducing charging time and mitigating the impact on the electrical grid during peak hours. Another critical challenge addressed in this research is the high ripples in charging current, which can adversely affect the performance and lifetime of EV batteries. The design and control of DC-DC converters play a central role in minimizing these ripples and enhancing the lifetime of energy storage systems. This research contributes to improving the efficiency, reliability, and performance of DC fast-charging stations, highlighting its advantages over existing approaches in the literature.

1.4 Objective and scope

In this study, the development of a high-performance off-board DC fast charging system for EVs, which uses PV-tied grid and storage system, to increase the availability, efficiently and reliability of the rapid charging station as well as overcome the ripple current, the proposed system showing the effect of employing energy storage devices on performance of the charging station.

To achieve these objectives, this thesis focuses on the following aspects:

1) Developing a model system of DC fast charge EVs using a hybrid power source to consider the inter-relationship between EV load needs, PV production, local storage energy levels and the grid.
2) Designing and implementing bidirectional power conversion topologies for the different power sources.

3) Coordinated Control Design: Design a coordinated control strategy to enhance charging performance, ensure system stability, and minimize current ripples. Specifically:
    - Develop a unity power factor control for the front-end AC-DC converter (grid/PV interface).
    - Design a PI controller for the bidirectional DC-DC converter connected to the battery storage.
    - Implement the Perturb and Observe (P&O) algorithm for the DC-DC boost converter associated with the PV system to support overall DC bus stability.
4) Developing an energy storage system (ESS) to reduce the charging cost and low-utilization loads.
5) Simulation Environment Development: Develop detailed simulation models of the proposed high-performance DC fast-charging station for EVs using the MATLAB/Simulink environment to evaluate system performance and validate the proposed designs.1.5 Research methodology

The research methodologies of this study focus on the development and implementation of a DC fast-charging system for EV station-based DC microgrids to address slow charging rates and mitigate current ripples. EV charging can impose additional stress and overloading on the power grid, which has motivated researchers to design fast-charging stations that integrate renewable energy sources (RESs), such as PV systems, with the utility grid and energy storage devices. High-voltage direct current (HVDC) PV-tied grid systems have become increasingly popular for DC fast-charging stations due to their high efficiency and relatively low cost. In such systems, DC-DC converters play a critical role, performing functions such as stepping up low-voltage PV output to high-voltage DC for the bus and stepping down high-voltage DC for low-voltage applications. The integration of PV with a three-phase utility grid, combined with appropriately designed converter topologies and coordinated control methods, enhances the efficiency of the converters. Specifically, control techniques such as PI controllers for DC-DC converters and Maximum Power Point Tracking (MPPT) for PV systems help to optimize power flow, reduce voltage and current ripples, and improve both dynamic and steady-state performance. Additionally, DC-AC converters are employed to interface with AC loads or the utility grid, further improving output efficiency and reliability of the fast-charging station. Through these coordinated power electronics and control strategies, the proposed system achieves higher efficiency, better power quality, and superior performance during fast-charging operation, while minimizing the impact on the distribution network.

The proposed system of off-board DC fast charging station contains the source supply of PV-tied grid through an LC filter, a three-phase rectifier followed by front end converter, a DC-DC

converter, and a bidirectional converter using PI controller and P&O algorithm technique connect to a DC bus and battery storage system. The proposed DC fast charging system configuration for an electric vehicle is demonstrated in Figure 1.2. This thesis presents the study conducted, and the developed model is used with MATLAB/Simulink and Typhoon HIL software. The simulation results are analysed to evaluate the performance of the proposed development.

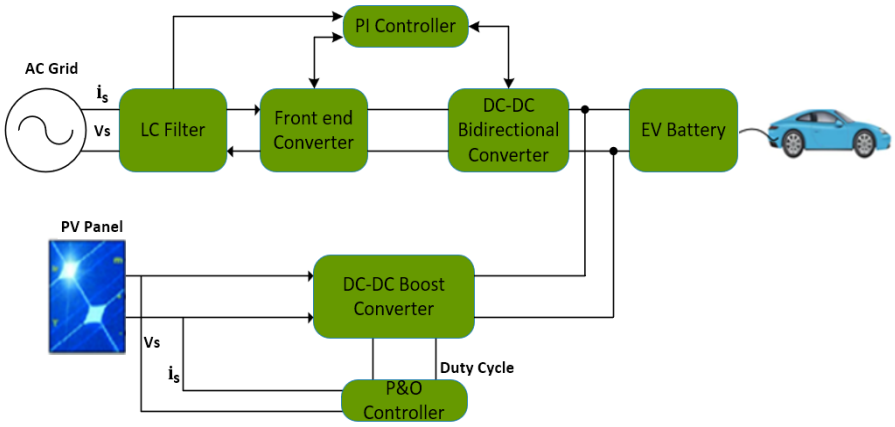

Figure 1.2: DC fast charging system configuration for electric vehicle.

1.6 Organization of the thesis

Chapter one began with an introduction to the background of the thesis by presenting the development of DC fast charging used for electric vehicles, highlighting the research problem and its significance. The aims and objectives were clearly defined, guiding the investigation throughout. The thesis structure was outlined to provide a logical flow of the research. Finally, the contributions of this research were reinforced through published works that emerged from the study.

Chapter Two provided an in-depth review of EV charging technologies, highlighting recent advancements, emerging challenges, and key trends in response to global EV adoption were discussed. It explores different charging methods, including inductive, ultra-fast, and DC fast charging, along with the required infrastructure. The chapter emphasizes improvements in charging speed, the integration of renewable energy to minimize dependence on fossil fuels, and the role of energy management strategies, V2G technology, and energy storage systems in maintaining grid stability. Additionally, it discusses the importance of standardized charging protocols and efficient battery management systems, evaluating various charging architectures such as AC, DC, and hybrid microgrids. Lastly, the chapter outlines the ongoing evolution of EV charging technologies and the research efforts aimed at overcoming challenges related to infrastructure costs, charging efficiency, power quality, and energy sustainability, contributing to a more reliable and eco-friendly charging network were presented.

Chapter Three deals with the development and modeling of a DC fast charging system for electric vehicles, presenting a detailed mathematical analysis of its key components. The system is structured into three main stages: the PV stage, the AC grid stage, and the charger stage, all working together to ensure efficient and reliable charging. The PV stage includes a solar array and a DC-DC boost converter with MPPT to optimize solar energy utilization. The AC grid stage features a front-end converter and a PI controller to regulate energy flow and maintain grid stability. The charger stage integrates a Dual Active Bridge (DAB) bidirectional DC charger with a PI controller to enhance charging performance and facilitate bidirectional power flow for grid and home integration.

A DC bus interconnects these stages, maximizing renewable energy utilization while improving charging efficiency and grid stability. The lithium-ion battery model for EVs incorporates a voltage source, internal resistance, and RC networks to simulate dynamic charging and discharging under fast charging conditions. The Battery Management System (BMS), developed using the Constant Current Constant Voltage (CCCV) method, ensures battery protection and efficiency. It was designed to monitor the state of charge (SoC) and manage power distribution between the sources and battery load demand at fast charging stations. Finally, a MATLAB/Simulink model was implemented to simulate and validate the system's performance.

Chapter Four evaluated the developed DC fast charging system for EVs, which incorporated a PV-tied grid, energy storage, and advanced control strategies through MATLAB/Simulink simulations. The system’s performance was tested under various case scenarios, demonstrating stable hybrid power integration, efficient bidirectional power conversion, minimized voltage and current ripples, and reduced reliance on the grid.

The results showed how variations in Park transform gain, VCO parameters, and RL filter inductance influenced stability, power quality, and grid synchronization. The boost converter’s performance was analyzed under different SoC conditions, confirming stable power output and effective MPPT using the P&O algorithm. The system exhibited low total harmonic distortion, strong transient and steady-state performance, and improved charging efficiency. Furthermore, the use of advanced control techniques, such as PI controllers and harmonic compensation strategies, validated the system’s reliability. The integration of an energy storage system and grid-tied converters further enhanced cost efficiency and power stability, confirming the system as a viable high-performance DC fast charging solution.

Chapter five concludes key findings from previous chapters of this thesis and offers some recommendations for further research work.

1.7 Publications

The following publication emanated from this doctoral research:

- Zentani, A. Almaktoof, A.M.A. & Kahn, M.T.E. 2025. Performance Evaluation and Control Stability Analysis of a DC Fast Charging System for Electric Vehicles. IET Power Electronics, currently under review.
- Zentani, A. Almaktoof, A.M.A. & Kahn, M.T.E. 2025. Exploring Review of Advancements in Fast - Charging Techniques and Infrastructure for Electric Vehicles Revolution. Energy Science & Engineering: 1–11.
- Zentani, A. Almaktoof, A.M.A. & Kahn, M.T.E. 2024. A Comprehensive Review of Developments in Electric Vehicles Fast Charging Technology. Applied Sciences (Switzerland), 14(11).
- Zentani, A. Almaktoof, A.M.A. & Kahn, M.T.E. 2024. Control Technique of MPPT Utilizing for Boost Converter Applied to Small Renewable Energy System and a DC Microgrid for Remote Area. 2024 IEEE 4th International Maghreb Meeting of the Conference on Sciences and Techniques of Automatic Control and Computer Engineering, MI-STA 2024 - Proceeding, (May): 245–250.
- Zentani, A. Almaktoof, A.M.A. & Kahn, M.T.E. 2022. DC-DC Boost Converter with PO MPPT Applied to a Stand-Alone Small Wind Turbine System. Proceedings - 30th 29 Southern African Universities Power Engineering Conference, SAUPEC 2022: 1–5.
- Zentani, A. Almaktoof, A.M.A. Kahn, M.T.E. & Elmezughi, M.K. 2022. An Effectual Control Technique for Islanded Operation of a Step-Up Power Converter Fed by Small Wind Turbine System. 2022 International Conference on Electrical Engineering and Sustainable Technologies, ICEEST 2022 - Proceedings: 1–6.

1.8 Summary

This chapter provided the foundational context for the research on DC fast charging technology for electric vehicles. It outlined the research problem and highlighted the significance of the study in addressing current challenges in the field. The chapter also clearly stated the research aims and objectives and presented an overview of the thesis structure. Finally, a list of publications derived from this research was included, demonstrating the contribution of the study to academic discourse.

CHAPTER TWO
LITERATURE REVIEW

2.1 Introduction

As fossil fuel resources dwindle and environmental and pollution-related health concerns intensify, the adoption of hybrid electric vehicles (HEVs) and EVs is gaining significant global attention. The success and widespread acceptance of EVs, which are the primary focus of this research, largely depend on the efficiency and speed of their charging processes, as well as the driving range that these vehicles can achieve. The global EV market has the potential for substantial growth if charging stations can offer fast and reliable services, making EV charging as convenient and quick as refuelling traditional combustion vehicles. EVs are playing a crucial role in the electrification of transportation and are becoming increasingly prevalent. Consequently, there is a clear need for more charging stations to support this rapid growth. The number of charging stations, including fast chargers and standard chargers, is on the rise, and new technologies such as wireless fast chargers are under development. However, several challenges must be addressed, including the cost of infrastructure, EV mileage range, charging time, availability of fast chargers, and power quality issues. The primary goal of introducing EVs to the market is to reduce greenhouse gas emissions and promote environmental sustainability. However, a significant portion of the energy required to charge EVs still comes from fossil fuel-based sources. To align with environmental goals, it is essential to power EVs using RESs such as wind turbines and solar panels. To manage grid constraints during peak load periods, integrating energy storage systems and implementing V2G technology can help stabilize the grid. The former is more practical, as V2G relies on EV owners being willing to sell back excess energy from their batteries, which is less likely due to concerns about battery lifespan. Given the demands of EVs, it is crucial to develop fast chargers that not only reduce charging time and cost but also minimize current ripple to stabilize the energy storage systems of EVs. The SAE J1772 standard categorizes EV chargers into three levels based on power output: Level 1, Level 2, and Level 3 also known as DC Fast Charging.

Level 1 chargers are primarily used for home-based charging with a power rating of up to 1.4 kW (120V) supply and up to 2 kW for a 230 V supply. This is the slowest charging method, utilizing a single-phase grounded outlet and taking between 4-8 hours to fully charge an EV, depending on the grid voltage level.

Level 2 chargers are common in both private and public settings. They charge depleted batteries with rated power from 3.6 kW to 19.2 kW for a 208 V to 240 V supply within 1 to 6 hours.

Level 3 chargers offer DC fast charging with a maximum power rating of up to 400 kW for a 50 V to 1000 V supply, significantly reducing the charging time to less than 1 hour. This charging mode is suitable for highway charging stations and city charging points.

Level 1 and Level 2 chargers are more appropriate when charging duration is not a priority. In contrast, Level 3 chargers, which are the focus of this research, are used for fast charging processes. Fast charging, which can fully charge a battery within a short period (i.e., an hour), requires charging with a current higher than the battery's rated capacity. The charging time for electric vehicles can be significantly reduced by transferring higher currents to the battery, a process known as ultrafast charging. However, while high current reduces charging time, it can also negatively affect battery polarization and lifespan. For example, the maximum tolerable charging current for lithium-ion batteries is often expressed in terms of the *C-rate*, where *1C* corresponds to charging the entire battery capacity in one hour. Thus, *2C* indicates charging at twice the battery's rated capacity (e.g., a 30 Ah battery charged at 60 A). The allowable charging current varies depending on the specific battery chemistry and design, and manufacturers specify these limits. Fast and ultrafast charging modes also impose substantial loads on power grids. Charging a 30-kWh EV within an hour, for instance, generates a load nearly twenty times that of a typical home's hourly energy consumption. This significant demand can create high transients at the bus where the EV charger is connected, leading to serious issues for power grids, such as overloading, transients, regulatory voltage violations, and harmonics [20].

Fast and ultrafast EV charging present even greater challenges in islanded microgrids. In these systems, where power generation relies primarily on renewable energy sources, the limited and variable power supply can struggle to meet high load demands consistently. Connecting bulk loads like fast/ultrafast chargers to an islanded microgrid can destabilize the system, especially in the face of load variations, source intermittency, and parameter uncertainties.

2.2 Advanced fast charging techniques for electric vehicles

Research and development in fast charging techniques for EVs are becoming increasingly crucial as they aim to significantly reduce charging times and enhance the overall convenience of EV ownership [21]. According to the International Energy Agency's (IEA) 2022 report, global electric car sales have experienced a remarkable increase, comprising 14% of all new car purchases, up from 9% in 2021 and less than 5% in 2020. In the first quarter of 2023, over 2.3 million electric cars were sold, marking a 25% increase from the previous year. According to the IEA, nearly 14 million electric vehicles (battery-electric and plug-in hybrids) were registered globally in 2023, making up approximately 18% of all new car sales. Under their stated policies scenario, electric car sales are forecasted to reach about 35% globally by 2030 [22], [23]. This rising popularity emphasizes the necessity for efficient fast charging methods to support

widespread EV adoption. As EV adoption grows, addressing the time required to recharge EV batteries becomes a critical challenge. A survey by McKinsey & Company revealed that 80% of EV owners consider the availability of fast charging to be essential in their purchase decisions [24], [25]. Fast charging infrastructure is also vital for commercial sectors like taxi fleets and delivery services to minimize vehicle downtime and improve operational efficiency. Significant advancements in fast charging systems for EVs have been made to meet the growing demand for high-power charging, enabling shorter charging times compared to traditional methods. Key fast charging techniques include inductive charging, ultra-fast charging, DC fast charging, Tesla Superchargers, bidirectional charging with V2G (vehicle-to-grid) integration, and battery swapping as illustrated in Figure 2.1.

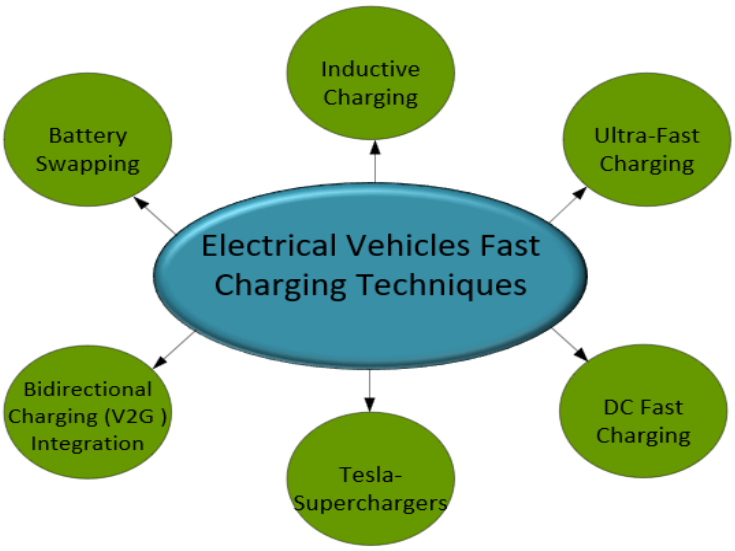

Figure 2.1: EV charging techniques.

2.2.1 Inductive charging

Inductive charging, also known as wireless charging, eliminates the need for physical cables by using an electromagnetic field to transfer energy between a ground-based charging pad and a receiver on the EV [26]. Although not as fast as some wired methods, it offers significant convenience by allowing automatic charging without connecting cables [26]. The concept, rooted in Nikola Tesla's early 20th-century experiments, is now utilized in smart cities for e-mobility, employing inductive power transfer (IPT) and capacitive power transfer (CPT) [27], [28]. Enhancements in IPT efficiency focus on optimizing coil design, alignment, and electromagnetic field shielding. Despite potential safety risks like foreign object hazards and moderate weatherproofing, inductive charging simplifies the connection process and is scalable. However, its efficiency is lower than traditional methods due to energy losses in the magnetic field. Static inductive charging systems, often found in parking lots and traffic lights,

achieve up to 85% efficiency by converting AC power through a high-frequency inverter to create an electromagnetic field that induces AC power in the vehicle's receiver coil. Misalignment issues, which can reduce efficiency, are a significant focus of ongoing research [29]–[32]. Dynamic inductive charging, or on-the-go charging, enables vehicles to charge while in motion using coils embedded in the road and mounted on the vehicle chassis. This technology, currently under exploration in various pilot projects, aims to extend EV range for long-distance travel [33], [34].

2.2.2 Ultra-fast charging (UFC)

Ultra-fast charging (UFC) technology significantly reduces EV charging times by delivering high power levels, typically exceeding 350 kW, to the vehicle's battery [35], [36]. This makes EV charging more comparable to refuelling a conventional vehicle and helps alleviate range anxiety [37], [38]. UFC systems employ advanced control strategies, such as Constant Current (CC) and Constant Voltage (CV) modes, along with temperature monitoring for efficient power delivery and battery management. Although still in the early stages of deployment and less widespread than traditional infrastructure, the number of UFC stations is increasing, particularly along major highways [39]. To support these high power levels, both the charging infrastructure and EVs require advancements in station design and battery technology. Automakers and charging providers are developing UFC technologies and introducing new standards like Combined Charging System (CCS) and CHAdeMO 3.0 to support higher power levels [40], [41]. Ongoing research aims to further improve charging speeds, infrastructure, and battery technologies. While UFC offers unparalleled convenience with rapid charging times and minimal user interactions, it also poses safety concerns, particularly the risk of overheating [39]. Therefore, precautions are necessary to prevent such incidents. UFC stations are designed to be moderately weatherproof, ensuring reliable operation in various conditions. However, their widespread availability is limited, and compatibility is primarily restricted to newer EV models. High charging currents associated with UFC can also lead to slightly accelerated battery degradation over time. Nevertheless, the scalability and upgradability of UFC stations are significant advantages, allowing for future modifications to support even faster charging speeds. Despite their high efficiency, some energy loss still occurs during the charging process.

2.2.3 DC fast charging (DCFC)

DC fast charging, or level 3 charging, is a high-power method that delivers DC electricity directly to an electric vehicle's battery, bypassing the on-board charger used in slower AC methods [42], [43]. It utilizes advanced control strategies like CC and CV modes and temperature monitoring to ensure safe and efficient charging. DC fast charging systems, with

power outputs ranging from 50 kW to 350 kW, can drastically reduce charging times to as little as 30 minutes or less for a full charge, depending on the vehicle's battery capacity and the charging power level [10], [44], [45]. The global expansion of DC fast charging infrastructure, particularly along highways and in urban areas [46], [47], helps mitigate range anxiety and supports broader EV adoption. However, charging capabilities vary based on the vehicle model and battery technology, influencing charging rates and maximum power support [48], [49]. While DC fast charging offers faster charging times compared to standard AC methods, it requires some user interaction and prioritizes thermal management to avoid overheating. These systems are moderately weatherproof and widely integrated into existing infrastructure at dedicated charging stations. DC fast charging is compatible with most EV models, though not universally. The high charging currents can lead to slightly accelerated battery degradation compared to slower methods. Nevertheless, the stations are scalable and upgradable, allowing for future enhancements to deliver even higher power outputs. Despite their high efficiency, some energy loss occurs during the conversion process inherent to DC fast charging.

2.2.4 Tesla superchargers

Tesla Superchargers are specialized fast-charging stations designed exclusively for Tesla vehicles, providing up to 250 kW of power and potentially adding 200 miles of range in just 15 minutes [50]. However, actual charging rates can vary due to factors like battery level and temperature [51]. These chargers employ various control strategies for optimal performance and safety, including constant current/voltage modes and advanced communication protocols. Tesla continually improves its Supercharger network, expanding stations and increasing charging capacity to enhance convenience and reduce range anxiety for Tesla owners. While Superchargers offer rapid charging and a user-friendly experience, access is limited to Tesla vehicles, and some energy loss occurs during charging

2.2.5 Bidirectional charging integration

Bidirectional charging, or vehicle-to-grid integration, enables electric vehicles to both draw energy from and discharge stored energy back into the grid, making them mobile energy storage resources [52]. This concept supports grid stability, load management, and renewable energy integration through advanced communication and control systems [53]. Successful implementation relies on compatible infrastructure, communication protocols, and regulatory support. While bidirectional charging offers convenience and moderate weatherproofing, it requires careful management due to added complexity. Integration depends on the availability of compatible charging stations and home setups, limiting widespread accessibility [53], [54]. Some EVs can be made compatible with additional hardware, but universal compatibility across all models is lacking. Although it may slightly accelerate battery degradation, future

upgrades could improve scalability and efficiency. Despite its advantages, bidirectional charging tends to be less efficient than other faster charging methods due to additional conversion steps [55], [56].

2.2.6 Battery swapping

Battery swapping offers a solution to long charging times by allowing drivers to exchange depleted batteries for fully charged ones quickly, typically taking just a few minutes. This benefits fleet management and long trips by reducing downtime [56]. Dedicated swapping stations use advanced automation and communication technologies to ensure safe and efficient operations [57]. Advantages include reduced charging times, convenience, and potentially lower battery degradation [58]. However, challenges such as standardization and infrastructure costs need to be addressed for widespread implementation. While generally safe, standardized procedures and automated mechanisms ensure safety during swapping. Battery swapping stations are designed for repeated swaps and offer moderate weatherproofing. However, their integration with existing infrastructure is limited, and compatibility depends on EVs having compatible battery packs. Battery degradation may occur slightly faster due to handling and thermal stress during swaps. Despite its advantages, expanding a swapping network can be slower than upgrading charging stations, although battery swapping boasts high efficiency, with some energy loss occurring during handling and charging/discharging cycles.

2.3 Electric Vehicle Battery Chargers Categories and Integrated Fast-Charging Stations

Electric vehicle battery chargers can be classified based on their charging capabilities, physical configurations, and intended applications as either on-board or off-board chargers. On-board chargers are integrated within the vehicle, and their capacity determines the charging rate, making them compatible with various charging infrastructures. Off-board chargers, external units found in public and private charging points, offer a higher charging rate and are essential for situations where on-board charging is impractical. The limitations of on-board charging, such as during long-distance travel or the need for faster charging, underscore the importance of off-board chargers in providing quick and accessible solutions. Integrating a battery storage system into a fast-charging station extends its functionality, benefiting different applications. This integration, achieved using a DC-DC converter connected to the DC link of the fast-charging station, allows independent control of the battery voltage and power. During station battery charging mode, a single DC-DC converter is sufficient to regulate power flow to the local energy storage system. In contrast, during EV battery charging mode, two DC-DC converters are employed to regulate power transfer between the DC link and the EV battery, although this mode operates with slightly lower efficiency. This setup supports peak shaving

operations, buffering high power peaks to reduce grid stress, and enables fast-charging at grid connection points with limited power availability, ensuring continuous high-power charging events.

2.3.1 On-board charging

On-board charging (ON-BC) in electric vehicles entails converting external AC power into DC power to charge the vehicle's battery pack. This essential process relies on various components, such as rectifiers and transformers, to ensure that charging is both safe and efficient [40]. The on-board charger (ON-BC), typically integrated into the vehicle's powertrain or located near the battery pack, can be built into the vehicle or included as part of the charging cable [59], as illustrated in Figure 2.2. Common charging methods include Level 1, using standard outlets, and Level 2, utilizing dedicated charging stations that offer higher voltage. On-board charging offers convenience, enabling EVs to be charged at home, work, or other accessible locations. Level 1 charging (120 volts) is economical, while Level 2 (240 volts) provides greater flexibility without the need for specialized infrastructure [8]. Owners can charge their vehicles wherever suitable outlets or stations are available [60]. Popular models and manufacturers of on-board chargers include the Tesla Supercharger, which offers fast-charging capabilities for Tesla vehicles; the Nissan CHAdeMO, compatible with the Nissan Leaf for fast charging at CHAdeMO-equipped public stations; the BMW i3, which supports both AC and DC charging for flexibility at various public stations; and the Chevrolet Bolt EV, with an on-board charger capable of accepting both AC and DC charging for fast charging at compatible public stations.

On-board chargers offer several advantages and disadvantages, such as the ability to charge anywhere with an outlet, and the integration of an on-board rectifier to control the battery management system (BMS). However, they have a lower rate of energy transfer (kW), resulting in slower charging times. Additionally, they add weight and size to the vehicle, and their compatibility with charging infrastructure is limited. Specific outlets may be required, and potential battery heating issues can arise.

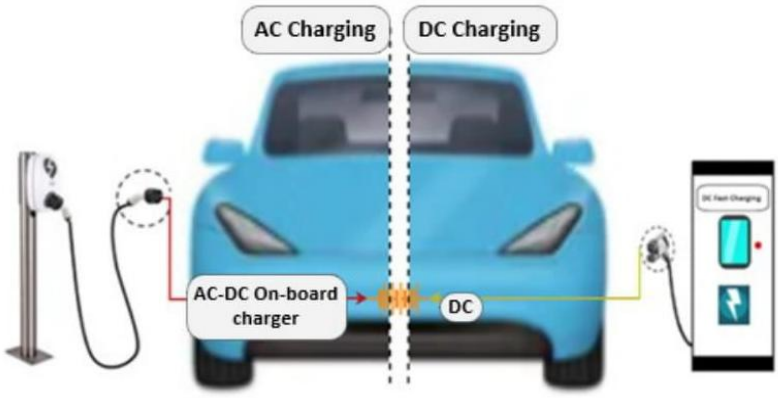

Figure 2.2: Illustrated on-board/off-board EVs fast charging.

2.3.2 Off-board charging

Off-board charging (OFF-BC) involves replenishing EV batteries at external stations or infrastructure, rather than within the vehicle itself [61], as shown in Figure 2.2, Researchers are particularly interested in off-board and DC-based charging methods for their potential to improve power quality and efficiency [4]. Common methods include public charging stations, DC fast charging (Level 3), and wireless inductive charging [62]. These methods are more efficient due to fewer conversion stages, especially with a DC power supply, which avoids the need for AC-DC conversion and power factor correction. Although DC chargers are not yet widely adopted in EVs, they hold promise for integrating solar PV power. Some studies propose dual-input EV chargers that can utilize both AC grid power and standalone PV systems, operating in grid-connected mode during low solar irradiation and in V2G mode during idle hours [63]. Off-board chargers can be categorized into isolated and non-isolated converters; isolated converters are preferred at higher voltage levels, while non-isolated topologies are feasible for lower power levels [10], [64], [65]. Examples of off-board chargers include the Tesla Supercharger network, strategically placed along highways and major routes to provide high-speed charging for long-distance travel. Public charging points often offer both Level 2 AC chargers and DC fast chargers, commonly found in parking lots and commercial premises for convenient access. Additionally, industries provide fast-charging stations supporting multiple standards like CCS and CHAdeMO, primarily located along major highways and urban areas. Many EV owners also install home charging stations, typically Level 2 AC chargers, in their garages or driveways for convenient overnight charging or during low electricity demand periods.

In contrast, Off-board chargers offer several advantages and disadvantages provide a higher energy transfer rate (kW) and faster charging speeds. They enable charging at higher power levels and reduce the weight within the vehicle. Off-board chargers can potentially enhance

BMS systems and address battery heating problems. However, they offer limited flexibility, as they require compatible charging stations. They also present challenges with the battery management system, higher costs and complexity, accountability of charging stations, and limited ability to identify defective battery cells.

2.4 Advanced Infrastructure for DC Fast Charging of Electric Vehicles

A crucial aspect of the evolving electric vehicle landscape involves the development of advanced infrastructure for fast DC charging. This consists of implementing state-of-the-art systems and technologies that enable efficient and fast charging of electric vehicles [66]. Table 2.1 provides the power level charging ratings and classification standards of the different charging stations. The levels are categorized based on the supply system, maximum power rating (in kW), and maximum current rating (in A). DC fast charging, commonly referred to as Level 3 charging, offers much faster charging times [40]. It makes use of a higher-voltage power supply, often in the 400 to 800 volt range, which makes it possible for EVs to charge significantly more quickly, frequently providing up to 80% charge in as little as 20 to 30 min for a 200-mile range [40]. This thesis focuses on DC fast chargers, as illustrated in Figure 2.3.

Figure 2.3: EV DC Charger stations.

Table 2.1: Power level charging rating [67], [68]

Level of Charging Rating (A)	Supply System	Maximum Power Rating (kW)	Maximum Current Rating (A)

Level 1 (AC) (IEC*)	240 V	4.7	16
Level 2 (AC) (IEC*)	240 V	11.5	32
Level 3 (AC) (IEC*)	415 V	90	250
Fast DC Charging (DC) (IEC*)	600 V	150	400
Level 1 (AC) (SAE**)	120 V	2	16
Level 2 (AC) (SAE**)	208–240 V	20	80
Level 3 (AC) (SAE**)	300-920 V	120-350	500
Fast DC Charging (DC) (SAE**)	−400 V		

*International Electrotechnical Commission (IEC), **Society of Automotive Engineers (SAE).

The trend involves integrating renewable energy sources and energy storage systems into fast-charging networks to reduce their environmental impact and bolster sustainability. Planning approaches, simulation models, and optimization techniques are scrutinized to refine charging station locations and grid integration. Vehicle-to-grid technology is gaining attention for its potential to ease the strain on the power grid and enhance reliability. However, detailed assessments of its operational mode in planned stations are limited. Integrating V2G into fast charging infrastructure planning is emerging as a strategy to optimize power system analyses, although current research often side lines this aspect in favour of prioritizing losses and voltage stability [32]. Many important elements and factors contribute to the sophisticated infrastructure needed for DC fast charging. Below are several crucial aspects of the charging standards and charging modes control.

2.4.1 Charging standards

The creation and observance of charging standards are essential elements in the field of advanced infrastructure for DC fast charging [40], [69]. For owners of EVs, charging standards enable compatibility, interoperability, and seamless charging experiences across multiple charging networks and hardware providers [70]. The significant standards for EV charging systems are presented in Table 2.2, along with some crucial points about the charging specifications for cutting-edge DC fast charging infrastructure.

Table 2.2: Major standards of EV charging systems [71]–[75]

Standard	Description
IEC 60038	Specifies the standard voltage levels used for electrical power systems and charging applications.

IEC 62196	Standards conductive charging components for connectors, cables, outlets, plugs, inlets, and communication protocols used in AC charging of electric vehicles.
IEC 60664-1	Insulation coordination for equipment within low-voltage systems.
IEC 62752	Provides guidelines for connecting electric vehicles to information and communication technology, ICT, networks.
IEC 61851	Covering various charging modes, communication protocols, and safety features.
SAE J1772	Requirements for the electrical connectors and communication protocols for Level 1 and Level 2 charging used for AC charging of electric vehicles in North America.
SAE J2344	Provides guidelines and test procedures for evaluating the crashworthiness and safety of electric vehicle battery systems.
SAE J2894/2	Requirements for the power quality and conductive charge coupler used in DC fast charging electric vehicles.
SAE J2953	Standards for interoperability to provide guidelines for conductive automated charging systems for electric vehicles.
SAE J2847/1	Communication between vehicles as a distributed energy source and the grid.
SAE J3068	Wireless power transfer for light-duty plug-in/electric vehicles and alignment methodology.
SAE J2931/7	Evaluating the electrical performance of components used in hybrid and electric vehicles.
ISO* 15118	Standards for V2G communication protocols and interfaces between vehicle and charging infrastructure.
ISO* 17409	Specifications and reliable measurement of energy consumption allow for accurate comparisons and evaluations of different EV models.

***** International Organization for Standardization (ISO).

2.4.1.1 Organizations for standardization

International bodies like the International Electrotechnical Commission (IEC), the Society of Automotive Engineers (SAE), and the International Organization for Standardization (ISO) are frequently responsible for developing and maintaining charging standards [76]. These groups work with industry participants to establish technical requirements and charging protocol standards for EVs.

2.4.1.2 Charging connector types

Various connector types and setups have been examined to ensure a dependable and safe link between the charging station and the electric vehicle. Commonly utilized connectors for DC fast charging include CHAdeMO and CCS [42], connectors [74]. These connectors guarantee compatibility between EVs made by various manufacturers and the charging infrastructure.

2.4.1.3 Communication protocols

Communication protocols that enable data transmission between the charging station and the EV are also included in charging standards. These protocols allow for essential features to be controlled, including identification, control over power distribution, and real-time monitoring of charging conditions [75]. The Open Charge Point Protocol (OCPP) and ISO 15118 are two instances of communication protocols [77].

2.4.1.4 Power level and charging speeds

The power levels and charging speeds enabled by the infrastructure are defined by charging standards. DC fast charging power levels can vary from 50 kW to several hundred kW, facilitating rapid charging durations [78]. Guidelines have established the upper limits for power and voltage to ensure safe and efficient charging procedures.

Table 2.3 provides a comprehensive overview of the specifications for commercial Plug-in Hybrid Electric Vehicles, Fuel Cell Electric Vehicles (FCEVs), and Extended-Range Electric Vehicles (E-REVs). Key details encompass a variety of vehicle models, classification by powertrain type, battery capacity measured in kilowatts (kW), driving range expressed in kilometres (KM), and connector types required for charging.

Table 2.3: Specifications of commercial electric vehicles [17], [77], [79]–[82]

Category	Model	Type	Battery (kWh)	Range (Km)	Connector
Plug-in Hybrid (PHEV)	Chevrolet Volt	PHEV	18.4	85 (battery)	Type 1 J1772
	Mitsubishi Outlander	PHEV	20	84 (battery)	CCS, Type 2
	Volvo XC40	PHEV	10.7	43 (battery)	CCS, Type
	Toyota Prius Prime	PHEV	8.8	40 (battery)	SAE J1772
	Nissan Leaf	PHEV	64	480	CHAdeMO, Type 2
Electric Vehicle (BEV)	Tesla Model S	BEV	100	620	Supercharger
	Tesla Model X	BEV	100	500	Supercharger
	Tesla Model 3	BEV	82	580	Supercharger
Fuel Cell Electric Vehicle (FCEV)	Toyota Mirai	FCEV	1.6 (hydrogen capacity)	647	N/A
	Hyundai Nexo	FCEV	40 (hydrogen capacity)	570	N/A
	Honda Clarity	FCEV	25.5 (hydrogen capacity)	550	N/A

Extended Range Electric Vehicle (E-REV)	BYD Atto3	E-REV	60.4	420 (battery)	CCS, Type 2

2.4.2 Charging modes control

Charging modes are crucial in the field of modern fast charging infrastructure for maximising charging effectiveness and catering to the various needs of EV owners [77]. “Charging modes” refers to the many power distribution and charging methods used with DC fast charging infrastructure. The battery charging process curve is shown in Figure 2.4, which illustrates the constant-current constant-voltage (CCCV) charging method commonly applied to lithium-ion batteries. In this process, the blue line represents the charging current profile, which is initially maintained at a constant level during the constant-current phase before gradually decreasing in the constant-voltage phase. The red line represents the battery voltage profile, which increases steadily during the constant-current phase and is then held constant during the constant-voltage phase until the battery reaches full charge.

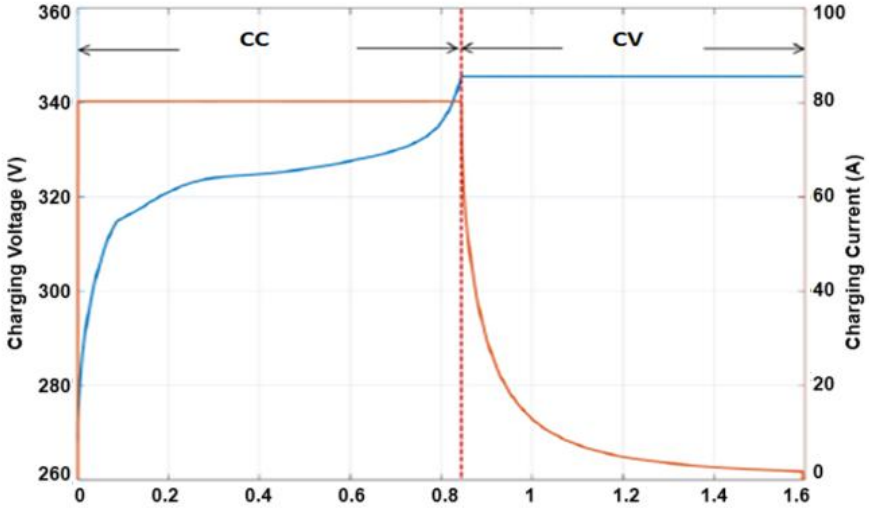

Figure 2.4: Battery charging process curve showing battery voltage (red line) and charging current (blue line) under the constant-current/constant-voltage (CCCV) method.

2.4.2.1 Constant current charging

In this mode of control, the charging station feeds the EV battery a steady current while it is being charged. During the initial phases of charging, when the battery’s SoC remains relatively low, this mode control method is frequently employed [78]. Constant current charging facilitates faster charge rates, ensuring prompt replenishment of the battery’s capacity.

2.4.2.2 Constant voltage charging

As the battery's SoC reaches a predefined level, the charging station transitions to constant voltage charging. In this control mode, the charging station gradually reduces the charging current while sustaining a consistent voltage. Constant voltage charging is employed during the final stage to prevent overcharging the battery and ensure its longevity. Throughout this stage, the charging system continuously monitors the battery voltage and adjusts the current to prevent it from surpassing the designated level.

2.4.2.3 Constant power charging

The constant power charging mode adjusts the current and voltage to uphold a consistent power level throughout the charging procedure. This mode optimizes the charging speed and ensures an efficient utilization of available resources by dynamically adapting the charging conditions based on the battery's status and temperature [79]. When the battery's SoC is low, it enables quicker charging rates and automatically lowers the charging power when the battery gets close to capacity. Dynamic power control also enables load management and helps balance the power demand and supply within the charging infrastructure.

2.4.2.4 Demand–response charging

Demand–response charging capabilities may be included in advanced DC fast charging infrastructure. With this mode of control, the charging station can dynamically modify the charging power depending on the capacity of the grid and the electricity demand [17]. Reducing the charging power during heightened demand or when the electrical grid is strained allows for grid resources to be utilized efficiently.

2.4.2.5 Bidirectional flow charging

Bidirectional power flow is supported by cutting-edge fast charging infrastructure, allowing energy to be transmitted to and from the EV's battery. By employing this capability, EVs receive grid-based charging and discharge energy back into the grid or supply power to other consuming devices [80]. Vehicle-to-grid applications, where EVs can help to stabilise the grid and offer grid services, may be supported via bidirectional charging [81]. Different charging modes are implemented in sophisticated DC fast charging infrastructures, giving EV owners and grid operators flexibility and optimisation options based on battery state, grid limitations, and user choices; it also enables efficient charging [70]. EVs may be charged quickly while preserving battery health, grid stability, and economical power usage by utilising the correct charging mode. Furthermore, intelligent charging algorithms and communication protocols that enable real-time monitoring, control, and coordination of the charging process are frequently used in conjunction with charging modes [82]. These characteristics facilitate grid integration, optimise power distribution, and guarantee secure and dependable charging operations.

Implementing charging modes within advanced DC fast charging infrastructure enhances the user experience for electric vehicle owners during charging sessions. Additionally, it promotes optimal energy utilization and contributes to the broader adoption of EVs as a sustainable transportation option [83].

2.4.2.6 Temperature monitoring and control

DC fast charging produces heat because of the substantial charging currents it employs. Temperature monitoring and control techniques have been implemented to safeguard the battery against overheating. Temperature sensors are positioned inside the battery pack to monitor its temperature throughout the charging process [84]. The charging system utilizes these data to modify charging parameters like current or voltage, ensuring the battery remains within safe temperature thresholds. This practice is crucial for preserving optimal battery performance and extending its longevity [85]. The good news is that advancements in lithium-ion batteries continue to be made, opening doors for next-generation options like solid-state batteries. Material research is key to overcoming challenges and making electric vehicles more sustainable. By focusing on improving the heat resistance of materials, using venting mechanisms, and employing eco-friendly bio-based flame retardants, researchers are working to prevent thermal runaway, a critical safety concern.

2.4.2.7 State of charge (SoC) estimation

Accurate estimation of the battery's SoC is crucial for efficient charging. Control strategies utilize algorithms and models to estimate the SoC based on various parameters such as voltage, current, and temperature measurements [4], [63], [86]. These methods consider the battery's discharge and charge characteristics to provide a reliable estimate of its state of charge [86]. SoC estimation helps regulate the charging process, ensuring the battery is neither undercharged nor overcharged [87].

2.5 Planning EV Charging Infrastructure in Power Distribution Networks

The integration of EV charging systems into distribution systems (DS) requires meticulous planning to ensure grid stability and efficiency. This involves assessing the current grid capacity, potential load impacts, and the need for infrastructure upgrades to accommodate the increased demand from EVs. Advanced grid modelling and simulation techniques are employed to predict the effects of EV charging on load profiles, voltage stability, and transformer loading [88]. Effective planning considers the optimal placement of charging stations to minimize distribution losses and improve reliability. Coordination between utilities, policymakers, and EV charging providers is essential to develop strategies that enhance grid resilience while meeting the growing demand for EV charging.

2.5.1 Strategic planning for EV charging in transportation systems

Planning EV charging systems within the transportation system focuses on ensuring accessibility and convenience for EV users. This involves identifying strategic locations for charging stations, such as urban centres, highways, and public transport hubs, to create a comprehensive and user-friendly charging network [89]. Planners consider traffic patterns, travel behavior, and EV adoption rates to determine optimal station placement. Additionally, integrating EV charging infrastructure with public transportation systems can encourage multimodal transportation solutions, reducing overall traffic congestion and emissions. Collaboration with city planners, transportation authorities, and private stakeholders is crucial to develop an efficient and sustainable charging network that supports the mobility needs of EV users.

2.5.2 Managing uncertainties in EV charging infrastructure planning

Uncertainties in EV charging system planning stem from several factors, including varying EV adoption rates, technological advancements, user behavior, and regulatory changes. These uncertainties can significantly impact demand forecasts, infrastructure requirements, and investment decisions [90]. Scenario analysis and probabilistic modeling are employed to address these uncertainties, allowing planners to evaluate different outcomes and develop flexible strategies. Sensitivity analysis helps identify critical variables that influence charging demand, enabling more robust planning. By considering a range of potential scenarios and their implications, planners can design adaptable and resilient EV charging systems that accommodate future changes and uncertainties in the EV market.

2.5.3 Incorporating distributed generation into EV charging network planning

Integrating distributed generation (DG) sources, such as solar and wind, into EV charging system planning offers significant benefits for enhancing sustainability and reducing reliance on centralized power plants. This approach involves incorporating renewable energy generation at or near charging stations, which can provide a local and clean energy supply for EVs [91]. Hybrid systems that combine DG with energy storage solutions can further enhance reliability and efficiency. Planning for DG integration requires assessing local renewable energy potential, grid connectivity, and the technical compatibility of DG systems with charging infrastructure. By leveraging distributed generation, EV charging systems can achieve greater energy independence, lower carbon footprints, and improved grid stability. Collaboration between renewable energy developers, utilities, and EV infrastructure providers is essential to successfully integrate DG into EV charging system planning [92].

2.5.4 Integration of renewable energy sources with EV charging facilities

Various charging architectures exist for EVs, including hybrid power sources (combining renewable energy, battery storage systems, and the grid) or a dedicated single power source. This prompts an examination of the advantages of hybrid sources over a single power source for fast charging EVs [93]. Numerous strategies are proposed to enhance the integration of RES with the electricity grid for EV charging. Key benefits include (i) lowering the cost of fast charging EVs through the use of free electricity generated by RES, and (ii) decreasing fuel consumption by the grid [94]. Additionally, the EV charging process can be maintained under unfavourable weather conditions by either directly charging from the main grid or utilizing RES in case of grid failure to meet the necessary electrical demands. Moreover, installing batteries as energy buffers can store excess RES energy. The energy generated can be fed back into the grid to provide ancillary services or to support EV charging. However, connecting renewable energy sources to the grid typically involves higher penetration levels compared to stand-alone RES installations. The main grid serves as a stable source/load to balance RES fluctuations [95]. Among these sources, solar energy is particularly advantageous for EV charging because it can generate energy during peak power tariff hours, reducing charging costs. Photovoltaic modules are favored for their simple structure, small size, lightweight, ease of transport, and straightforward installation. They also have a short construction period and can be flexibly combined to meet various charging capacities, making them suitable as on-site sources. However, PV energy production is highly influenced by ambient temperature and irradiation levels, leading to discontinuous and intermittent power generation throughout the day [96]. Directly connecting PV panels to the load without auxiliary systems can negatively impact the charging system's performance. Therefore, energy storage systems are crucial for stabilizing and mitigating the variability of solar power output. This thesis proposes integrating a lithium-ion battery energy storage system (BESS) with the PV array to ensure continuous and reliable power delivery to the EV load, even under fluctuating solar conditions. The BESS operates as a buffer: it absorbs surplus PV generation during periods of low demand and discharges during PV shortages or high charging demand. In this way, the storage system supports power smoothing, peak-shaving, and grid assistance, thereby improving overall charging station reliability. The coordinated operation of the PV system, BESS, and the utility grid not only enhances renewable energy utilization but also reduces dependency on grid supply, contributing to lower operational costs, improved system efficiency, and increased availability of fast charging services.

2.6 Advanced Control Architecture for EV Charging Stations

Fast EV charging stations are critical infrastructure for connecting electric vehicle users to the power grid. A well-designed station, incorporating renewable energy sources and supported

by energy storage systems, can not only provide convenient charging but also contribute to cost-effective grid operation. Here's a breakdown of key aspects in the hierarchical control of such stations:

a. Advanced energy management:

i. This involves optimizing charging schedules and power delivery based on real-time factors.
ii. The system considers the SoC of energy storage units to ensure efficient utilization of renewable energy and minimize reliance on the main grid.
iii. This can involve using algorithms and machine learning to predict charging demand and optimize energy flows.

b. Dynamic power balancing:

i. The control system constantly monitors and adjusts power flow to maintain a stable equilibrium between electricity generation including renewables and the charging load from EVs.
ii. This helps prevent overloading the grid and ensures reliable power delivery for both charging and other grid functions.

c. Precise output regulation:

i. This ensures the charging system delivers the correct voltage and current to connected EVs.
ii. The hierarchical control system regulates these outputs based on individual EV needs and pre-defined charging protocols.
iii. This maintains safe and efficient charging for all connected vehicles.

d. Improvements of the Hierarchical Control Architecture:

i. Focus on real-time optimization: The original text mentioned reference generation based on SoC, but advanced systems go beyond pre-defined references. They use real-time data and predictions to dynamically optimize energy management.
ii. Highlight renewables and storage: The updated text emphasizes the role of renewable energy sources and energy storage in cost-effective and sustainable charging infrastructure.
iii. Clearer breakdown of functions: The three key aspects are explained in more detail to provide a clearer picture of the hierarchical control system's functionalities.

Hierarchical control for EV charging systems is an advanced approach to managing and optimizing the charging process, designed to address the complex demands of EV charging

infrastructure. This control structure is typically divided into three levels: primary, secondary, and tertiary controls, each with distinct functions and objectives. This hierarchical control for EV charging systems integrates these three levels to create a comprehensive and efficient management structure, ensuring that EV charging is safe, efficient, and well-coordinated with the broader energy system. The hierarchical control is depicted in Figure. 2.5.

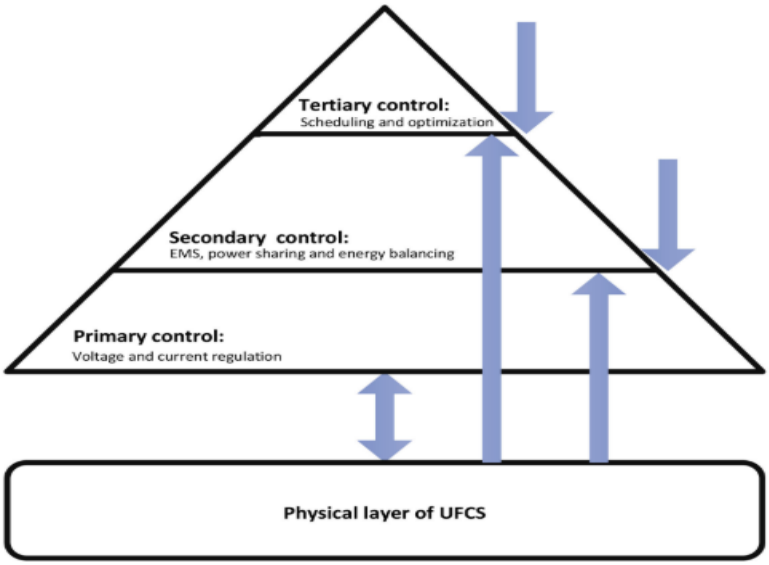

Figure 2.5: Hierarchical control of EV charging stations [97].

2.6.1 Primary control

The primary control level is responsible for managing real-time operations and ensuring an immediate response to local conditions. It performs functions such as real-time adjustment, where it manages the instantaneous charging power and adjusts it based on real-time conditions [98]. For example, if an EV battery is nearly full, the system reduces the charging power to prevent overcharging. It also handles voltage regulation, ensuring that the voltage supplied to the EV is stable and within the acceptable range to protect both the vehicle and the charging equipment. Safety protections are included in this level, which involves immediate safety features such as shutting down the charger in case of faults like short circuits or overheating to protect users and equipment. The speed of response at this level must react within milliseconds to seconds to ensure stable and safe operation. Primary control operates locally at each charging station, enabling it to quickly respond to specific conditions without waiting for instructions from higher levels.

2.6.2 Secondary control

The secondary control level coordinates and balances the load among multiple EV chargers, ensuring system stability. It manages load distribution by distributing the charging loads across

a network of chargers to prevent overloading any single charger or segment of the grid, allocating power based on demand and availability [99]. State of Charge management is another function, where it monitors the SoC of connected EVs and prioritizes charging for those with lower SoC to ensure efficient use of resources. Additionally, secondary control integrates renewable energy and storage by utilizing local renewable energy sources (e.g., solar panels) and energy storage systems to supplement grid power, optimizing energy use and reducing reliance on fossil fuels [100]. This level coordinates with the local grid to balance supply and demand, reducing the strain on the grid during peak hours by scheduling charging during off-peak times. It also uses battery storage systems to buffer excess renewable energy, ensuring a steady supply even when renewable sources are intermittent.

2.6.3 Tertiary control

The tertiary control level handles long-term planning, economic optimization, and strategic decisions. It optimizes charging schedules by planning and scheduling charging sessions based on factors such as electricity prices, grid conditions, and user preferences, aiming to minimize costs and maximize efficiency [101]. Predictive analytics and demand forecasting use advanced algorithms to predict future demand and supply conditions, enabling proactive management of the charging infrastructure. Additionally, tertiary control manages V2G operations, which involves managing bidirectional energy flow, allowing EVs to return stored energy to the grid during high-demand periods, thus supporting grid stability and reliability [102].

2.7 Fast-Changing Technologies and Hybrid Energy Charging System Architectures

Charging electric vehicles involves drawing power from the electrical grid and converting it to a form that is suitable for the vehicle's battery system using power electronics. This process is illustrated schematically in Figure 2.6. Depending on the specific charging method, the required power conversion equipment may be located either on-board the EV or off-board in the charging infrastructure. The implementation of this conversion process varies based on the type of grid supply (AC or DC) and the battery system in the EV. Currently, the standard grid supply for end-users is AC, but there is potential for DC grids to become more common in future EV charging applications.

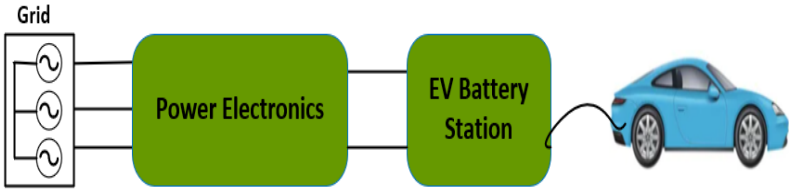

Figure 2.6: Generalized charging system.

Electric vehicles continue to gain significant traction globally due to their role in reducing transportation emissions. Modern commercial EVs commonly use high-voltage battery packs, ranging from 400V to 800V, with a growing trend towards even higher voltages exceeding 800V [103]. These higher voltages enable the use of proportionally lower currents to achieve the same power transfer. This translates to lighter and more compact cables and connectors within the vehicle. Additionally, utilizing the maximum rated charging current significantly reduces charging times, approaching the refuelling speeds of conventional gasoline vehicles [104]. The selection of a power conversion system for EV charging goes beyond just battery voltage and grid type. It also considers whether the system needs to support bidirectional power flow, enabling features like V2G applications where EVs can feed power back into the grid [105]. The charging system components can reside entirely within the EV on-board charger, entirely within the charging station off-board charger, or use a combination of both [106]. Connections between EVs and the grid can be established through conductive charging (plugs) or inductive charging (wireless) [107]. While fast-charging systems are typically off-board due to the weight, size, and cost of high-power electronics, advancements are being made to address these limitations. Research is ongoing to minimize the drawbacks of on-board chargers by leveraging the existing traction inverter power electronics already present in most EVs. This could lead to a future where faster charging capabilities can be integrated directly into EVs, offering more flexibility and convenience for users.

DC fast chargers (DCFC) can connect to the grid through AC or DC distribution, each offering distinct advantages and considerations [47]. In AC distribution systems, a transformer is used to step down medium-voltage AC to a lower-voltage AC bus (typically 250–480 V). The operating frequency depends on the region, being 60 Hz in North America and 50 Hz in many other parts of the world. Each DCFC unit then uses its own AC-DC converter to generate the high-voltage DC required for EV batteries. This approach utilizes mature and readily available technology but has drawbacks such as increased conversion stages, reduced efficiency, and higher system complexity. Despite these challenges, AC distribution remains popular due to its established technology and lower upfront costs, exemplified by Tesla's Supercharger station in Mountain View, California, and ABB's DC fast charger in Euroa, Australia. On the other hand, DC distribution uses a central AC-DC converter to create a high-voltage DC bus, typically below 1000V, to serve all DCFC units at the station [108]. Each charger connects directly to the DC bus using a DC-DC converter, eliminating the need for individual AC-DC stages, which improves efficiency, simplifies control, streamlines grid connection, and enhances scalability. However, challenges include a lack of established standards and the need for effective protection and metering systems for high-voltage DC buses. The choice between AC and DC distribution depends on factors such as initial investment costs, desired efficiency, scalability

plans, and regulatory environment. While AC distribution offers lower upfront costs and established technologies, DC distribution presents a more efficient and potentially scalable solution. As standards for DC bus protection and metering evolve, DC distribution is likely to become increasingly popular for new DCFC station deployments [109]. Furthermore, hybrid source-based charging system architectures for EVs are emerging as a promising solution to address the limitations of traditional single-source charging methods [110]. These systems combine the reliability of grid power with the sustainability of renewable energy sources, offering a more resilient and environmentally friendly approach to EV charging. They leverage advanced power electronics and energy management strategies to optimize the distribution and utilization of available energy, ensuring efficient and stable charging [111]. Key components include multi-source converters, smart controllers, and energy storage systems, which collectively enhance the flexibility and efficiency of the charging process. The review highlights significant advancements in hybrid architectures, such as the development of algorithms for dynamic source allocation and real-time energy optimization. Additionally, the integration of V2G capabilities allows EVs to not only draw power from the grid but also feed excess energy back into it, further enhancing grid stability and promoting renewable energy usage [112]. Despite the advantages, challenges remain in terms of cost, complexity, and the need for robust infrastructure to support hybrid systems. Research indicates a growing trend towards the deployment of hybrid charging stations, particularly in regions with high renewable energy potential. Integrating battery storage systems (BSS) with photovoltaic panels is gaining traction due to its ability to provide stable and cost-effective power for EV charging stations [113]. This approach involves a microgrid where a BSS is connected to both PV panels and the main grid to supply power for EV chargers. Independent power converters ensure efficient conversion for each source (PV, BSS, grid) and the EV chargers themselves. The three main hybrid power source architectures for EV charging include DC microgrids with DC/DC converters connecting PV, BSS, and grid to a common DC bus, which then connects to the grid via a bidirectional AC-DC converter; AC microgrids where each source (PV, BSS, grid) has its own rectifier converting power to AC for a common AC bus feeding the EV chargers; and hybrid AC-DC microgrids combining elements of both DC and AC microgrid approaches. EV charging stations can be classified based on their AC-DC operation, location, power rating, and charging time. Decentralized AC charging stations, typically found in parking spaces, use a plug-and-charge approach with a low current (around 15A) and require 5-8 hours or more for a full charge [114]. Conventional charging stations, located near business districts, offer medium or fast charging, with conventional charging taking 3-4 hours and fast charging using DC taking less than 30 minutes to 2 hours, reaching states of charge exceeding 80% with currents between 150A and 400A [115]. Large charging stations, equipped with multiple chargers and battery storage, can charge many EVs simultaneously, offering regular and fast

charging, centrally charging the BSS (usually slow charging), and participating in V2G applications for grid stability [116]. The demand for EV charging varies depending on factors like economics, lifestyle, climate, and location. To optimize charging infrastructure and grid integration, researchers are exploring how different types of RES can be combined with charging stations [117]. Decentralized stations and distributed RES, often found in residential areas or public spaces, are well-suited for integration with rooftop solar panels (photovoltaic systems or PV) due to their decentralized nature and flexible charging patterns, particularly relevant in rural areas. Conventional stations and distributed RES can integrate with one or more distributed RES systems depending on the local weather, utilizing small wind turbines (SWTs) in regions with strong winds and solar panels in areas with abundant sunlight. Large and medium stations and RES production cater to commercial and passenger vehicles with predictable driving patterns and parking locations, establishing a direct connection with larger RES sources like nearby solar plants, promoting local renewable energy consumption. Regardless of the specific energy sources used, hybrid microgrid configurations for EV charging stations show great potential. These microgrids combine multiple sources, such as PV and BSS, to ensure a stable and cost-effective power supply. This dissertation explores a microgrid-based approach in which a BESS is coordinated with PV generation and the utility grid to supply EV fast chargers. Each source and charging unit is interfaced through dedicated power converters, providing operational flexibility, fault isolation, and enhanced control. Three microgrid architectures are reviewed: DC microgrids with a common DC bus, AC microgrids with a common AC bus, and hybrid AC–DC microgrids that combine the benefits of both. Among these, the dissertation emphasizes the DC microgrid configuration due to its suitability for EV fast charging, reduced conversion stages, and compatibility with DC-based energy storage and PV generation.

2.7.1 A Medium voltage DC fast charger for EV with a common AC bus

One approach to integrating RES with EV charging stations is through AC microgrids Figure 2.7. In this setup, solar panels, BSS, and EV chargers all have separate converters. AC microgrids offer flexibility for connecting various power sources like PV and the grid, but they require multiple power conversions, leading to efficiency losses. Despite this, they are popular due to advantages like direct connection to the existing AC grid using a common AC bus, simplifying integration with conventional grids and equipment. AC microgrids with a Point of Common Coupling (PCC) switch on the AC bus enable V2G functionality, allowing EVs to feed power back to the grid during low-demand periods [118].

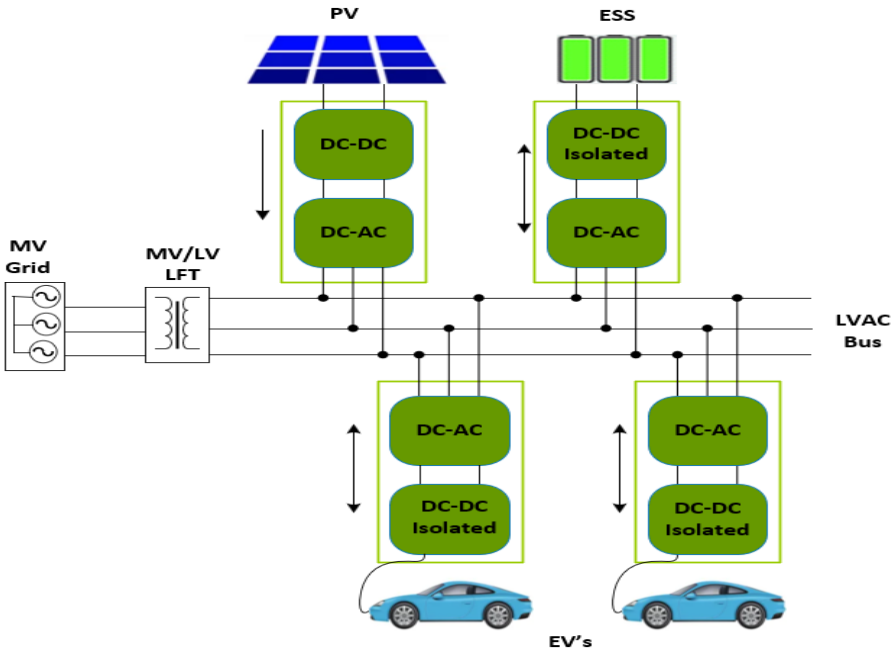

Figure 2.7: A DC's LFT-base architectures. Station with common AC bus.

On the other hand, a Medium Voltage DC Fast Charger (MVDCFC) with a common Medium Voltage AC (MVAC) bus designed to facilitate high-power fast charging for EVs. This MV AC bus setup ensures efficient power distribution and minimizes the need for multiple low-voltage transformers, leading to improved system efficiency [119]. The Medium Voltage AC Bus typically operates at voltage levels ranging from 11kV to 33kV and connects to the grid to supply power to multiple chargers. This configuration reduces the need for numerous low-voltage transformers, enhancing power distribution efficiency. The common bus architecture integrates multiple chargers on a common MVAC bus, providing scalability to add more chargers as demand grows and offering redundancy for a reliable power supply with redundant configurations [120]. High conversion efficiency reduces energy losses and efficient power distribution with a common MVAC bus enhances overall performance. The modular design allows easy expansion, making it suitable for large-scale EV charging stations. This system is cost-effective, reducing infrastructure costs by minimizing the need for low-voltage transformers and lowering installation and maintenance costs due to fewer components. The robust design with multiple protection features ensures reliability, and redundant power supply configurations further enhance reliability. Applications for this setup include public charging stations, where it is ideal for large EV charging hubs, fleet charging, suitable for commercial fleets requiring rapid turnaround, and urban infrastructure, perfect for integrating into city power grids to support widespread EV adoption [121]. This Medium Voltage DC Fast Charger with a

common Medium Voltage AC bus provides a highly efficient, scalable, and reliable solution for the growing demand for fast EV charging infrastructure.

2.7.2 A Medium voltage DC fast charger for EV with a common DC bus

DC microgrids offer an innovative and efficient alternative for EV charging stations as shown in Figure 2.8, by utilizing direct solar panel power through a common DC bus, minimizing conversion losses and maximizing efficiency. A simplified control system manages voltage and power flow through the DC bus, coordinating energy sources like PV, BSS, and the grid [122]. A central inverter/rectifier connects the DC bus to the AC grid, enabling V2G functionality and managing power flow imbalances between PV generation and EV charging demands. Advantages of DC microgrids include reduced system costs and improved efficiency due to fewer conversion stages, elimination of reactive power leading to higher transmission capacity and reduced losses, inherent reliability, and simplified operation [123].

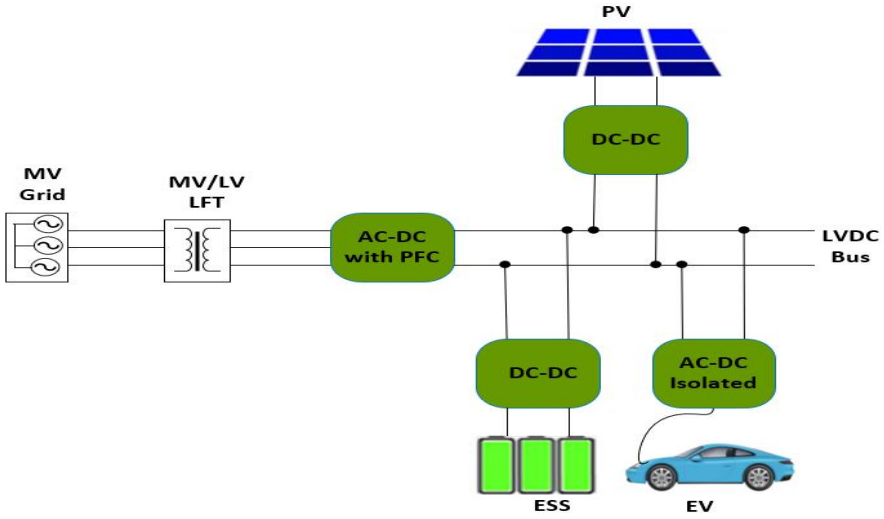

Figure 2.8: A DC's LFT-base architectures for station with common DC bus.

In contrast, modern DC fast chargers, designed for high-power fast charging of EVs, employ either AC-Link or DC-Link architectures to connect to the MVAC grid:

1. **AC-Link architecture:** Utilizes multiple independent AC-DC rectifiers connected to the MVAC grid via a step-down low-frequency transformer (LFT). This setup allows various loads and distributed energy sources (DESs) to connect independently, enhancing reliability and system stability but increasing complexity and cost due to harmonic effects during high-power operations [124].
2. **DC-Link architecture:** Uses a single AC-DC conversion unit from the LFT to create a shared DC distribution bus, simplifying power conversion stages and improving overall

system efficiency. The DC-Link system integrates well with RESs and ESSs, reducing power conditioning issues and offering superior performance in terms of power quality, charging rate, efficiency, and stability compared to AC-Link architectures [125].

The Medium Voltage DC Fast Charger with a common Medium Voltage DC (MVDS) bus designed to enable high-power fast charging for electric vehicles. This system improves power distribution efficiency and reduces the need for multiple low-voltage transformers, leading to a more streamlined and efficient setup. The Medium Voltage DC Fast Charger with a common Medium Voltage DC bus allows for efficient and scalable charging infrastructure [126]. This system integrates several charging units connected to a common MVDC bus, simplifying the overall design and enhancing performance. The Medium Voltage DC bus typically ranges from 1 to 35kV, connecting to the power grid and distributing DC power to multiple chargers, enhancing power distribution efficiency by reducing the need for AC-DC conversion at each charger [127]. The Medium Voltage DC Fast Charger can have a power rating from 150 kW to 350 kW per charger, with an output voltage up to 1000V DC, suitable for fast charging a wide range of EVs, featuring high DC-to-DC conversion efficiency. High DC-to-DC conversion efficiency reduces energy losses and efficient power distribution with a common MVDC bus enhances performance [128]. The robust design with multiple protection features ensures reliability, and redundant power supply configurations further enhance reliability. Applications for this setup include public charging stations, where it is ideal for large EV charging hubs, fleet charging, suitable for commercial fleets requiring rapid turnaround, and urban infrastructure, perfect for integrating into city power grids to support widespread EV adoption. This Medium Voltage DC Fast Charger with a common Medium Voltage DC bus provides a highly efficient, scalable, and reliable solution for the growing demand for fast EV charging infrastructure [10].

2.7.3 A Medium voltage DC fast charger for EV with a common hybrid AC-DC bus

The hybrid AC-DC microgrid depicted in Figure 2.9 is emerging as a promising solution for integrating EVs and renewable energy sources (RES) into charging infrastructure. These microgrids simultaneously cater to both AC and DC loads, allowing EVs to connect via a primary DC-DC converter for fast charging or to feed power back to the grid. They also support conventional AC chargers and stations through the AC grid. Hybrid systems feature an interlinked power converter (ILC) that manages power transmission and energy balance between the AC and DC sides, operating in rectification or inverter mode as needed [129].

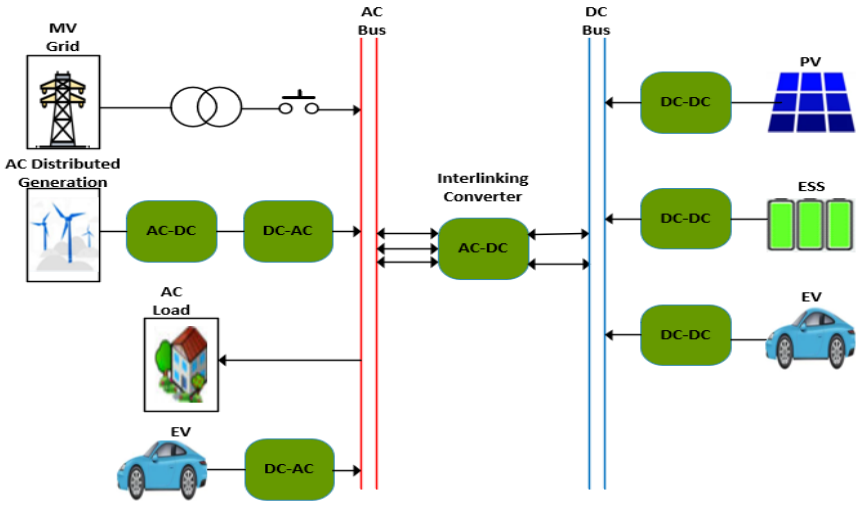

Figure 2.9: Hybrid AC-DC microgrids.

The common bus architecture integrates multiple chargers on a common MV AC-DC bus, providing scalability to add more chargers and other loads as demand grows and offering redundancy for a reliable power supply with redundant configurations [130]. It also features multiple protection mechanisms such as over-voltage, over-current, short-circuit, and thermal protection, and meets international standards for safety and performance, such as IEC and UL. The benefits of this setup are numerous. High conversion efficiency reduces energy losses and enhanced power distribution with a hybrid AC-DC microgrid improves overall performance. The modular design allows for easy expansion, making it suitable for large-scale EV charging stations and other hybrid microgrid applications [120]. This system is cost-effective, reducing infrastructure costs by minimizing the need for multiple low-voltage transformers and converters and lowering installation and maintenance costs due to fewer components. The robust design with multiple protection features ensures reliability, and redundant power supply configurations further enhance reliability. Applications for this setup include public charging stations, where it is ideal for large EV charging hubs that require both AC and DC power, fleet charging, suitable for commercial fleets requiring rapid turnaround and flexible power management, and urban and rural infrastructure, perfect for integrating into city and rural power grids to support widespread EV adoption and other hybrid microgrid applications. This Medium Voltage DC Fast Charger with a common Medium Voltage Hybrid AC-DC Microgrid provides a highly efficient, scalable, and reliable solution for the growing demand for fast EV charging infrastructure [126].

2.8 State-of-The-Art in EV DC Charging Solutions

The advancement of solid-state transformers (SSTs) is set to significantly enhance the future of DC and ultra-fast EV charging. Unlike traditional bulky transformers, SSTs offer compact,

lightweight alternatives that simplify construction, reduce installation space, and improve performance [131]. SSTs provide higher efficiency, leading to lower energy losses and reduced operational costs for charging stations and EV users. Furthermore, their advanced control features, such as improved current regulation, enhance safety and contribute to grid stability [132].

2.8.1 Solid-State Transformers (SSTs) for EV DC Charging

SSTs also enable the seamless integration of DC loads into the charging ecosystem through a common DC link. For instance, battery storage systems can store excess renewable energy for use during peak times, and solar panels can be incorporated for more sustainable charging. Figure 2.10, classifies SSTs by various design aspects, showing how different topologies such as single-phase single-port converters, multi-level converters, and modular systems can be adapted to specific applications. Despite the advantages, SST technology faces challenges, primarily due to the high material costs and complex design requirements for high-voltage grids. Expensive components like Silicon Carbide (SiC) MOSFETs are often required, adding to the cost. However, promising research results indicate that SST-based systems can achieve efficiencies above 95% and power ratings of up to 350 kW. As research continues to address cost and high-voltage challenges, SSTs are expected to play a critical role in the future of EV charging infrastructure, paving the way for more efficient, cost-effective, and sustainable charging solutions.

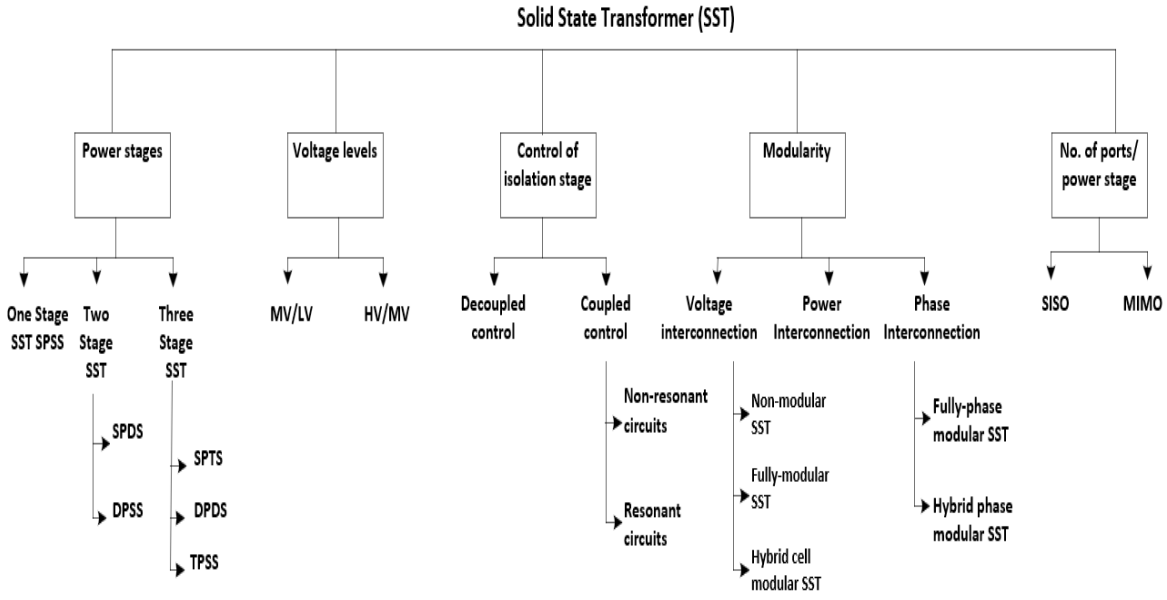

Figure 2.10: Classifications of SST [133]**.**

In recent years, advancements in SST technology have revolutionized the design of DC fast chargers for electric vehicles. While traditional DC fast chargers relied on bulky 60Hz transformers for voltage conversion, SSTs have provided a more efficient and compact alternative. The traditional approach involved a two-stage process: first, an AC-DC rectification stage with Power Factor Correction (PFC) converted the medium voltage (MV) AC input to a lower voltage DC [134]. Then, a DC-DC conversion stage further regulated the DC voltage to the specific level required for EV battery charging. Figure 2.11 illustrates a single-module charger lacking galvanic isolation between the grid and the EV. It comprises a low-frequency transformer, input filter, AC-DC rectifier, non-isolated DC-DC converter, and battery load. While potentially reducing costs and size, this configuration raises safety concerns due to the absence of isolation, limiting its suitability for certain applications.

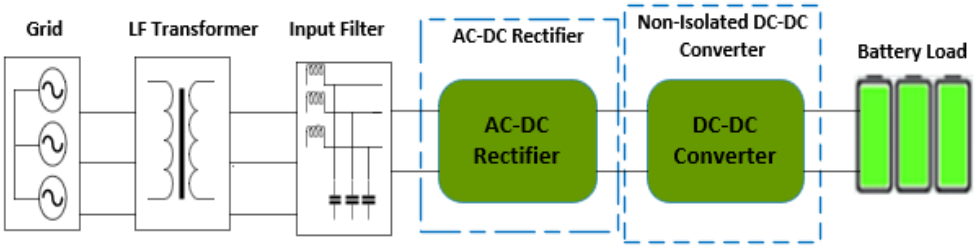

Figure 2.11: Single module charger with non-isolated dc-dc converter.

A single-module charger with an isolated DC-DC converter illustrated in Figure 2.12, is a sophisticated system designed to provide safe, reliable, and efficient charging for EV batteries. This system includes several key components that work together to condition the power from the grid and provide galvanic isolation. The input filter is the first component in the system, reducing Electro-Magnetic Interference (EMI) and harmonics from the AC grid. It ensures that the charger does not introduce significant noise back into the grid and complies with Electromagnetic Compatibility (EMC) standards. Typically, the input filter consists of inductors and capacitors that filter out high-frequency noise and harmonics.

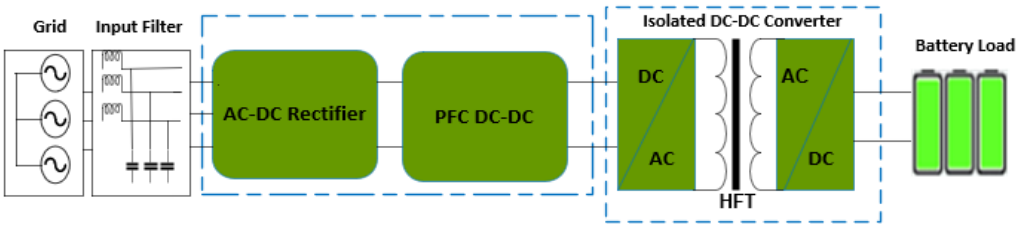

Figure 2.12: Single module charger with isolated DC-DC converter.

Next, the AC-DC rectifier converts the alternating current (AC) from the grid into direct current (DC). This rectifier uses diodes or controlled rectifiers like Silicon-Controlled Rectifiers (SCRs) or thyristors to perform the rectification process. Following the rectification, the Power Factor Correction DC-DC converter improves the power factor of the input AC supply, making the charger more efficient and reducing the reactive power drawn from the grid [135]. This converter regulates the DC voltage and shapes the input current waveform to be in phase with the voltage waveform, thereby improving power factor. The isolated DC-DC converter is the core component that provides galvanic isolation between the grid and the EV battery [136]. This isolation enhances safety by preventing potential fault currents from reaching the battery. The converter uses a high-frequency transformer to transfer energy across an isolation barrier, with the primary side connected to the grid and the secondary side connected to the EV battery [137]. This configuration also allows for voltage and power level adjustments. These chargers are able to deliver high-power charging at levels exceeding 350 kW, enabling faster charging times for EVs [138], [139]. Finally, the battery load is the stage where the conditioned and isolated DC power is supplied to the EV battery. The battery load receives the isolated DC power for charging, ensuring it receives the correct voltage and current for safe and efficient charging. The benefits of using an isolated DC-DC converter in this configuration are substantial. Galvanic isolation enhances safety by protecting against electrical faults and leakage currents that could harm users or damage equipment. It improves reliability by reducing the risk of component failure due to high voltages and providing protection against transient surges from the grid. The isolated design also has better EMC performance, reducing interference with other electronic devices. Additionally, it allows for a wider voltage and power range, accommodating a broader range of EV battery specifications.

A multi-module charger configuration, as depicted in Figure 2.13, enhances output power by paralleling multiple individual charger modules, each comprising a non-isolated DC-DC converter, an input filter, and an AC-DC rectifier, while sharing a common low-frequency transformer and grid connection. This setup increases output power significantly compared to a single-module charger and offers modularity, allowing for flexible scaling of charging capacity by adding or removing modules as needed. The potential for redundancy in this configuration can improve system reliability, and the shared LF transformer and grid connection can reduce costs and simplify overall system design. However, challenges such as load balancing, current sharing, and safety concerns due to the non-isolated nature of the DC-DC converters must be addressed to ensure equal power distribution, avoid uneven current distribution, and mitigate electrical hazards. Multi-module chargers with non-isolated DC-DC converters are suitable for high-power charging applications where increased output capacity and modularity are essential, with power parameters typically ranging from 50 kW to 350 kW per module [140], [141].

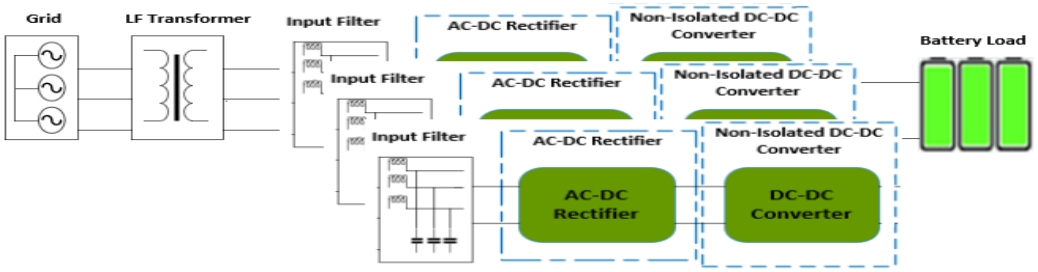

Figure 2.13: Multiple parallel modules with LF transformer.

Figure 2.14 illustrates a multi-module charger, an example of Tesla Supercharger which has 12 modules connected in parallel. Its configuration featuring multiple isolated DC-DC converters connected in parallel, enhancing the system's power capacity and redundancy compared to a single-module charger. Each module contains an isolated DC-DC converter, an input filter, an AC-DC rectifier, and a PFC DC-DC converter, all connected in parallel at both the input AC side and output DC side to distribute the load and increase total output power [142]. The modules share a common grid connection, simplifying integration into the power grid, and the modular design allows for flexible expansion by adding or removing modules as needed to match varying power requirements. This configuration offers increased charging capacity, modularity, scalability, improved reliability through redundancy, and enhanced safety with galvanic isolation between the grid and EV batteries. However, key challenges in modular operation include load balancing, current sharing, and synchronization, which must be carefully managed to ensure reliable power distribution and reduce the complexity of coordinating multiple modules. Multi-module chargers with isolated DC-DC converters are ideal for high-power charging stations, fleet charging depots, and applications where high charging capacity, reliability, and safety are critical, with power parameters typically ranging from 50 kW to 350 kW per module [141].

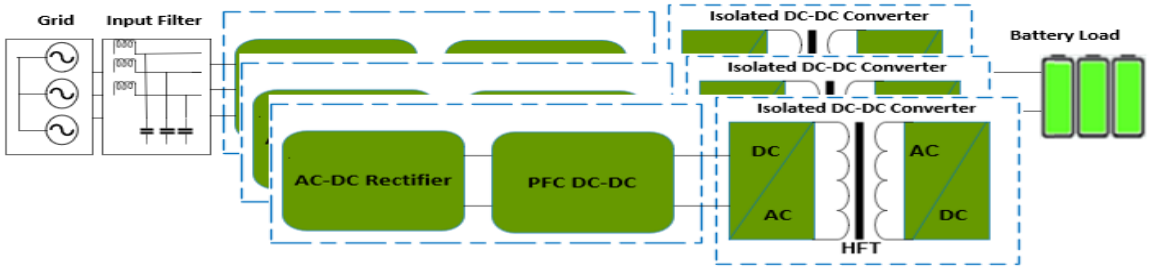

Figure 2.14: Multiple parallel models with HF transformer.

Solid State Transformers represent a transformative approach to power conversion and distribution in DC fast charging stations for electric vehicles. Utilizing the Input-Series, Output-Parallel (ISOP) configuration as shown in Figure 2.15, to enhance the performance and reliability of these systems. Central to SSTs, the HFT operates at high frequencies, allowing for significant size and weight reductions compared to conventional transformers. SSTs incorporate advanced power electronics to achieve AC-AC, AC-DC, and DC-DC conversion stages using semiconductor devices like IGBTs and MOSFETs.

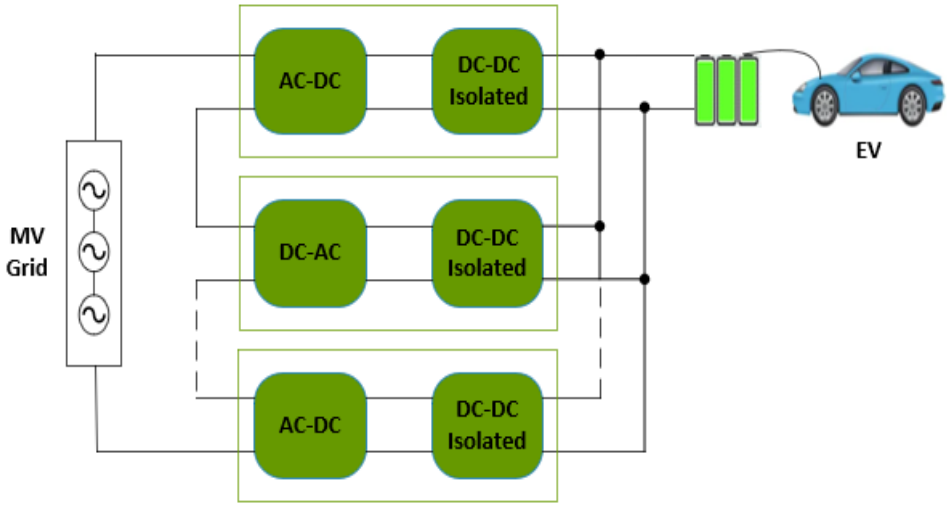

Figure 2.15: SST based DCFC using ISOP modules [143]**.**

The ISOP configuration arranges multiple converter modules in series on the input side, enabling each module to handle a fraction of the total input voltage, reducing voltage stress on individual components and simplifying scalability [144]. On the output side, the converter modules are connected in parallel, distributing the load current among multiple modules to enhance reliability and ensure no single module is overloaded. The initial stage involves converting the medium voltage AC - MVAC from the grid to medium voltage DC - MVDC using an active front-end rectifier, which provides PFC, reactive power compensation, and harmonic elimination. The MVDC is then fed into a high-frequency transformer coupled with a DAB, converter to ensure galvanic isolation and regulate power flow [145]. The final stage involves further stepping down the voltage to a low voltage DC (LVDC) level suitable for EV battery charging using a DC-DC converter. The ISOP configuration minimizes switching losses and maximizes efficiency by operating at optimal voltage and current levels. The use of HFT and advanced power electronics results in compact and lightweight designs, allowing higher power densities and reduced installation space. Series and parallel configurations ensure reliable operation with built-in redundancy to handle module failures without disrupting the charging process. The modular nature of ISOP allows easy scalability to meet varying power demands

and future expansion requirements. SSTs with ISOP can integrate sophisticated control algorithms for dynamic power management, enabling optimal energy utilization and seamless integration with renewable energy sources and energy storage systems

Using a single high-power module circuit as shown in Figure 2.16 ensures efficient power transfer and voltage conversion, catering to the demanding requirements of modern EV charging infrastructure. An SST-based DC fast charger typically integrates three main stages: AC-DC conversion, high-frequency isolation, and DC-DC conversion. The first stage involves an active front-end rectifier that converts medium voltage AC-MVAC from the grid into medium voltage DC-MVDC. This stage includes PFC to ensure that the current drawn from the grid is in phase with the voltage, reducing reactive power and minimizing harmonic distortion. This rectifier stage is crucial for maintaining grid stability and complying with regulatory standards.

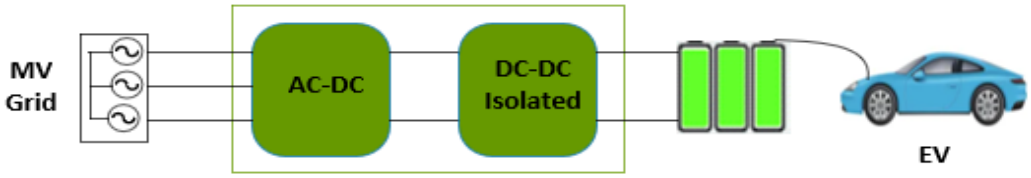

Figure 2.16: SST based DCFC using single module circuit.

The second stage features an HFT that provides galvanic isolation and steps down the voltage. The high-frequency operation significantly reduces the size and weight of the transformer compared to conventional low-frequency transformers. This stage often uses a Dual Active Bridge DC-DC converter, which enables efficient power transfer between the MV DC and the LVDC required by EV batteries. The DAB converter operates with Zero Voltage Switching (ZVS) or soft switching techniques, minimizing switching losses and enhancing overall efficiency. The final stage involves a DC-DC converter that further adjusts the LVDC to the specific voltage level needed for charging EV batteries. This stage is critical for ensuring that the charging voltage matches the battery's requirements, optimizing the charging process, and protecting the battery from damage. Advanced control algorithms are employed to manage the power flow dynamically, optimizing energy utilization and ensuring stable and efficient charging. A single high-power module circuit SST eliminates the need for multiple stages of conversion typically found in other configurations, such as input-series, output-parallel ISOP setups. This single module design simplifies the overall system, reducing the number of components, and improving reliability. By integrating advanced semiconductor devices such as Silicon Carbide (SiC) or Gallium Nitride (GaN) transistors, these SSTs can operate at higher frequencies with lower losses, further enhancing their performance. In addition to efficiency and compactness, SSTs with single high-power modules offer several advantages, including

bidirectional power flow capability, enabling V2G applications. This allows EVs to discharge power back into the grid, providing ancillary services such as load balancing and frequency regulation, thereby supporting grid stability and promoting the integration of renewable energy sources. Despite their numerous benefits, the development and deployment of SST-based DC fast chargers face challenges such as high initial costs, the need for robust control strategies, and ensuring compliance with safety standards. Ongoing research and technological advancements are addressing these challenges, paving the way for widespread adoption of SSTs in EV charging infrastructure. SST-based DC fast chargers utilizing a single high-power module circuit offer a highly efficient, scalable, and reliable solution for EV charging. By integrating advanced power electronics, high-frequency isolation, and dynamic control algorithms, these systems ensure optimal power transfer, voltage conversion, and grid integration, meeting the evolving needs of the EV market.

2.8.2 Integration of SSTs with DC Microgrids

The Electric Power Research Institute (EPRI) has developed a fast charging technology for EVs based on the Intelligent Universal Transformer (IUT), which incorporates solid-state transformer technology. The IUT replaces traditional power conversion units and transformers with a single interface system capable of fast charging EVs. This system provides an intermediate DC bus voltage at the 400V level, suitable for direct use in DC distribution systems or fast EV charging. This technology allows utilities to offer fast charging directly from medium voltage (4-15kV) distribution systems, enhancing the practicality and efficiency of EV charging infrastructure. In 2012, EPRI demonstrated a prototype 2.4kV, 45kVA solid-state direct-current fast charger at its Knoxville, Tennessee laboratory. This utility direct fast charger technology enables rapid charging of Plug-in Electric Vehicles (PEVs) and serves as a utility-owned asset for other electricity delivery purposes. The UFC is designed to be more efficient and simpler than current commercial DC fast charging systems, with an expected overall efficiency of 96-97%, compared to the 89-91% efficiency of conventional systems. The UFC technology offers significant operational benefits, including reduced installation costs and improved efficiency. By eliminating the need for a conventional transformer, the system achieves substantial size and weight reductions, with the entire EPRI IUT-based DC fast charger electronics weighing less than 150 lbs. This compact and efficient design makes the UFC an attractive option for urban environments, parking structures, and buildings, allowing for fast charging infrastructure that supports the expansion of PEVs markets and enhances grid stability. EPRI's Medium Voltage (MV) Fast Charger Functional Specifications highlight the system's capabilities, such as a single-phase 2.7/8 kV, 60 Hz utility AC input, a maximum output power of 50 kW, and an overall system efficiency greater than 95%. The system complies with CHAdeMO standards

and is adaptable to other connector interfaces. Additionally, the UFC includes advanced protection schemes, remote access capabilities, and optional features like integrating energy storage and multiple AC Level 2 charging spots. The approach in [146] development of the MV fast charger topology by Virginia Tech and EPRI, as illustrated in Figure 2.17, represents a significant advancement in EV MV fast charger topology developed by Virginia Tech and EPRI. This topology employs a solid-state transformer to enhance power transfer and voltage conversion efficiency, integrating RES and energy storage systems (ESS). With a three-stage configuration including MVDC and LVDC links, the system facilitates efficient power flow regulation and bidirectional power capabilities, supporting both EV charging and broader grid applications. The comprehensive approach of EPRI and Virginia Tech ensures that this MV fast charger topology not only meets current EV charging demands but also paves the way for future innovations in the field.

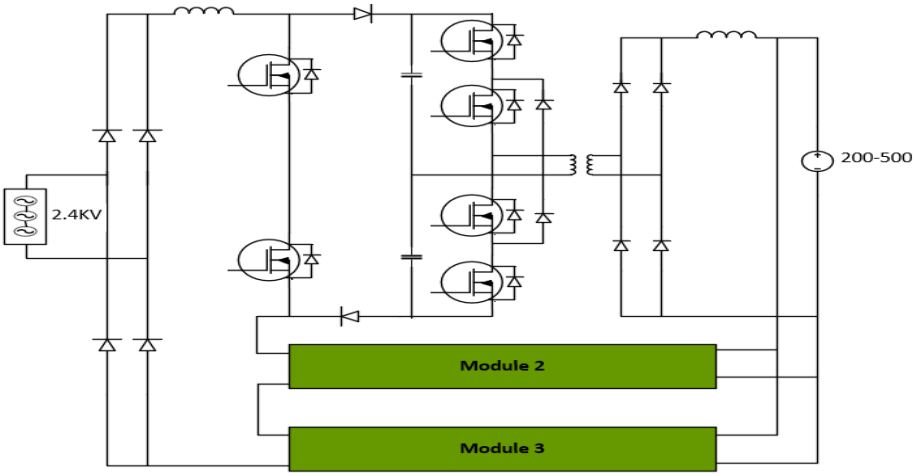

Figure 2.17: MV fast charger topology developed by Virginia Tech and EPRI [147]**.**

A prototype 15-kV single-phase IUT presented in [148], and shown in Figure 2.18, has been successfully developed and tested, demonstrating promising results in voltage conversion and regulation. This IUT, featuring an 8kV AC input and 240V AC output, employs a three-stage topology comprising an Active Front-End (AFE), an isolated DC/DC converter, and a soft-switched DC/AC inverter. Packaged into a single module with ten such modules connected in an ISOP configuration, it achieves a peak efficiency of 97.5% at 25 kW and maintains steady-state heat sink temperatures below 55°C. Key measurements include a DC bus voltage of 403V, an output voltage of 240V RMS, and a Total Harmonic Distortion (THD) of under 2.5%. The IUT excels in voltage regulation under varying conditions, offers superior power quality, and utilizes commercial 1.2kV SiC devices. While its overall efficiency is currently slightly lower than conventional transformers, its advantages in voltage regulation, power quality, and intelligent features make it suitable for applications such as electric vehicle charging and DC

microgrids. Future efficiency improvements and market identification are necessary for broader adoption, and the IUT's compact design also shows promise for medium voltage power conversions in sectors like marine and railway systems.

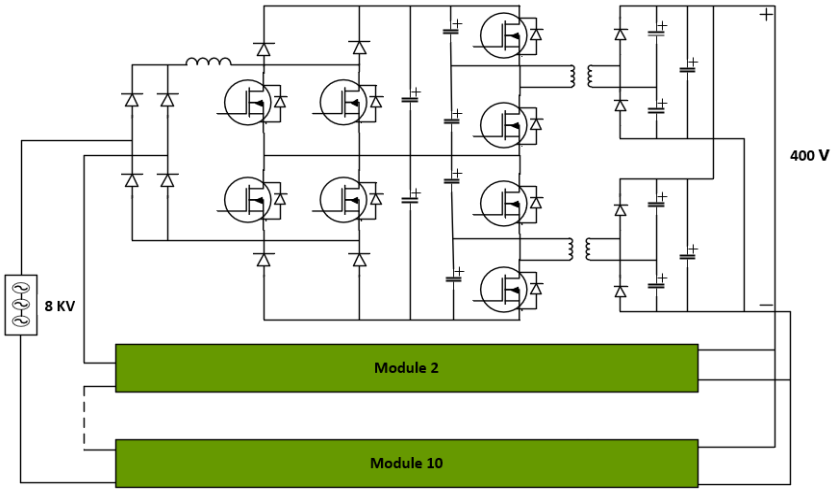

Figure 2.18: AC-DC stage of Intelligent Universal Transformer [139]**.**

A SiC-based high-performance medium-voltage fast charger for plug-in electric vehicles shown in Figure 2.19, approach in [149], details the creation and evaluation of an efficient, medium-voltage fast charger utilizing SiC power devices. This charger, which converts a 50 kW 2.4 kV input to a variable DC output, achieves over 96% efficiency. Its modular design with an input-series-output-parallel topology allows for scalable input voltage and output power. The use of Wide Bandgap (WBG) power devices significantly reduces the charger's volume and weight while exceeding the efficiency of current fast chargers by over 1.5% [150]. The design was validated through simulations and a prototype. Future improvements focused on higher output power testing, enhanced input stage control, and further efficiency gains through reduced switching frequency and synchronous rectification. This development offers a promising advancement in EV charging technology.

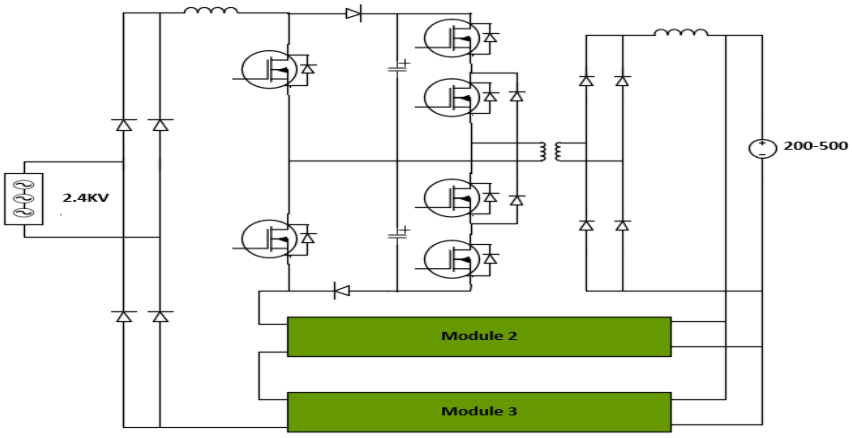

Figure 2.19: 2.4kVac input 50kW charger circuit [139].

Proposes in [151] development single ac-dc stage and ISOP modules in the dc/dc stage as shown in Figure 2.20, utilizing 3.3 kV SiC MOSFETs, has been successfully demonstrated with a down-scaled prototype, confirming its continuous power transfer capability and enhancements in ZVS regions through variable input voltage and switching frequency. Future research directions include system level testing for MV grid-connected EV chargers and studying accurate battery charging profiles. The MV DAB converter, designed for high efficiency, high power density, and fast dynamic response, employs phase-shift modulation and operates under soft-switching conditions. It is equipped with key characteristics such as a 2500 V input voltage, 520 V - 820 V output voltage range, and a 50 kHz switching frequency. The 3.3 kV SiC MOSFET features a SiC DMOSFET device type, TO-247 package, and 70 mΩ on-state resistance, making it suitable for high-power and bidirectional applications in medium voltage EV fast-charging systems.

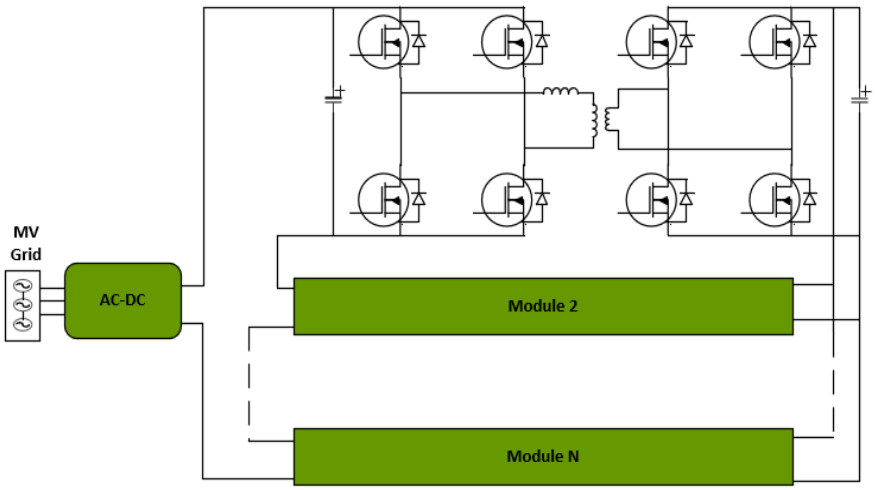

Figure 2.20: Charger architecture of single AC-DC stage and ISOP modules [139].

The paper employs a modified multi-cell boost topology to implement the charger [152], as illustrated in Figure 2.21. The paper presents the design and development of a 12.47 kV, 350 kW electric vehicle fast charger using 10 kV SiC MOSFETs. The key aspects include: the use of 10 kV SiC MOSFETs and Schottky diodes to enable direct connection to the MV grid without a service transformer; detailed characterization of the 10 kV SiC MOSFETs; selection of a modified multi-cell boost topology; optimization of the system design, including operating frequency and passive component selection, to achieve a simulated efficiency exceeding 98% and input current THD lower than 2%; and an overall power density of 1.6 kW/L, demonstrating the advantages of this high-voltage SiC MOSFET-based MV fast charger design.

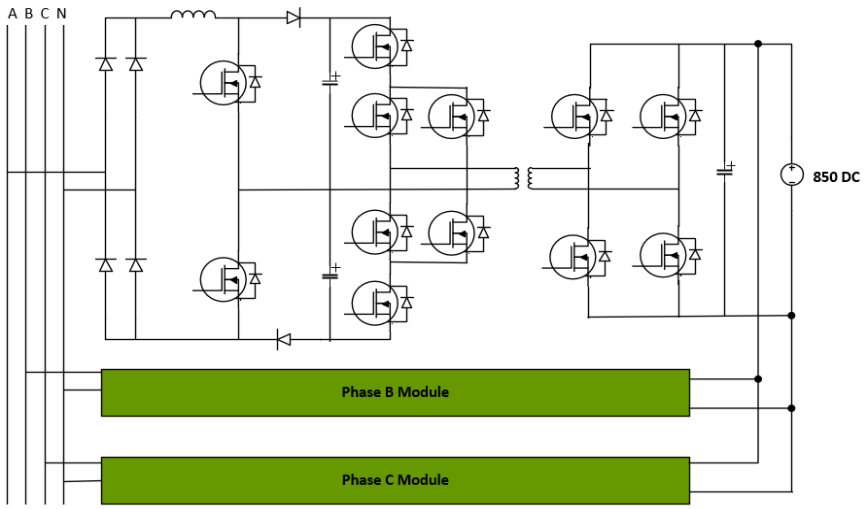

Figure 2.21 Figure: 12.47kV ac three phase 350kW XFC [153]**.**

The research [154] presents the design and realization of a 25 kW, single-phase AC-DC power factor correction rectifier stage of an MV three-phase inverter, operating from 3.8 kV AC to 7 kV DC, based on 10 kV SiC MOSFETs as shown in Figure 2.22. The goal is to develop a simple and efficient MV AC-DC input stage for an SST that could directly power server racks of several tens of kilowatts from the MV grid. The focus is on the realization of the MV inductors and their electrical insulation, the LCL input filter to limit electromagnetic interference emissions, as well as the challenges due to cable resonances when connecting the SST to the MV grid via an MV cable. Despite the large insulation distances required for MV, the realized MV PFC rectifier achieves an unprecedented power density of 3.28 kW/L (54 W/in3) and a full-load efficiency of 99.1%, measured using a calorimetric test bench described.

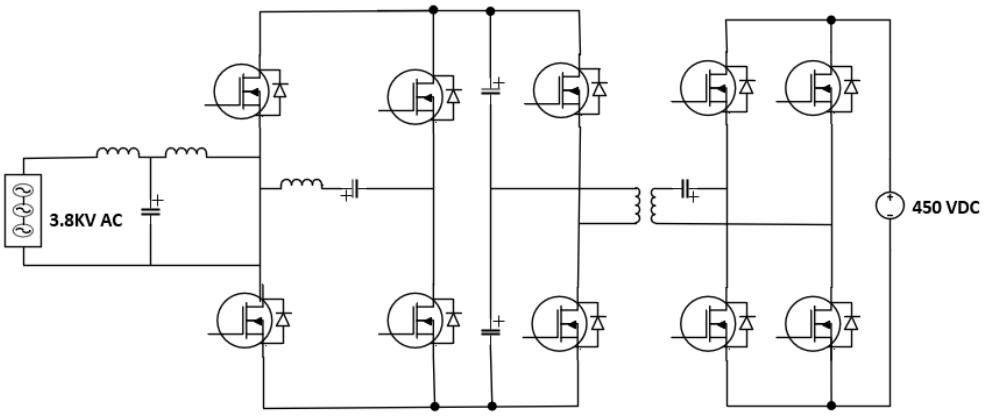

Figure 2.22: 5 MV AC-DC soft-switching circuit [153]**.**

In [155] describes the design and operation of a 3.6kV high-performance SST based on 13kV SiC MOSFET and JBS diode devices as shown in Figure 2.23. The paper introduces the concept of distribution network SST and its role in integrating distributed renewable energy resources and energy storage devices with the distribution grid, characterizes the high-voltage 13kV SiC MOSFET devices, designs the rectifier and DC/DC converter stages of the 3.6kV SST prototype, and presents experimental results demonstrating the functionalities of the designed SST prototype, including pre-charge, start-up, and regeneration operations when connected to the 3.6kV distribution grid. In conclusion, the 3.6kV SST prototype developed in this work utilizes 13kV SiC MOSFET and JBS diode devices to achieve high conversion efficiency and energy density, enabling it to interface with the medium-voltage distribution grid and provide both 400V DC and 240/120V AC outputs, highlighting the potential of SiC-based power electronics for future power distribution applications.

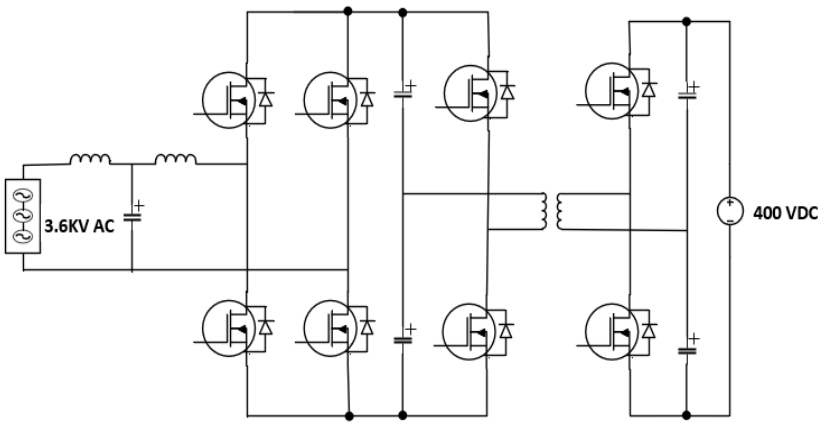

Figure 2.23: MV SST circuit [153]**.**

2.9 DC Fast Charging Converter Topologies

DC fast chargers are essential for providing rapid charging to EVs by efficiently converting AC grid input into DC output, which is required for vehicle batteries. The primary components responsible for this conversion are grid-facing converters. These converters must exhibit specific characteristics to ensure optimal performance and reliability: Key features of grid-facing converters including are low AC-side distortion is one of the critical requirements for grid-facing converters is to minimize AC-side distortion. This is essential for maintaining power quality and ensuring that the grid operates efficiently without introducing significant harmonics that can affect other connected loads. Low distortion helps in complying with grid codes and standards, ensuring smooth integration with the electrical grid. In the other hand regulated DC voltage is another important feature is the ability to provide a stable and regulated DC output voltage. This regulation is vital for the efficient charging of EV batteries, as it ensures that the voltage levels are within the required range, preventing damage to the batteries and ensuring fast charging times. Popular converters options include as details below:

2.9.1 AC-DC Rectifiers

In the realm of EVs, efficient and reliable power conversion is critical to ensure effective battery charging and overall vehicle performance. Rectifiers play a pivotal role in this process by converting the AC power from the grid into the DC power required for charging EV batteries. Several advanced rectifier topologies have been developed to meet the demanding requirements of EV applications, each offering unique benefits in terms of efficiency, power quality, and system integration. Among these, the three-phase active PWM rectifier with LCL filter, the Neutral-Point-Clamped (NPC) rectifier, the Vienna rectifier, and the buck rectifier are particularly notable. These rectifiers are designed to handle high power levels with minimal harmonic distortion, ensuring efficient energy transfer and reducing strain on the electrical grid. This introduction delves into the specific characteristics and advantages of these rectifiers, highlighting their importance and application in the evolving landscape of electric vehicle technology.

2.9.1.1 Three-phase active PWM rectifier with LCL filter

A three-phase active (PWM) rectifier with an LCL filter is a sophisticated component crucial for efficient AC to DC conversion in electric vehicle DC fast charging systems. Designed to interface with the grid, this rectifier shown in Figure 2.24, employs advanced semiconductor devices like IGBTs or MOSFETs to convert three-phase AC voltage into a regulated DC output suitable for charging EV batteries rapidly and reliably. Pulse width modulation techniques control the switching of these devices, ensuring precise regulation of output voltage and shaping of input current to maintain a sinusoidal waveform, thereby minimizing harmonic distortion [156]. The integration of an LCL filter inductors and capacitors is critical to attenuate

high frequency switching harmonics generated during rectification. This filter improves power quality by reducing EMI, ensuring that the current drawn from the grid remains as close to a pure sinusoid as possible. The design and implementation of the LCL filter require careful consideration of component values to balance filtering performance with system stability, especially in EV charging applications where power quality and reliability are paramount [157]. Advanced control techniques are implemented to manage the rectifier's operation effectively. Inner current control loops track and adjust the reference currents to compensate for disturbances, while outer voltage control loops maintain the desired DC output voltage level. Active damping strategies are often employed to mitigate the resonance effects of the LCL filter, enhancing overall system stability and dynamic response.

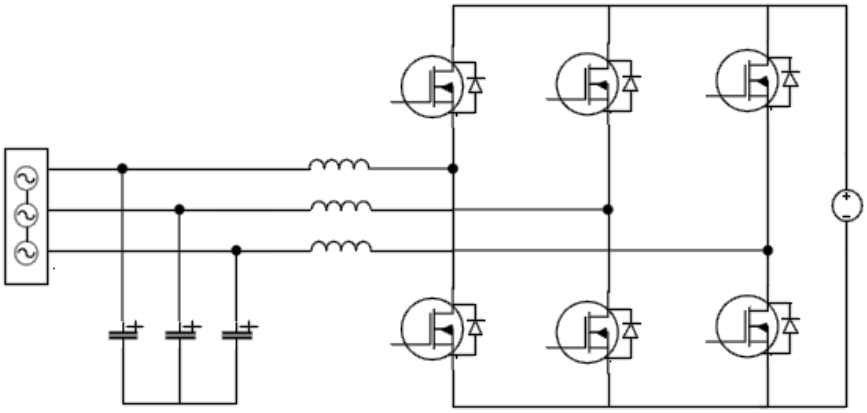

Figure 2.24: Three phase PWM rectifier with LCL filter [158]**.**

One of the significant advantages of a three-phase active PWM rectifier in EV applications is its high efficiency. This efficiency is achieved using modern semiconductor devices and sophisticated control algorithms, which optimize energy conversion processes. The rectifier's bidirectional capability allows it to not only supply power to charge EV batteries but also to absorb power, facilitating energy flow management in smart grid environments and enabling integration with renewable energy sources and energy storage systems [100]. Recent advancements in this field include the adoption of Model Predictive Control (MPC), which enhances dynamic performance and robustness by optimizing switching patterns in real-time. Digital control platforms, such as Digital Signal Processors (DSPs) and Field-Programmable Gate Arrays (FPGAs), provide enhanced processing capabilities for implementing complex control algorithms with high precision and responsiveness. Moreover, the use of wide bandgap semiconductors like SiC and GaN further enhances efficiency by allowing higher switching frequencies, improved thermal conductivity, and lower losses compared to traditional silicon devices [159]. Enhanced filter designs and grid-interactive features, such as voltage support

and reactive power compensation, are also becoming increasingly prevalent. These features enable the rectifier to actively participate in stabilizing the grid and supporting the seamless integration of distributed energy resources, making it a versatile and future-proof solution for modern EV charging infrastructure.

2.9.1.2 NPC Rectifier

The neutral-point-clamped (NPC) rectifier is a essential technology in power electronics, widely adopted for its effectiveness in high-power and medium-voltage applications, particularly in EV fast charging infrastructure. It utilizes a three-level voltage structure that divides the DC bus voltage into positive, negative, and neutral levels using capacitors and clamping diodes. This configuration reduces voltage stress on individual semiconductor devices like IGBTs or MOSFETs, enabling the use of components with lower voltage ratings, thus enhancing efficiency and cost-effectiveness. The NPC rectifier shown in Figure 2.25, operates by switching these devices to convert AC input voltage into a three-level DC output, significantly minimizing harmonic distortion in the input current. Complex modulation techniques such as Space Vector Modulation (SVM) or PWM are employed to optimize switching patterns, achieving high power factor and low total THD [160]. Integration with an LCL filter further improves power quality by attenuating high-frequency switching harmonics. Advanced digital control techniques using microcontrollers or DSPs enhance dynamic response and precision. Moreover, advancements in wide bandgap semiconductors like SiC and GaN contribute to higher switching frequencies and improved thermal management, enhancing overall efficiency and reliability. The NPC rectifier's robust performance and scalability make it ideal for EV charging stations, where efficiency, reliability, and power quality are critical considerations.

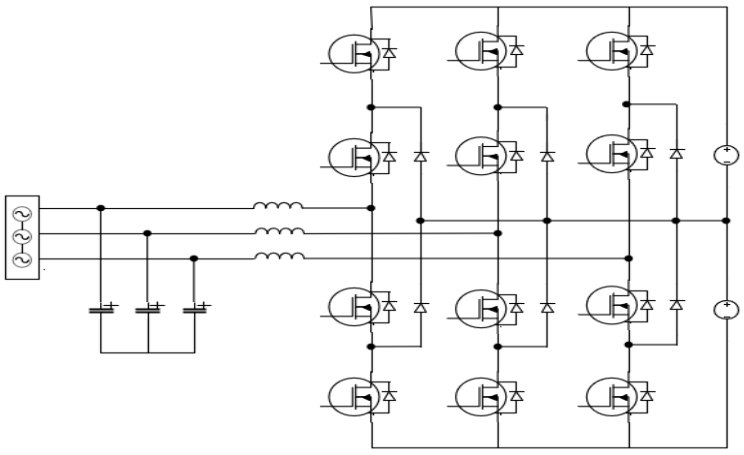

Figure 2.25: Neutral-point-clamped NPC rectifier [161]**.**

2.9.1.3 Vienna rectifier

The Vienna rectifier is a three-level, unidirectional power converter renowned for its efficiency and low harmonic distortion, making it ideal for demanding applications like electric vehicle charging stations. Operating with a three-phase input voltage, the rectifier transforms it into a stable DC output using three bidirectional switches, six diodes, and three capacitors. This configuration enables the Vienna rectifier shown in Figure 2.26, to generate a three-level voltage waveform, effectively reducing voltage stress on components such as IGBTs, MOSFETs, or advanced wide bandgap semiconductors like SiC and GaN. Lower switching losses and minimized EMI enhance overall system efficiency and power quality [162]. Control strategies incorporate advanced modulation techniques like SVM or sinusoidal PWM to precisely regulate output voltage and current, achieving nearly unity power factor and minimal THD.

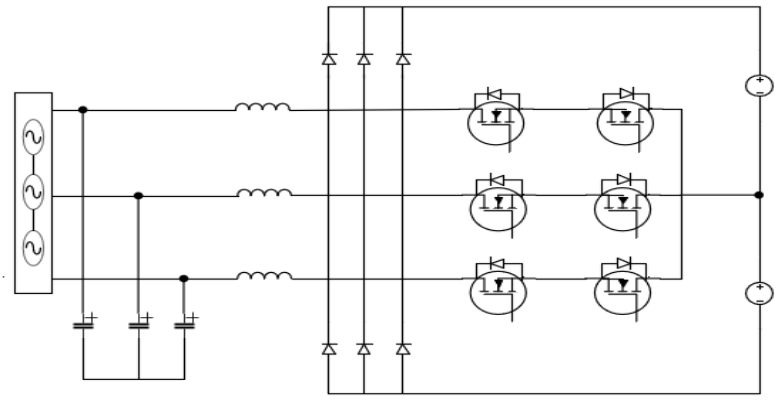

Figure 2.26: Vienna rectifier [163]**.**

This high power factor optimizes grid connection efficiency by reducing reactive power. Additionally, the rectifier inherently produces low ripple output voltage, crucial for sensitive applications such as EV batteries and DC motors. Integration of an LCL filter further improves output quality by suppressing high-frequency switching harmonics. Recent advancements in digital control technology, leveraging powerful microcontrollers or DSPs, have further enhanced dynamic response and control accuracy [164]. Adoption of wide bandgap semiconductors allows for higher switching frequencies, reducing the size and cost of passive components. The Vienna rectifier's robust design, combined with its efficiency, scalability, and superior power quality, positions it as a dependable solution for modern power conversion needs where reliability and efficiency are paramount.

2.9.1.4 Active front-end converter

The topology of single-phase active front end rectifier (AFE) is shown in Figure 2.27, also known as PWM rectifier connected at the utility front of grid. The AFE acts as rectifier during grid to vehicle operation and is used to obtain dc supply from the ac mains for battery charging [165]. It fulfils the requirements such as bidirectional power flow, dc bus voltage control with fast dynamic response and maintains unity power factor at the input. phase AC power supply. The control of this converter should be designed such that it generates bus voltage reference and power factor reference quickly, which in turn improves the fast dynamic response.

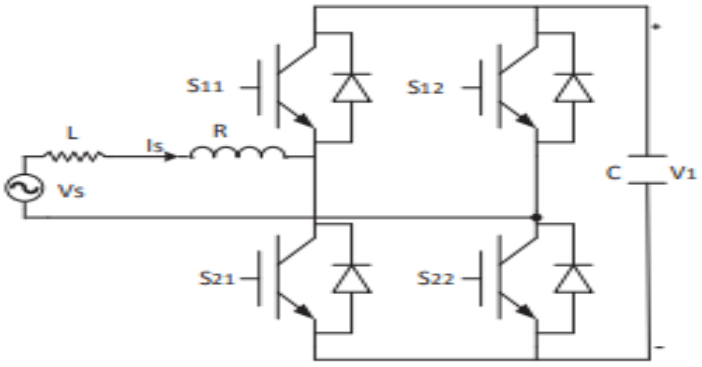

Figure 2.27: AFE converter topology [166].

2.9.2 DC-DC Converters

Following the grid-facing converter in electric vehicles, a DC-DC converter plays a pivotal role in efficiently managing the interface between the high-voltage DC bus and the vehicle's battery or energy storage system. Isolation from ground is critical to ensure safety and reliability, typically accomplished through high-frequency transformers integrated within the DC-DC stage. Isolated DC-DC converters commonly used in EV applications include the Phase-Shifted Full Bridge (PSFB) and LLC resonant converters. The PSFB converter offers high efficiency across a range of load conditions but may exhibit limitations at light loads and non-unity voltage ratios. On the other hand, the LLC resonant converter provides efficient operation with reduced switching losses and high power density, making it suitable for high-power applications in EVs. Additionally, the DAB converter is employed for its bidirectional capability and wide voltage range compatibility, enabling efficient power flow control between the DC bus and the vehicle's energy storage. These converters utilize advanced control techniques such as digital PWM or MPC to optimize efficiency, regulate voltage, and ensure precise power delivery to the vehicle's electrical systems. Recent advancements in semiconductor technology, including the adoption of wide bandgap materials like SiC and GaN, have further enhanced the performance of isolated DC-DC converters in EVs by enabling higher switching

frequencies, reduced losses, and increased power density. These innovations contribute to improving overall system efficiency, reliability, and scalability in electric vehicle applications, supporting rapid advancements in EV charging infrastructure and energy management systems.

2.9.2.1 Phase-shifted full bridge (PSFB)

The Phase-Shifted Full Bridge converter plays an important role in EVs by efficiently converting high-voltage DC from the grid or renewable sources to levels suitable for charging EV batteries. This converter topology consists of four switches arranged in a full bridge configuration, coupled with a high-frequency transformer that provides isolation between the input and output sides [167]. The operation of the PSFB converter in Figure 2.28 involves precisely controlling the phase shift between the switching signals of the bridge legs. This phase shifting technique minimizes the time during which multiple switches conduct simultaneously, thereby reducing switching losses and enhancing overall efficiency, which is critical for fast charging applications where minimizing charging times and maximizing energy transfer efficiency are paramount. In the context of EVs, the PSFB converter's design includes advanced control strategies such as digital pulse width modulation (PWM) or adaptive control algorithms [168]. These techniques optimize the converter's performance across various load conditions, ensuring stable output voltage regulation and high power conversion efficiency. Moreover, the integration of wide bandgap semiconductors like SiC and GaN in PSFB converters has revolutionized their capabilities. These semiconductor materials enable higher switching frequencies, lower conduction losses, and improved thermal management compared to traditional silicon-based devices.

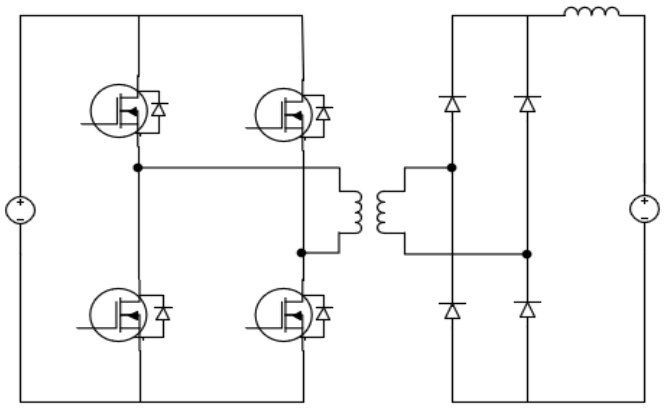

Figure 2.28: Phase shift full bridge converter [169]**.**

As a result, PSFB converters can achieve higher power densities and reliability while reducing the size, weight, and cost of power electronics in EV charging infrastructure. Recent advancements have also focused on enhancing the PSFB converter's robustness and

scalability. Innovations in control techniques and semiconductor technology continue to drive improvements in efficiency and performance, addressing the increasing demand for fast, reliable, and efficient charging solutions in the EV market. The flexibility of the PSFB converter makes it adaptable to evolving EV battery technologies and charging standards, supporting the transition towards more sustainable and efficient transportation solutions globally.

2.9.2.2 LLC Resonant converters

LLC resonant converters are integral to EV charging systems, facilitating efficient conversion of high-voltage AC grid power to the DC voltage required for charging EV batteries [170]. This converter topology, shown in Figure 2.29, operates on the principle of resonant switching, utilizing an inductor, a capacitor, and a resonant tank circuit LLC to achieve soft switching transitions. In EV applications, LLC resonant converters offer several advantages, including high efficiency across a wide load range and reduced EMI due to their soft-switching characteristics [171]. The LLC topology allows for seamless regulation of output voltage and current, crucial for maintaining battery health and maximizing charging efficiency. Advanced control techniques such as frequency modulation and phase-shift modulation optimize the resonant operation, ensuring minimal switching losses and improved overall system reliability. The integration of wide bandgap semiconductors like SiC and GaN further enhances efficiency by enabling higher switching frequencies and reducing losses. This scalability and efficiency make LLC resonant converters well-suited for both high-power fast charging stations and on-board chargers in EVs, supporting rapid adoption and deployment of electric mobility solutions worldwide [172].

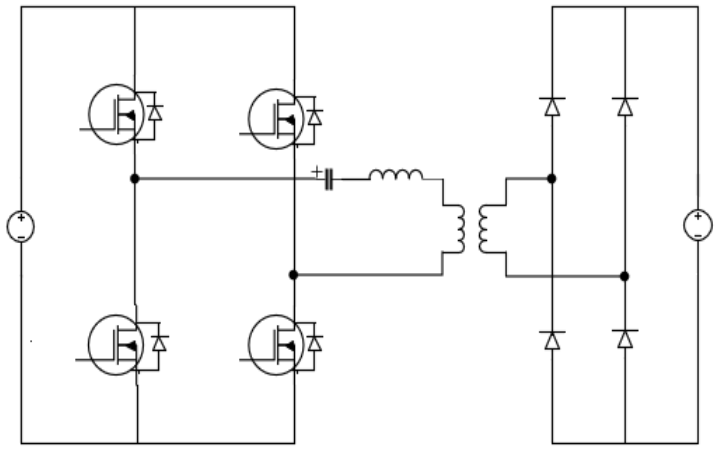

Figure 2.29: LLC resonant converter [173]**.**

2.9.2.3 Dual active bridge (DAB) converter

The Dual Active Bridge converter is a sophisticated power electronics topology that excels in EV applications due to its ability to efficiently manage high-power levels and bidirectional energy flow. In an EV context, the DAB converter shown in Figure 2.30, typically interfaces between the high-voltage DC battery pack or energy storage system and the vehicle's low-voltage DC bus [174]. This topology consists of two sets of switches typically, IGBTs or MOSFETs arranged in a bridge configuration. Each bridge includes an isolation transformer, which provides galvanic isolation between the high-voltage and low-voltage sides, crucial for safety and electrical isolation requirements. The DAB converter operates by dynamically adjusting the phase shift between the switching of the bridges. This phase-shift modulation allows precise control over the voltage and current delivered to the vehicle's electrical system, ensuring efficient power conversion and minimal losses [175]. The bidirectional capability of the DAB converter enables it to seamlessly switch between charging the battery from an external source, such as a DC fast charger and supplying power to the vehicle's traction motor or other on-board systems.

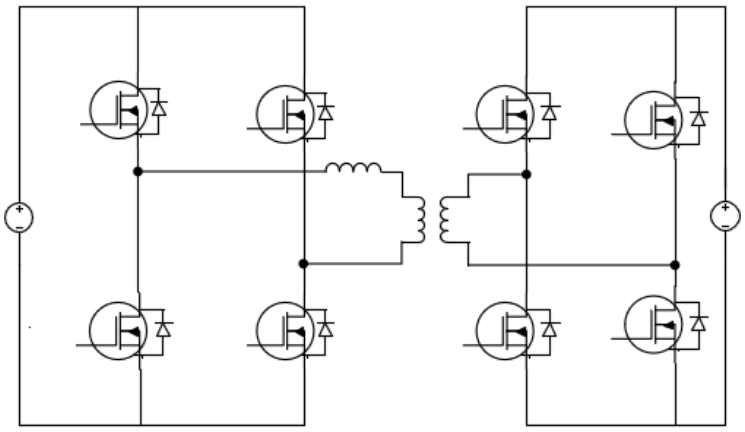

Figure 2.30: DAB converter [176]**.**

Key advantages of the DAB converter in EVs include its wide input voltage range compatibility, which accommodates varying battery voltages and charging scenarios. This flexibility is particularly advantageous in hybrid and electric vehicles where the battery voltage may vary significantly depending on charge level and operating conditions. Moreover, the DAB converter's ability to handle high-frequency switching and advanced control algorithms, such as MPC or advanced PWM, ensures high efficiency across different load conditions and operational states [177]. Recent advancements in DAB converter technology focus on improving efficiency through the use of wide bandgap semiconductors SiC and GaN, which offer lower switching losses, higher switching frequencies, and improved thermal management capabilities. These advancements contribute to reducing the size and weight of the converter

while enhancing overall system reliability and performance. The scalability of the DAB converter makes it suitable for future EV applications requiring higher power densities and faster charging capabilities, positioning it as a critical component in advancing the efficiency and sustainability of electric transportation.

2.9.2.4 CLLC Resonant converter

The Capacitor–Inductor–Inductor–Capacitor (CLLC) resonant converter is a specialized topology increasingly employed in electric vehicles for its efficiency, reliability, and ability to handle high-frequency operation. In EV applications, the CLLC resonant converter typically serves as a DC-DC converter, interfacing between the high-voltage DC battery pack and the lower-voltage DC bus that powers various vehicle systems. The converter shown in Figure 2.31 consists of a combination of inductors (L), capacitors (C), and transformers, designed to resonate at a specific frequency. The CLLC resonant converter achieves efficient power conversion by leveraging the resonance phenomenon, which minimizes switching losses and enhances efficiency compared to traditional PWM converters. The operation of the CLLC converter involves careful control of the switching frequency and phase angles to maintain resonance and optimize power transfer [178]. This control is typically managed by advanced modulation techniques such as phase-shift control or frequency modulation. The resonant nature of the converter also reduces EMI, contributing to cleaner power delivery and improved system reliability. In recent developments, the integration of wide bandgap semiconductors like Silicon Carbide and Gallium Nitride has further enhanced the performance of CLLC resonant converters. These materials enable higher switching frequencies, lower conduction losses, and improved thermal management, leading to higher efficiency and power density in EV applications.

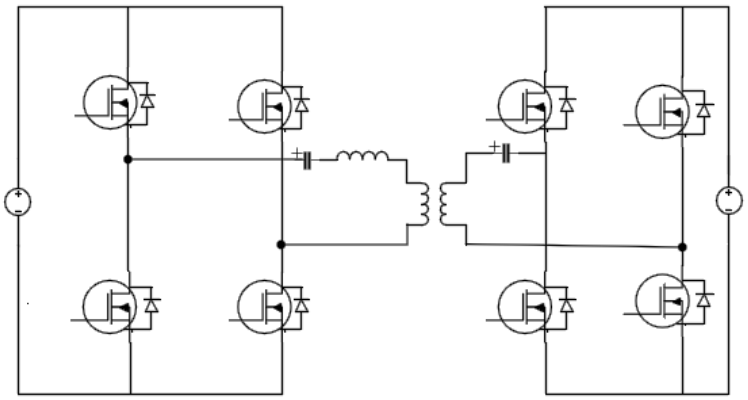

Figure 2.31: CLLC converter [179]**.**

2.10 Control Techniques Used for Power Electronics Conversion System

Power electronics conversion systems play a critical role in modern energy applications, enabling efficient control and transformation of electrical power. These systems are essential in various fields, including electric vehicle charging, renewable energy integration, and industrial automation. The performance of power electronics largely depends on the control techniques employed to manage switching operations, voltage, current, and overall energy flow within the system. Proper control strategies not only improve efficiency but also ensure stability, reliability, and safety across various operating conditions. This section explores several advanced control techniques used in power electronics conversion systems, each tailored to address specific requirements of efficiency, accuracy, and robustness. The use of digital and analog control methods is vital for optimizing power conversion processes in systems.

2.10.1 Space vector modulation (SVM)

Space Vector Modulation (SVM) is a sophisticated technique for controlling AC power converters and is widely used in motor drives and power quality improvement. It optimizes the switching patterns of the power electronic switches in the NPC rectifier, controlling the voltage vectors to maximize DC bus utilization and minimize harmonic distortion [180]. The main principle of SVM is to generate a reference voltage vector and modulate the switches accordingly. This results in a high power factor and low THD, enhancing the converter's efficiency and power quality. As it is shown in Figure 2.32, the space vector hexagon has six sectors and four regions per sector.

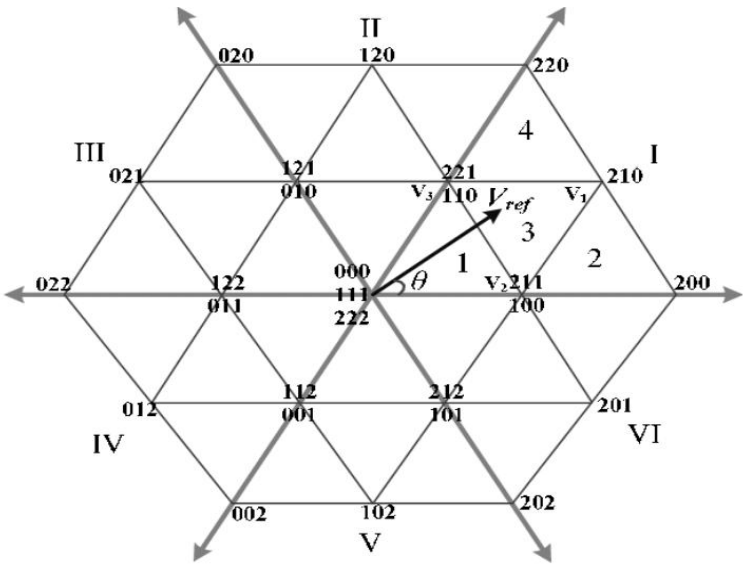

Figure 2.32: Three level-SVM hexagon including six sectors and four regions per sector [181]**.**

The reference voltage vector V_{ref} is given by equation (2.1) [182]

$$V_{ref} = V_m . sin\ (\omega_t + \theta) \quad (2.1)$$

Where:

- V_m is the peak phase voltage,
- ω_t is the angular frequency, and
- θ is the phase angle.

The SVM technique involves the following steps:
The reference voltage vector is generated using the above equation.
The space vector diagram is divided into six sectors. The sector in which the reference voltage vector lies is determined.
The time durations for which the active and zero vectors should be applied are calculated. These are given by:

$$T_a = T\ .[\frac{\sqrt{3}}{2}\ .V_{ref}\ .sin\ (\omega_t - \theta) + 0.5] \quad (2.2)$$

$$T_b = T\ .[\frac{\sqrt{3}}{2}\ .V_{ref}\ .sin\ (\omega_t - \theta - A = \frac{2\pi}{3}) + 0.5] \quad (2.3)$$

$$T_c = T - T_a - T_b \quad (2.4)$$

where,
T is the sampling period,
$T_a, T_b,$ and T_c are the time durations for which the active vectors should be applied.
Switching Sequence Generation**:** Based on the calculated times and the sector in which the reference voltage vector lies, the appropriate switching sequence is generated. By controlling the switching patterns of the power electronic switches in this way, SVM optimizes the DC bus utilization and minimizes harmonic distortion, resulting in a high power factor and low THD [183]. This enhances the converter's efficiency and power quality.

2.10.2 Phase-shifted full bridge (PSFB) with digital pulse width modulation (PWM)

The Phase-Shifted Full Bridge (PSFB) converter is designed to improve efficiency and reduce switching losses by using a phase-shift control technique. This converter is often used in applications requiring high efficiency and high power density. The PSFB converter uses a full-

bridge topology and operates by phase-shifting the switching signals of the bridge transistors to control the power flow [184].

The effective duty cycle of the power converter depends on the primary voltage, inductor filter, and the voltage drop across the leakage inductor. It is given by:

$$D_{eff} = D + d_{eff} \tag{2.5}$$

Where D the nominal duty is cycle and d_{eff} represents small variations due to inductor current and input voltage changes. The small changes in duty cycle $(d_i \; and \; d_v)$ due to the filter inductor current and input voltage are given by:

$$d_i = \frac{nLr\, \int siL}{V_{in}} \tag{2.6}$$

$$d_v = \frac{nLr\, \int sV_{in}}{V_{in}} \tag{2.7}$$

The transfer function from the equivalent circuit is expressed as:

$$G_d(s) = \frac{V_o}{d} = \frac{nV_{in}}{R\left(\frac{L}{RLC} + s + \frac{1}{sC} + \frac{R}{LC}\right)} \tag{2.8}$$

Figure 2.33 illustrates the principle of operation for the full bridge phase-shifted power converter, demonstrating the switching signals and the resultant current and voltage waveforms.

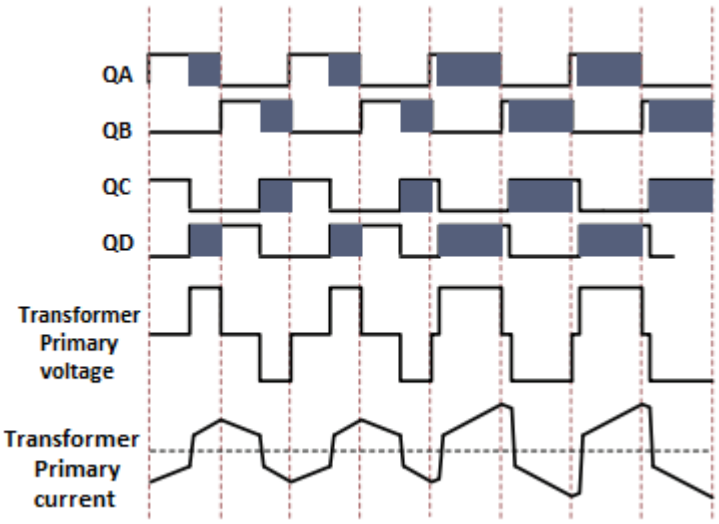

Figure 2.33: Full bridge phase-shifted power PWM waveforms [185].

2.10.3 Model predictive control for dual active bridge (DAB)

MPC is a control strategy that utilizes a model of the system to predict future behavior and optimize performance over a specified prediction horizon. In the context of a DAB converter, MPC can be used to achieve efficient and precise control of power flow between two DC sources [186]. The concepts prediction model, algorithm uses a mathematical model of the DAB converter to predict future states of the system based on current measurements and control inputs. The optimization at each control interval, the algorithm solves an optimization problem to find the control inputs that minimize a predefined cost function over the prediction horizon. Receding horizon optimization is performed in a receding horizon manner, meaning only the first control input of the optimized sequence is applied to the system. The process is repeated at each time step. MPC is based on iterative, finite-horizon optimization of a plant model it allows the control of processes while satisfying a set of constraints [187].

The MPC for dual active bridge DC–DC converters emphasize advanced control methodologies to enhance the performance of DAB converters, particularly in renewable energy systems and electric vehicles. The conclusion focuses on MPC's ability to improve dynamic response, optimize power transfer, and minimize reactive power by adjusting phase-shift ratios. MPC provides precise regulation of the converter's output voltage and current under various load conditions and disturbances. Equations related to phase-shift modulation and voltage dynamics in the DAB converter are central to the controller's operation [188]. For instance, the inductor current in the DAB converter can be expressed as a Fourier series expansion in terms of the phase shift δ and the state-space representation of the converter:

$$i_{sn}L(t) = \frac{4}{\pi}\sum_{L=o}^{\infty}\frac{1}{2L+1}\cdot\frac{NV_{in}}{|Z(L)|}sin[(2L+1)ft] \tag{2.9}$$

where NNN is the transformer turns ratio, V_{in} is the input voltage, $Z(L)$ is the impedance at harmonic order L, and the summation captures both the fundamental and higher-order harmonic components of the current. These harmonic terms are significant because they influence current stress and soft-switching behavior. The MPC uses this predictive current model, derived from the applied voltage waveforms, to dynamically adjust the phase shift and optimize performance, thereby reducing reactive power, improving ZVS, and enhancing efficiency under various load conditions. In Figure 2.34, the MPC controller receives measurements of the converter states, such as currents and voltages and uses these to predict future states based on the system model. The optimization algorithm then computes the optimal control inputs to minimize the cost function while satisfying constraints. The first control input of the optimized sequence is applied to the DAB converter, and the process repeats at each sampling interval.

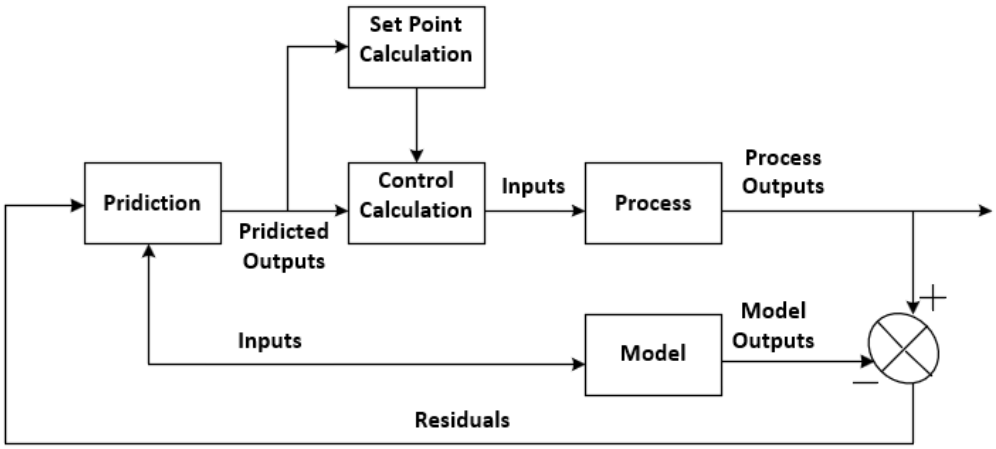

Figure 2.34: Block Diagram for Model Predictive Control.

MPC provides a powerful control strategy for DAB converters, enabling precise regulation of power flow and improved system performance. By solving an optimization problem at each control interval, MPC can handle multivariable interactions and constraints effectively, making it suitable for complex power electronic systems.

2.10.4 PI Controller

Proportional Integral (PI) controller for fast charging systems is used in regulating the output voltage and current of the charging system as shown in Figure 2.35, particularly in the rear-stage DC-DC converter. This control algorithm helps maintain the stability and precision of the charging process, ensuring the desired CC and CV charging phases for electric vehicle batteries [189].

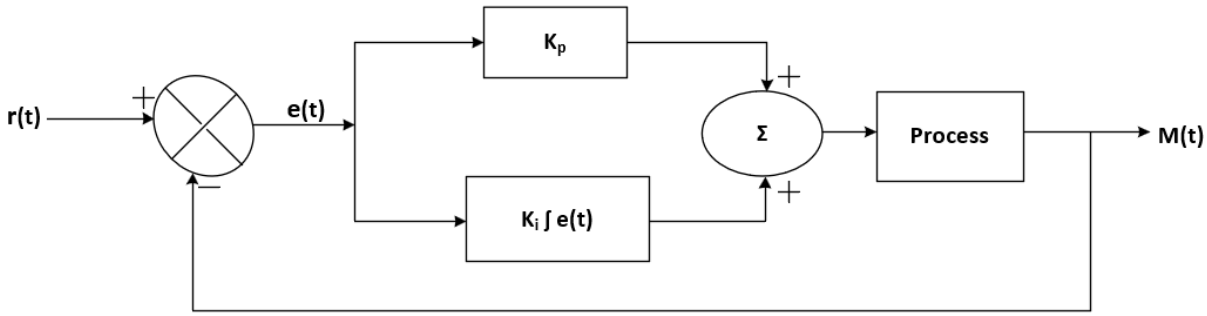

Figure 2.35: Control system with PI controller.

The PI controller typically employs the following control law:

$$u(t) = K_p\, e(t) + K_i \int_o^t e(\tau)\, d_\tau \tag{2.10}$$

where,

u is the control signal.

K_p is the proportional gain, which adjusts the error magnitude response.

Ki is the integral gain, responsible for eliminating steady-state errors by integrating the error over time.

$e(t)$ is the error signal, defined as the difference between the setpoint and the process variable. In the charging system, the PI controller processes the voltage and current feedback to adjust the duty cycle of the DC/DC converter switches. By continuously adjusting the control signal based on error feedback, the PI controller helps achieve smooth and reliable charging, while ensuring minimal overshoot and rapid convergence to the desired charging states.

2.10.5 Digital control

The digital control system receives a continuous-time error signal and converts it into a format that can be processed by a computer via an A/D interface. After processing, the discrete signal is fed to a controller, and its output is then applied to the system converter. The general structure of the digital controller is depicted in Figure 2.36. Due to the availability of high-speed microcontrollers, digital control strategies have become popular for use in bidirectional fly-back converters [190]. The primary control challenge in these converters is to minimize capacitive switching losses and electromagnetic interference without sensing high-voltage side signals, regardless of whether the converter is in charging or discharging mode of the capacitive load.

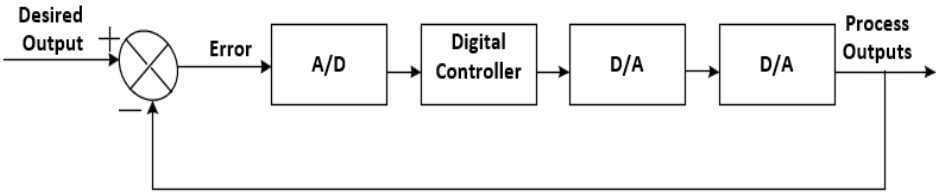

Figure 2.36: The structure of the digital controller.

The proposed method utilizes a valley switching technique controlled by a digital controller. It compares the input supply voltage with the drain-source voltage of the LV MOSFET using a high-speed comparator. The resulting signal is processed by a microcontroller, which generates a fixed on-time pulse, optimizing charge/discharge speed and efficiency. Accurate modelling of a DAB converter requires understanding its modulation method and accounting for interactions with EMI filters. DSPs are employed due to high computational efficiency, flexibility, EMI immunity, and fault-monitoring capabilities. Intelligent digital control algorithms such as deadband, switch, and soft-start control manage bidirectional power flow and protect the converter during startup [191]. The system operates under zero-voltage switching (ZVS), enhancing efficiency by eliminating the need for additional circuit protection components. Future power systems integrating loads, renewable energy, and storage benefit from FPGA-

based digital control platforms that offer flexibility and efficiency through software-reconfigurable modules. This approach reduces costs and development time while improving system reliability. Advances in digital control, including the hybrid digital adaptive controller, enhance transient responses in synchronous buck converters [192]. This control method ensures system stability through Lyapunov functions and discrete-time sliding-mode analysis, even under disturbances. Minimum-time solutions in power electronics use advanced geometric digital control techniques for optimal performance, relying on raster surfaces for complex processing within digital controllers.

2.10.6 Maximum power point tracking algorithms techniques

MPPT Algorithms are crucial techniques utilized in renewable energy systems, such as PV arrays, wind turbines to ensure the extraction of maximum available power from the source. In the context of the SST system, MPPT algorithms may be employed to optimize the power harvesting from connected distributed renewable energy resources. The primary purpose of MPPT algorithms is to continuously track the maximum power point of the PV array or other renewable energy source, even as environmental conditions (such as irradiance and temperature) change. By operating the renewable energy source at the MPP, the MPPT algorithm ensures that the maximum amount of power is delivered to the SST system, thereby maximizing the overall efficiency and energy conversion capabilities. Some commonly used traditional and advanced MPPT algorithms include:

2.10.6.1 Perturb and observe algorithm

The P&O algorithm is a widely used MPPT technique that can be effectively employed in the SST system to optimize the power extraction from connected renewable energy sources, such as PV arrays. The P&O algorithm operates by periodically perturbing the operating voltage of the PV array and observing the resulting change in the output power, and then adjusting the voltage in the direction that increases the power, effectively tracking the MPP of the PV array [193]. The explores a control technique using the P&O method for MPPT in renewable energy systems. This approach aims to optimize power extraction from variable energy sources, particularly during fluctuating conditions. The P&O algorithm adjusts the operating conditions based on observed power output, maintaining or reversing perturbation direction depending on whether power increases or decreases [194]. This demonstrates the effectiveness of the P&O method in enhancing power extraction and ensuring stable operation in renewable energy systems under varying conditions The P&O concept depicted in Figure 2.37.

Power output equation**:**

$$P_{Pv} = V_{pv} \, . I_{Pv} \tag{2.11}$$

Relationship between input and output voltage:

$$V_{Pv} = \left(\frac{1}{1-D}\right) V_{dc} \quad (2.12)$$

Output voltage expression:

$$V_o = \frac{V_S}{1-D} \quad (2.13)$$

Inductor current variation (when switch is closed):

$$\Delta i_L = \frac{V_S.D.T}{L} \quad (2.14)$$

Inductor current variation (when switch is open):

$$\Delta i_L = \frac{(V_S - V_o).(1-D).T}{L} \quad (2.15)$$

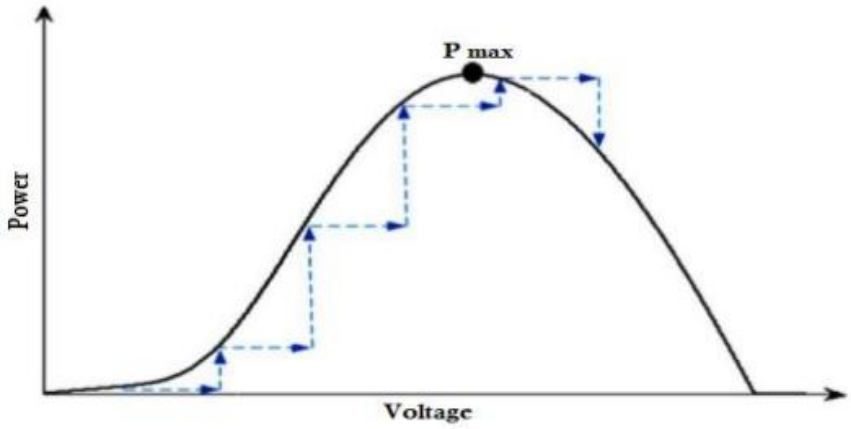

Figure 2.37: P&O Control process [195].

2.10.6.2 Incremental conductance (IC) algorithm

The IC is a refined maximum power point tracking technique used in photovoltaic systems to optimize energy harvesting by accurately identifying the MPP. It operates by comparing the incremental conductance $\left(\frac{dI}{dV}\right)$ to the instantaneous conductance $\left(\frac{I}{V}\right)$ of the PV module. The algorithm relies on the condition that at the MPP, the derivative of power with respect to voltage is zero, i.e., $\left(\frac{dP}{dV}\right) = 0$. This translates to the equation $\frac{dI}{dV} = -\frac{I}{V}$. If the calculated conductance is greater than the instantaneous conductance $\left(\frac{dI}{dV} > -\frac{I}{V}\right)$, the operating point is to the left of

the MPP, and the voltage should be increased, if less ($\left(\frac{dI}{dV} < -\frac{I}{V}\right)$ the voltage should be decreased [196]. By iteratively adjusting the operating voltage or current, the IC algorithm maintains operation at the MPP, reducing oscillations and improving energy extraction efficiency, particularly under dynamic environmental conditions. While this method provides more accurate and stable performance compared to simpler algorithms such as P&O, it requires more computational power, adding complexity and cost to the control system. The flowchart of the incremental conductance method is depicted in Figure 2.38.

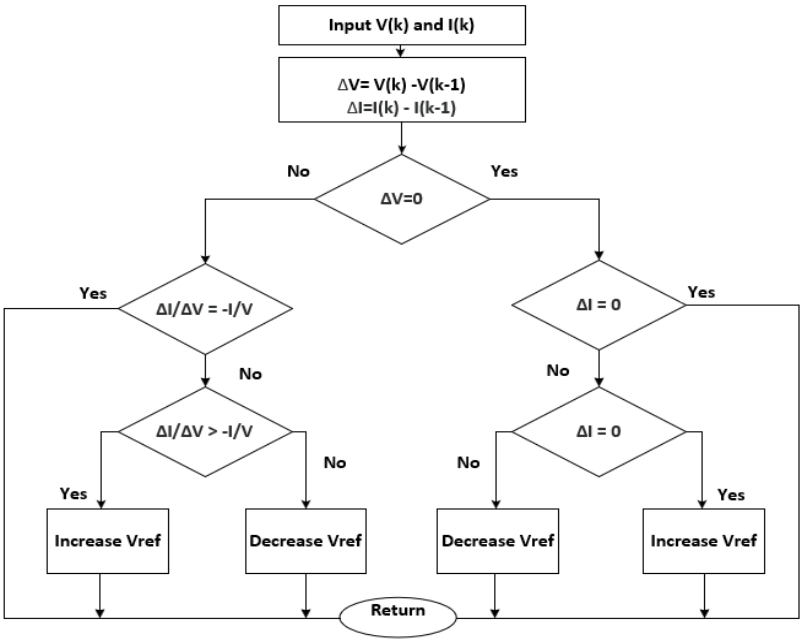

Figure 2.38: Flowchart of the incremental conductance method [197]**.**

2.10.6.3 Constant voltage algorithm

The CV algorithm is a straightforward MPPT technique used in PV systems, where the PV array voltage is maintained at a constant value, close to the MPP voltage. This method is based on the observation that the voltage at the $\boldsymbol{V_{MPP}}$ does not vary significantly with changes in irradiance or temperature. The algorithm involves measuring the open-circuit voltage $\boldsymbol{V_{OC}}$ of the PV module periodically, calculating a reference voltage $\boldsymbol{V_{ref}}$ as a constant fraction of $\boldsymbol{V_{OC}}$ (typically between 0.7 and 0.8), and adjusting the operating voltage of the PV module to this reference voltage [198]. The advantages of the CV algorithm include its simplicity and minimal computational requirements, making it suitable for systems with stable environmental conditions. However, it is less efficient under varying irradiance and temperature conditions due to its assumption of a fixed relationship between $\boldsymbol{V_{MPP}}$ and $\boldsymbol{V_{OC}}$, leading to potential power

loss [199]. This method is often used in small-scale PV systems, off-grid solar-powered devices, and small solar chargers. The CV-CC is shown in Figure 2.39.

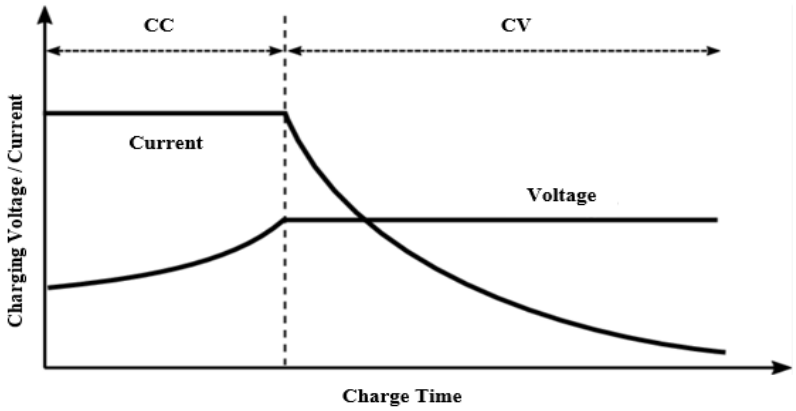

Figure 2.39: Constant-current constant-voltage (CC-CV) charging.

2.10.6.4 Fuzzy logic control (FLC)

Fuzzy Logic Control (FLC) is an advanced MPPT technique used in PV systems, characterized by its ability to handle non-linear and variable conditions without requiring a precise mathematical model. FLC mimics human decision-making processes by converting crisp input values such as voltage, current, and power into fuzzy variables using membership functions [200]. These inputs are then processed through a set of "IF-THEN" rules to produce an output. The algorithm steps include fuzzification, where input variables are converted into fuzzy values; rule evaluation, which combines the results of multiple fuzzy rules; and defuzzification, which converts the fuzzy output back into a crisp control action.

The main equations for the FLC technique are as follows:

Fuzzification

In this step, input variables such as the change in power (ΔP) are converted into fuzzy values using membership functions. For example, the triangular membership function for ΔP can be expressed as:

$$\mu\Delta P\ (x) = \left(\max\ (0, \min\frac{x-a}{b-a}, \frac{c-x}{c-b})\right) \quad (2.16)$$

Where, a, b, and c define the shape of the triangle.

Rule Evaluation

The fuzzy rules are then evaluated using logical operators. For instance, the minimum operator can be used for the AND condition as follows:

$$\mu output = \min\left(\mu\Delta P(x), \mu\Delta \mathrm{V}(\mathcal{Y})\right) \quad (2.17)$$

Defuzzification

Finally, the output is converted back into a crisp value using the centroid method:

$$V_{new} = \frac{\int_a^b x \,.\mu output\,(x)dx}{\int_a^b \mu output\,(x)dx} \tag{2.18}$$

This method is robust against uncertainties and variations, making it effective in dynamic environments with frequent changes in irradiance and temperature [201]. However, FLC is more complex to design and requires expertise in fuzzy logic theory. It is particularly suitable for large-scale solar power plants and residential systems with dynamic shading patterns, providing high efficiency and adaptability compared to traditional methods like P&O and CV. The fuzzy logic controller is shown in Figure 2.40.

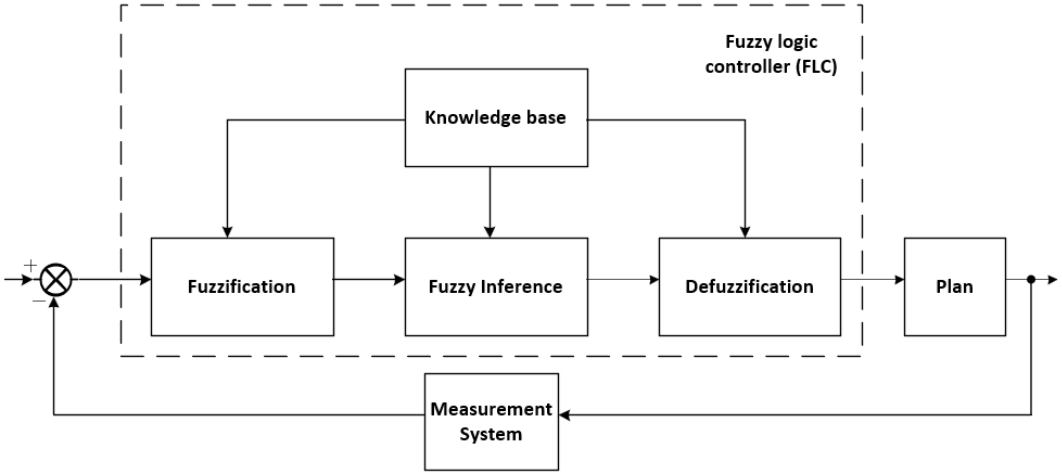

Figure 2.40: Fuzzy logic control system structure [202]**.**

2.10.6.5 Artificial neural networks (ANN)

Artificial Neural Networks (ANNs) are increasingly used in EV fast charging systems, particularly for MPPT. ANNs offer adaptive and accurate solutions by learning from historical data and current operating conditions [203]. Here's an overview of the updated information and equations relevant to ANN-based MPPT for EV fast charging are structure, training and prediction. Structure ANNs used for MPPT typically consist of multiple layers, including an input layer, hidden layers, and an output layer. The input layer receives parameters such as voltage, current, temperature, and irradiance. The hidden layers process this information, and the output layer provides the optimal operating point. The ANN is trained using a dataset that includes historical data of the system's performance under various conditions. This dataset must be extensive to cover a wide range of operating conditions. Once trained, the ANN can predict the MPP by analyzing the current operating conditions. This prediction helps in

adjusting the operating point to maximize the power extraction from the source [204]. As a result, each input neuron communicates with all hidden layer neurons, but every hidden layer neuron interacts with both the output layer through weights, as shown in Figure 2.41.

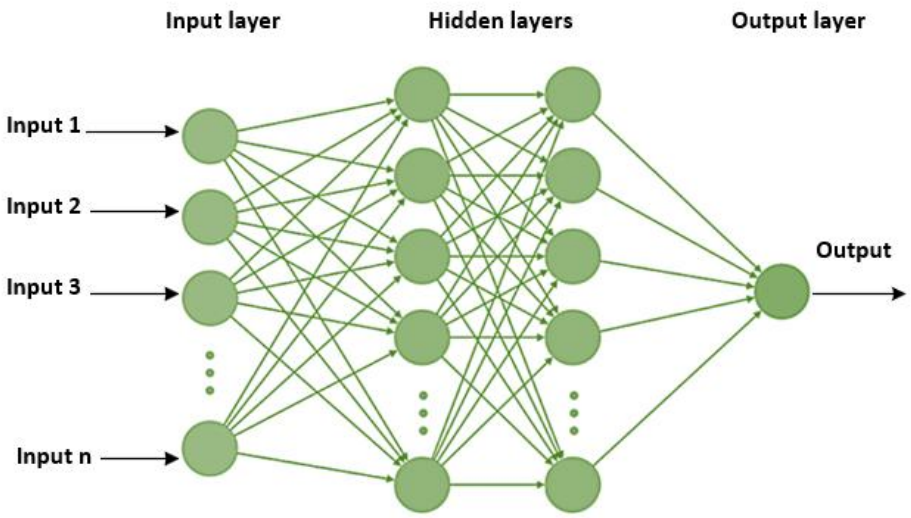

Figure 2.41: Diagram of an artificial neural network [205]**.**

Input Vector (X), the input to the ANN is a vector consisting of parameters affecting the MPP. For example:

$$\mathrm{X} = [V_{in}, I_{in}\ T, G] \tag{2.19}$$

where, V_{in} is the input voltage, I_{in} is the input current, T is the temperature, and G is the irradiance.

The output Y of the ANN is the predicted optimal voltage or current that corresponds to the MPP. For instance, if the output is the optimal voltage V_{opt}, we have:

$$Y = V_{opt} \tag{2.20}$$

Each neuron in the ANN uses an activation function to introduce non-linearity. Common activation functions include sigmoid, tanh, and ReLU (Rectified Linear Unit):

Sigmoide:

$$\sigma\,(x) = \frac{1}{1+e^{x}} \tag{2.21}$$

$$tanh \quad (x) = \frac{e^{x} - e^{x}}{e^{x} + e^{x}} \tag{2.22}$$

$$ReLU\ \ (x) = (0, x) \tag{2.23}$$

During forward propagation, the input vector is passed through the layers of the ANN. The output of each neuron is calculated as:

$$\alpha_j = \phi\left(\sum_i wijxi + b_j\right) \tag{2.24}$$

where, α_j is the activation of the neuron, wij are the weights, xi are the inputs, b_j are the biases, and ϕ is the activation function.

The performance of the ANN is evaluated using a cost function, which measures the difference between the predicted and actual values. A common cost function is the Mean Squared Error (MSE):

$$J = \frac{1}{n}\sum_{i-1}^{n}(Y_i - \hat{Y}_i)^2 \tag{2.25}$$

where, Y_i is the actual value, $\hat{Y}_i$ is the predicted value, and n is the number of training samples.

To minimize the cost function, the ANN adjusts the weights and biases using the backpropagation algorithm. The gradients of the cost function with respect to the weights are calculated, and the weights are updated using gradient descent:

$$w_{ij} \leftarrow w_{ij} - \eta\frac{\partial J}{\partial w_{ij}} \tag{2.26}$$

where, η is the learning rate.

The ANN is deployed in the EV fast charging system, where it continuously monitors the input parameters and predicts the MPP in real-time [206]. Regular performance monitoring is essential to update the training data with new operating conditions, ensuring better accuracy. The advantages of this approach include high accuracy in predicting the MPP, the ability to adapt to changing conditions, and improved efficiency in power extraction. However, the challenges involve the need for significant computational resources for training, a large and diverse dataset for effective training, and the computational intensity of real-time implementation. By leveraging ANN-based MPPT, EV fast charging systems can achieve higher efficiency and reliability, optimizing the charging process and reducing energy losses.

2.10.6.6 Particle swarm optimization (PSO)

Particle Swarm Optimization (PSO) is a swarm intelligence method inspired by the behavior of birds and fish. It has been widely applied in various engineering fields due to its strong global optimization capability, achieved through the cooperation and competition of group agents

[207]. In PV systems, PSO as illustrated in Figure 2.42, is used to track the MPP even under Partial Shading Conditions (PSC).

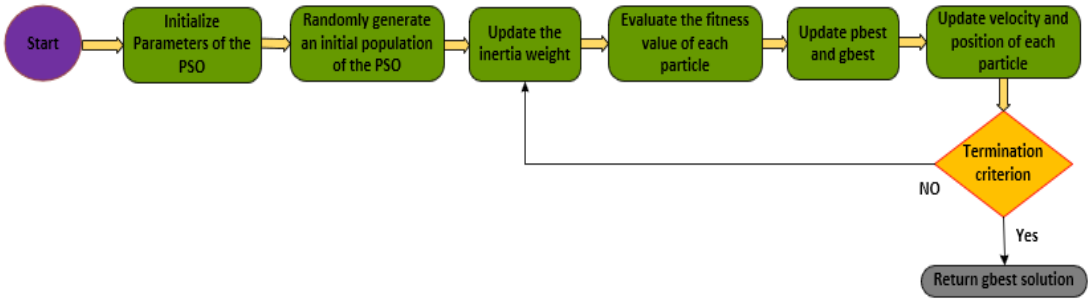

Figure 2.42: The flowchart of the PSO algorithm.

The operation of PSO relies on two basic principles: communication and learning. The method involves a group of particles, each with a position $(X_i(t))$ and a velocity $V_i(t))$. The best position found by each particle, known as the personal best $P_{best}(t))$, is stored in memory, while the best position found by the entire group, known as the global best $G\ (t))$, guides the swarm [208]. In each iteration, the velocity of the particles is updated using the following equation [2.27].

$$V_i\ (t+1) = wV_i(t) + r_1c_1\ (P_{best\ i}(t)) - X_i\ (t)) + r_2c_2\ (\ G(t) - X_i(t)) \tag{2.27}$$

Where the inertia coefficient is indicated by w. $c_1\ , c_2$ are the coefficient of acceleration, $r_1\ , r_2$ are the uniform distributed coefficients in between range 0 and 1.

The position of the agent is updated by Equation [2.28].

$$X_i\ (t+1) = X_i(t) + V_i(t+1) \tag{2.28}$$

Where $X_i\ (t+1)$ is the updated position, $X_i\ (t)$ denotes position, $V_i(t+1)$ is updated velocity position.

By utilizing the above equation, PSO operates efficiently. However, it is prone to falling into local optima (LO) instead of finding the global maxima (GM). Additionally, it has a higher standard deviation and lower efficiency compared to improved grey wolf optimization.

2.11 Summary

Chapter Two provided a comprehensive review of EV charging technologies, including inductive, ultra-fast, and DC fast charging methods, as well as renewable integration, energy

management, and microgrid architectures. While significant progress has been made, the review identified key research gaps: DC fast charging systems still face stability challenges under fluctuating renewable generation, grid-connected PV chargers introduce harmonic distortion and power quality concerns, and the coordination of energy storage with PV and grid supply remains limited. Furthermore, modular converter topologies such as the Dual Active Bridge (DAB) encounter issues with current sharing, soft switching, and harmonic suppression. To address these gaps, this dissertation proposes a PV–BESS–grid-supported DC fast charging system that integrates advanced converter control, harmonic compensation, energy management strategies, and optimized DAB operation to enhance stability, reliability, and efficiency in renewable-based EV fast charging.

CHAPTER THREE
SYSTEM ARCHITECTURE AND DC FAST CHARGING MODELLING

3.1 Introduction

The past decade has seen rapid advancements in EV charging technologies and grid integration, driven by the growing adoption of EVs and the demand for faster, more efficient charging solutions. This chapter focuses on developing a model of a DC off-board fast charging system that comprises three main stages, as shown in Figure 3.1, that PV stage, the AC grid stage, and the charger stage. The PV stage includes a PV array consisting of multiple solar panels that convert sunlight into direct current electricity, paired with a DC-DC converter featuring Maximum Power Point Tracking to optimize power extraction. The AC grid stage involves a front-end converter that connects the system to the AC grid, managing energy flow between the DC bus and the grid, thus facilitating energy draw or feed-back as needed. To enhance performance in this stage, a PI controller is implemented to regulate battery side DC voltage and current, ensuring stable operation. In the charger stage, a bidirectional DC charger converts the power for charging the EV battery while also allowing energy to flow back to the grid or home system when necessary. This stage also employs a PI controller to optimize the charging process and maintain battery health, ensuring efficient energy transfer and management across the system. The interconnection of these stages via a DC bus enables the DC fast charging system to operate optimally while maximizing the use of renewable energy, forming the basis for the detailed exploration of modeling and control strategies in this chapter. Additionally, the system's architecture has been modeled in MATLAB/Simulink to address key issues like charging efficiency and grid stability during peak demand periods, reducing the load on the grid by leveraging renewable energy sources. The detailed parameters of this study system are listed in Table 3.1.

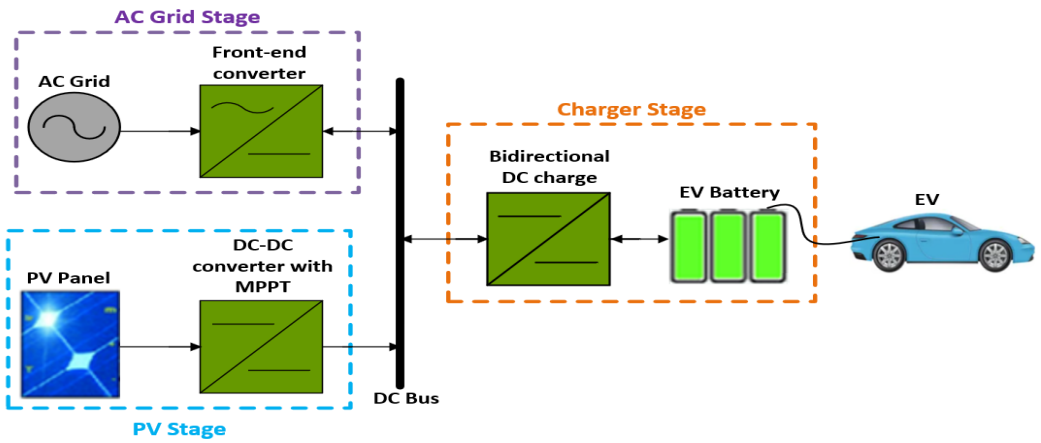

Figure 3.1: PV-grid-tied off-board EV charging system structure.

Table 3.1: Parameters of Grid Source Components in a DC fast charging system

Parameter Description	Value Rated
AC line voltage	400 V
AC line current	100 A
Line resistance	0.02 Ω
Line inductance	1.21 mH
Line capacitance	5000 μF
Transfer function coefficient	1e-06 s
Kp, Ki PI parameters of current loop	0.248 – 21.692
Kp, Ki PR parameters of PLL	0.05, 1.571
Voltage controlled oscillator (VCO).	6.28
Switch frequency	10 kHz
System frequency	50 Hz

The parameter values in Table 3.1 were obtained from a combination of control design methodologies, standard practice in literature, and validation through MATLAB/Simulink simulations. The PI and PR gains were tuned using the converter's small-signal model and grid synchronization requirements, while the VCO value corresponds to the grid angular frequency (2π × 50 Hz). The switching frequency of 10 kHz reflects a common trade-off between dynamic performance and switching losses in medium-power converters.

The load profile used for this study was analytically generated based on defined system parameters and typical EV fast charging demand patterns reported in the literature. This approach provides a realistic representation of daily charging demand for simulation purposes. The load profile illustrated in Figure 3.2, for three EV charging strategies demand charging, off-peak charging, and off-peak with Vehicle-to-Home (V2H) charging was analyzed over a 24-hour period, demonstrating their impact on grid load and energy management. Demand charging peaks in the early morning, stabilizing during the day, creating higher stress on the grid during peak demand. Off-peak charging shifts energy consumption to low-demand periods, gradually increasing usage in the evening, which reduces grid strain and improves efficiency. The off-peak + V2H strategy involves charging during off-peak times and discharging energy back to the grid during peak hours, showing negative power values and enhancing grid stability through bidirectional energy flow. Variability within ±2 standard deviations highlights fluctuations in power demand due to charging patterns and battery SOC.

The integration of PV energy using a DC-DC boost converter with MPPT, a front-end converter with a bidirectional converter managing grid interaction, and a lithium-ion battery model for fast charging further supports the system's efficiency, optimizing renewable energy use and grid reliability.

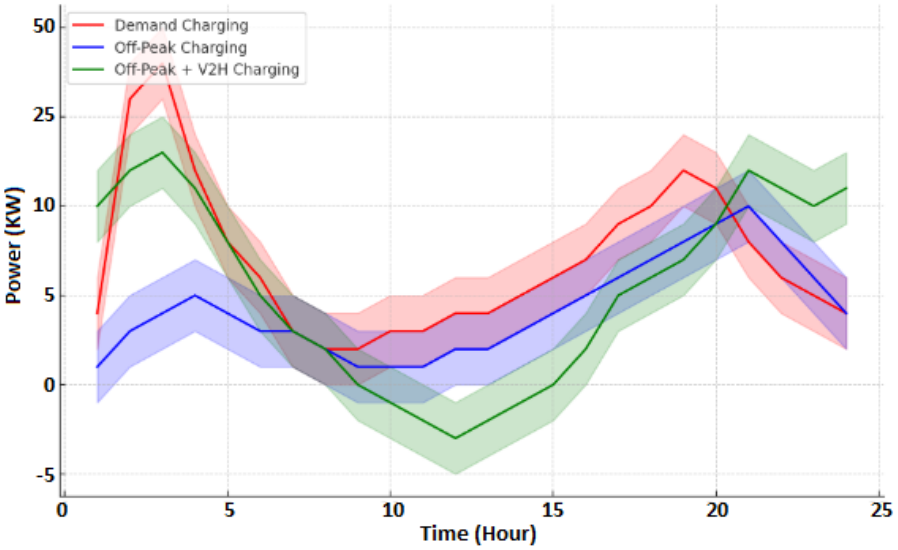

Figure 3.2: Load profile for DC fast charging in EV system.

3.2 Three-Phase Voltage Source Modeling

In the developed DC fast charging system model for EVs, the grid is modeled as a balanced three-phase voltage source operating at 50 Hz. This voltage source provides the AC input to the AFE rectifier, which converts the AC power to DC to support fast charging. The grid is represented by a low-voltage three-phase network. This method focuses on the mathematical representation and application of the three-phase voltage source within the AC-DC conversion stage of the system. The grid input is modeled as three balanced sinusoidal voltages of equal amplitude and frequency, with each phase shifted by 120 degrees [209]. The instantaneous voltages for the three-phase (abc) are represented as:

$$v_a(t) = V_m \sin(\omega t) \tag{3.1}$$

$$v_b(t) = V_m \, sin\left(\omega t - \frac{2\pi}{3}\right) \tag{3.2}$$

$$v_c(t) = V_m \, sin\left(\omega t + \frac{2\pi}{3}\right) \tag{3.3}$$

where,

$v_a(t), v_b(t), v_c(t)$ are the instantaneous voltages of phases a, b, and c, respectively.

V_m is the peak voltage of each phase.
$\omega = 2\pi f$ is the angular frequency of the system, where f is the grid frequency (typically 50 Hz or 60 Hz).
t is time.
In the phasor domain, these voltages can be expressed as:

$$V_a = V_m \angle 0^o \tag{3.4}$$

$$V_b = V_m \angle -120^o \tag{3.5}$$

$$V_c = V_m \angle +120^o \tag{3.6}$$

For practical calculations, the Root Mean Square (RMS) values of the voltages are used. The relationship between the peak voltage V_m and the RMS voltage V_{rms} is given by [210]:

$$V_{rms} = \frac{V_m}{\sqrt{2}} \tag{3.7}$$

In a three-phase system, the line-to-line voltages (voltages between any two phases) are related to the line-to-neutral voltages by a factor of $\sqrt{3}$:

$$V_{LL} = \sqrt{3} \, . V_{LN} \tag{3.8}$$

where,
V_{LL} is the line-to-line voltage.

V_{LN} is the line-to-neutral voltage (same as V_{rms} for a single phase).

3.3 LC Filter

The LC filter is implemented in the system model to remove unwanted harmonics from the AC supply before the AC-DC conversion stage in the active front-end rectifier. This ensures that a clean and smooth AC signal is fed into the rectifier, minimizing distortion and improving power quality. The LC filter consists of an inductor L_f and a capacitor C_f , which form a second-order low-pass filter. The primary goal is to attenuate high-frequency harmonic components generated by the switching actions of the rectifier while allowing the fundamental grid frequency (50 Hz) to pass with minimal attenuation.
The transfer function of the LC filter in the Laplace domain is expressed as [211]:

$$H(s) = \frac{V_{out}(s)}{V_{in}(s)} = \frac{1}{LCs^2+RCs+1} \quad (3.9)$$

Here, $V_{in}(s)$ represents the input AC voltage containing harmonic components, while $V_{out}(s)$ is the filtered output voltage. The filter consists of an inductance L, a capacitance C, and a series resistance R, which models resistive losses in the filter. The variable s is the Laplace operator (complex frequency variable), used as a multiplier in the denominator terms to represent the system dynamics in the frequency domain. The filter's cut-off frequency f_c is designed to be below the switching frequency of the rectifier, typically in the kilohertz range, to ensure that harmonics beyond this frequency are significantly attenuated:

$$f_c = \frac{1}{2\pi\sqrt{L_f C_f}} \quad (3.10)$$

The values of L_f and C_f are selected based on the desired attenuation of harmonics while maintaining low impedance at the grid frequency (50 Hz). The filter ensures that the fundamental frequency passes with minimal attenuation while significantly reducing harmonic components above f_c.

3.3.1 Sinusoidal pulse width modulation (SPWM)

The SPWM technique is implemented as a critical method for controlling the Voltage Source Converter (VSC). SPWM operates by comparing a sinusoidal reference waveform (representing the desired output) with a high-frequency triangular carrier waveform to generate precise switching pulses. These pulses drive the switching devices in the DAB converter, controlling the flow of power between the AC grid and the electric vehicle's battery.

In this design, the carrier waveform is typically triangular, while the reference signal is sinusoidal. The comparison between the two is essential for producing the desired output voltage. If the sinusoidal reference signal exceeds the triangular carrier, the output of the converter produces a positive DC voltage; if it is less, the output voltage becomes negative. This logic can be mathematically expressed as follows:

$$V_{out} = \begin{vmatrix} +V_{DC}, V_{carrier} < V_{reference} \\ -V_{DC}, V_{carrier} < V_{reference} \end{vmatrix} \quad (3.11)$$

In the applied SPWM method utilized in the DAB converter for DC fast charging systems, the modulation index plays a crucial role in minimizing switching losses while maintaining a balanced condition for the rectifier. The MI directly impacts the output voltage level, making it a key parameter in optimizing converter performance. It is defined as the ratio of the sinusoidal

reference voltage $V_{sinusoidal}$ to the triangular carrier voltage $V_{triangular}$. This relationship can be mathematically expressed as [212].

$$MI = \frac{V_{sinusoidal}}{V_{triangular}} \tag{3.12}$$

Here, MI represents the modulation index, with its maximum value being 1. However, there are some drawbacks to using SPWM. One major disadvantage is its inability to directly control the harmonics in the output signal. Additionally, it imposes limitations on the DC bus voltage. Although SPWM is an analog technique, its implementation is often done in the digital domain using a microcontroller, which introduces complexity in real-time signal conversion [213].

3.3.2 Park –clark transform

By addressing time-domain variable issues, this technique contributes to the efficient and reliable operation of DC fast charging infrastructure. The transformation shifts the AC signals from the stationary reference frame (ABC) into a rotating reference frame dq as mention in equations (3.13), (3.14), allowing for more effective control of electric machines and grid synchronization, by transforming time-varying signals into steady-state values [214].

$$P_\theta = \frac{2}{3}\begin{bmatrix} cos\theta & cos(\theta - 120^o) & cos(\theta + 120^o) \\ -sin\theta & -sin(\theta - 120^o) & -sin(\theta + 120^o) \\ 1/2 & 1/2 & 1/2 \end{bmatrix} \tag{3.13}$$

$$\begin{bmatrix} V_d \\ V_q \\ V_0 \end{bmatrix} = P_\theta \begin{bmatrix} V_A \\ V_B \\ V_C \end{bmatrix} \tag{3.14}$$

When a three-phase system is transformed into the orthogonal reference frame αβ, it is referred to as the Clark transform. This transformation allows the conversion of three-phase currents or voltages into two orthogonal components, simplifying analysis and control in power systems is represented by the following equation:

$$C_{\alpha\beta} = \frac{2}{3}\begin{bmatrix} 1 & -1/2 & -1/2 \\ 0 & \sqrt{3}/2 & -\sqrt{3}/2 \\ 1/2 & 1/2 & 1/2 \end{bmatrix} \tag{3.15}$$

$$\begin{bmatrix} V_\alpha \\ V_\beta \\ V_\gamma \end{bmatrix} = C_{\alpha\beta} \begin{bmatrix} V_A \\ V_B \\ V_C \end{bmatrix} \tag{3.16}$$

3.3.3 Inverse Park Transform

When the dq-stationary frame is transformed back to the phase ABC frame, it is referred to as an inverse park transform. This transformation is represented by equations (3.17) and (3.18), which are known as the inverse-park transformation [215],[216].

$$\begin{bmatrix} v_\alpha \\ v_\beta \end{bmatrix} = \begin{bmatrix} cos\delta & sin\delta \\ \sin\delta & cos\delta \end{bmatrix} \begin{bmatrix} v_d \\ v_q \end{bmatrix} \tag{3.17}$$

$$\begin{bmatrix} V_A \\ V_B \\ V_C \end{bmatrix} = I_{dq-abc} \begin{bmatrix} V_d \\ V_q \\ V_0 \end{bmatrix} \tag{3.18}$$

3.3.4 PI controller

Section 2.10.4 provides the standard PI controller formulation and a brief review of its use in charging systems. Building on that background, this section describes the PI controller as implemented in the developed DC fast-charging model. The controller used in the model is given in the time domain by equation (3.19) and in the Laplace domain by equation (3.20). In the implemented system, the proportional-integral controller is applied to maintain a stable feedback control loop by continuously measuring the error between the actual output and the reference set-point. The controller adjusts the system's response until the error is reduced to zero, ensuring accurate synchronization and smooth operation. However, in some cases, the PI controller may exhibit a slower response, particularly when external disturbances affect the system [217]. This is especially important in the context of DC fast charging for EVs, where fast and precise control is needed to manage voltage and current during the charging process. The PI controller in this system is mathematically represented by the equation [218]:

$$v_{PI}(t) = K_p e(t) + K_i \int_0^t e(\tau)dt \tag{3.19}$$

where, K_p is the proportional gain, K_i is the integral gain, and $e(t)$ is the error signal at time t. By adjusting these gains, the PI controller helps optimize the charging process, improving system stability and response time. In the Laplace domain, the output of the PI controller can be expressed as $V(s)$. This representation allows the system to manage dynamic behavior and disturbances by regulating the output in proportion to both the present error and the accumulated past error. The PI controller's transfer function in the Laplace domain is given by [219]:

$$V(s) = K_p E(S) + \frac{k_I}{s} E(s) \tag{3.20}$$

In this research, the PI controller is employed both in the Phase-Lock Loop (PLL) and in the voltage and current control loops**.** The primary function of the PI controller within the PLL is to

generate the correct phase angle for the voltage by minimizing the error between the actual and reference signals. Similarly, in the voltage and current control loops, the PI controller works by comparing the actual values to the reference set-points, adjusting the output until the error is reduced to zero, ensuring smooth and accurate control. By adjusting the proportional and integral gains, the error can be further minimized, enhancing system performance. A trial-and-error PI tuning method has been applied in this system to optimize the gains, stabilizing the output and ensuring a steady-state response.

3.3.5 Phase-lock loop (PLL)

To develop appropriate controllers, AC variables are represented within a rotating reference frame. This reference frame aligns with the angular velocity of the grid voltage phasor, $\bar{v}_{ac}$. In practical implementations, this alignment is achieved using a PLL [220], a control system designed to ensure that the angle of the d_q-reference frame θ_{dq}, accurately tracks the angle of the AC system, θ_{ac}. The PLL typically demonstrated in Figure 3.3, consists of three key components: a phase detector (PD), a loop filter (LF), and a voltage-controlled oscillator (VCO). The grid voltage $\bar{v}_{ac}$ can, thus, be expressed in the d_q-frame as follows in equation (3.21), [221]:

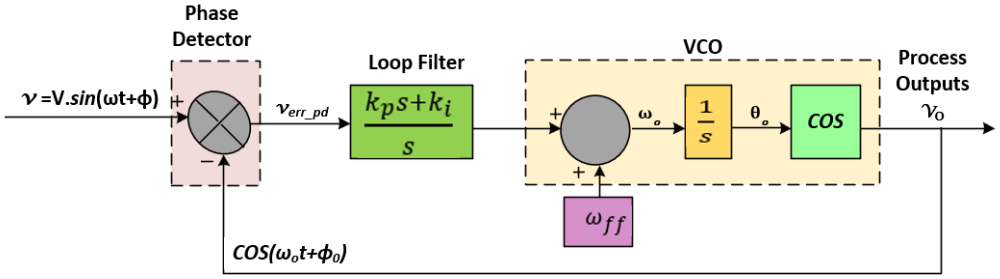

Figure 3.3: Structure of PPL.

$$v_{ac,d} + jv_{ac,q} = v_{ac}(cos(\theta_{ac} - \theta_{dq}) + j\ sin(\theta_{ac} - \theta_{dq})) \tag{3.21}$$

The PLL control loop incorporates a phase detector that measures the phase difference between the grid voltage and the internal reference signal. The PI controller implemented in the Simulink model follows the standard form given in Eq. (2.10). The same formulation is applied in the final integrated system analysis (previously Eq. 3.78). This phase error is then processed by a PI controller, which generates a control signal to adjust the reference angle accordingly. The loop aims to minimize the error between the measured grid phase and the estimated reference phase, ensuring accurate synchronization with the grid [222].

$$\theta_{PLL}\ (t) = K_p\ .e(t) + K_i \int e(\tau)dt \tag{3.22}$$

The output of the PLL provides the phase angle θ_{PLL}, which is used to transform the grid voltage into the synchronous reference frame.

Transformation to the synchronous reference frame $\boldsymbol{dq0}$ in the system model, the three-phase grid voltages $\boldsymbol{v_a(t), v_b(t), v_c(t)}$ are transformed to the $\boldsymbol{dq0}$ synchronous reference frame using Park's transformation [223]. This allows for simpler control of the rectifier in the synchronous $\boldsymbol{d-q}$ axes.

The transformation equations are:

$$v_d = \frac{2}{3}\left[v_a cos(\theta_{PLL}) + v_b cos\left(\theta_{PLL} - \frac{2\pi}{3}\right) + v_c \cos\left(\theta_{PLL} + \frac{2\pi}{3}\right)\right] \quad (3.23)$$

$$v_q = \frac{2}{3}\left[v_a sin(\theta_{PLL}) + v_b sin\left(\theta_{PLL} - \frac{2\pi}{3}\right) + v_c sin\left(\theta_{PLL} + \frac{2\pi}{3}\right)\right] \quad (3.24)$$

where,

v_d and v_q are the direct and quadrature components of the grid voltage in the synchronous reference frame. θ_{PLL} is the phase angle provided by the PLL.

In the developed DC fast charging system for EVs, the control scheme ensures efficient power conversion and stable operation, as illustrated in Figure 3.4 shows the grid-side voltage-oriented control (VOC) of the two-level VSI. The DC-link voltage controller provides Id_ref (outer loop) while the reactive/PF controller sets Iq_ref (outer reactive setpoint). The current errors $\Delta d = Id\_ref - id\_meas$ and $\Delta q = Iq\_ref - iq\_meas$ are regulated by PI current controllers; their outputs are fed to the PWM modulator which drives the two-level VSI. For the simulations in this work, $Iq\_ref = 0$ is used to maintain unity power factor unless stated otherwise.

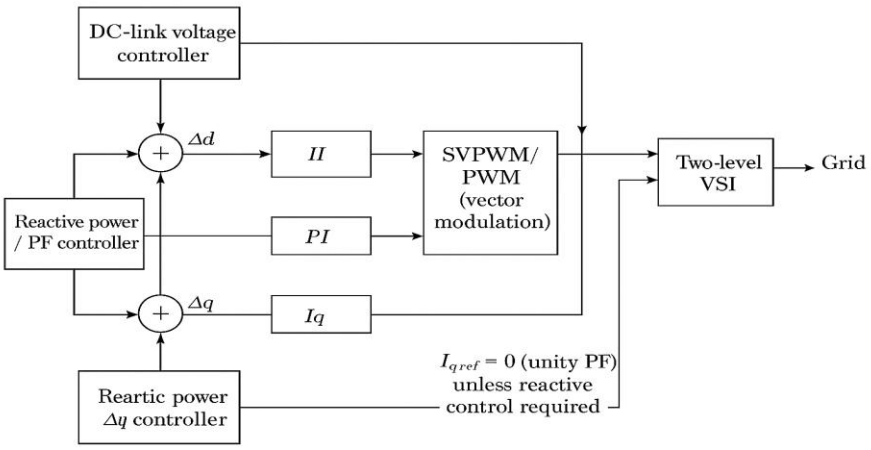

Figure 3.4: Control Scheme of the phase grid voltage and current conversion [224].

Figure 3.4 grid-side VOC block diagram for the two-level VSI. Outer DC-link voltage controller generates Id_ref the reactive power / power-factor controller provides Iq_ref (set to 0 for unity power factor). Inner current control loops regulate id and iq (PI controllers), whose outputs are modulated by PWM and applied to the two-level inverter. Measured grid currents are Clarke/Park transformed using the PLL angle to produce *id_meas* and iq_meas for feedback.

3.4 Front-End AC-DC Converter

The Active Front-End (AFE) converter has been implemented and designed as a key component in the DC fast charging system for electric vehicles, performing both AC-DC conversion and PFC as illustrated in Figure 3.5. The AFE is connected to the utility grid through a filter to ensure efficient power conversion. During the system's design phase, a typical AFE control strategy based on voltage-oriented control was employed.

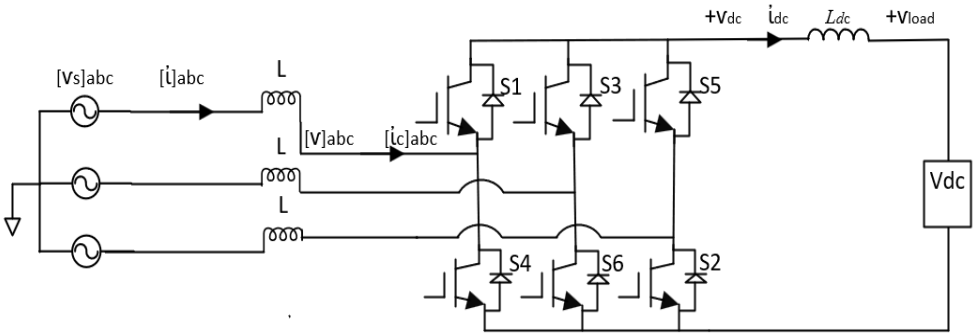

Figure 3.5: Frontend converter and DC link capacitor subcircuit.

To analyze the front-end converter, the following mathematical equations are utilized. Here, L_s and R_s represent the inductance and resistance of the boost inductor on the input side, respectively, and ω denotes the natural frequency. The terms V_{dq}, i_{dq}, and $V_{conv.dq}$ correspond to the grid-side voltages, grid-side currents, and converter-side voltages, respectively, in the d_q reference frame. Additionally, I_{dc} and I_{load} represent the total DC current and the DC load current, respectively [225].

$$V_d = i_d R_s + L_s \frac{di_d}{dt} - \omega L_s i_q + V_{conv.d} \tag{3.25}$$

$$V_q = i_q R_s + L_s \frac{di_q}{dt} - \omega L_s i_d + V_{conv.q} \tag{3.26}$$

Additionally, the DC load side of the front end can be represented mathematically as follows.

$$C_{dc}\frac{dV_{dc}}{dt} = I_{dc} - I_{load} \tag{3.27}$$

In this system, PFC is essential to improve the efficiency of power transfer from the grid. The IGBT bridge controls the input current to follow the grid voltage phase. The power factor is calculated as [226]:

$$cos(\phi) = \frac{P}{S} = \frac{V_{rms}I_{rms}}{\sqrt{V_{RMS}^2 + I_{rms}^2}} \tag{3.28}$$

where,

In the system, P represents the active power, while S is the apparent power. The variables V_{rms} and I_{rms} correspond to the root-mean-square values of the grid voltage and current, respectively. This method ensures the current drawn from the grid remains sinusoidal and aligned with the voltage, optimizing the grid's utilization for EV charging. The purpose of the grid-side inductor is to reduce any remaining harmonics that are not effectively filtered by L_c and C_f. The inductor limits the rate of current change, while the capacitor smooths the voltage by providing a low-impedance path for high-frequency components [227].

The transfer function of a basic LC filter is given by:

$$H(s) = \frac{V_{out}(s)}{V_{in}(s)} = \frac{1}{1 + sRC + s^2LC} \tag{3.29}$$

where, R represents the equivalent series resistance (ESR) of the components, L is the inductance value, C is the capacitance value, and s is the Laplace transform variable.

The cut-off frequency f_c is selected based on the switching frequency of the IGBT bridge, ensuring it effectively filters out higher-order harmonics while maintaining system stability:

$$f_c = \frac{1}{2\pi}\sqrt{\frac{L_g + L_f}{L_g L_f C_f}} \tag{3.30}$$

This determines the frequency beyond which attenuation occurs. The LC filter components L_g, L_f and C_f are chosen to ensure that high-frequency harmonics (in the kHz range) are sufficiently attenuated, with typical total harmonic distortion reduction to below 5%, meeting IEEE 519 standards. For an LC low-pass filter, the characteristic impedance is given by:

$$Z_0 = \sqrt{\frac{L}{C}} \tag{3.31}$$

which determines the filter's ability to reject high-frequency noise.

In the applied system, the LC filter's design minimizes the THD in the current waveform, improving power quality by ensuring the harmonic content is reduced:

$$THD = \frac{\sqrt{\sum_{n=2}^{\infty} I_n^2}}{I_1} \tag{3.32}$$

where,

I_n is the RMS value of the nth harmonic,

I_1 is the RMS value of the fundamental component.

The LC filter ensures a clean AC signal fed into the rectifier, reducing THD and improving the efficiency of the DC fast charging system. Table 3.2 presents the power converter component parameters.

Table 3.2: Parameters of Grid Components in the Power conversion system

Parameter Description	Value Rated
AC line voltage	400 V
Rated DC bus voltage	800 V
Converter output voltage	900 V
Converter output current	100 A
DC Charger power	90 kW
Inductance L	10e-6 H
Capacitance C_{DC}	1200 μF
Switch frequency	10 kHz
System frequency	50 Hz
Kp, Ki PI parameters of DC-DC	0.248 – 21.692
Sample time	2 s
Power efficiency η	0.95 %
Power factor	0.998
EV battery capacity	50 Ah
Response time	1 s
Nominal temperature	25 ℃
Initial battery SoC	25 %

3.5 Dual Active Bridge Converter in DC Fast Charging System

In the developed DC fast charging system for electric vehicles, the DAB converter, as shown in Figure 3.6, is implemented to ensure efficient energy transfer between the AC grid and the

EV battery. This DAB converter regulates both the DC voltage and current during the charging process, providing essential galvanic isolation and enabling bidirectional power flow. The system's design includes two active bridges—one on the input side connected to the AC-DC conversion stage and one on the output side connected to the EV battery. These bridges are interconnected through a high-frequency transformer and a series inductance L_k, which allow for efficient power transfer. The converter's switches, S_1 to S_8, are actively controlled to manage the power flow, ensuring accurate voltage and current regulation as required by the battery charging profile. This setup allows the system to handle voltage step-up or step-down operations with minimal power loss. By integrating the DAB converter into the system, the fast charger achieves optimized energy transfer, ensuring that the EV battery is charged rapidly and safely. The soft-switching capability of the DAB also minimizes switching losses, contributing to the high efficiency and stability of the developed charging system. This ensures that the power delivered to the EV is precise, meeting the demand for fast and reliable charging.

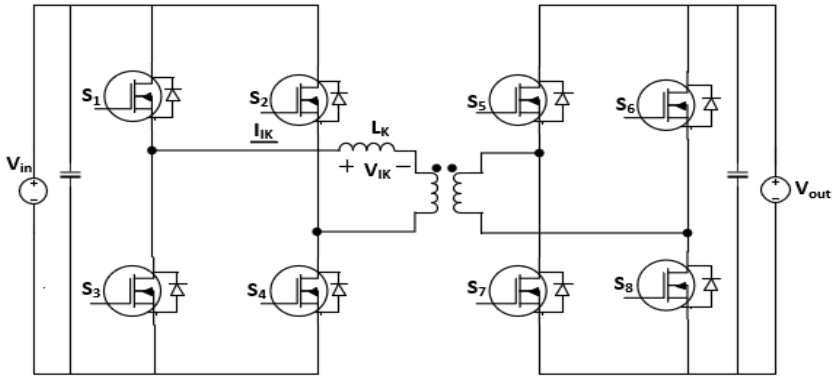

Figure 3.6: Dual active bridge converter.

3.5.1 Power flow analysis

In the developed DC fast charging system for electric vehicles, the dual active bridge DC-DC converter plays a critical role in managing bidirectional power flow between the AC grid and the vehicle's battery. This bidirectional capability enables both the charging and discharging processes, including V2G functionality. In the applied system, power flow is regulated by adjusting the phase shift between the primary and secondary bridges, which directly controls the magnitude and direction of the power transfer. This phase-shift control is essential for maintaining stable DC bus voltage while following the CC and CV charging profiles, which are critical for efficient and safe battery charging. Key components such as the leakage inductance L_k and the high-frequency transformer are integral to the power transfer dynamics. Their interaction with the phase-shift control determines the system's overall efficiency and energy conversion capabilities. To further optimize performance, wide-bandgap semiconductor

materials like SiC are used in the switching devices. These SiC devices allow for high power handling with reduced losses, especially when operating at high frequencies. The DAB converter in this system consists of two full-bridge circuits, each utilizing complementary square-wave pulses to drive the switching devices. The increased switching frequency takes advantage of the high-frequency properties of SiC, reducing the impact of the transformer's magnetizing inductance and allowing the system to focus on the leakage inductance for power transfer. The power equation governing the converter's operation is derived from the square-wave voltages applied across the high-frequency transformer's terminals, ensuring efficient, reliable power conversion for the DC fast charging process, as shown in Figure 3.7. This design provides the robust performance required to support modern fast charging infrastructure while ensuring safety and efficiency throughout the charging cycle.

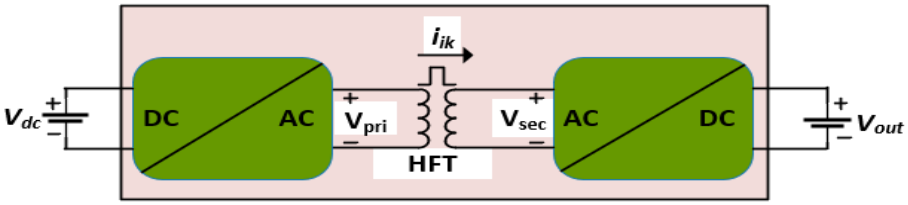

Figure 3.7: High frequency equivalent dual active bridge.

In the implementation of the DAB converter for DC fast charging systems, the power flow is controlled through a method known as phase shift modulation. This technique adjusts the phase angle between the control pulses of the primary and secondary bridges, thereby managing the direction and magnitude of power transfer between the two DC buses. In the applied design, as illustrated in Figure 3.8, power transfer from the primary bridge to the secondary bridge is achieved by phase-shifting the control pulses of switches $S1$ and $S4$ on the primary side and switches $S5$ and $S8$ on the secondary side by a positive phase angle $+\delta$. Conversely, when the phase shift is applied negatively, the secondary bridge becomes the leading bridge, and power flows back from the secondary bridge to the primary bridge.

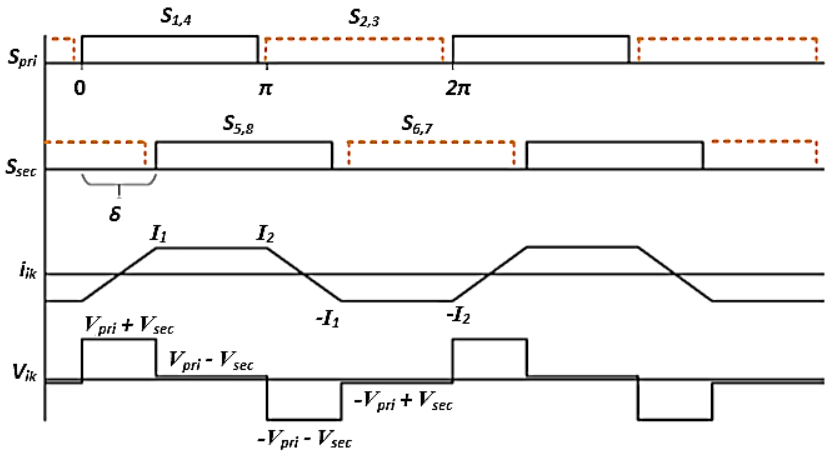

Figure 3.8: Dual active bridge waveforms.

The symmetry of the current waveform $i_{ik}(t)$, which flows through the leakage inductance, plays a crucial role in simplifying the power flow analysis. This symmetry allows for an analysis over just half of the switching period, reducing computational complexity while maintaining the accuracy of the results. The design approach, as depicted by the current derivative equation (3.33), simplifies the representation of the inductor current by focusing on the voltage difference between the primary and secondary windings of the high-frequency transformer. By leveraging this symmetrical waveform, the system's power transfer behavior becomes more predictable, aiding in the precise control and design of the converter.

$$\frac{di_{ik}(t)}{dt} = \frac{V_{pri}(t) - V_{sec}(t)}{L_k} \tag{3.33}$$

A half-cycle consists of two distinct intervals: the first spans from $(0 < \theta < \delta)$, while the second covers $(\delta < \theta < \pi)$. Based on the current waveform shown in Figure 3.8, solving equation (3.30), yields the respective expressions for these two time periods in (3.34), is fundamental to understanding how the voltage difference between the primary and secondary sides drives the current change through the leakage inductance L_k over the switching time interval dT.

$$V_{in} + \frac{V_{out}}{n} = L_k \frac{I_1 + I_2}{dT}, for\ 0 < t < dT \tag{3.34}$$

The equation (3.35) represents the voltage-current relationship during the second portion of the switching period in a power converter. It describes how the input and reflected output voltages continue to drive the current through the leakage inductance during the time interval $(1 - d)T$, which follows the primary switching phase.

$$V_{in} + \frac{V_{out}}{n} = L_k \frac{I_1 + I_2}{(1-d)T}, for\ dT < t < T \quad (3.35)$$

This equation defines key parameters in the system. Here, n represents the transformer turns ratio, while T denotes the duration of a half-cycle within the switching period. The variables I_1 and I_2 correspond to the inductor current at specific switching events. Additionally, D signifies the phase shift duty ratio between the two bridges, commonly referred to as the converter's duty cycle.

By combining the results of equations (3.36) and (3.37), as demonstrated in [228], the average output current and corresponding power expression of the converter can be derived. Equation (3.36) provides the average output current, while Equation (3.37) relates this current to the converter's power transfer capability. Together, they highlight how the average output current and output power depend on input voltage, duty cycle, transformer turns ratio, and leakage inductance:

$$I_{out} = \frac{(1-|d|)dTV_{in}}{nL_k} \quad (3.36)$$

To calculates the power P delivered by a power converter. factors influence the power transfer, with the power being directly proportional to V_{in} and V_{out}, and inversely proportional to n and L_k.

$$P = V_{out}I_{out} = \frac{(1-|d|)dTV_{in}V_{out}}{nL_k} \quad (3.37)$$

For the energy transfer inductance while analyzing key system parameters, including the switching frequency f_s and the maximum power duty cycle d. The leakage inductance L_k is expressed as a function of the input and output voltages, duty cycle, switching frequency, transformer turns ratio, and maximum power:

$$L_k = \frac{(1-|d|)dV_{in}V_{out}}{2f_s nP_{max}} \quad (3.38)$$

It is important to note that the half-cycle period T has been redefined in terms of the converter's switching frequency to establish a clearer foundation for future discussions and graphical representation. Figure 3.9 illustrates the relationship between energy transfer inductance and varying switching frequencies, with maximum power occurring at different duty cycles. As shown, a higher switching frequency significantly reduces the required inductance for optimal power transfer. While the duty cycle also influences the inductance value, its impact becomes less pronounced at higher switching frequencies.

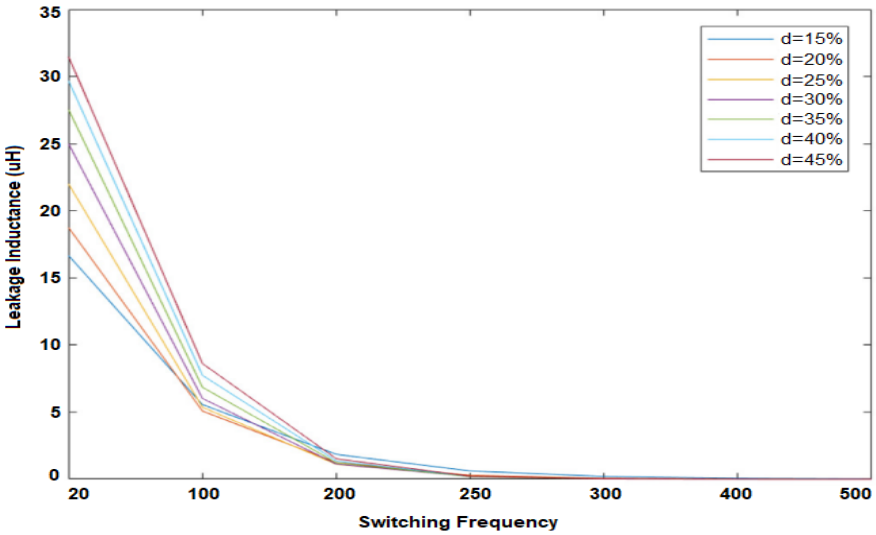

Figure 3.9: Inductance dimension.

The condition where the inductor currents become equal, i.e., $I_1 = I_2$, implies that under certain operating points, the currents flowing through the leakage inductance in both directions (during different portions of the switching period) are the same. This symmetry can simplify the analysis of the DAB converter, as it shows that the energy transfer from the input side to the output side is balanced when the currents I_1 and I_2 are equal.

$$I_1 = \frac{T}{2L_k}\left(2\frac{V_{out}}{n}d + V_{in} - \frac{V_{out}}{n}\right) \tag{3.39}$$

$$I_2 = \frac{T}{2L_k}\left(2V_{in}d - V_{in} + \frac{V_{out}}{n}\right) \tag{3.40}$$

When the primary reflected output voltage matches the input voltage, the current expressions can be simplified as follows:

$$I_1 = \frac{T}{2L_k}\left(2\frac{V_{out}}{n}d\right) \tag{3.41}$$

$$I_2 = \frac{T}{2L_k}(2V_{in}d) \tag{3.42}$$

$$\therefore I_1 = I_2 \tag{3.43}$$

This shows that under the condition $\frac{V_{out}}{n} = V_{in}$, the inductor currents I_1 and $I_2$are equal, confirming the symmetry in energy transfer during each half cycle.

Determining the resonant frequency of an LC circuit is essential for optimizing energy transfer by properly balancing inductance and capacitance.

$$f_r = \frac{1}{2\pi\sqrt{L_k C_s}} \tag{3.44}$$

Here, f_r represents the resonant frequency, and C_s denotes the snubber capacitance. The current flowing instantaneously through the capacitance is expressed as:

$$I_{CS} = C_S \frac{dV_{CS}}{dt} \tag{3.45}$$

Since the equivalent capacitance observed by the inductor during the switching intervals is twice that of a single snubber capacitor, due to the complementary transistor pair, the total inductor current can be expressed as:

$$I_{Lk} = 2I_{CS} = 2C_S \frac{dV_{CS}}{dt} \tag{3.46}$$

The modulation index (M), also referred to as the voltage gain, is a key parameter that quantifies the ratio of output voltage to input voltage, normalized by the turns ratio of the transformer. If $M = 1$, the output voltage is equal to the input voltage [228], adjusted by the turns ratio. If $M > 1$, the output voltage is greater than the input voltage (boost operation), and if $M < 1$, the output voltage is lower than the input voltage (buck operation).

$$M = \frac{V_{out}}{nV_{in}} \tag{3.47}$$

The equations below for currents I_1 and I_2 describe their relationships with input voltage, switching period, leakage inductance, modulation index, and duty cycle in a converter's operation. For I_1, the term $2Md$ highlights the modulation index and the duty cycle's impact, while $1 - M$ captures additional modulation effects, illustrating current dynamics during one phase of the switching cycle. Conversely, I_2 emphasizes the duty cycle's influence through $2d$ and includes the term $-1 + M$ for extra modulation effects, reflecting how current flow is adjusted in another part of the switching period based on input conditions and control strategies.

$$I_1 = \frac{TV_{in}}{2L_k}\,(2Md + 1 - M) \tag{3.48}$$

$$I_2 = \frac{TV_{in}}{2L_k}\,(2d - 1 + M) \tag{3.49}$$

Equation (3.50) compares the energy stored in the leakage inductance L_k and the capacitor C_s in circuit. The inequality states that the energy in the leakage inductance must be at least four times greater than the energy in the capacitor,

$$E_{Lk} \geq E_{CS} \rightarrow \frac{1}{2} L_k i_{ik}^2 \geq 4\left(\frac{1}{2} C_s V_{CS}^2\right) \tag{3.50}$$

where

E_{Lk} is the energy stored in the leakage inductance, E_{CS} represents the energy stored in the snubber capacitor.

The emphasis is that maintaining a sufficiently high current is essential for proper circuit operation in equation (3.51). Higher voltage across the capacitor results in a greater required current through the inductor, while the circuit's natural frequency is affected by both capacitance and inductance.

$$i_{Lk} \geq 2V_{CS}\sqrt{\frac{C_s}{L_k}} \tag{3.51}$$

Equations (3.52) and (3.53) outline minimum current requirements for a converter's operation. Equation (3.52) specifies that the current through the leakage inductance during a specific part of the switching cycle must meet a threshold based on the input voltage, switching period, leakage inductance, modulation index, and duty cycle. Equation (3.53) similarly establishes a minimum current during another phase of the switching cycle, ensuring sufficient current for efficient energy transfer from the input to the output.

$$I_1 = \frac{TV_{in}}{2L_k}\,(2Md + 1 - M) \geq 2V_{in}\sqrt{\frac{C_s}{L_k}} \tag{3.52}$$

$$I_2 = \frac{TV_{in}}{2L_k}\,(2d - 1 + M) \geq 2V_{out}\sqrt{\frac{C_s}{L_k}} \tag{3.53}$$

This equation provides a lower bound for the duty cycle d. It considers the modulation index M, which governs the voltage conversion, and the resonant interaction between the leakage inductance L_k and the capacitance $C_{s,i}$.

$$d \geq \frac{M-1}{2M} + \frac{2\sqrt{L_k C_{s,i}}}{TM} \tag{3.54}$$

To ensure that the duty cycle is large enough to allow for proper voltage conversion and energy transfer in the system as depicted in equation (3.55).

$$d \geq \frac{M-1}{2} + \frac{2Mn\sqrt{L_k C_{s,o}}}{T} \tag{3.55}$$

Equation (3.57) is used to calculate the peak current on the low-voltage side of the converter during the on-state of the switching cycle. This expression shows that as either the duty cycle or the output voltage increases, the peak current also rises. Equation (3.58) converts the peak current from equation (3.57) into its RMS equivalent. RMS current is a metric for assessing the heating effect and power dissipation in circuit components of transformers and inductors. For a sinusoidal waveform, the RMS value is $\frac{1}{\sqrt{2}}$ of the peak value.

$$I_{SPeak,LV} = \frac{T}{2L_k}\left(2\frac{V_{out}}{n}d\right) \tag{3.57}$$

$$I_{SRMS,LV} = \frac{I_{SPeak,LV}}{\sqrt{2}} \tag{3.58}$$

Equation (3.59) is used to calculate the conduction losses in a single switch of the converter. These losses depend on the on-state resistance R_{ds} of the switch and the square of the RMS current, and can be derived using Ohm's Law [229]. The total conduction losses in the converter by summing the losses from all four switches. Since each switch contributes to the total losses, the total power dissipation is four times the conduction loss of a single switch as depicted in equation (3.60).

$$P_{cond,sw} = R_{ds} I_{SRMS,LV}^2 \tag{3.59}$$

$$P_{cond,bridge} = 4P_{cond,sw} = 4R_{ds} I_{SRMS,LV}^2 \tag{3.60}$$

The voltage on the primary side of the converter is controlled by the switching states of switches S_1 and S_2. The difference between the two switching functions determines whether the input voltage V_{in} is applied across the primary winding of the converter or whether the winding is short-circuited (i.e., no voltage is applied). When both switches are in the same state, no voltage is applied. By adjusting the switching pattern (the timing of turning S_1 and S_2 on or off), the primary side voltage V_{pri} can be modulated to achieve the desired power transfer. The voltage on the secondary side of the converter is controlled by the switching states of switches S_5 and S_6. As with the primary side, the difference between these two switching functions determines whether the output voltage V_{out} is applied across the secondary winding

of the transformer. When S_5 and S_6 are in opposite states, the output voltage is applied. When they are in the same state, no voltage is applied. The switching control on the secondary side is essential for managing the power delivered to the load battery. By adjusting the timing and sequence of the switching functions, the secondary voltage V can be modulated to regulate the power flow on the output side.

$$V_{pri} = V_{in}\{S_1 - S_2\} \tag{3.61}$$

$$V_{sec} = V_{out}\{S_5 - S_6\} \tag{3.62}$$

The electrical energy is transferred between the primary and secondary sides of the transformer. The equation (3.63) represents how the capacitor balances the energy flow between the input and output. When i_{dc} the input DC current is higher than i_{out}, the excess current is temporarily stored in the capacitor. This smooths out the power delivery, preventing sudden surges to the output and stabilizing the charging process. When i_{out} exceeds i_{dc}, the capacitor discharges, providing the deficit to maintain a steady output current to the EV battery. Table 3.3 shows the switching state of the output bridge.

$$i_C = i_{dc} - i_{out} \tag{3.63}$$

Table 3.3: Switching state of the output bridge

S_5	S_6	i_{dc}
0	0	0
0	1	$-i_{lk}$
1	0	i_{lk}
1	1	0

The equation (3.64) signifies that the DC current i_{dc} is directly proportional to the leakage inductance current i_{lk}, modulated by the switching behaviour. When the switches are appropriately controlled, i_{lk} contributes to i_{dc}, transferring power from the source to the battery. When S_5 is on and S_6 is off (or vice versa), the converter operates in a particular mode that determines the direction and magnitude of current flow.

$$i_{dc} = i_{lk}\{S_5 - S_6\} \tag{3.64}$$

This equation (3.65) represents the balance of voltages and currents within the system during operation. It ensures that the energy supplied from the primary side matches the energy delivered to the secondary side, factoring in losses due to load resistance and the behaviour of the leakage inductance.

$$V_{pri} - \frac{N_p}{N_s} V_{sec} - R_L i_{lk} - L_k \frac{di_{lk}}{dt} = 0 \tag{3.65}$$

Equation (3.66) describes the inductor current dynamics in the DAB converter, illustrating how the input and output voltages, along with the transformer turns ratio, impact current flow through the leakage inductance during switching intervals. To represent the switching functions S_1, S_2, S_5, and S_6 in the time domain, they can be expanded using the Fourier transform.

$$R_L i_{lk} + L_k \frac{di_{lk}}{dt} = V_{in} \{S_1 - S_2\} - \frac{N_p}{N_s} V_{out} \{S_5 - S_6\} \tag{3.66}$$

Figure 3.10 demonstrates the distribution of power loss components across varying output power levels in a MOSFET-based system. As the output power increases, the total power loss also grows, with switching losses in the secondary components representing the largest portion of the total losses, especially at higher power levels. In contrast, primary conduction losses remain relatively minor, while both primary switching losses and secondary conduction losses make moderate contributions. This pattern emphasizes the impact of secondary switching losses on the system's thermal management and the need for efficiency optimization, particularly at elevated power outputs.

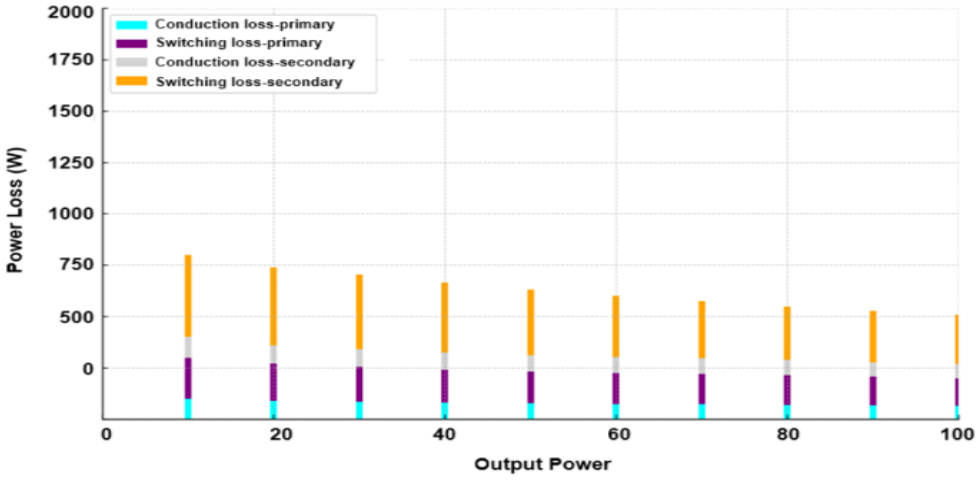

Figure 3.10: Power loss distribution in MOSFET components across varying output power levels.

The harmonic structure of the switching signal in a DAB converter used for DC fast charging of electric vehicles. The Fourier series expansion of the switching waveform allows for precise control of power transfer by adjusting the amplitude and phase of the harmonics. Properly managing the harmonic content is essential for optimizing the performance of the converter, minimizing losses, and ensuring efficient energy transfer from the grid to the EV battery.

$$S_k = \frac{1}{2} + \frac{2}{\pi}\sum_{n=0}^{N} \frac{\sin([2n+1]\{\omega_s - \alpha_k\})}{[2n+1]}, N \geq 0, K = 1,2,3 \ldots \quad (3.67)$$

where,

S_k represents the switching signal for the $k-th$ harmonic component in the converter. $\frac{2}{\pi}\sum_{n}^{N} = 0$ is the Fourier series expansion of the switching waveform. The fundamental frequency is ω_s, and α_k represents the phase shift of the $k-th$ harmonic. The $[2n+1]$ corresponds to the odd harmonics in the Fourier series. $N \geq 0$ indicates the number of harmonics. $K = 1,2,3 \ldots$, this indicates the harmonic order. The value of K determines which harmonic component is being described. Based on the Fourier theory, increasing the number of harmonics in the summation brings the Fourier series representation closer to the original signal. This is illustrated in Figure 3.11, where adding more harmonics leads to a closer approximation of the ideal square wave.

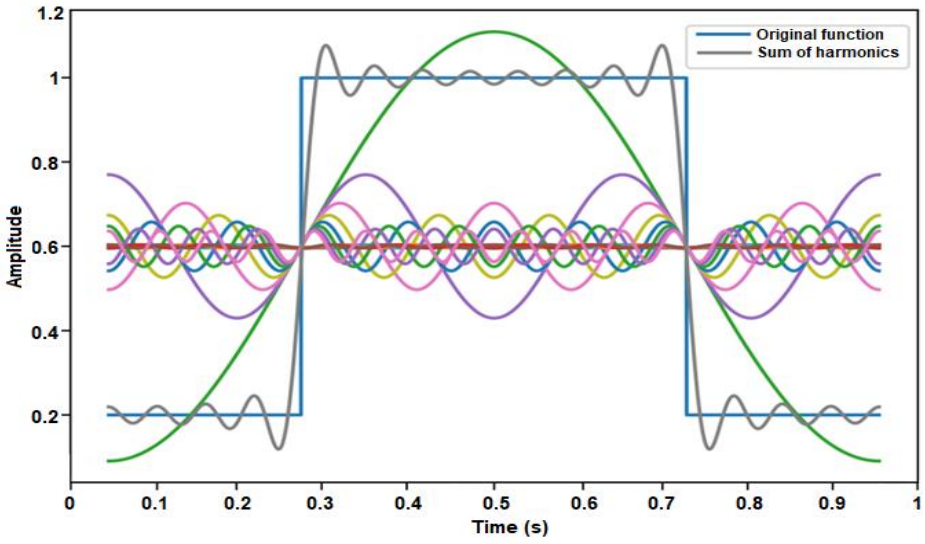

Figure 3.11: Fourier series approximation of a square wave.

Equations (3.68.a–3.68.d) describe the relationships among input and output voltages and currents, power, phase shift angles, harmonics, and efficiency. By controlling the phase shift angles, these parameters can be effectively managed.

The equations for S_1, S_2, S_3, S_4, S_5 and S_6 in a converter for DC fast charging are expressed as Fourier series, representing the complex switching waveforms of the transistors. These waveforms are composed of a fundamental component and higher-order harmonics, which influence the converter's performance. S_1 describes the first switch's waveform, oscillating around a midpoint with harmonic components adjusting its shape. S_2 is similar but phase-shifted by π radians, delaying it by half a cycle to control power flow. S_5 represents the secondary-side switch, phase-shifted by δ to modulate power transfer, while S_6 mirrors S_5 with an additional π phase shift to ensure synchronized switching for efficient power transfer between the primary and secondary sides of the converter.

$$S_1 = \frac{1}{2} + \frac{2}{\pi}\sum_{n=0}^{N}\left[\frac{\sin([2n+1]\{\omega_s t\})}{[2n+1]}\right], N \geq 0, k = 1,2,3 \ldots \quad (3.68.a)$$

$$S_2 = \frac{1}{2} + \frac{2}{\pi}\sum_{n=0}^{N}\left[\frac{\sin([2n+1]\{\omega_s - \pi\})}{[2n+1]}\right], N \geq 0, k = 1,2,3 \ldots \quad (3.68.b)$$

$$S_5 = \frac{1}{2} + \frac{2}{\pi}\sum_{n=0}^{N}\left[\frac{\sin([2n+1]\{\omega_s - \delta\})}{[2n+1]}\right], N \geq 0, k = 1,2,3 \ldots \quad (3.68.c)$$

$$S_6 = \frac{1}{2} + \frac{2}{\pi}\sum_{n=0}^{N}\left[\frac{\sin([2n+1]\{\omega_s - \delta - \pi\})}{[2n+1]}\right], N \geq 0, k = 1,2,3 \ldots \quad (3.68.d)$$

The equations below describe the output voltage rate of change ($\frac{dV_{out}}{dt}$) in the converter, crucial for managing voltage during electric vehicle fast charging. The right-hand side indicates that this change is a function of the output voltage V_{out} and the phase shift (δ) between primary and secondary switching signals, which controls power transfer. Load current $(-i_{load})$ decreases the voltage, so the converter compensates to maintain stable operation. Capacitance C_{out}) influences voltage dynamics, with larger capacitance smoothing out variations. The transformer's turns ratio (N_p/N_s) scales the voltage from primary to secondary. The harmonic series summation reflects the impact of harmonics on power transfer, while impedance terms ($Z[n]$ and $\phi Z[n]$) govern how current flows and timing is controlled across harmonic frequencies. The interaction between input voltage, output voltage, and impedance affects how effectively power is transferred through the converter.

$$\frac{dV_{out}}{dt} = f(V_{out}, \delta) = -i_{load} + \frac{8}{C_{out}\pi^2}\frac{N_p}{N_s}\sum_{n=0}^{N}\left[\frac{1}{[2n+1]^2} \times \left\{\frac{V_{in}}{|Z[n]|}cost([2n+1]\delta - \varphi_Z[n]) - \frac{N_p}{N_s}\frac{V_{out}}{|Z[n]|}cost(\varphi_z[n])\right\}\right] \quad (3.69)$$

Where, $Z[n] = \sqrt{R_L^2 + (2\pi f_s[2n+1]L_k)}$ and $\varphi_Z[n] = tan^{-1}\left(\frac{2\pi f_s[2n+1]L_k}{R_L}\right)$. (3.70)

A standard linearization technique based on the small-signal analysis is then applied to derive a linearized model. The dynamic behavior of the output voltage (V_{out}) in the converter during DC fast charging of electric vehicles, showing how small variations in output voltage, load current, and phase shift affect the voltage's rate of change. The steady-state behavior is represented by the base function $f(V_{out0}, \delta_0 i_{load0})$ while the partial derivatives account for sensitivities to changes in voltage (ΔV_{out}), load current (Δi_{load}), and phase shift ($\Delta\delta$). These variations reflect how the converter responds to perturbations, helping to analyze and control its stability and efficiency in power transfer to the battery in the equation [3.68].

$$\frac{d(V_{out}+\Delta V_{out}}{dt} \approx f\left(V_{out0,}\delta_{0,}i_{load0}\right) + \frac{\partial f}{\partial V_{out}}|_0\, \Delta V_{out} + \frac{\partial f}{\partial i_{load}}|_0\, \Delta i_{load} + \frac{\partial f}{\partial \delta}|_0\, \Delta\delta \quad (3.71)$$

The various parameters influence voltage behavior over time. Equation (3.72.a) shows changes in output voltage ΔV_{out} evolve due to variations in phase shift $\Delta\delta$ and load current Δi_{load}, with coefficients A, $B_{\delta,}$ and B_I quantifying the sensitivities of the output voltage to those changes. Equation (3.72.b) specifies that coefficient A quantifies the impact of output voltage variation on its rate of change, incorporating the transformer turns ratio $\left[\frac{N_p}{N_s}\right]$, output capacitance ($C_{out}$), and the effects of harmonics. Equation (3.72.c) describe B_δ which captures phase shift variation influences output voltage, depending on transformer characteristics, circuit impedance and phase differences. The equation (3.72.d) presents B_I indicating the direct influence of load current variations on output voltage, inversely proportional to output capacitance.

$$\frac{d\Delta V_{out}}{dt} = A\Delta V_{out} + B_\delta \Delta\delta + B_I \Delta i_{load} \quad (3.72.a)$$

$$A = \frac{-8}{C_{out}\pi^2}\left(\frac{N_p}{N_s}\right)^2 \sum_{n=0}^{N}\frac{\cos(\varphi_Z[n])}{[n+1]^2|Z[n]|} \quad (3.72.b)$$

$$B_\delta = \frac{-8}{C_{out}\pi^2}\frac{N_p}{N_s}\sum_{n=0}^{N}\left[\frac{\cos(\varphi_Z[n]-[2n+1]\delta_0)}{[2n+1]|Z[n]|}\right] \quad (3.72.c)$$

$$B_I = -\frac{1}{C_{out}} \tag{3.72.d}$$

3.5.2. Bidirectional DAB current controller design

The bidirectional dual active bridge converter in a DC fast charger serves to regulate battery side DC voltage and current efficiently. It achieves this by controlling the phase shift between the primary and secondary H-bridges, allowing bi-directional power flow with high efficiency. The key to controlling the DAB converter is the phase shift δ between the two bridges. This phase shift governs how much power is transferred through the transformer, and the DAB control loop adjusts this phase shift to match power demand. The DAB control system uses a current control loop where the output current is regulated based on reference signals. The detailed bidirectional DAB current control loop is depicted in Figure 3.12.

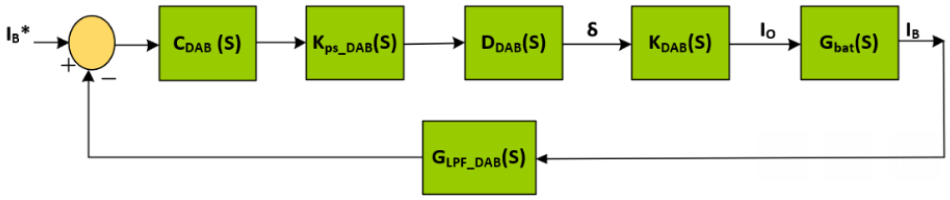

Figure 3.12: Current control structure.

Where the PI controller, as shown in equation (3.73), governs how the phase shift δ influences the output current. The transfer function for the system is:

$$G(S) = \frac{B_\delta}{s-A} \tag{3.73}$$

A PI controller is implemented to reduce the error between the actual output and the reference signals. Given that the plant function is first-order, a PI controller is an optimal choice, as it ensures zero steady-state tracking error [230],[231]. The transfer function of the PI controller, as defined in equation (3.74), is:

$$G(S) = K_p + \frac{K_i}{s} \tag{3.74}$$

Here, K_p is the proportional gain, addressing immediate voltage errors, while K_i is the integral gain, eliminating steady-state errors.

The control system transfer function, combining the PI controller and system transfer function, is given by equation (3.75).

$$F(s) = C(s)G(s) = \left(K_p + \frac{K_i}{s}\right)\left(\frac{B\delta}{s-A}\right) \tag{3.75}$$

This captures 3.13 how the controller adjusts the phase shift δ to regulate the DAB converter's output voltage in response to load conditions, ensuring efficient power delivery.

The system uses a closed-loop feedback mechanism that continuously monitors the output voltage V_{out} and current I_{out} of the DC-DC converter as shown in Figure 3.13. These values are compared to predefined reference values for voltage V_{ref} and current I_{ref}, which align with the charging profile of the EV. The system then adjusts the duty cycle of the converter's switching devices to maintain stable charging conditions. In the developed system, sensors actively measure the output voltage and current, feeding this data into the control loop for real-time comparison with the reference values.

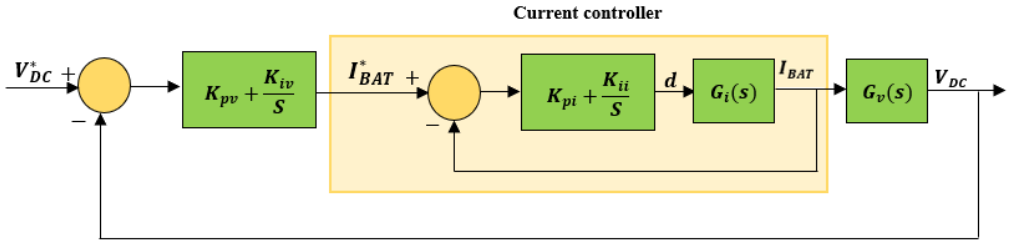

Figure 3.13: Voltage controller closed-loop block diagram.

The PI controllers are applied to minimize the difference between the reference and actual values. For voltage control, the error is calculated as:

$$e_v(t) = V_{ref}(t) - V_{out}(t) \tag{3.76}$$

And for current control:

$$e_i(t) = I_{ref}(t) - I_{out}(t) \tag{3.77}$$

These error values are processed by the PI controllers, generating the required control signals to adjust the converter's duty cycle (3.78):

$$u(t) = K_p e(t) + K_i \int_0^t e(\tau)dt \tag{3.78}$$

This output from the PI controller determines the duty cycle D, which regulates the power delivered to the EV battery. The duty cycle D of the DC-DC converter's switching devices directly affects the output voltage, as expressed by:

$$V_{out} = D \,.\, V_{in} \tag{3.79}$$

The open-loop and closed-loop performance of the system is illustrated through Bode plots and step response curves, as shown in Figure 3.14 and Figure 3.15, demonstrating its stability and control characteristics.

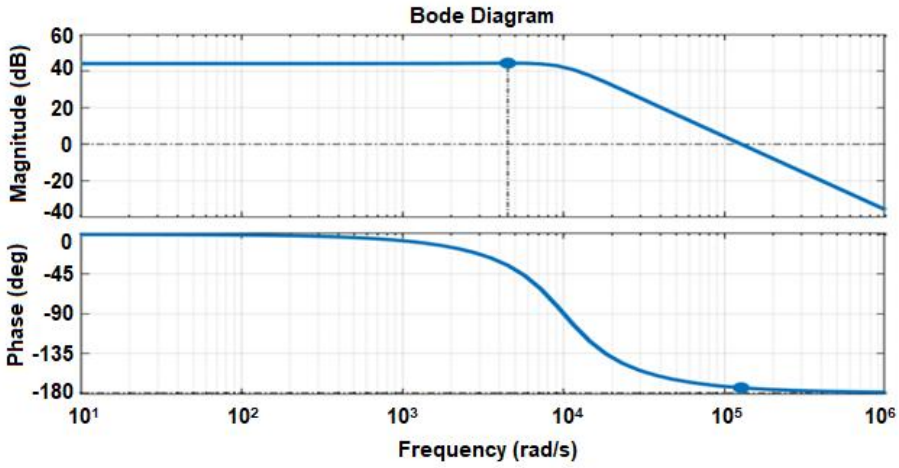

Figure 3.14: Open-loop Bode plot of DAB current controller.

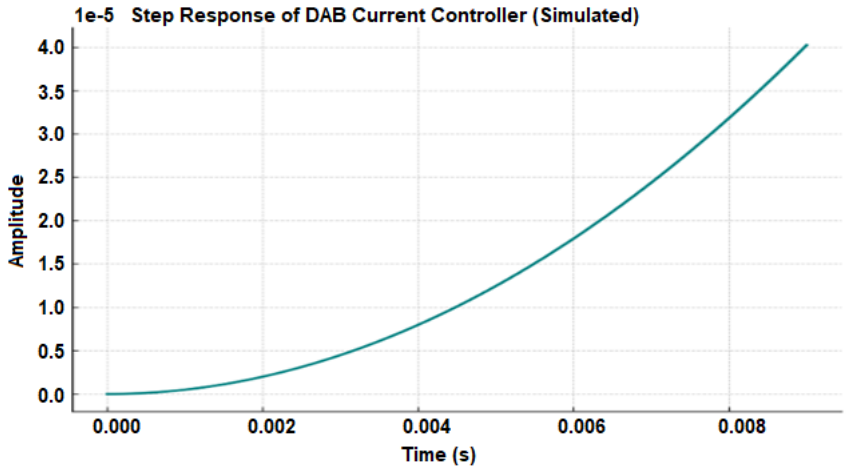

Figure 3.15: Closed-loop step response of DAB current controller.

By dynamically adjusting the duty cycle, the control system ensures that the output voltage and current are stable and follow the predefined reference values, enabling efficient charging. During CC mode, where high current is needed initially for fast charging, the duty cycle is adjusted to maintain a constant current:

$$D = \frac{I_{out}}{I_{ref}} \tag{3.80}$$

As the battery approaches its full charge, the system transitions to CV mode, and the duty cycle is adjusted to maintain a constant voltage:

$$D = \frac{V_{ref}}{V_{out}} \tag{3.81}$$

This seamless transition between CC and CV modes is essential for adhering to the battery's charging profile and ensuring safe operation throughout the process.

The PI controller's integral term eliminates any steady-state error, while the proportional term responds quickly to dynamic changes in the charging process. This is especially important when the system switches between CC and CV modes. The control strategy not only prevents overcharging or overheating but also maximizes efficiency in energy conversion. The average output current from the DAB stage can be expressed as:

$$I_{o\_ave} = \frac{V_{DC} N \delta}{\omega_{sw} L_{ik} \pi} \tag{3.82}$$

The relationship between the phase shift δ and output current is inherently nonlinear but can be linearized for controller design, allowing for better performance across a range of power levels.

3.6 Photovoltaic Modelling

When investigating the integration of PV systems into the grid or standalone systems, it is essential to comprehend the operational principles of a solar PV panel. A solar PV panel consists of an array of numerous PV cells interconnected in series and parallel configurations. These PV cells are typically constructed from layers of p-type and n-type silicon. In the PV stage, a unidirectional DC-DC converter is typically used to maximize power extraction from each solar module in a PV array while maintaining the voltage at the converter's output, which is connected to the system's DC bus. Table 3.4 demonstrates the PV system component parameters.

Figure 3.16 illustrates the current-voltage (I-V) and power-voltage (P-V) characteristics of a PV module, emphasizing the short-circuit current (I_{SC}), which occurs when the voltage is zero, and the open-circuit voltage (V_{OC}), which is the maximum achievable voltage when the current is zero. The product of voltage and current at specific set-points determines the power extracted from the PV module. The P-V curve reveals a distinct MPP, defined by a particular current (I_{MPP}) and voltage (V_{MPP}) under steady irradiance. A DC-DC converter's key role in a PV system is to maintain operation at the MPP [232].

Table 3.4: PV system component parameters

Parameter Description	Value Rated
Rated voltage ($Vmpp$)	54.7 V
Rated current ($Impp$)	5.58 V
Open-circuit voltage (Voc)	64.2 V
Short-circuit current (Isc)	5.96 A
Input current	400 A - 200 A
Input voltage	200 V - 100 VDC
Output voltage	440 V -220 VDC
Output current	175 A - 87.46 A
Output power	76.85 Kw – 19.76 kw
Battery current	80 A
Battery voltage	443 V
Battery power	35.4 KW
Duty cycle	0.5286 s
Power temperature coefficient	−0.35%/°C
Voltage temperature coefficient	−0.2727 mV/°C
Current temperature coefficient	0.06175 mA/°C

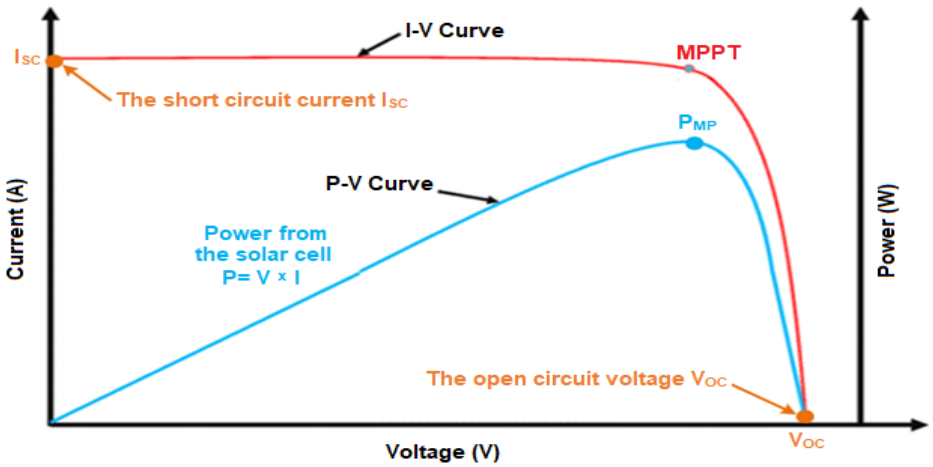

Figure 3.16: I–V and P–V curve characteristics of a PV module.

Figure 3.17 illustrates the single-diode model. In this model, the electrical energy produced by the PV panel is represented by a photo-current I_{ph}, which is directly proportional to solar irradiance [233]. The series resistance R_s accounts for the internal resistance of the PV panel, while the shunt resistance R_{sh} represents the leakage current.

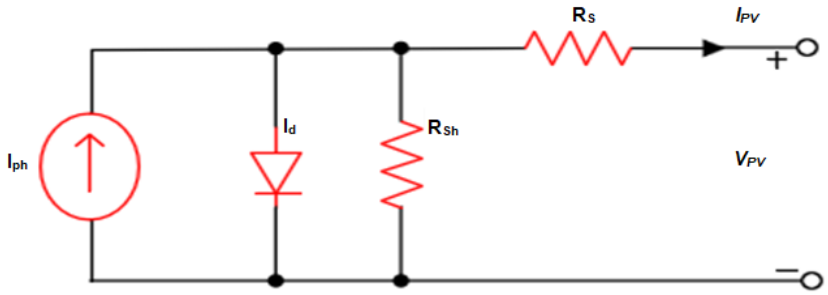

Figure 3. 17: Single diode model of solar PV module.

The output current of the PV module is described by the single-diode model with series and shunt resistances. The implicit equation used is

$$I_{pv} = I_{ph} - I_d\left(exp\left(\frac{V_{pv}+I_{pv}R_{pv}}{nV_T}\right) - 1\right) - \frac{V_{pv}+I_{pv}R_s}{R_{sh}} \quad (3.83)$$

The diode current I_{ph} is defined as follows:

$$I_d = I_o\left(e^{\left(\frac{V_d+I_{PV}R_s}{aV_t}\right)} - 1\right) \quad (3.84)$$

The photo-current I_{ph} is given by:

$$I_{ph} = \left(I_{SC} + K_1\left(T_{cell} - T_{ref}\right)\right)\lambda \quad (3.85)$$

The terms in the equations above are defined as follows:

V_d: Diode voltage;

I_o: PV cell saturation current;

$\frac{KT}{q}$: Thermal voltage of the PV cell, where k is the Boltzmann constant $(1.38\,.10^{-23}\,J/K)$, T is the temperature of the PV cell in Kelvin (K), and q is the electron charge $(1.6 \times 10^{-19}C)$;

A: ideality factor of the p-n junction diode;

I_{SC}: Short-circuit current of the PV cell at standard test conditions, which are 1000 W/m^2 and 25°C;

K_1: Temperature coefficient of the PV cell's short-circuit current;

T_{cell} and T_{ref}: Operating and reference temperatures of the PV cell, respectively.

λ: Solar irradiance in W/m^2.

The non-linear model depicted in Figure 3.17, can be simplified by disregarding the effects of both series resistance R_s and shunt resistance R_{sh}. Furthermore, by neglecting ground leakage and the minor diode currents under zero terminal voltage and given that $I_{ph} \gg I_O$, it can be concluded that $I_{SC} \cong I_{ph}$. Consequently, the equivalent circuit of the single-diode model can be simplified as shown in Figure 3.18, where the diode current I_d is represented by Ae^{B*Vpv}. In this expression, A denotes the reverse saturation current of the PV panel, B represents the inverse of the thermal voltage of the PV panel, and V_{pv} is the output voltage of the PV panel.

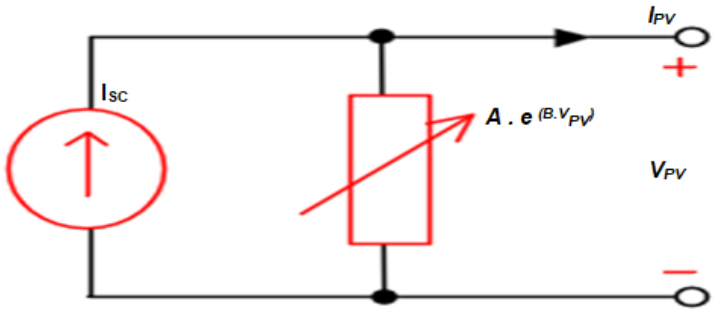

Figure 3.18: Simplified equivalent circuit of a single diode solar PV model.

The equation for the simplified non-linear model can be expressed as:

$$I_{pv} = I_{SC} - Ae^{B*Vpv} \quad (3.86)$$

The model where the PV array supports the grid, this approach is highly effective for electrical simulations. While the complexity of the system can make control analysis and design challenging, a linear modeling approach has been applied to simplify these aspects. Linear models, like the Norton equivalent model, are utilized to accurately represent the behavior of PV panels near the MPP. For voltages below V_{MPP}, the Norton model provides a response comparable to the non-linear model, making it suitable for integration in the grid-supportive PV system [234]. Figure 3.19 demonstrates this Norton model in the context of the system.

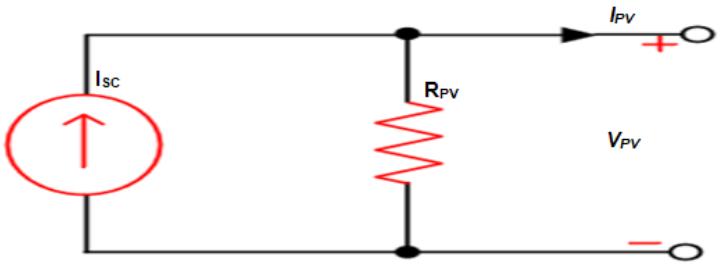

Figure 3.19: Norton equivalent model of PV panel.

As depicted in Figure 3.19, this model incorporates the short-circuit current I_{SC}, which is proportional to the irradiance. This feature enables the analysis of the PV system under varying irradiance conditions [235].

The equivalent resistance of the Norton model, denoted as R_{pv} can be expressed as:

$$R_{pv} = \frac{V_{MPP}}{I_{SC} - I_{MPP}} \tag{3.87}$$

Figure 3.20 presents a comparison of the current-voltage and power-voltage characteristic curves for the single-diode simplified model and the Norton equivalent model, corresponding to Figures 3.20 (a) and (b), respectively.

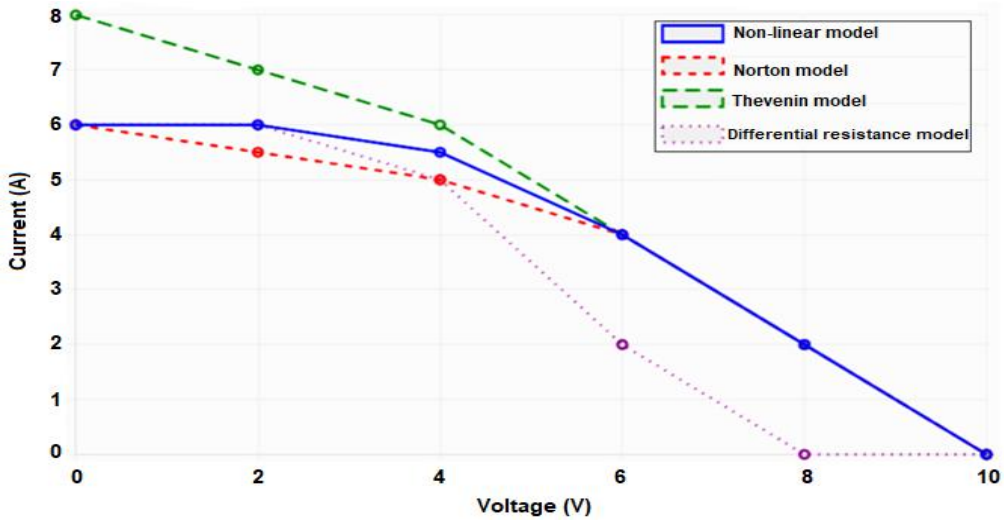

(a)

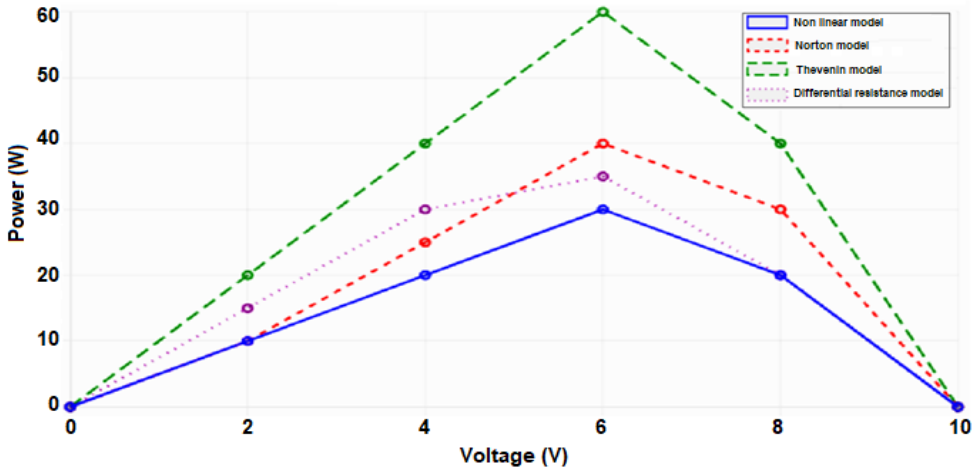

(b)

Figure 3.20: PV panel model curves: (a) current–voltage characteristic; (b) power-voltage characteristic.

3.6.1 DC-DC Boost converter

A boost converter steps up the source DC voltage. It is used to attain a constant voltage by varying its duty ratio (D), which can be adjusted between 0 to 1. Boost converter uses a DC input switch IGBT, diode and a capacitive filter and load. The DC-DC boost converter can increase the voltage while decreasing the current and keeping the same power at the output side. By changing the value of D, output voltage of converter is varied [236], [237]. Basic circuit connection of the boost converter is demonstrated in Figure 3.21.

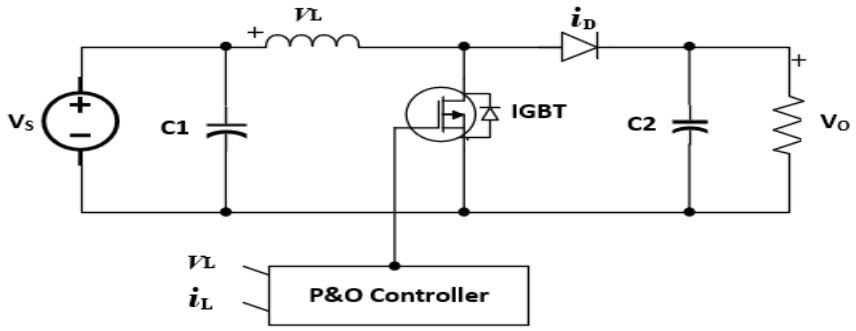

Figure 3.21: Basic circuit connection of boost converter.

Design considerations

Figure 3.22 illustrates a boost converter, a type of switching converter that functions by repeatedly turning an electronic switch on and off. It is referred to as a boost converter because it produces an output voltage that exceeds the input voltage. Most boost converters are designed for continuous-current operation, with the necessary inductance for this mode calculated using equation [3.96]. Equations [3.98] and [3.101] express the output voltage ripple. High switching frequencies are desirable because they reduce the size of both the inductor and the capacitor. Specifically, as the switching frequency increases, the minimum size of the inductor required to maintain continuous current and the minimum size of the capacitor needed to limit output ripple both decreases. However, higher switching frequencies can also increase power loss in the switches, thereby decreasing the converter's efficiency.

Typical switching frequencies are above 20 kHz to avoid audio noise and can extend into the MHz range. Some designers consider switching frequencies around 500 kHz to be the best compromise between small component size and efficiency. Others prefer frequencies around 50 kHz to minimize switching losses, while some opt for frequencies above 1 MHz. Assumptions made in this section include the following:

- Steady-state conditions are presented.
- The switching period is $\boldsymbol{T}$, with the switch closed for duration $\boldsymbol{DT}$ and open for $(\boldsymbol{1-D})\boldsymbol{T}$.
- The inductor current remains continuous (always positive).
- The capacitor is very large, maintaining a constant output voltage $\boldsymbol{V_0}$.

- All components are ideal.

The analysis continues by evaluating the inductor's voltage and current during the intervals when the switch is closed and when it is open.

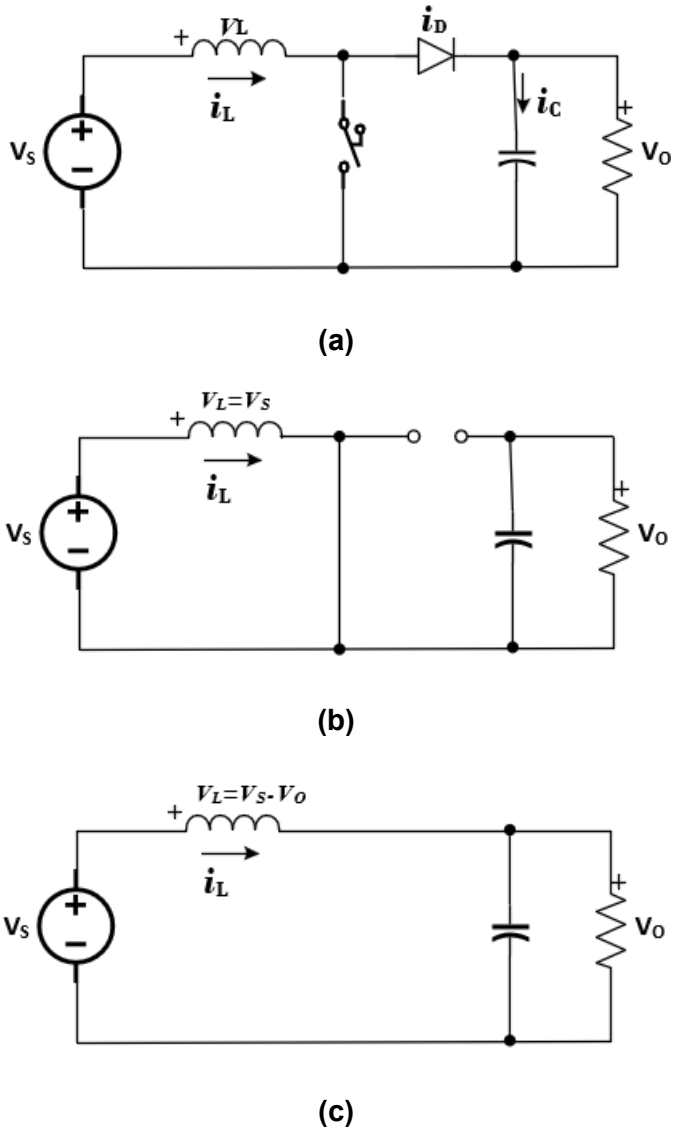

Figure 3.22: DC-DC boost converter. (a) circuit diagram; (b) equivalent circuit with the switch closed; (c) equivalent circuit with the switch open [238]**.**

With the switch closed, the diode becomes reverse-biased, preventing current flow through it. Applying Kirchhoff's voltage law to the loop that includes the source, inductor, and the closed switch yields:

$$V_S = L\frac{di_L}{dt} \tag{3.88}$$

The operation and behavior of the boost converter can be better understood by examining the key waveforms associated with its components during one complete switching cycle. These waveforms are illustrated in Figure 3.23, which presents the time-domain profiles of (a) inductor voltage $\boldsymbol{v_L}$, (b) inductor current $\boldsymbol{i_L}$, , (c) diode current $\boldsymbol{i_D}$, and (d) capacitor current $\boldsymbol{i_C}$.

Figure 3.23(a) shows the inductor voltage waveform over a switching period $\boldsymbol{T}$. When the switch is closed (during the interval $\boldsymbol{0 < t < DT}$), the inductor is directly connected to the source, and the voltage across it is equal to the source voltage $\boldsymbol{V_s}$. In this interval, the diode is reverse-biased and prevents current flow to the output stage. When the switch opens (during $\boldsymbol{DT < t < T}$), the inductor discharges its stored energy through the diode to the output, and the inductor voltage becomes $\boldsymbol{V_s - V_o}$.

Figure 3.23(b) illustrates the corresponding inductor current $\boldsymbol{i_L}$, which increases linearly while the switch is closed, due to the constant voltage $\boldsymbol{V_s}$, across the inductor. When the switch opens, the inductor current decreases linearly as energy is delivered to the load. The ripple in the inductor current, denoted as $\boldsymbol{\Delta i_L}$, depends on the inductance value and switching interval.

Figure 3.23(c) presents the diode current $\boldsymbol{i_D}$, which is zero during the switch-on interval (when the diode is reverse-biased), and equals the inductor current during the off interval (when the diode conducts). This waveform reflects the unidirectional conduction nature of the diode in a boost converter.

Figure 3.23(d) shows the capacitor current $\boldsymbol{i_C}$, which receives current from the inductor through the diode during the switch-off period. During the switch-on interval, the capacitor supplies the load alone, resulting in a current of $\boldsymbol{-V_o/R}$, where $\boldsymbol{R}$ is the load resistance. The shaded area under the waveform indicates the net charge variation in the capacitor over one switching cycle.

The current variation rate is constant, resulting in a linear increase in current while the switch is closed, as illustrated in Figure 3.23b. The change in inductor current is described by equations (3.89) and (3.90) as follows:

$$\frac{\boldsymbol{\Delta i_L}}{\boldsymbol{\Delta t}} = \frac{\boldsymbol{\Delta i_L}}{\boldsymbol{DT}} = \frac{\boldsymbol{V_S}}{\boldsymbol{L}} \tag{3.89}$$

Solving for $\boldsymbol{\Delta i_L}$ for the switch closed

$$(\boldsymbol{\Delta i_L})_{\boldsymbol{closed}} = \frac{\boldsymbol{V_S DT}}{\boldsymbol{L}} \tag{3.90}$$

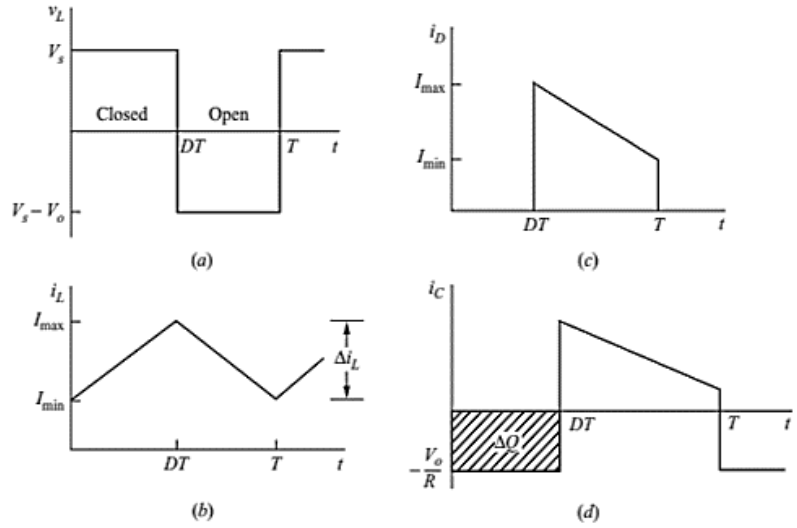

Figure 3.23: Boost converter waveforms: (a) Inductor voltage, (b) inductor current, (c) diode current, and (d) capacitor currents [238]**.**

When the switch is opened, the inductor current cannot change instantaneously. Consequently, the diode becomes forward biased. The voltage across the inductor and the resulting variation in the inductor current are described as follows:

$$\boldsymbol{v_L = V_S - V_O = L\frac{di_L}{dt}} \tag{3.91}$$

$$\boldsymbol{\frac{di_L}{dt} = \frac{V_S - V_O}{L}} \tag{3.92}$$

The rate of variation of the inductor current remains constant; therefore, the current changes linearly while the switch is open. the change in inductor current while the switch is open is [238]:

$$\boldsymbol{\frac{\Delta i_L}{\Delta t} = \frac{\Delta i_L}{(1-D)T} = \frac{V_S - V_O}{L}} \tag{3.93}$$

Solving for $\boldsymbol{\Delta i_L}$

$$\boldsymbol{(\Delta i_L)_{open} = \frac{(V_S - V_O)(1-D)T}{L}} \tag{3.94}$$

In steady-state operation, the net variation in inductor current is zero. Consequently, using equations (3.90) and (3.94),

$$(\Delta i_L)_{closed} + (\Delta i_L)_{open} = 0$$

$$\frac{V_S DT}{L} + \frac{(V_S - V_O)(1-D)T}{L} = 0 \tag{3.95}$$

Solving for V_o,

$V_s(D + 1 - D) - V_o(1 - D) = 0$

$V_o = \frac{V_s}{1-D}$ (3.96)

In steady-state periodic operation, the average voltage across the inductor over one complete switching cycle must be zero. This condition ensures that the inductor's current returns to its initial value at the end of each cycle. Mathematically, this can be expressed by calculating the time-averaged inductor voltage over a full switching period.

$V_L = V_S D + (V_S - V_O)(1 - D) = 0$ (3.97)

The average current through the inductor is assessed by equating the average power supplied by the source to the average power absorbed by the load. Consequently, the output power can be determined as:

$$\boldsymbol{P_O = \frac{V_O^2}{R} = V_O I_O}$$

(3.98)

The average current through the inductor can be expressed as:

$$\boldsymbol{I_L = \frac{V_S}{(1-D)^2 R} = \frac{V_O^2}{V_s R} = \frac{V_O I_O}{V_s}}$$ (3.99)

The maximum inductor current $\boldsymbol{I_{max}}$ and the minimum inductor current $\boldsymbol{I_{min}}$ are defined as follows:

$$\boldsymbol{I_{max} = I_L + \frac{\Delta i_L}{2} = \frac{V_S}{(1-D)^2 R} + \frac{V_S DT}{2L}}$$ (3.100)

$$\boldsymbol{I_{min} = I_L - \frac{\Delta i_L}{2} = \frac{V_S}{(1-D)^2 R} - \frac{V_S DT}{2L}}$$ (3.101)

For a boost converter to be designed for continuous-current operation, the inductor value must exceed L_{min}. The minimum inductance required for continuous current operation in the boost converter is given by:

$$\boldsymbol{L_{min} = \frac{D(1-D)^2 R}{2f}}$$ (3.102)

The inductance L can be expressed in terms of the desired variation in the inductor current Δi_L as follows [238]:

$$\boldsymbol{L = \frac{V_S DT}{\Delta i_L} = \frac{V_S D}{\Delta i_L f}} \quad (3.103)$$

Voltage Ripples

The previous equations assumed a constant output voltage, which corresponded to an infinite capacitance. In practice, a finite capacitance results in fluctuations in the output voltage, leading to voltage ripples. The peak-to-peak voltage ripple can be assessed from the capacitor current depicted in Figure 3.23d. The variation in capacitor voltage can be determined as follows:

$$\boldsymbol{\frac{\Delta V_O}{V_O} = \frac{D}{RCf}} \quad (3.104)$$

where $\boldsymbol{f}$ is the switching frequency.

Therefore, the capacitance can be expressed in terms of voltage ripples as:

$$\boldsymbol{C = \frac{D}{R\left(\frac{\Delta V_O}{V_O}\right)f}} \quad (3.105)$$

The equivalent series resistance (ESR) of the capacitor can significantly affect the voltage ripple. The peak-to-peak variation in capacitor current, as shown in Figure 3.23d, closely resembles the maximum current through the inductor. The voltage ripple due to the ESR is given by [238]:

$$\Delta V_{o,ESR} = \Delta i_C r_C = I_{L,max} r_C \quad (3.106)$$

3.6.2 PV system / boost converter control for maximum power extraction

To optimize power extraction under varying solar irradiance conditions, the PV system must regulate its output through control of the converter switch. In this context, the converter is managed using the MPPT algorithm based on the P&O method, which is favored for its simplicity and ease of implementation. The duty cycle is automatically adjusted to generate the voltage needed to extract the maximum power from the PV array. The output power P_{PV} of the PV system can be expressed as:

$$\boldsymbol{P_{PV} = V_{PV}\ I_{PV}} \quad (3.107)$$

Where V_{PV} and I_{PV} represent the voltage and current of the photovoltaic system, respectively. The relationship between the PV voltage V_{PV} and the DC link voltage V_{dc} is described by the following equation [239]:

$$V_{PV} = \left(\frac{1}{1-D}\right) V_{dc} \quad (3.108)$$

3.6.2.1 Perturb and observe method control strategy

The voltage and current of the PV system, as illustrated in Figure 3.24, are measured and used as inputs for the MPPT controller. These measurements are processed using the P&O algorithm to track the MPP. The output signal from the P&O MPPT controller is fed into the boost converter to maintain the operating voltage at the MPP by adjusting the converter's duty cycle. A small perturbation is introduced to induce a variation in the power output of the PV system. If the power increases as a result of the perturbation, the perturbation continues in the same direction. When the maximum power is reached and power decreases in the subsequent instant, the perturbation reverses. At steady state, the algorithm oscillates around the MPP. To minimize power fluctuations, the size of the perturbation is kept small.

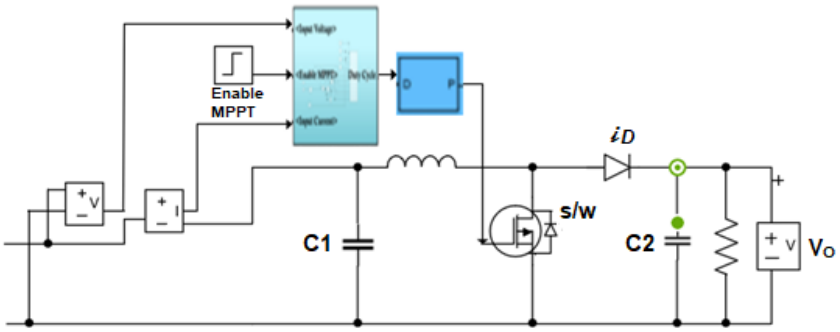

Figure 3.24: Perturb and observe method to regulate the output voltage.

Figure 3.25 illustrates the flowchart of the developed algorithm. The operating voltage of the PV system is perturbed by a small increment dV, resulting in a change dP in power. If dP is positive, the perturbation in the operating voltage is continued in the same direction as the initial increment. Conversely, if dP is negative, indicating that the operating point has moved away from the MPP, the perturbation direction is reversed.

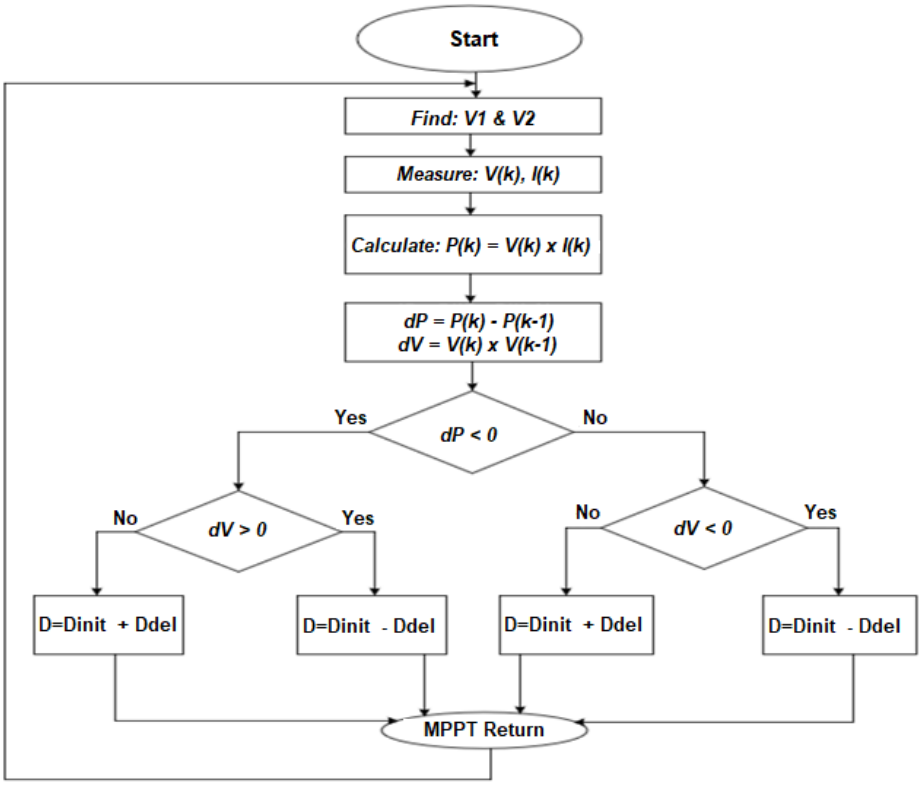

Figure 3.25: Flowchart of P&O MPPT algorithm for PV with boost converter.

Although solar irradiance levels fluctuate significantly over time, the variation in power absorbed by the photovoltaic system occurs more gradually due to the relatively slow dynamic response of the PV panels. The adjustment of the converter duty cycle can be evaluated using the following expression [240].

$$\boldsymbol{D = D_{init} + C_1 \frac{\Delta P_{k-1}}{\Delta D_{init}}} \tag{3.109}$$

Where D and D_{init} are the duty ratios at iterations D and D_{init}, respectively. $\frac{\Delta P_{k-1}}{\Delta D_{init}}$ represents the power gradient of the PV system at step D_{init} and $C1$ is the step change factor.

To ensure convergence towards the MPP of the PV system amidst variations in solar irradiance, the function must possess a single extremum point. This is illustrated in Figure 3.26 (originally referenced as Figure 3.16), which shows that the MPP is attained when:

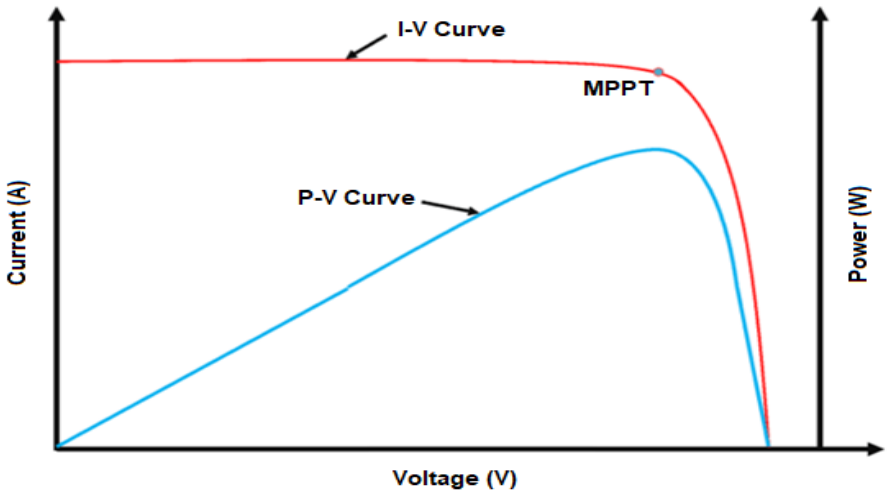

Figure 3.26: Typical characteristic of a common PV cell.

$$\frac{d_p}{d_v} = 0 \tag{3.110}$$

Where dv represents the voltage of the PV system. Applying the chain rule can be expressed as:

$$\frac{dp}{d_v} = \frac{dp}{dD} = 0 \tag{3.111}$$

The process of power maximization is illustrated in Figure 3.26. The adjustment of the duty ratio follows the direction of $\frac{dp}{dD}$. In the high-speed region of the PV system's characteristic curve, increasing the duty ratio leads to a decrease in the operating voltage, which in turn increases the power output and moves the system towards the MPP. Conversely, if the starting point is in the low-speed region, adjusting the duty ratio according to $\frac{dp}{dD}$ results in a decrease in the duty ratio, causing the system to converge towards the MPP as the PV system's operating voltage is gradually increased.

$$V_{PV} = (1 - D)V_{O,} \frac{dV_{PV}}{dD} = V_O \neq 0 \tag{3.112}$$

In the developed DC fast charging system model, the P&O algorithm is implemented to extract the maximum available power from the PV array by dynamically adjusting the operating point toward the MPP. The algorithm perturbs the reference voltage and monitors the resulting change in output power (ΔP) [241]. Depending on the direction of the perturbation and the power response, it determines the appropriate action for the next cycle. This process is governed by the relationship between the converter's duty ratio and the input resistance seen by the PV array. Any change in the duty cycle inversely affects the input resistance and subsequently alters the operating voltage. The system evaluates how this change influences the output power to decide whether to continue in the same direction or reverse it. The nature

of the output power response depends on whether the present operating point lies before or beyond the knee of the PV power-voltage (P–V) curve, as shown in Figure 3.26. For instance, if a reduction in duty cycle results in an increase in operating voltage and a simultaneous increase in output power, the operating point is still before the MPP, and the next cycle should further reduce the duty cycle to continue approaching the MPP. Conversely, if the power decreases, it implies that the operating point has moved beyond the MPP, and the direction of perturbation should be reversed. This tracking mechanism ensures that the PV system consistently operates near the MPP despite changes in environmental conditions. To summarize this logic, Table 3.5 presents a decision matrix based on the sign of the perturbation and the resulting power change. Although the table alone does not represent the full algorithm, it clearly outlines the decision-making criteria embedded in the system's control loop for effective and stable MPP tracking.

Table 3.5: Perturb & Observe algorithm

Perturbation (+Ve)	Change in Power ΔP	Resulting Change
Positive (+Ve)	Negative (-Ve)	Move Positive
Positive (+Ve)	Positive (+Ve)	Move negative
Negative (-Ve)	Negative (-Ve)	Move Positive
Negative (-Ve)	Positive (+Ve)	Move negative

3.7 EV Lithium-ion Battery Controller

In this study models the lithium-ion (Li-ion) battery for EVs as a voltage source in series with a resistor, with additional refinements such as internal resistance, RC networks to simulate transient charging and discharging behaviors, and thermal models to account for temperature changes. These improvements enhance the accuracy of battery performance under fast charging conditions. A high energy lithium-ion battery is used for energy storage and carefully modelled as a voltage source connected in series with a resistance, as shown in Figure 3.27. The BMS manages the charging process using CC, CV, and a hybrid CCCV approach. In the CCCV method, charging starts with constant current to prevent overcurrent, then transitions to constant voltage as the battery nears full charge, reducing the current to prevent overvoltage and ensure battery protection. Figure 3.28 presents the characteristic current and voltage profiles for the charging process using CCCV control.

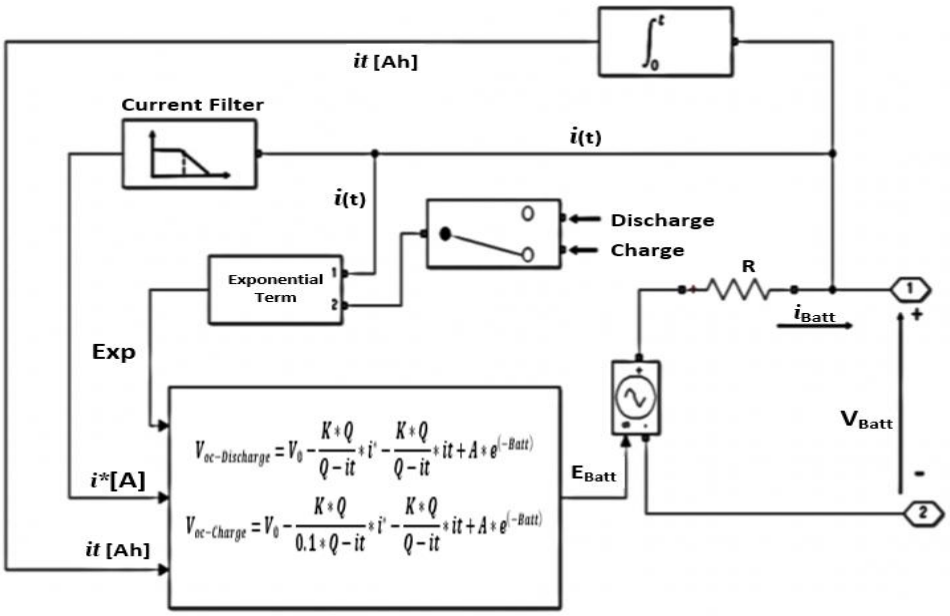

Figure 3.27: Schematic diagram of the battery model [242].

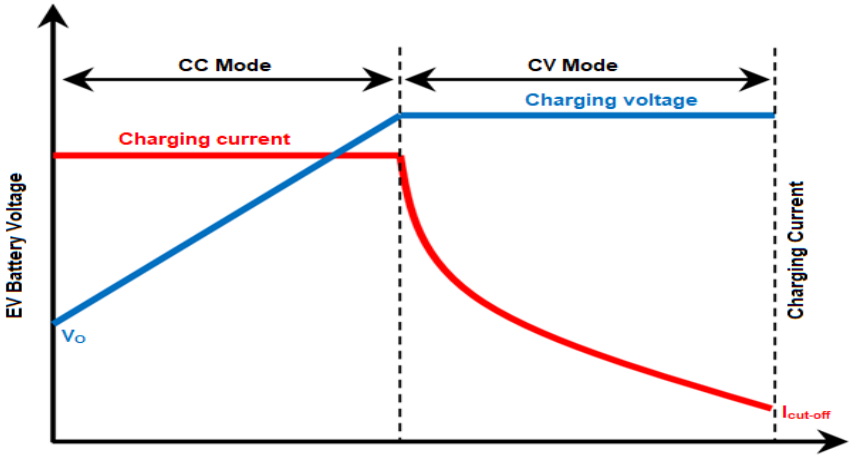

Figure 3.28: Waveforms of the charging profiles using CCCV method for the EV battery.

In the implemented system model, the lithium-ion battery model used is based on MATLAB/Simulink and falls under the category of equivalent circuit models, specifically designed for DC fast charging applications. This model, initially proposed and later refined, integrates key elements to accurately reflect the dynamic behavior of the battery during fast charging [243], [244]. To address the limitations of earlier models, the implemented model includes a controlled voltage generator, which simulates the Open-Circuit Voltage (OCV) and its variation with the SoC, along with a series resistor to account for internal voltage drops. The model has been enhanced by incorporating an exponential term to better capture the voltage

behavior during maximum charge and discharge phases, and a polarization parameter (K) is added to represent the non-linear characteristics of the OCV.

The equations that describe the battery voltage and the open-circuit voltage are as follows:

$$V_{battery} = E_o - \frac{K*Q}{Q-it} i(t) - Ri(t) \quad (3.113)$$

$$V_{OC} = E_o - \frac{K*Q}{Q-it} * i(t) \quad (3.114)$$

E_O Represents the no-load voltage when the battery is fully charged and is a constant value. Q denotes the maximum capacity of the battery, which corresponds to the discharged capacity calculated by integrating the current flowing through the battery. K is the bias constant, while R signifies the internal resistance. The polarization parameter K can be described using the following equation:

$$K = \beta V_{full} - V_{nom} + A(exp^{-BQ_{nom}} - 1)\frac{Q_{full}-Q_{nom}}{Q_{nom}} \quad (3.115)$$

V_{full} represents the maximum voltage of the battery, while V_{nom} refers to the nominal voltage. Q_{nom} and Q_{full} indicate the capacity at nominal voltage and the capacity when the battery is fully charged, respectively. The equations that characterize the no-load voltage behavior of the battery are differentiated based on whether the battery is in a charged or discharged state. For lithium-ion batteries, the following equations are employed to describe the variation in no-load voltage as a function of the discharged capacity:

$$V_{OC_{Discharge}} = E_0 - \frac{K*Q}{Q-it} * i^* - \frac{K*Q}{Q-it} it + A\, exp^{(-B*it)} \quad (3.116)$$

$$V_{OC_{Charge}} = E_0 - \frac{K*Q}{0.1*Q-it} * i^* - \frac{K*Q}{Q-it} it + A\, exp^{(-B*it)} \quad (3.117)$$

The state of charge SoC can be calculated using the equation below:

$$SOC = 1 - \frac{1}{Q}\int_0^t i(t) * dt \quad (3.118)$$

In this equation, the constant Q represents the maximum capacity of the battery. The parameters A and B are defined by the following equations:

$$A = V_{full} - V_{exp} \tag{3.119}$$

$$B = \frac{\alpha}{Q_{exp}} \tag{3.120}$$

The parameter A is defined as the difference between the battery voltage when fully charged and the battery voltage at the conclusion of the exponential segment, meaning A indicates the amplitude of the exponential voltage region. B represents the exponential capacitance, also known as the inverse time constant. This parameter is determined using the battery capacity at the end of the exponential segment and is associated with a constant parameter α, which is derived by fitting the model to actual battery data. Additionally, i^* denotes the measured current value that has been filtered through a first-order low-pass filter.

Figure 3.29 illustrates the simulated SoC behavior of a battery within a DC fast charging system, showing an increase from an initial level of 0.2 (20%) to approximately 0.202 (20.2%) over a short period. This steady, linear rise in SoC suggests that the fast charging system is delivering a controlled, low-rate charge during this phase. The incremental increase of only 0.2% indicates a gradual charging process, potentially representing a low-power charging stage implemented to enhance battery longevity and manage thermal conditions effectively. In the context of DC fast charging systems, such a controlled charging rate may be applied at the beginning or end of the charging cycle to mitigate stress on the battery cells and minimize heat buildup, both crucial for battery health and efficient energy transfer. The constant slope in the SoC increase implies stable power delivery, with no fluctuations in current or voltage, highlighting the fast charging system’s ability to maintain consistent charging conditions. This controlled charging phase exemplifies the system's design to prioritize reliability and safety in high-performance EV charging applications, ensuring stable operation while optimizing the battery's lifespan.

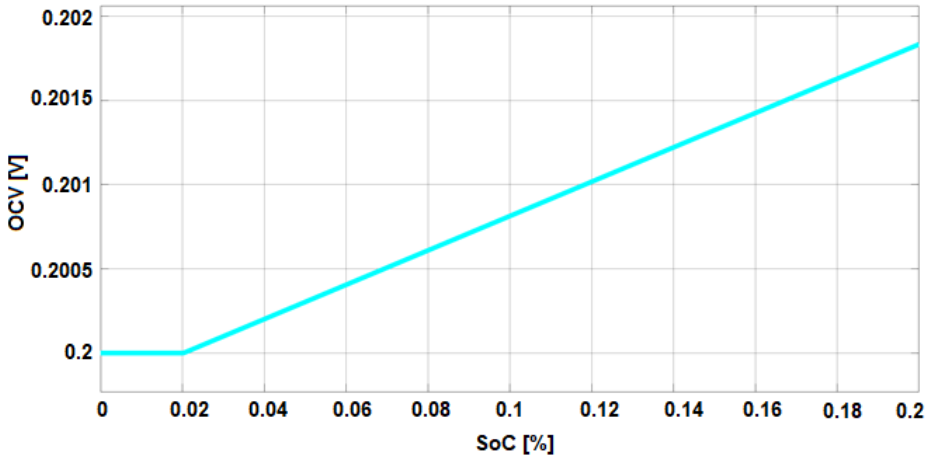

Figure 3.28: Battery state of charge [%].

3.8 Summary

This chapter presented the development modelling of a DC fast charging system for electric vehicles and mathematical modelling of the different components that have been thoroughly explored. The system components include three key stages: the PV stage, the AC grid stage, and the charger stage, which work in unison to provide efficient and reliable charging. Using a PV array and a DC-DC boost converter with MPPT, the system effectively harnesses solar energy, while the AC grid stage utilizes a front-end converter and PI controller to manage energy flow and maintain grid stability. The charger stage, equipped with a DAB bidirectional DC charger and PI controller, ensures optimal charging performance and energy management, supporting bidirectional power flow for grid or home system integration, was also presented. The interconnection of these stages through a DC bus maximizes the use of renewable energy, enhancing both charging efficiency and grid stability. The lithium-ion battery model for EVs, developed to incorporates features like a voltage source, internal resistance, and RC networks to simulate dynamic charging and discharging under fast charging conditions, was discussed. The BMS was developed using the CCCV method to ensure battery protection and efficiency was presented in detail. The BMS was designed considering battery SoC monitoring and electric vehicle load demand at fast charging stations, ensuring efficient power distribution between sources and the battery system, based on integrated stage requirements and battery load demand. A MATLAB/Simulink model of a DC fast charging system for electric vehicles was implemented.

CHAPTER FOUR
RESULTS AND DISCUSSION

4.1 Introduction

This chapter presents a comprehensive analysis of the modeling and simulation results for the proposed high-performance DC fast charging system. The system architecture integrated a photovoltaic PV-tied grid with advanced power electronic converters to enhance efficiency, reliability, and sustainability in EV charging. The primary objective of the simulations was to validate the effectiveness of the developed system under various operating conditions, focusing on key performance metrics such as charging efficiency, power quality, grid stability, and charging time reduction. To this end, a series of case studies were developed to examine system behavior in different scenarios, including grid-connected operation, photovoltaic integration, energy storage participation, and the influence of control parameters. These case studies allow for a structured evaluation of key performance aspects, such as the role of the AFE rectifier with voltage-oriented control, the dual active bridge DC-DC converter, and the battery interface. The study systematically evaluated the behavior of key system components, including the AFE rectifier with voltage-oriented control, the dual active bridge DC-DC converter, and the energy storage interface. A PI controller was implemented to regulate voltage and current, ensuring stable power flow and effective system operation. Additionally, MPPT was applied using the P&O algorithm to maximize energy extraction from the photovoltaic system, optimizing power delivery to the charging infrastructure.

Furthermore, the results provided insights into transient and steady-state performance, the influence of grid disturbances, and ripple current mitigation through advanced control techniques. The combined use of the PI controller and the MPPT P&O algorithm improved system response reduced steady-state errors, and ensured efficient energy conversion from renewable sources. A comparative analysis with conventional charging architectures highlighted the advantages of the proposed system in accelerating the charging process while minimizing power losses and maintaining compliance with grid regulations. Through extensive simulation studies, this chapter demonstrated how the proposed system improved energy utilization, reduced harmonic distortions, ensured stable grid interaction, and significantly shortened EV charging time. By integrating intelligent control strategies, including the PI controller and MPPT using the P&O algorithm, the proposed DC fast charging system contributed to the advancement of next-generation high-performance EV charging infrastructure. Through the MATLAB/Simulink simulation environment, detailed observations were made on the Hybrid PV-tied grid for EVs charging station, as shown in Figure 4.1, to assess the effectiveness of the control strategies employed.

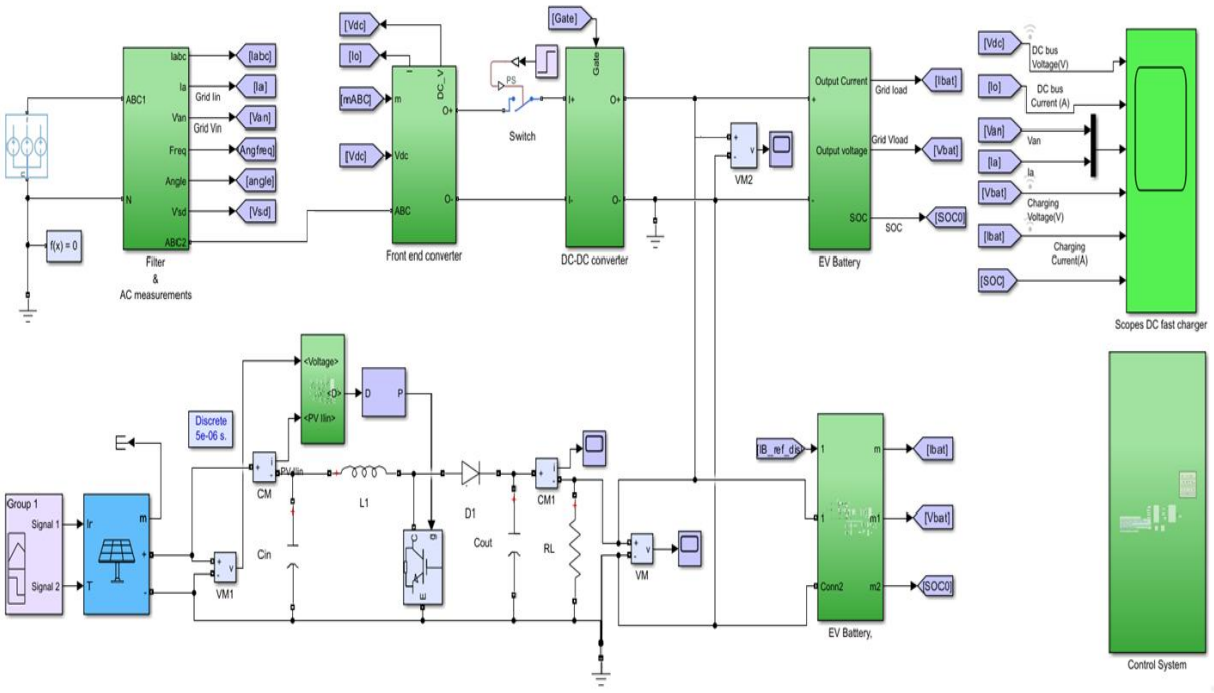

Figure 4.1: Hybrid PV-tied grid for EVs charging station Simulink model.

4.2 Overview of the DC Fast Charging System Block Diagram

The proposed DC fast charging system is designed to optimize power flow and enhance charging efficiency by integrating a PV-tied grid, an energy storage system (ESS), and advanced power converters. The system architecture includes an active front-end rectifier for grid interfacing with unity power factor correction, a dual active bridge DC-DC converter for bidirectional power transfer and galvanic isolation, and a PV-integrated Boost Converter with MPPT to maximize solar energy utilization. The ESS plays a critical role in reducing grid dependency and operational costs. Simulation results demonstrate stable performance, with the grid-side operating at 400V AC, 50Hz, and 100 A line current, while the regulated DC bus maintains 900 V. The battery charging process efficiently delivers 90 kW of power, increasing the initial state of charge from 25%. This configuration effectively minimizes ripple current, improves charging speed, and ensures system reliability.

4.2.1 Hybrid power sources: grid and PV integration

The system leverages hybrid power sources, combining grid electricity with PV generation and energy storage to ensure uninterrupted and efficient EV charging. The grid provides a stable three-phase AC supply at 400V and 50Hz, serving as a reliable backup when solar power is insufficient. Meanwhile, the PV system employs a P&O - MPPT algorithm to maximize power extraction under varying irradiance conditions. Simulation results indicate that the PV system operates with an input voltage of 200 VDC, which is boosted to 440 VDC, delivering an output

current of 175 A and a power output of 77 kW. The ESS, with a nominal voltage of 443 V and a power capacity of approximately 35 kW, supports the PV system, maintaining an initial SoC of 25%. This hybrid approach enhances energy utilization, reduces reliance on the grid, and contributes to a more sustainable and resilient fast-charging infrastructure.

4.2.2 Electrical and power electronics system model

The DC fast charging system incorporates advanced power electronic converters to ensure efficient and stable power conversion. The AFE rectifier converts three-phase AC power from the grid to DC while maintaining unity power factor and minimizing harmonic distortion. The Dual Active Bridge DC-DC converter facilitates bidirectional power flow, provides galvanic isolation, and regulates the output voltage to 900 V for optimal battery charging. Additionally, a Boost Converter is implemented on the PV side to maintain MPPT operation, ensuring maximum solar energy extraction. Key operational parameters include a switching frequency of 10 kHz for efficient power conversion and PI controller settings (Kp = 0.248, Ki = 21.692) for precise voltage and current regulation in the AC-DC stage. These components work synergistically to deliver stable power, minimize ripple effects, and enhance system reliability.

4.2.3 Control and simulation model

The system employs a combination of advanced control strategies to optimize performance and ensure stability. PI controllers are implemented in both the AFE rectifier and the DAB converter to regulate voltage and current, minimizing ripple and maintaining a stable DC bus voltage of 900 V. The P&O algorithm is used for MPPT in the Boost Converter, enabling efficient power extraction from the PV system under varying environmental conditions. Additionally, a PLL ensures synchronization between the grid voltage and current, reducing phase errors and enhancing system stability. These control mechanisms collectively improve charging efficiency, reduce harmonic distortions, and ensure seamless integration of renewable energy sources with the grid.

4.2.4 Results and discussion

Simulation results confirm the system's effective performance and integration. The PV system maintains a stable output voltage around 440 VDC, achieving an output power of 77 kW. On the grid side, the system ensures a stable input voltage of 400V and an output voltage of 900 VDC, ensuring efficient power transfer. The battery charging performance is optimized, with the battery power stabilizing at approximately 90 kW with minimal fluctuations. The system successfully integrates renewable energy with the grid, reduces harmonic distortions, and maintains voltage and current stability, demonstrating its effectiveness as a reliable and efficient solution for future EV infrastructure.

4.3 Simulation results and performance of grid source

Figure 4.2 shows the three-phase AC currents (i_a, i_b, i_c) in the DC fast charging system, each ranging between ±200 A. A small high-frequency oscillation from the rectifier switching is present but filtered, keeping the currents nearly sinusoidal. The zoomed inset (0.2–0.26 s) confirms a balanced three-phase system supplied at 400 V, 50 Hz.

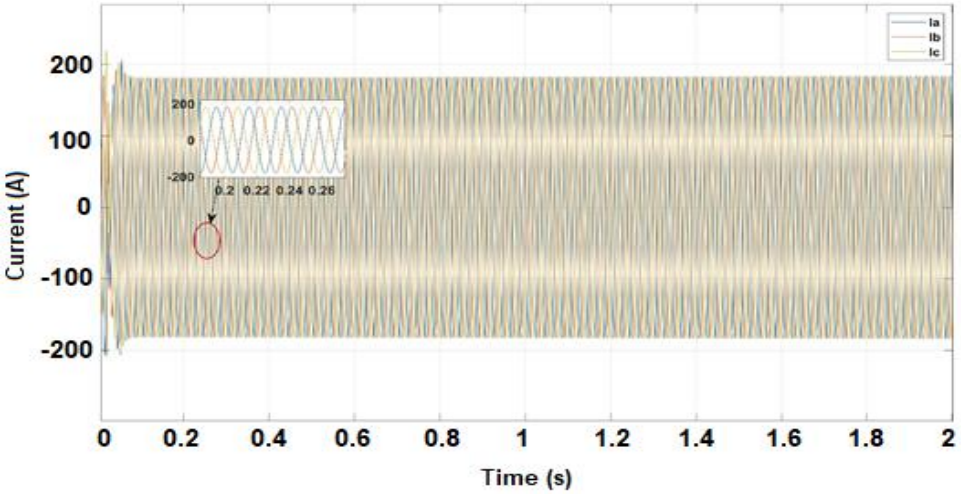

Figure 4.2: Three phase grid current.

Figure 4.3 presents the three-phase AC voltages (v_a, v_b, v_c) in a DC fast charging system for EVs with each oscillating between ±400 V. The zoomed inset from 0.2-0.26 s reveals sinusoidal waveforms with a 120° phase displacement, confirming a balanced three-phase system. Operating at 400 V and 50 Hz.

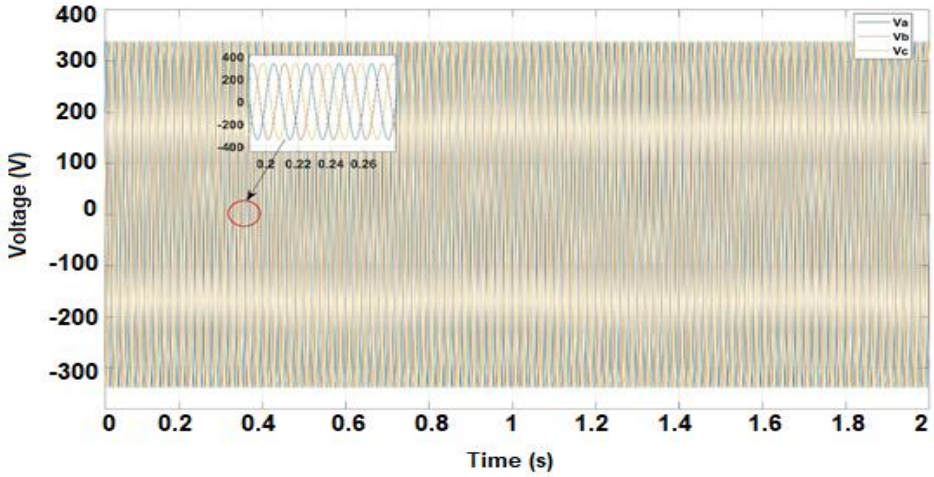

Figure 4.3: Three-phase grid voltage.

Figure 4.4, which shows the grid input current for the DC fast charging system, exhibits dynamic behavior with a maximum value of 322.6 A at 0.025 seconds and a minimum value

of -188.9 A at 0.035 seconds. The median current is approximately -0.1877 A, with an RMS value of 127.5 A, indicating effective power delivery to the system. Key transition points include a high of 176.8 A and a low of -176.1 A. The system shows a rise time of 5.727 ms and a fall time of 5.729 ms, corresponding to positive and negative slew rates of 49.302 A/ms and -49.278 A/ms, respectively. Minor deviations such as preshoot (+1.196%, -1.381%), overshoot (+0.972%, -1.997%), and undershoot (+1.997%, -1.196%) highlight the system's transient behavior but remain within acceptable limits, reflecting stable control performance.

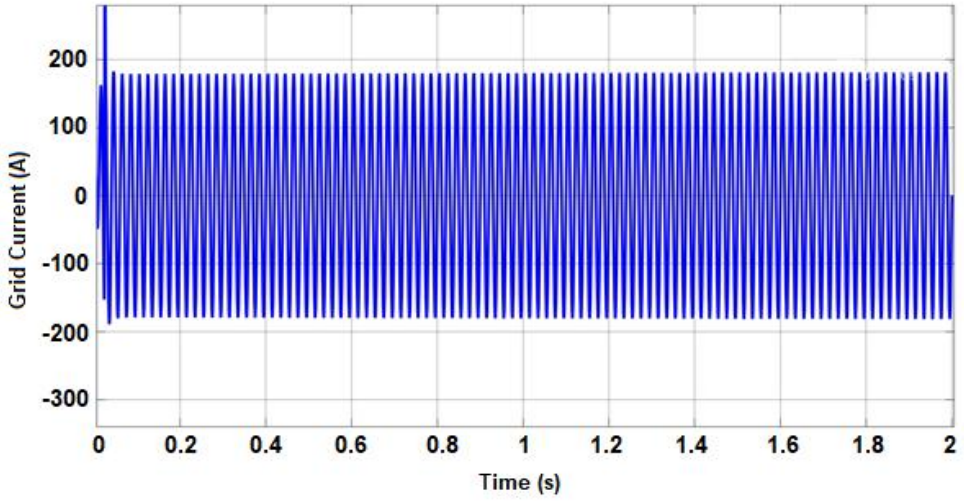

Figure 4.4: Grid input current.

Figure 4.5, which shows the grid input voltage in the DC fast charging system, demonstrates a sinusoidal waveform with a maximum value of 338.8 V at 1.125 seconds and a minimum value of -338.8 V at 0.015 seconds, indicating balanced positive and negative peaks. The RMS voltage is 239.6 V, highlighting efficient power delivery, while the amplitude reaches 670.9 V. The transitions for high and low values are 335.5 V and -335.5 V, respectively, with a rise and fall time of 5.819 ms each, reflecting consistent signal characteristics. The slew rate is 92.234 V/ms for rising edges and -92.234 V/ms for falling edges, indicating rapid voltage changes during transitions. The waveform exhibits minimal deviations, with a preshoot and overshoot of 0.505%, and an undershoot of 1.996%, underscoring the stability of the control strategy.

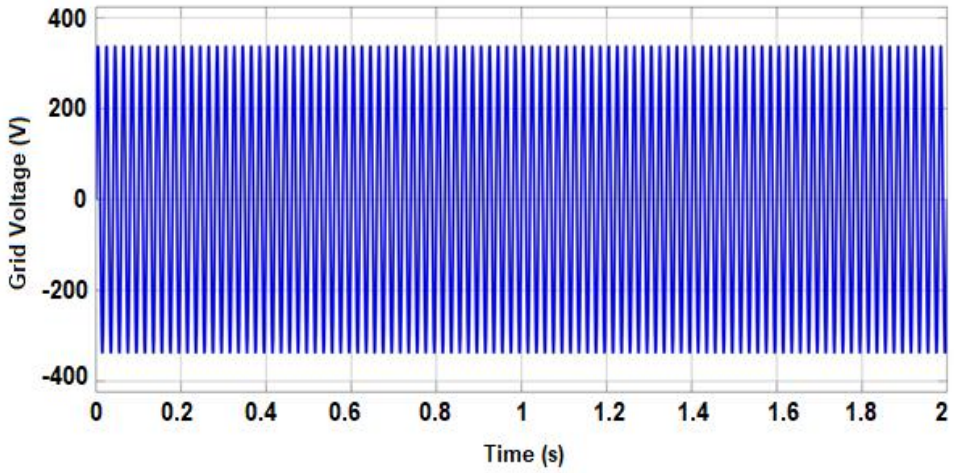

Figure 4.5: Grid input voltage.

Figure 4.6, which shows the grid input power for the DC fast charging system, demonstrates dynamic and efficient power delivery, reaching a maximum value of 109.3 kW at 0.025 s and a minimum value of -54.64 kW at 0.015 s. The median power is 30.08 kW, with an RMS value of 37.40 kW, reflecting the overall effective power transfer. Transition points show a high of 60.94 kW and a low of 0.2775 kW, with an amplitude of 60.66 kW. The rise time is 2.909 ms, with a positive slew rate of 17.338 W/ms, and the fall time is 2.922 ms, with a negative slew rate of -16.611 W/ms. Minor transient deviations are observed, including preshoot (+0.806%, -0.649%), overshoot (+0.644%, -1.996%), and undershoot (+1.995%, -0.458%), which remain within acceptable limits and indicate robust system control. Peaks occur at 1.093×10^5 W (0.025 s), 6.399×10^4 W (0.035 s), and 6.192×10^4 W (0.045 s), highlighting periodic power fluctuations due to system modulation.

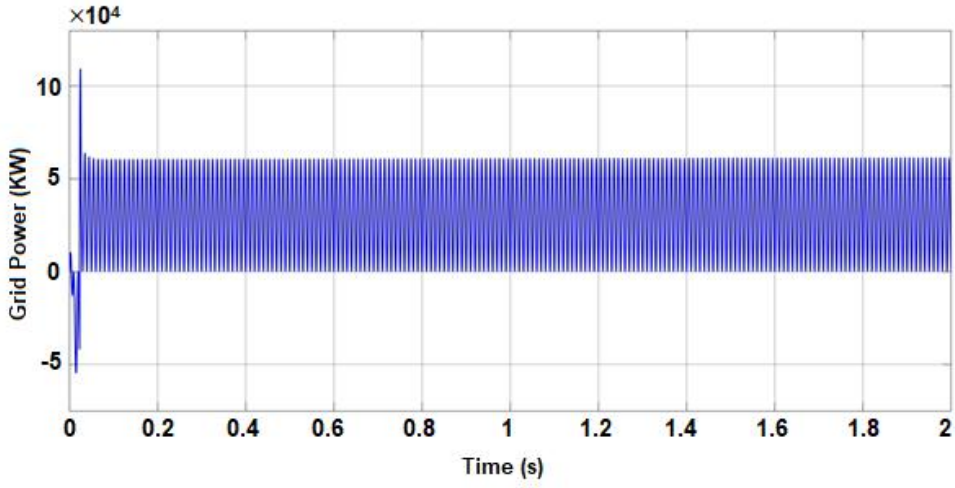

Figure 4.6: Grid input power.

Figure 4.7 illustrates the three-phase modulating signals $mabc$ for the control of grid-tied inverters in a DC fast charging system. These signals are sinusoidal, symmetric, and maintain their integrity even under disturbances applied to the control input, demonstrating the robustness of the vector control or PWM strategy. The inset zooms into a specific time range (0.5–0.58 s) to highlight the high-frequency switching behavior, showing no visible distortion despite disturbances.

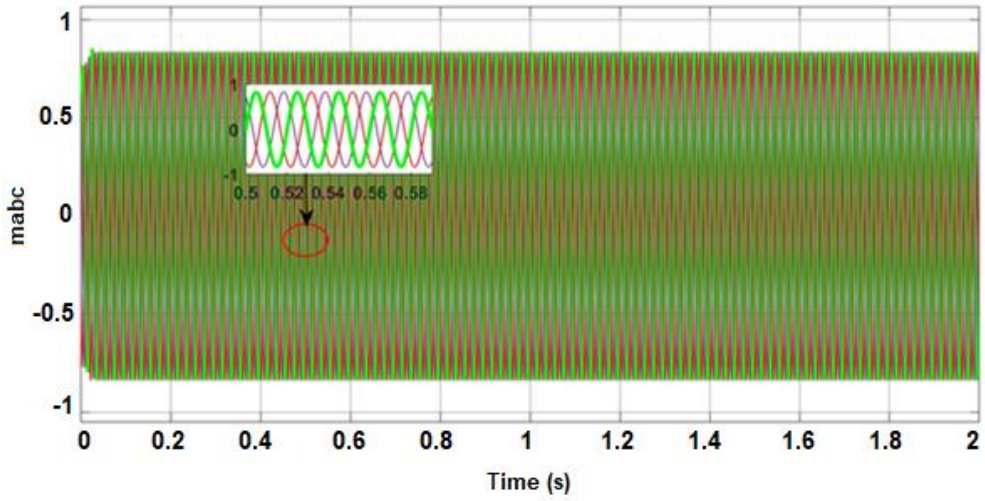

Figure 4.7: Modulating signal $mabc$.

Figure 4.8 illustrates the phase angle (θ) of the grid voltage as determined by the PLL system, which ensures accurate synchronization with the grid. The waveform exhibits a sinusoidal pattern, with a peak-to-peak amplitude of 6.283 radians and a mean value of 1.570 radians. The rise and fall times are 8.960 ms and 4.482 µs, respectively, indicating the speed of the PLL's response to changes in the grid voltage.

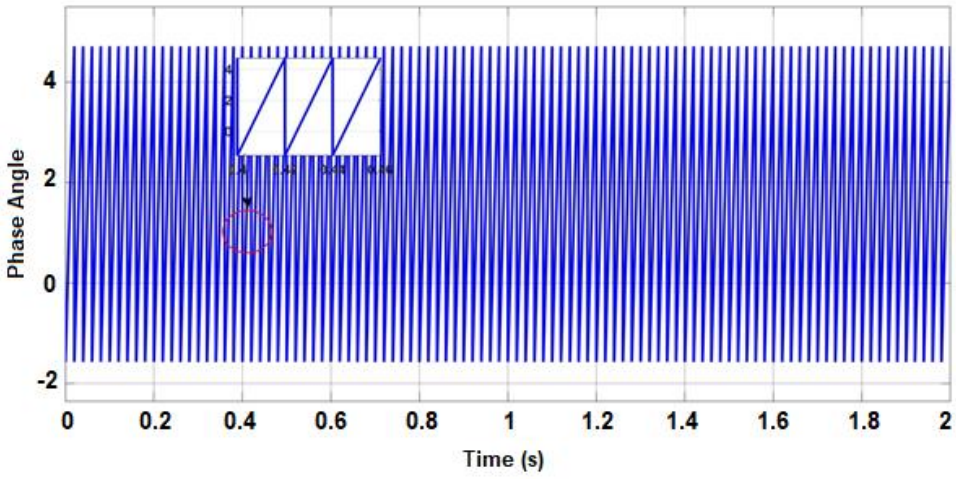

Figure 4.8: Phase Angle of PLL.

The V_q-axis voltage response, as illustrated in Figure 4.9, indicates the performance of the controller within the DC fast charging system. The voltage stabilizes around 0 V, with a peak deviation of approximately ±0.02 V within the first 0.2 seconds, showcasing the controller's quick response to dynamic changes in load conditions. The transient response exhibits a damped oscillation pattern, which settles down rapidly, achieving steady-state conditions by approximately 0.25 seconds. The minimal fluctuation in the V_q-axis voltage highlights the precision of the control strategy in maintaining system stability, which is critical for the reliable operation of the fast charging infrastructure.

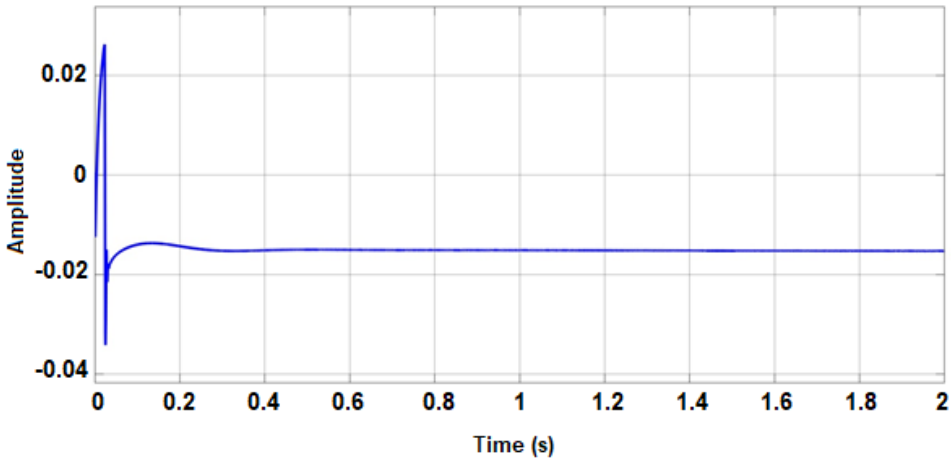

Figure 4.9: V_q-axis voltage.

The V_d-axis voltage response, as depicted in Figure 4.10, illustrates that the voltage stabilizes around 1.3 V, indicating a well-controlled response and reflecting a tight range of operation. The statistics reveal a minimal overshoot, with the system quickly stabilizing without significant oscillations, achieving a steady state shortly after 0.03 seconds.

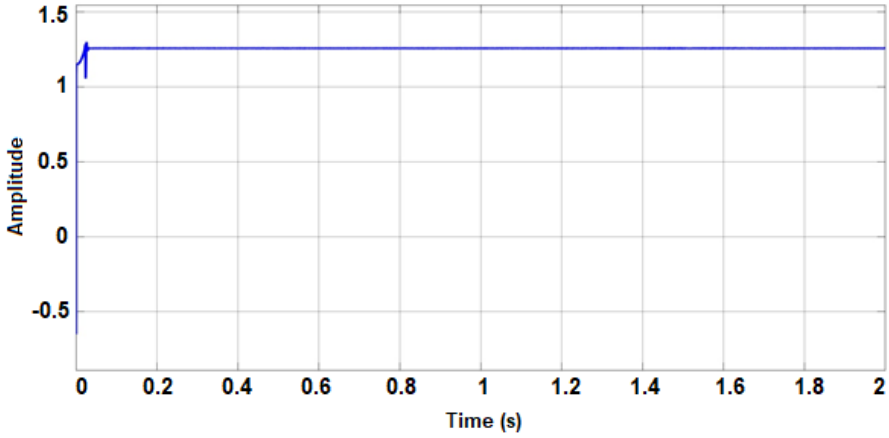

Figure 4.10: V_d-axis voltage.

4.3.1 Simulation results and performance of grid AC-DC converter

Figure 4.11 shows the input front-end converter voltage response over 2 seconds. Initially, the voltage spikes to about 445 V, then quickly stabilizes at around 400 V, maintaining this steady state with minimal oscillation. This response indicates effective voltage regulation and stability of the converter, minimizing ripple and handling load fluctuations well.

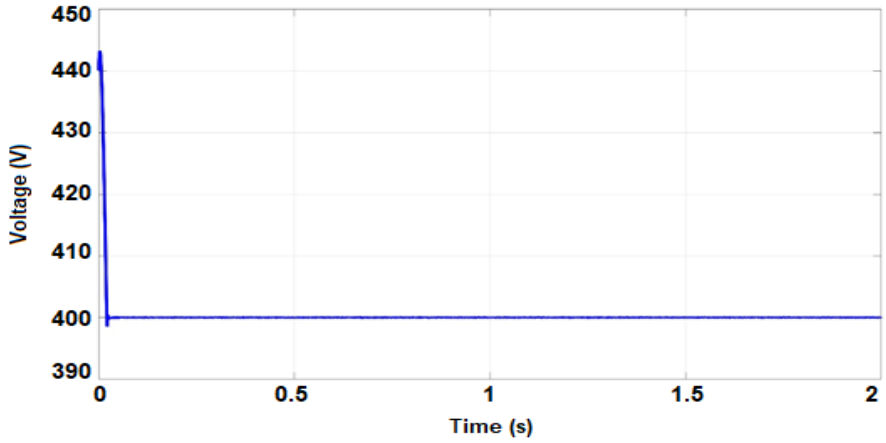

Figure 4.11: Voltage response of input front-end converter.

Figure 4.12 shows the voltage reference V_{ref} response over 2 seconds, where the reference has been set to 0 V as the baseline for control. This predefined zero reference voltage ensures stable regulation, with the controller maintaining accuracy without oscillations or drift.

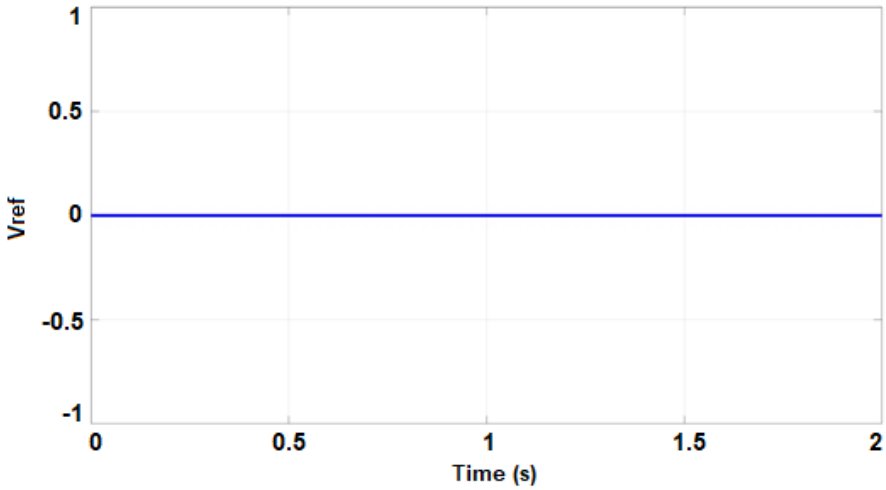

Figure 4.12: Voltage reference response.

Figure 4.13 presents the DC output voltage profile of the FEC, highlighting its transient and steady-state behaviors. The voltage stabilizes at 800 VDC after an initial transient phase, demonstrating reliable performance. During transients, the voltage peaks at 886 VDC, with an overshoot of 34.262% and an undershoot of -17.061%, before settling within 19.916 ms. The

transient amplitude is 212 VDC, with transition points at 811 VDC (high) and 588 VDC (low) respectively. The system exhibits a pre-shoot of 0.704% before settling to its nominal voltage within a setting time of 19.916 ms. The zoomed-in inset captures small voltage steps and oscillations near the stabilization point, emphasizing the system's controlled response and ability to minimize oscillatory deviations.

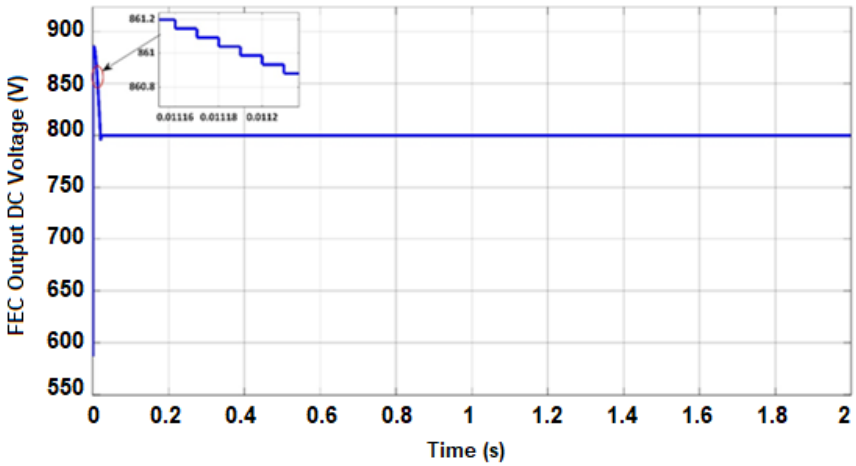

Figure 4.13: FEC Output DC link voltage.

Figure 4.14 illustrates the output voltage ripple of the front-end converter in the DC fast charging system, controlled by a PI controller. The mean output voltage is 800 V, with a minimal ripple amplitude of 0.1 V (peak-to-peak), highlighting the controller's effectiveness in maintaining stability. The system settles within 1.5 seconds, demonstrating a fast response to load changes. Brief voltage spikes occur due to transient conditions but are effectively dampened by the PI controller, ensuring smooth operation.

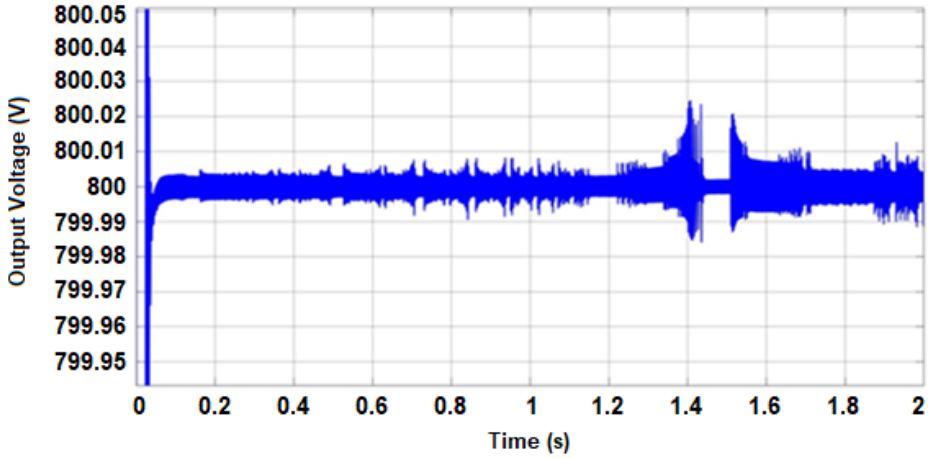

Figure 4.14: Ripple of the output voltage FEC.

Figure 4.15 shows the front-end converter DC bus current response over time, illustrating an initial transient followed by steady-state behavior. The current initially peaks at approximately 203.4 A and dips to -123.1 A, with a peak-to-peak variation of 326.5 A. After an overshoot of 38.19% and an undershoot of 1.835%, the system stabilizes at an average current of 112.8 A with minimal oscillations. The rise time of 671.386 µs indicates a rapid response, while the slew rate of 280.111 A/ms suggests a controlled current transition.

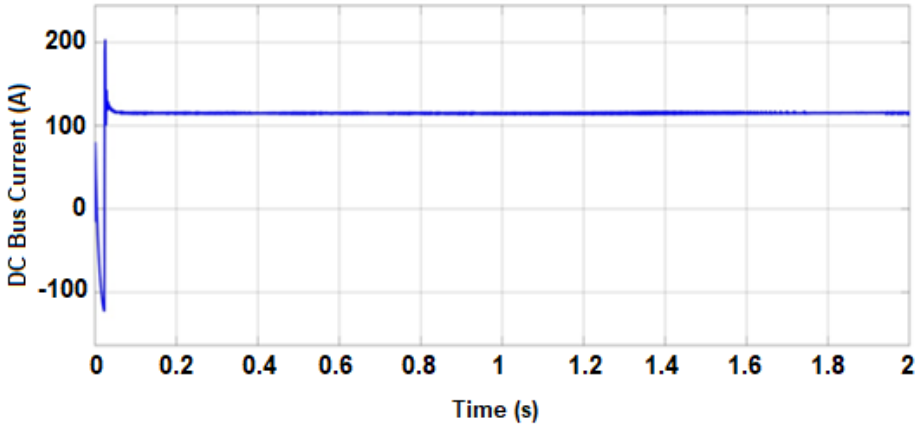

Figure 4.15: DC bus current.

4.3.2 Simulation results and performance of grid DC-DC dual active bridge converter

The output voltage waveform of the DAB converter in the DC fast charging system, shown in Figure 4.16, demonstrates excellent transient and steady-state performance. The steady-state voltage stabilizes at approximately 898.3 V DC, ensuring reliable and consistent charging for EV batteries, with minimal ripple and deviations. During the transient phase, the voltage exhibits a maximum peak of 940 V at 0.055 seconds and a low transition level of 357.7 V, resulting in an amplitude of 538.4 V. The rise time of 14.565 ms and slew rate of 29.572 V/ms indicate rapid voltage adjustment to the target level. The system shows controlled deviations with a preshoot of 0.543%, an overshoot of 8.152%, and an undershoot of 2.063%, effectively managing transient oscillations. The subfigure zooms into the transient region, highlighting damped oscillations between 949 V and 954 V, which diminish quickly as the system reaches stability. Statistical analysis confirms a median value of 896.6 V and an RMS value of 891.7 V, reflecting minimal fluctuation around the desired voltage.

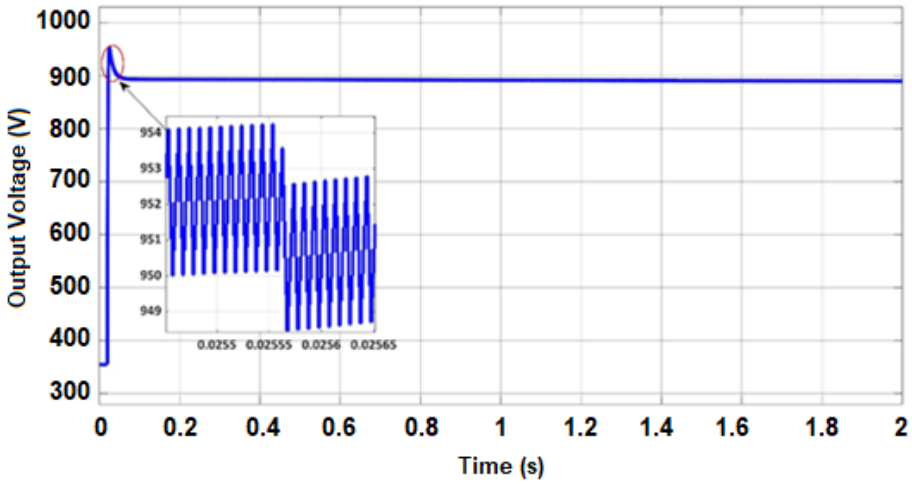

Figure 4.16: DAB Converter output voltage waveform.

Figure 4.17 illustrates the output current profile of a DAB converter, highlighting both steady-state and transient behaviors. The output current stabilizes at approximately 100 A after a brief transient phase during startup, indicating reliable steady-state operation. The transient behavior, shown in the zoomed-in inset, reveals a peak current of 113 A at t=0.026 seconds, accompanied by damped oscillations before settling. Key parameters include a rise time of 1.432 ms and a slew rate of 55.359 A/ms, reflecting the system's responsiveness. The waveform exhibits a positive overshoot of 11.798% and a minor undershoot of 2.608%, both well-controlled and typical for such systems. Signal statistics, including an RMS current of 99.54 A, and a peak-to-peak value of 111.3 A, further confirm stable operation. The zoomed-in view highlights the dynamics of the startup phase, showcasing the system's ability to handle transient conditions effectively with rapid settling and minimal deviation, making the DAB converter suitable for dynamic applications.

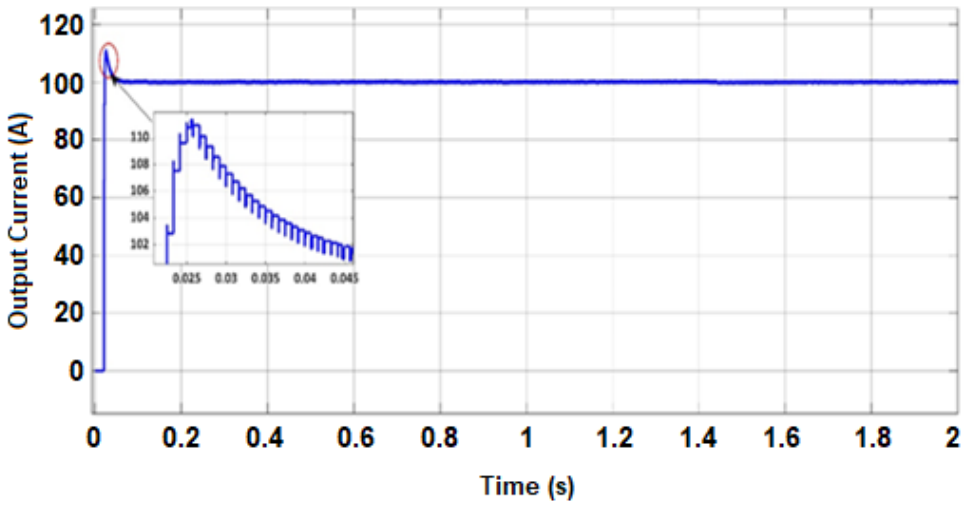

Figure 4.17: DAB Converter output current waveform.

Figure 4.18 illustrates the output power profile of a DAB converter, showcasing both steady-state and transient characteristics. The output power stabilizes at approximately 90.70 kW, indicating a consistent operational level after the initial transient period. The peak power reaches 106.2 kW at t 0.026 s, reflecting a transient overshoot of 19.88%, followed by damped oscillations and settling to the steady-state value. The rise time of 1.511 ms and a slew rate of 46.690 kW/μs demonstrate the converter's fast response capability. The zoomed-in inset highlights high-frequency oscillations during the transient phase, occurring around 0.0252 seconds, with small fluctuations indicative of minor control imperfections. Signal statistics, including an RMS power of 88.76 kW, median power of 89.14 kW, and a mean of 88.30 kW, confirm stable and efficient operation. The overall performance, with controlled undershoot (2.934%) and preshoot (0.602%), highlights the DAB converter's robustness in handling dynamic conditions and maintaining steady-state power output effectively.

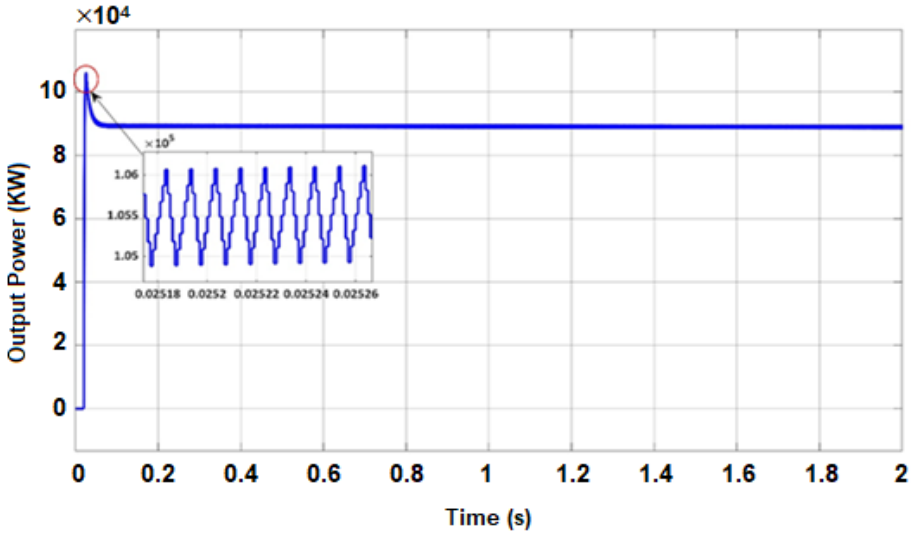

Figure 4.18: DAB Converter output power waveform.

Table 4.1: Battery specification

Parameters	**Value**
Chemistry	Li-ion battery
Nominal current	100 A
Nominal voltage	900 V
Nominal power	90 kW
Rated capacity	50 Ah

Initial battery SoC	25 %
Response time	1 s
Nominal temperature	25 °C

4.3.3 Analysis of SoC stability and dynamics

The SoC curve for the battery shown in Figure 4.19, in this DC fast charging setup, shows a steady increase over time, with a maximum SoC of 0.2703 at 2 seconds and a minimum of 0.2500 at 0.02 seconds, resulting in a peak-to-peak SoC variation of 0.02025. Both the mean and median SoC are 0.2600, closely aligned with the RMS value of 0.2601, indicating a stable charging process with minimal fluctuations. The transition data, with a high level of 0.2651, a low level of 0.2501, and an amplitude of 0.01499, along with a rise time of 1.169 seconds, suggest that the charging system maintains smooth control over the SoC increase. A high slew rate of 10.257 per second confirms a rapid SoC change, consistent with the requirements of fast charging.

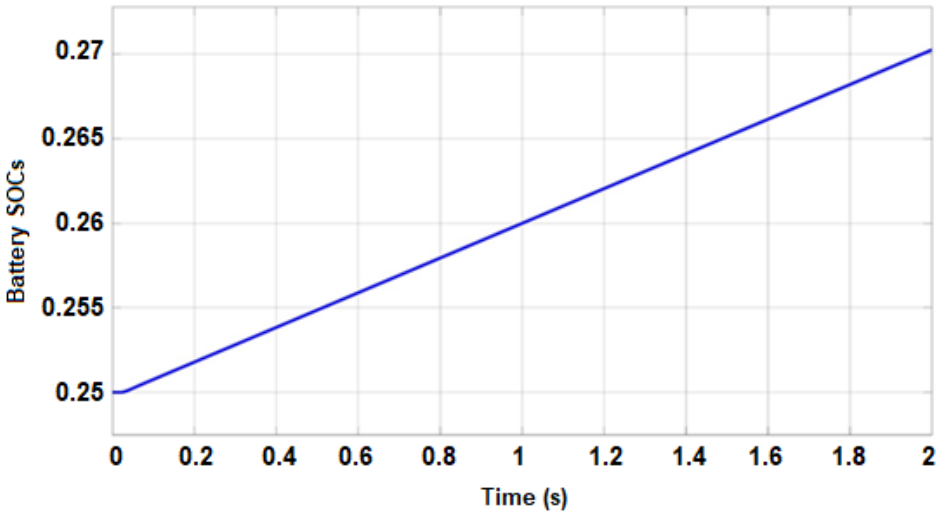

Figure 4.19: Battery state of charge.

4.3.4 Performance of harmonic distortion and frequency analysis

The harmonic distortion and frequency spectrum analysis provides insight into the performance of the DC fast charging system, as shown in Figure 4.20. The fundamental frequency (H1) shows a dominant amplitude of 119.28 $Vrms$, with successive harmonics (H2 to H6) exhibiting significantly lower magnitudes, confirming effective harmonic suppression. The THD is calculated as -70.625 dBc, indicating minimal distortion relative to the fundamental component. Signal-to-Noise Ratio (SNR) and Signal-to-Noise and Distortion Ratio (SINAD) are

measured at 64.68 dB and 63.69 dB, respectively, demonstrating high signal integrity and low noise levels. The Spurious-Free Dynamic Range (SFDR) is 73.60 dB, showcasing robust suppression of non-harmonic spurious signals.

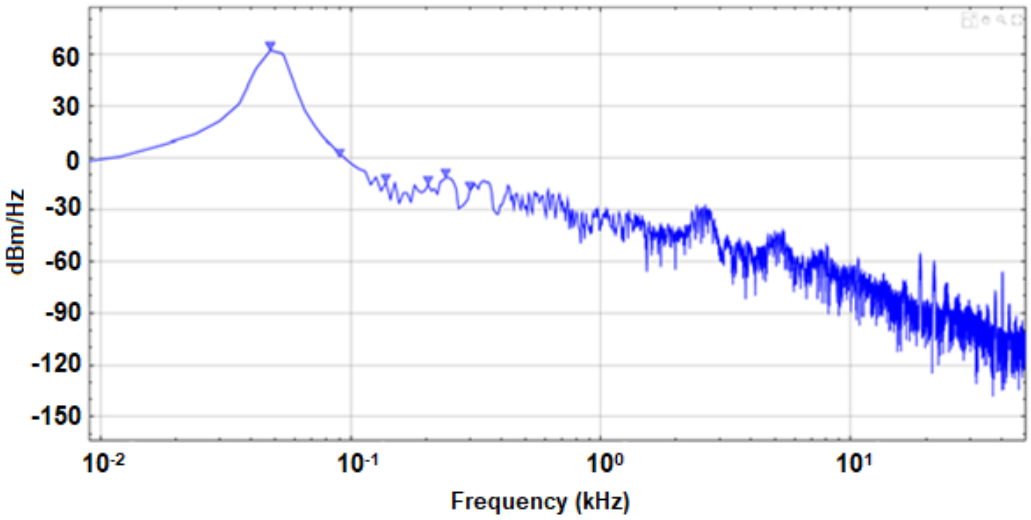

Figure 4.20: Harmonic Distortion Analysis.

4.4 Simulation results and performance of the PV source

The PV input power profile in Figure 4.21 shows the dynamic response of the PV system to changing conditions. At t = 0 s, PV power starts at approximately 38.7 kW and rapidly increases to about 88.6 kW within 0.15 s, reflecting the MPPT controller's fast tracking of the maximum power point as irradiance and system demand rise. Between 0.15 s and 1.5 s, PV power remains nearly constant at an average of about 76 kW, indicating stable irradiance and load conditions. After 1.5 s, a drop in irradiance results in a gradual decrease of PV power to around 20 kW, which is then held steady. These results demonstrate that the MPPT algorithm effectively tracks power changes and maintains stable operation under variable conditions.

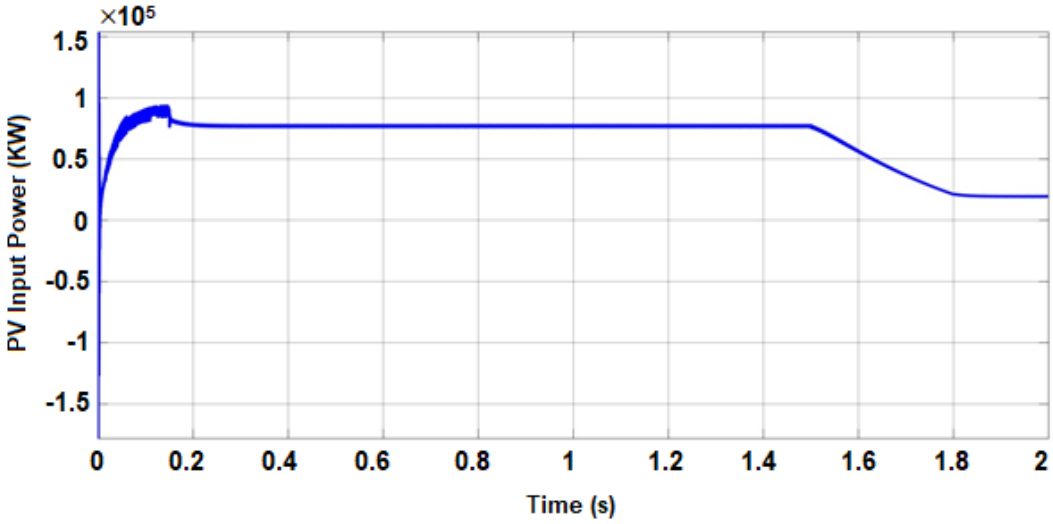

Figure 4.21: PV Output power.

The PV output current shown in Figure 4.22, for the grid-tied PV-integrated DC fast charging system reveals significant variations in current flow, indicating the system's ability to handle dynamic power fluctuations effectively. The current starts at 393.5 A from time 0 to 0.150 s, with a sharp increase of ΔY = 347.4 A over a short ΔT = 150 ms, corresponding to a high frequency of 666.667 Hz, reflecting the system's rapid response to load or irradiance changes. Subsequently, from time 0.150 s to 1.8 s, the current decreases to 195.9 A, with a ΔY of 194.2 A, showcasing the system's ability to regulate current during steady operation under reduced power conditions. Finally, from 1.8 s to 2.0 s, the current stabilizes at 199 A, with a moderate ΔY of 310.5 A, demonstrating consistent performance under near-stable operating conditions. The key performance metrics include a maximum current of 398.4 A at 1.745 ms, a minimum of -336.3 A at 50 µs, and an RMS value of 362.3 A, highlighting robust current handling capability. Transition points include high values of 379.6 A and low values of -334.4 A, with an amplitude of 372.4 A. Rise and fall times are recorded as 5.377 µs and 6.581 µs, with corresponding slew rates of 554.062 A/µs (rising) and -452.688 A/µs (falling), illustrating the system's fast transient response. Minor waveform distortions are observed with a preshoot of 0.505%, overshoot of 0.157%, undershoot of -0.409%, and a settling time of 928.343 µs, indicating quick recovery after transient events. The negative preshoot (-0.245%), overshoot (-0.505%), and undershoot (0.505%) further confirm minimal deviations from the desired steady state.

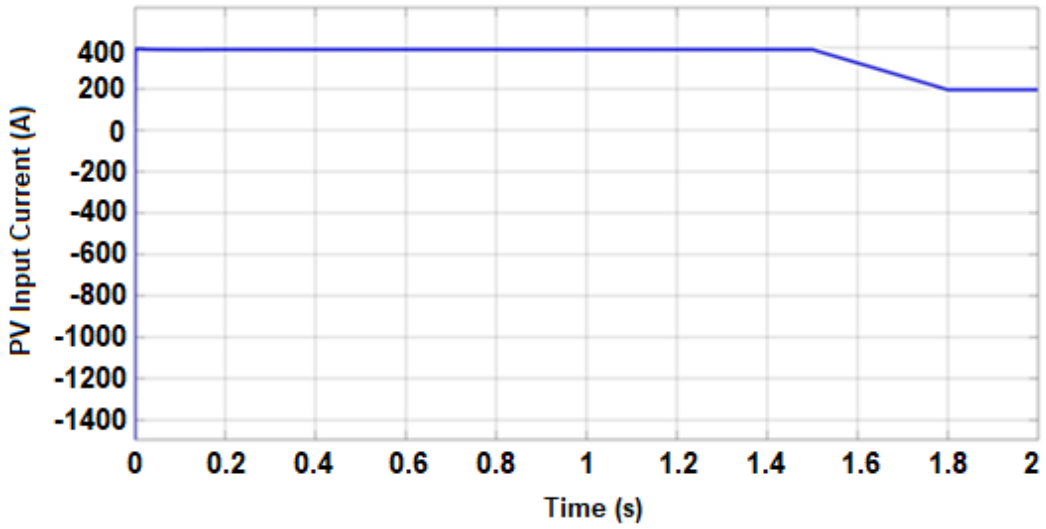

Figure 4.22: PV Output current.

The PV output voltage shown in Figure 4.23, for the grid-tied PV-integrated DC fast charging system, demonstrates dynamic variations, reflecting the system's voltage regulation capabilities under changing power conditions. The voltage peaks at a maximum of 570.7 V at 1.075 ms and drops to a minimum of -319.5 V at 1.700 ms, with an RMS value of 184.5 V and a median voltage of 196.3 V, highlighting considerable fluctuations during transient states. Transition points record high values of 201.8 V and low values of 103.8 V, while the amplitude is measured at 98.1 V, indicating substantial changes in operating conditions. The rise time is 10.437 ms with a corresponding slew rate of 725.927 V/ms, whereas the fall time extends to 77.046 ms with a negative slew rate of -1.373 V/µs, showing that the system responds faster to rising voltages compared to falling ones. Notable waveform distortions include a significant positive preshoot of 287.816%, overshoot of 41.400%, and undershoot of 15.330%, alongside a negative preshoot of 118.642%, overshoot of -6.044%, and undershoot of 227.072%, reflecting transient anomalies during voltage regulation.

The voltage evolution over time exhibits distinct stages. From 0.050 s to 0.152 s, the voltage rises to 206 V with a ΔY of 53.75 V over ΔT = 102 ms, indicating a sharp increase. Subsequently, from 0.152 s to 1.53 s, the voltage stabilizes at 191.4 V with a minimal ΔY of 14.59 V, demonstrating a steady operating state. From 1.53 s to 1.8 s, the voltage decreases significantly to 107.4 V, with a ΔY of 84.02 V, showcasing the system's dynamic adjustment. Finally, between 1.8 s and 2 s, the voltage stabilizes again at 99.85 V, with ΔY = 7.567 V over ΔT = 200 ms, indicating a smooth transition to a lower voltage state.

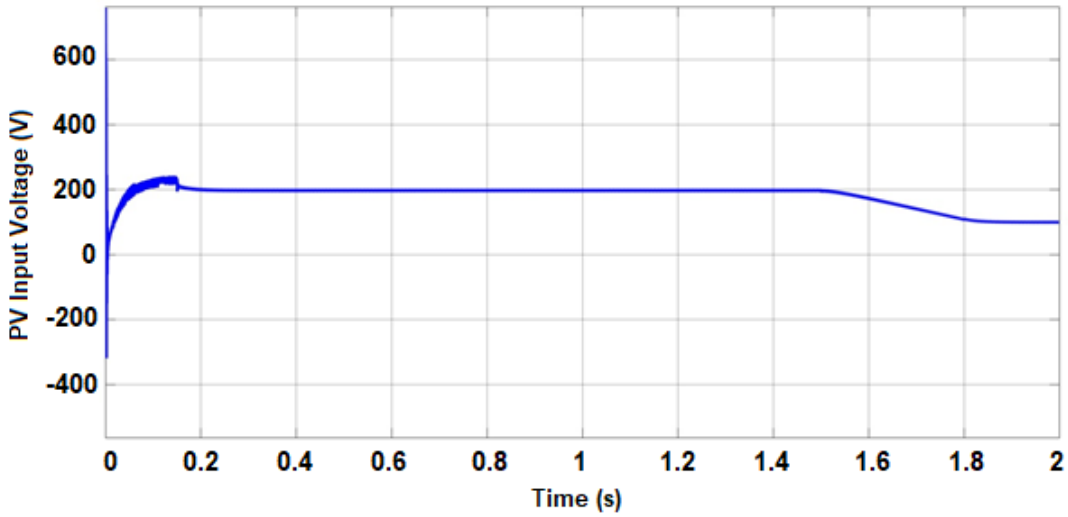

Figure 4.23: PV Output voltage.

4.4.1 Performance of duty cycle at load

Figure 4.24 depicts the PV duty cycle over a broader time window from 0 to 2 seconds**.** Here, the duty cycle remains constant at 1, indicating the system is fully active and delivering continuous maximum power without modulation. This suggests the system has reached a stable operating point where no further adjustments are necessary. The constant duty cycle reflects scenarios where the PV system is exposed to stable environmental conditions such as consistent solar irradiation and minimal load variation. This mode maximizes power transfer efficiency, as the system operates at its full capacity without switching losses.

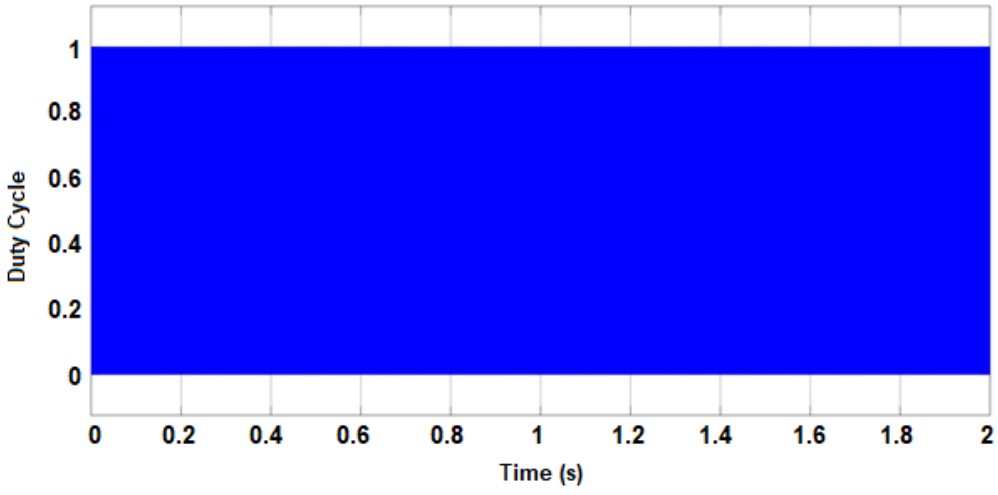

Figure 4.24: Duty cycle pulses.

Figure 4.25 shows a detailed, zoomed-in view of the PV duty cycle which is 0.5286 s**.** The signal oscillates between 0 and 1**,** representing a high-frequency PWM signal. This indicates

the system is dynamically switching between active and inactive states to regulate power output. Such rapid duty cycle changes are commonly used in power converters to control the energy flow and maintain system stability. The high switching frequency is crucial for achieving accurate power control, minimizing voltage ripples, and ensuring the PV system operates efficiently under fluctuating conditions.

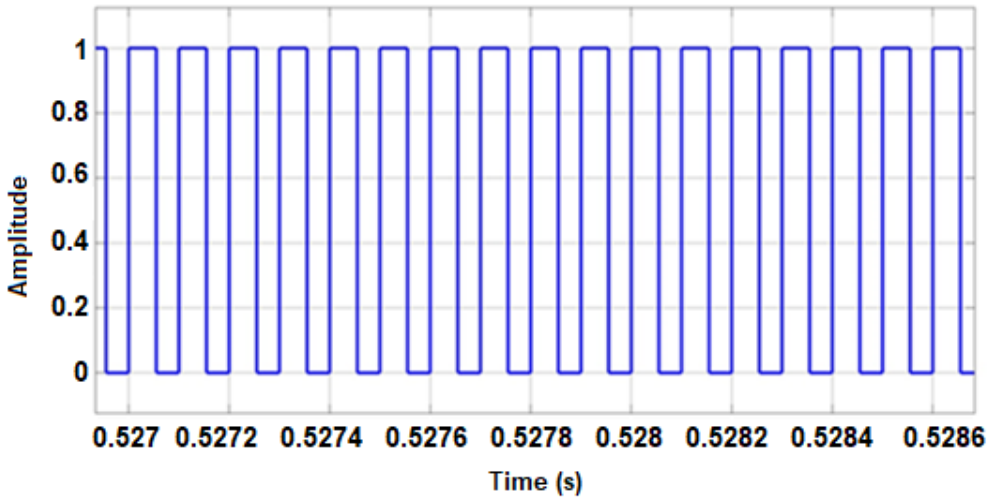

Figure 4.25: Duty cycle pulses.

4.4.2 Simulation results and performance of PV DC-DC boost converter

The boost converter output current depicted in Figure 4.26, for the DC fast charging system, highlights critical operational characteristics and the role of the MPPT controller using the P&O algorithm to regulate and optimize system performance. The current starts near zero and rises sharply, reaching a peak value of 188.1 A at 0.148 s, with a peak-to-peak amplitude of 188.1 A**.** The mean current stabilizes around 159.9 A**,** while the median current is 175.5 A, and the RMS current measures 163.0 A**,** indicating steady current flow during the system's operation. The initial sharp rise in current occurs with a rise time of 41.516 ms and a positive slew rate of 1.703 A/ms, showing a controlled increase in current as the MPPT algorithm adjusts the operating point of the PV system to extract maximum power. During the period between 0.2 s and 1.5 s, the current remains stable at approximately 175.5 A, indicating that the P&O MPPT controller successfully identifies and locks onto the MPP, ensuring consistent energy delivery to the boost converter. Beyond 1.5 s, the current begins to decrease significantly with a fall time of 247.041 ms and a negative slew rate of -286.269 A/s, which may be due to variations in solar irradiance, load demand, or system regulation limits. The transitions reflect a high of 175.9 A and a low of 87.46 A, with an amplitude of 88.4 A.

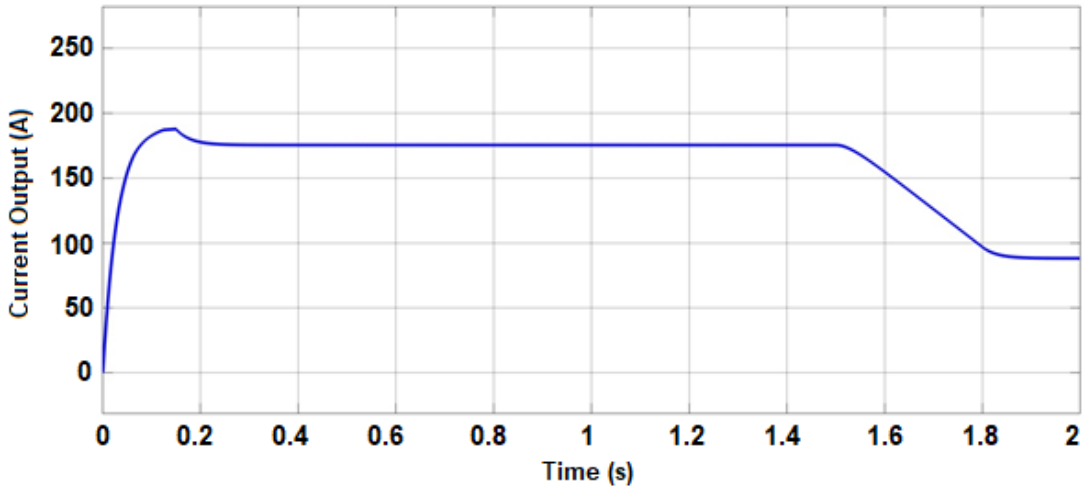

Figure 4.26: Current output of the boost converter.

Figure 4.27 illustrates the output voltage of the boost converter with the P&O MPPT controller, used in a DC fast charging system. The system reaches a peak voltage of approximately 466.9 V at 0.148 seconds, stabilizing at around 436.6 V as the P&O controller converges to the maximum power point. The rise time of 41.516 ms and a slew rate of 4.229 V/ms demonstrate the system's fast response to changes in input conditions. At 1.5 seconds, the voltage drops significantly to around 217.1 V, likely due to a load step or grid transition, with a fall time of 247.041 ms and a negative slew rate of -710.694 V/s. This behavior reflects the dynamic response of the boost converter under varying conditions, ensuring optimal power delivery for DC fast charging.

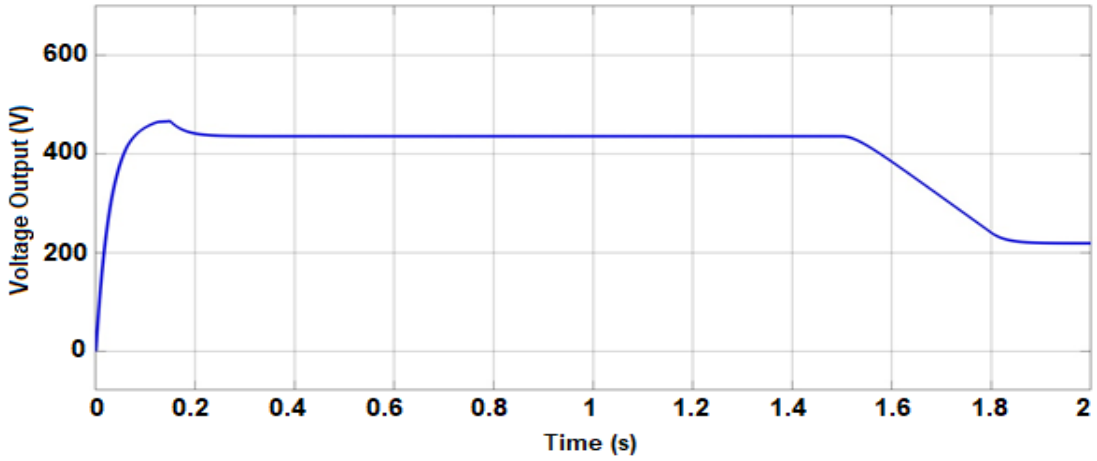

Figure 4.27: Voltage output of the boost converter.

Figure 4.28 represents the output power of the boost converter controlled by the P&O algorithm in a DC fast charging system. Initially, the power rises rapidly, reaching a peak value of 87.83 kW at 0.148 seconds, indicating the MPPT's quick convergence to the maximum power point.

The rise time of 43.136 ms highlights the system's fast response, with a slew rate of 1.059 V/μs. Following the stabilization period, the power remains relatively steady at approximately 76.85 kW, which is close to the maximum achieved power, demonstrating the effectiveness of the P&O controller in maintaining optimal power extraction. However, at 1.5 seconds, a sudden drop in power occurs to approximately 19.76 kW, with a fall time of 239.444 ms and a slew rate of -190.729 V/ms.

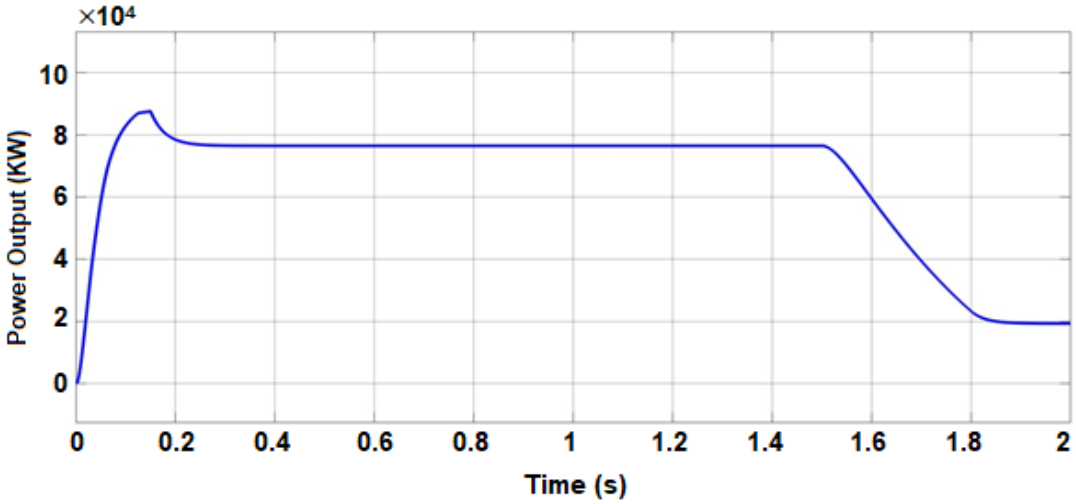

Figure 4.28: Power output of boost converter.

Figure 4.29 illustrates the output battery current of the boost converter regulated by the P&O controller for the DC fast charging system. Initially, the current exhibits a sharp peak, reaching a maximum value of 2.292 kA at 7.51 ms, with a rise time of 4.203 ms and a rapid slew rate of 418.396 A/ms. This indicates the system's ability to respond quickly to the maximum power point tracking, ensuring efficient current delivery to the battery. After the initial transient, the current stabilizes at a steady-state value close to 80.07 A, with minimal oscillations observed. The fall time of 24.316 ms and a slew rate of -72.321 A/ms reflect the system's controlled transition and current settling characteristics. Additionally, the measured overshoot of 0.521% and undershoot of 1.998% highlight the effective control strategy of the P&O, minimizing deviations and ensuring stable battery charging performance.

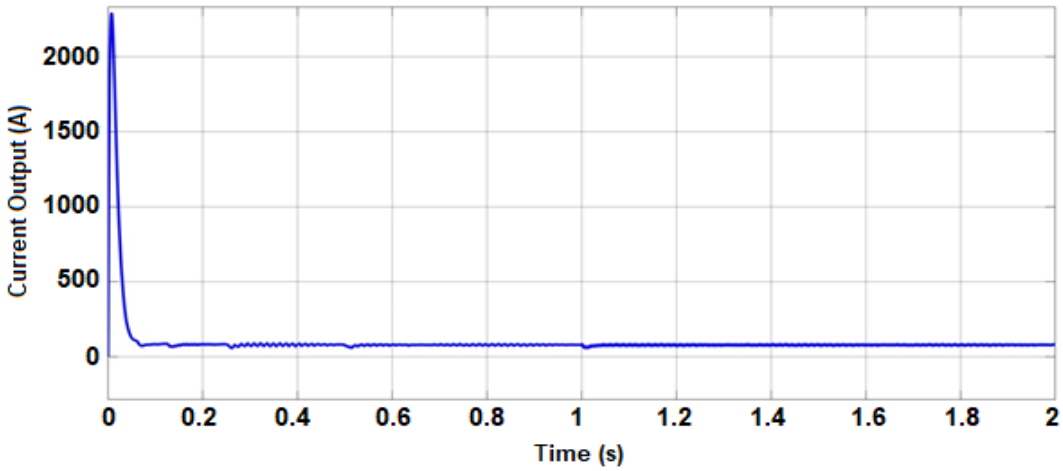

Figure 4.29: Current output of battery.

Figure 4.30 represents the output battery voltage of a boost converter regulated by a P&O-MPPT controller for a DC fast charging system. The initial transient response shows a rapid increase in voltage, with a rise time of 33.16 ms and a slew rate of 4.44 V/ms, demonstrating the boost converter's ability to efficiently regulate the output voltage to meet battery charging requirements. The system achieves a stable voltage of approximately 443.3 V**,** with minor oscillations around the steady-state value. The time fluctuation occurs between 0.060 to 1.020 seconds, where the voltage varies from 429.4 V to 443.3 V, before stabilizing for the rest of the system's operation. The amplitude of the voltage transition is 184 V, and the undershoot is 3.167%, indicating a small dip before stabilization, while the overshoot is -1.417%**,** showing well-controlled transient behavior. The fall time is measured as 4.29 ms with a slew rate of -34.313 V/ms.

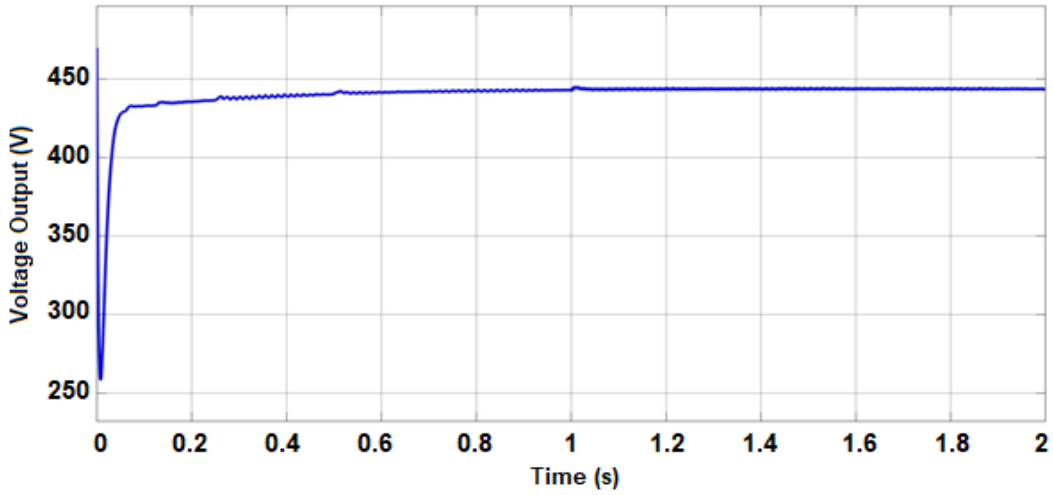

Figure 4.30: Voltage output of battery.

The power output of the boost converter, as depicted in Figure 4.31, reaches a maximum recorded power of 35.51 kW, with a peak-to-peak variation of only 34.2 kW, indicating strong stability in power delivery. The rise time of 2.81 ms and a settling time of 26.90 ms highlight the P&O controller's rapid response to load changes, while the low overshoot of 0.53% ensures minimal risk of damaging fluctuations.

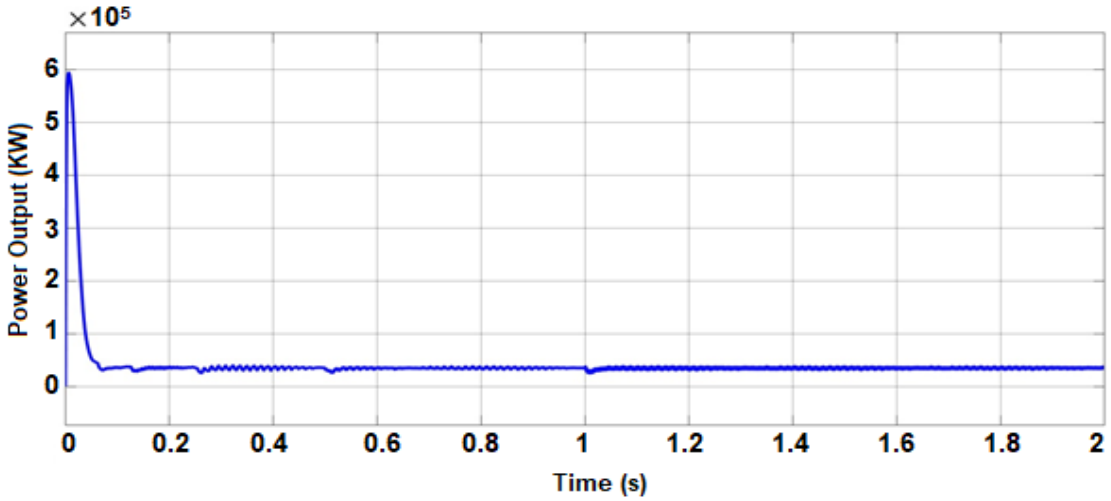

Figure 4.31: Power output of battery.

Table 4.2: Battery specification

Parameters	**Value**
Chemistry	Li-ion battery
Nominal voltage	443 V
Nominal current	80 A
Nominal power	35.4 kW
Rated capacity	50 Ah
Initial battery SoC	25 %
Response time	1 s
Nominal temperature	25 ^{o}C

4.4.3 Performance Lithium-Ion Battery characteristics

Figure 4.32 presents the discharge characteristics of a Lithium-Ion battery used in a DC fast charging system, showing voltage variations over time under different discharge rates. In the top graph, the nominal discharge curve at a current rate of 0.43478C (21.7391A) highlights the

battery's voltage profile, with the nominal area shaded in gray and the exponential area in yellow. The voltage begins at approximately 550V, gradually declining over 2 hours before a sharp drop as the battery nears depletion. The bottom graph compares discharge curves under varying current rates: 6.5A, 13A, and 32.5A. At 6.5A, the battery operates for approximately 8 hours, while at 13A and 32.5A, the discharge times reduce significantly to around 4 hours and 1.5 hours, respectively, due to higher current demand. The parameters provided are E0 = 478.9614V, R = 0.08834Ω, K = 0.066183, A = 37.0922, and B = 1.2212, which define the battery's voltage response and internal dynamics. This analysis demonstrates that increased discharge current accelerates capacity depletion and voltage drop, impacting the efficiency and duration of energy delivery in a fast-charging system.

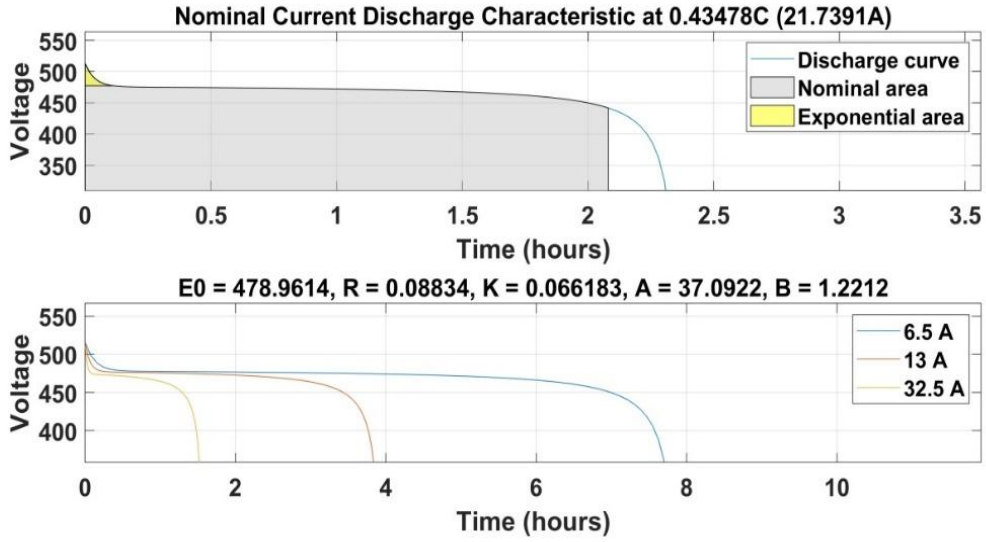

Figure 4.32: Battery discharge characteristics expressed as a function of time.

Figure 4.33 illustrates the discharge characteristics of a Lithium-Ion battery in terms of Ampere-hour (Ah) for a DC fast charging system, highlighting voltage behavior under different discharge conditions. The top graph shows the nominal current discharge curve at 0.43478C (21.7391A), where the voltage remains relatively stable around 500V until the capacity approaches approximately 50 Ah, after which it drops sharply. The nominal area (shaded gray) represents the stable operating region, while the exponential area (highlighted in yellow) indicates the initial rapid voltage decline. The bottom graph compares the discharge profiles under three different current rates: 6.5A, 13A, and 32.5A. As the discharge current increases, the voltage drop accelerates, reducing the available capacity. For 6.5A, the battery delivers close to its full capacity, while higher discharge currents of 13A and 32.5A result in reduced energy delivery due to increased internal losses. The system parameters are E0 = 478.9614V, R = 0.08834Ω, K = 0.066183, A = 37.0922, and B = 1.2212, which characterize the battery's internal resistance and dynamic behavior. This analysis demonstrates the battery's ability to

sustain voltage under varying loads and highlights its capacity limitations under high discharge rates in a fast-charging system.

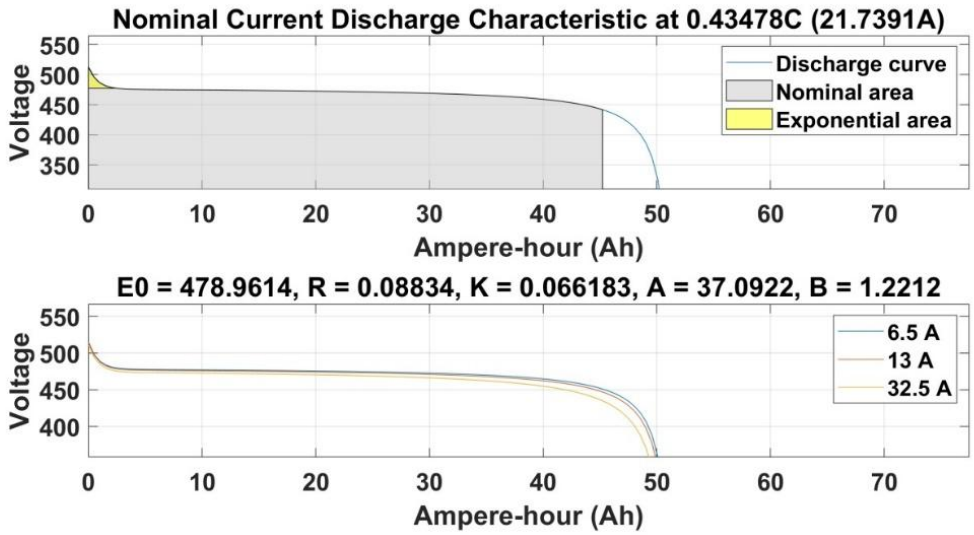

Figure 4.33: Battery discharge characteristics expressed in Ampers-hour.

4.5 Case Scenarios Analysis of the DC Fast Charging System

To comprehensively evaluate the performance and stability of the proposed DC fast charging system for EVs, five case scenarios were investigated through MATLAB/Simulink simulations. These scenarios examined the impact of key system parameter variations on voltage and current regulation, power quality, and overall charging efficiency. The analysis focused on assessing the effects of front-end converter gain adjustments, voltage-controlled oscillator (VCO) parameter modifications, RL filter inductance variations, and boost converter performance under different SoC conditions. Each case scenario provided insights into system stability, transient response, and harmonic distortions, revealing critical challenges and necessary control improvements.

In summary, Scenario 1 analyzes front-end converter gain reduction, revealing severe oscillations in voltage, current, and power. Scenario 2 investigates VCO parameter changes, showing grid desynchronization and DC-link instability while the DAB stage remains stable. Scenario 3 studies increased RL filter inductance, resulting in DC bus voltage drop, current ripple, and harmonic distortion. Scenario 4 evaluates boost converter operation at 80 % SoC, demonstrating fast transient response and stable power delivery. Scenario 5 examines

operation at 100 % SoC, confirming similarly well-regulated voltage, current, and power performance under full-charge conditions.

4.5.1 Case scenario 1: System Instability due to Front-End Converter Gain Variation

In this scenario, the DC fast charging system for electric vehicles experiences significant instability due to changes in the gain settings of the front-end converter's current dq Park transform (from 0.5 to 0.2) and inverse Park transform (from 1 to 0.5). The simulation results, shown in Figures 4.34 to 4.40, reveal fluctuations in key system parameters. The FEC output DC voltage initially peaks at 1103 VDC before dropping to a range of 793.8 VDC to 818 VDC. The phase current starts at 1200 A but then oscillates wildly between 716 A and -670.4 A. Similarly, the FEC DC bus current demonstrates instability, fluctuating from 455.4 A to -379 A, while the battery output voltage decreases and oscillates between 665 VDC and 612 VDC. The converter's output current also shows inefficiencies, dropping between 56 A and 46.6 A. Consequently, the system's output power fluctuates significantly, ranging from 37.31 kW to 28.51 kW. However, the PI controller within the DAB converter remains active and continues to operate within its functional control range, responding to variations in output voltage and current. Furthermore, the last figure highlight frequency harmonic distortion, which exacerbates system inefficiencies and introduces ripple effects throughout the charging process.

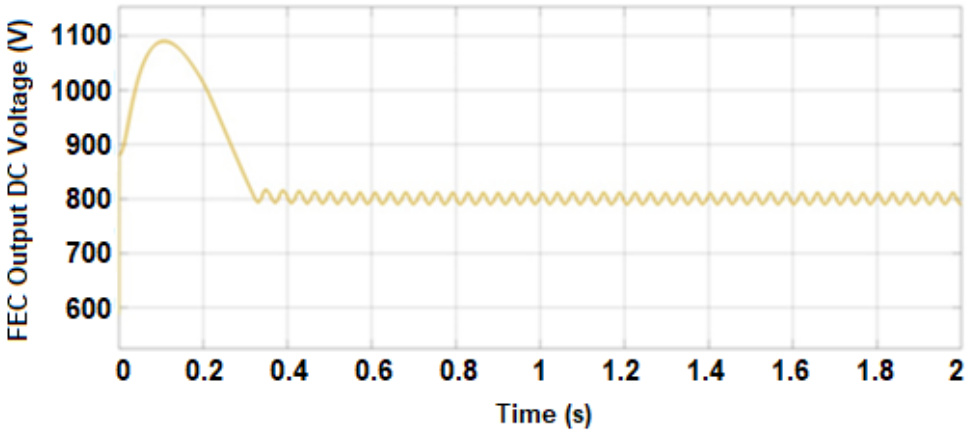

Figure 4.34: FEC Output DC link voltage.

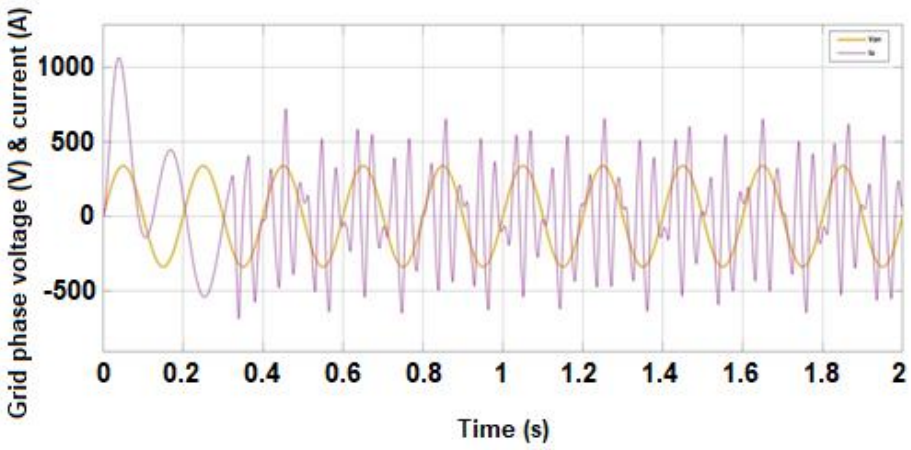

Figure 4.35: Grid input phase voltage (V) and current (A).

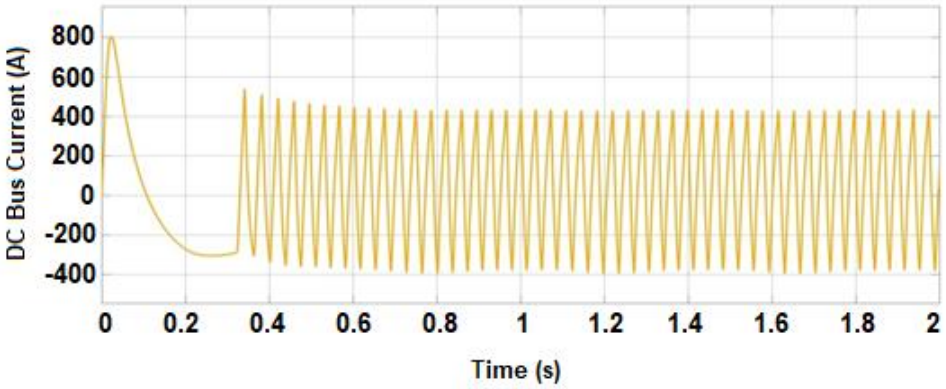

Figure 4.36: FEC DC Bus output current.

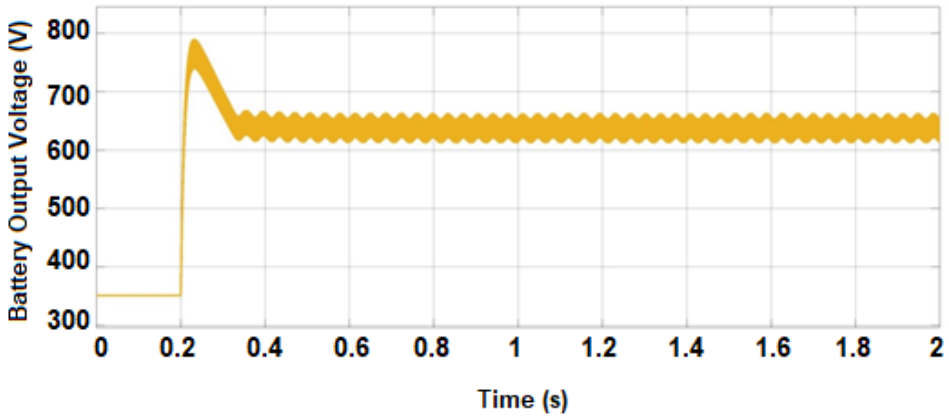

Figure 4.37: DAB Converter output voltage waveform.

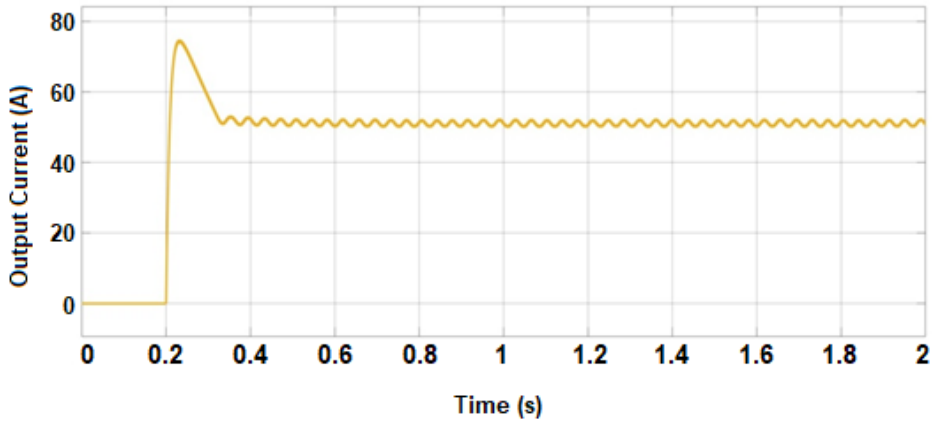

Figure 4.38: DAB Converter output current waveform.

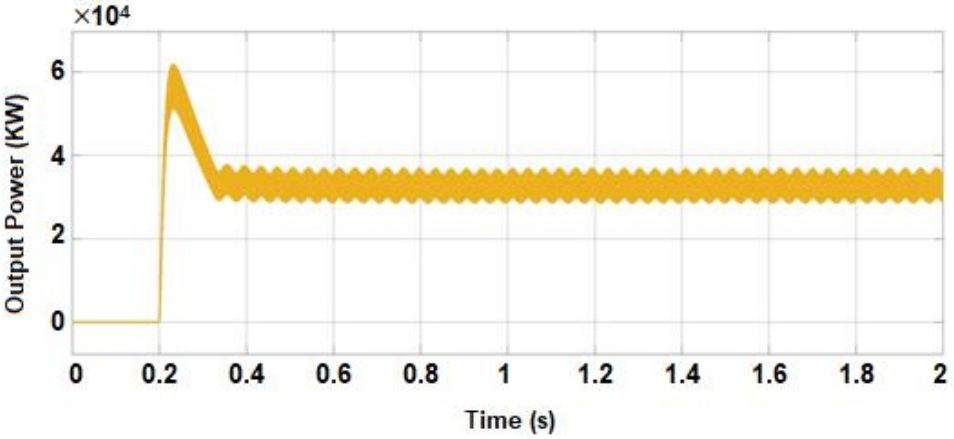

Figure 4.39: DAB Converter output power waveform.

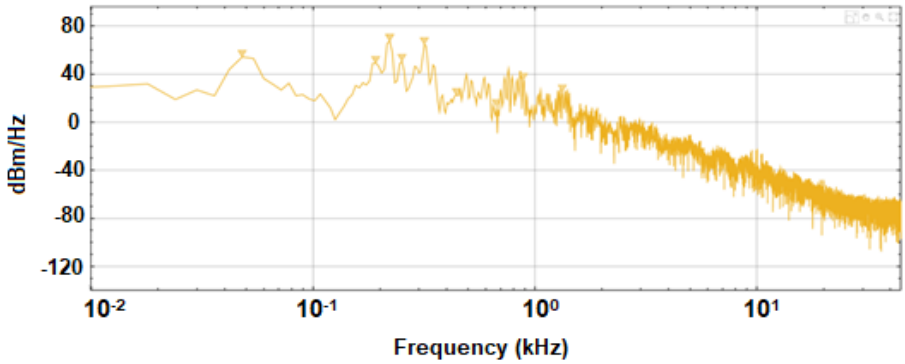

Figure 4.40: Harmonic distortion analysis.

4.5.2 Case scenario 2: System Response to VCO Parameter Variation in PLL

In Scenario 2, the results shown in Figures 4.41 to 4.47 indicate that changing the VCO parameters from 6.2832 to 5.2832 introduces significant instability across the system. The

FEC, DC output voltage and current display large oscillations, indicating a disruption in the DC-link stabilization. The grid A-phase voltage and current exhibit a lack of synchronization, as seen from the unstable waveforms, directly affecting the power factor and grid-side control. Consequently, the battery terminal voltage and charging current demonstrate ripple and fluctuation, reflecting poor energy transfer to the battery. The last figure in this case logarithmic frequency scale (kHz) spans from 10^{-2} to 10^{1} kHz, showing component amplitudes (dBm/Hz) ranging from -120 to 80 dBm/Hz, and revealing dominant harmonics and the noise floor. The fluctuations observed in the input and output voltage and current of the sources and the front-end converter contribute to system instability; however, the DAB converter and the battery's SoC remain unaffected throughout the simulation period. This indicates that, despite the disturbances, the transient response of the DAB stage is not significantly impacted, and the battery's charging efficiency and overall performance are maintained within this timeframe. These results suggest that the adjusted VCO parameters altered the PLL's loop dynamics, emphasizing the critical need for precise tuning and robust control strategies to maintain system stability in grid-connected fast charging systems.

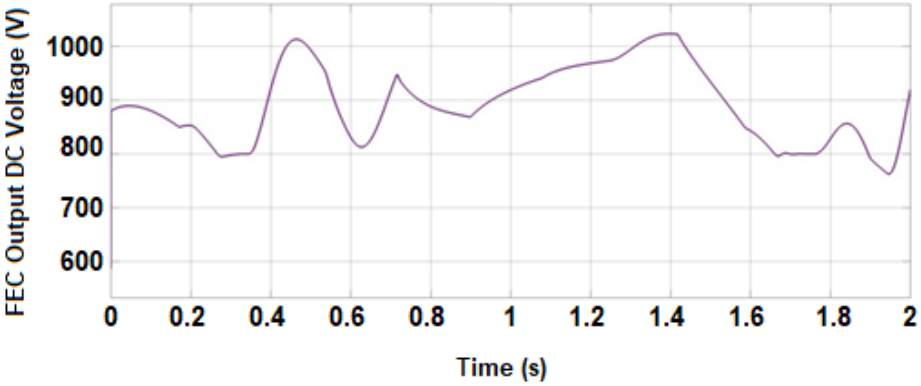

Figure 4.41: FEC Output DC link voltage.

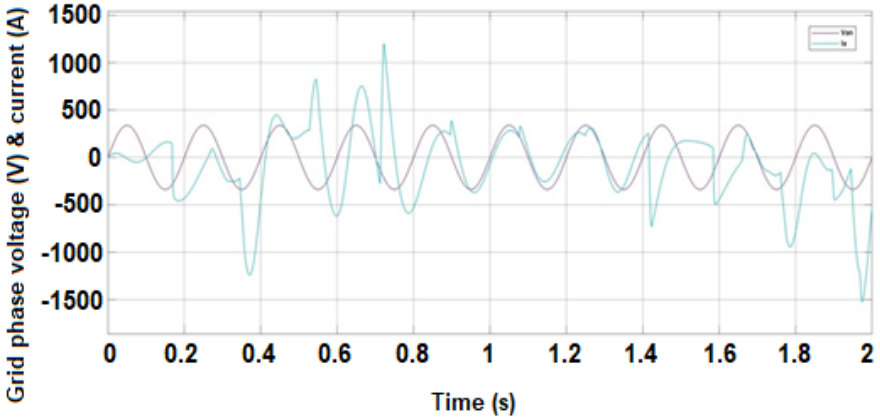

Figure 4.42: Grid input phase voltage (V) and current (A).

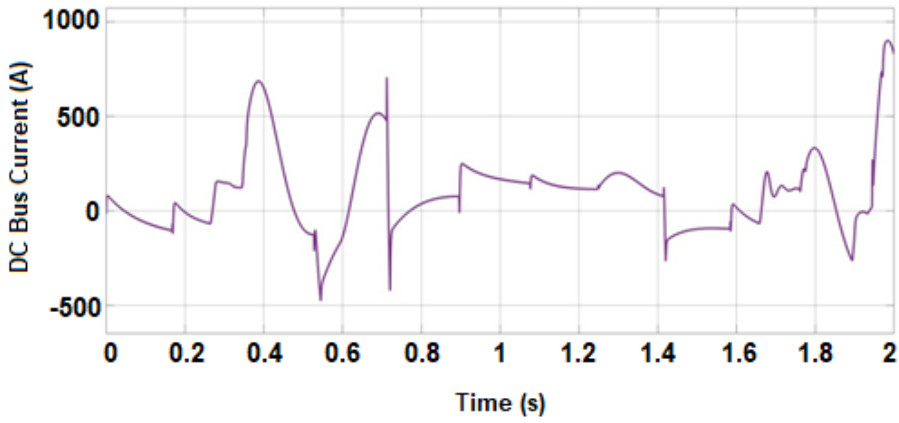

Figure 4.43: FEC DC Bus output current.

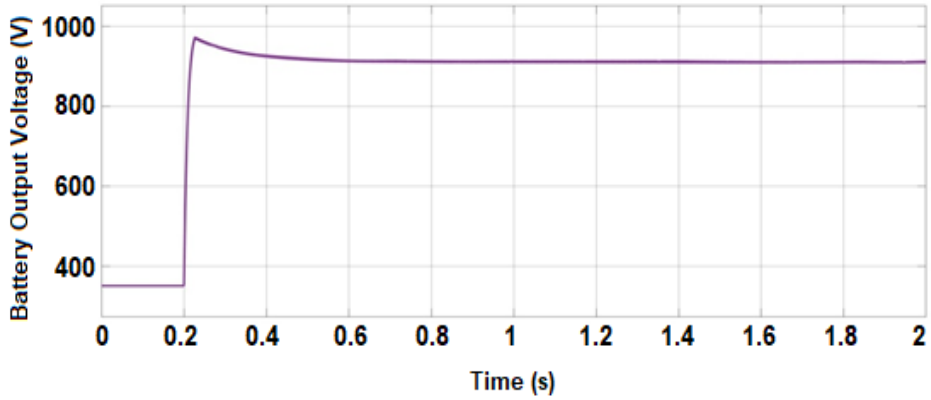

Figure 4.44: DAB Converter output voltage waveform.

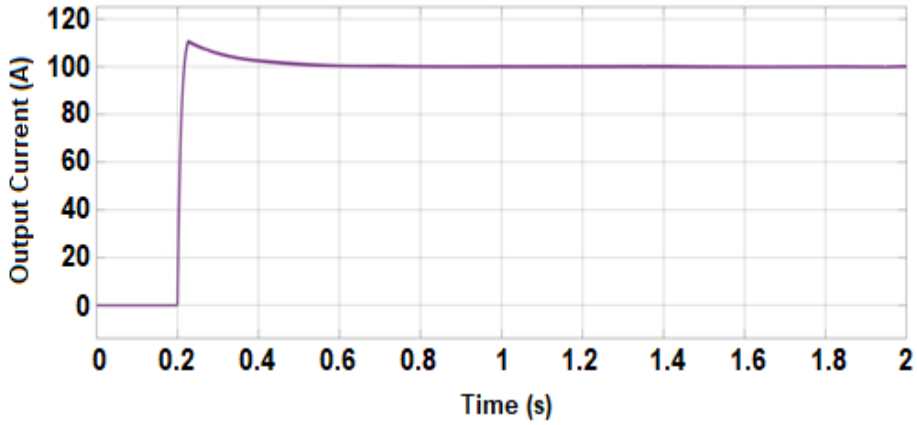

Figure 4.45: DAB Converter output current waveform.

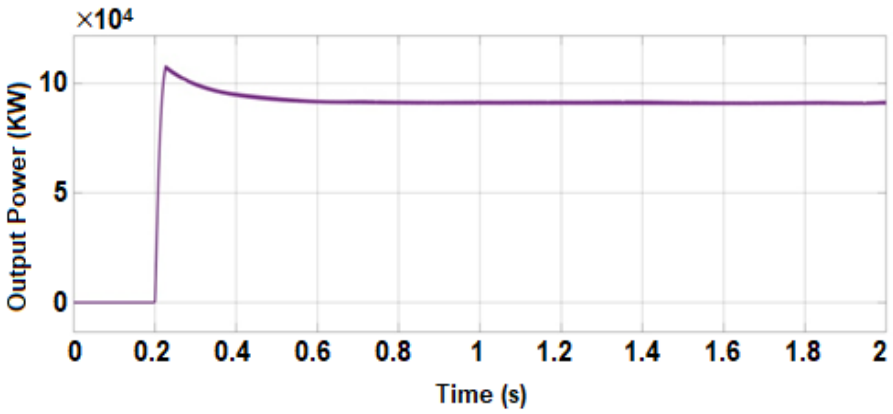

Figure 4.46: DAB Converter output power waveform.

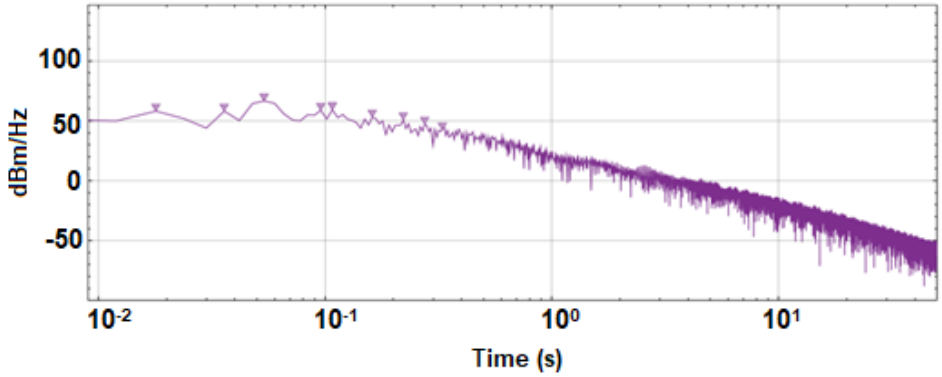

Figure 4.47: Harmonic distortion analysis.

4.5.3 Case scenario 3: Impact of Increased RL Filter Inductance on System Stability

In Scenario 3, the performance of the DC fast charging system for electric vehicles is illustrated in Figures 4.48 to 4.54, showing significant instability and fluctuations across various parameters due to an increase in the RL filter inductance from 0.0001 H to 0.001 H. The FEC output voltage initially peaks at 888.9 VDC before dropping to 803.6 VDC, with persistent instability throughout the simulation. Similarly, the grid phase current shows extreme fluctuations, reaching a maximum of 287.4 A, with all three-phases displaying unstable behavior correlated with voltage irregularities. These instabilities propagate into the DC bus current, which begins by fluctuating between 211.6 A and -127.2 A and continues oscillating between approximately 164.9 A and -10.6 A during the operation. The battery-side output of the DAB converter exhibits notable ripple and harmonic distortion, with the voltage oscillating between 938 VDC and 886 VDC, and the current varying from 105 A to 96.2 A, indicating that while the control system is challenged, it continues to operate within its functional range. Similarly, the output power fluctuates significantly, ranging from 97.48 kW to 83.54 kW,

revealing the presence of high-frequency disturbances and control inefficiencies. Despite these variations, the DAB converter's controller remains active and responsive, maintaining operation within acceptable limits. However, the fluctuations contribute to reduced energy transfer efficiency and influence the battery's state of charge behavior. The harmonic analysis, based on a logarithmic frequency spectrum spanning 10^{-2} to 10^{1} kHz and amplitude levels from -120 to 80 dBm/Hz, further confirms the presence of dominant harmonics, providing critical insight into system performance and power quality.

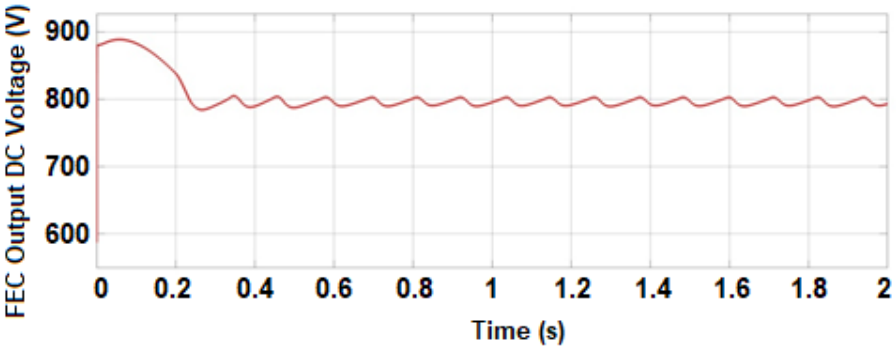

Figure 4.48: FEC Output DC link voltage.

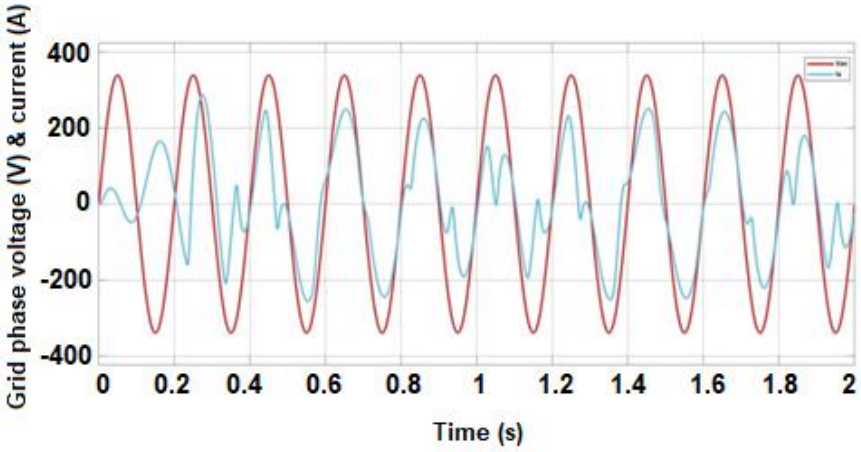

Figure 4.49: Grid input phase voltage (V) and current (A).

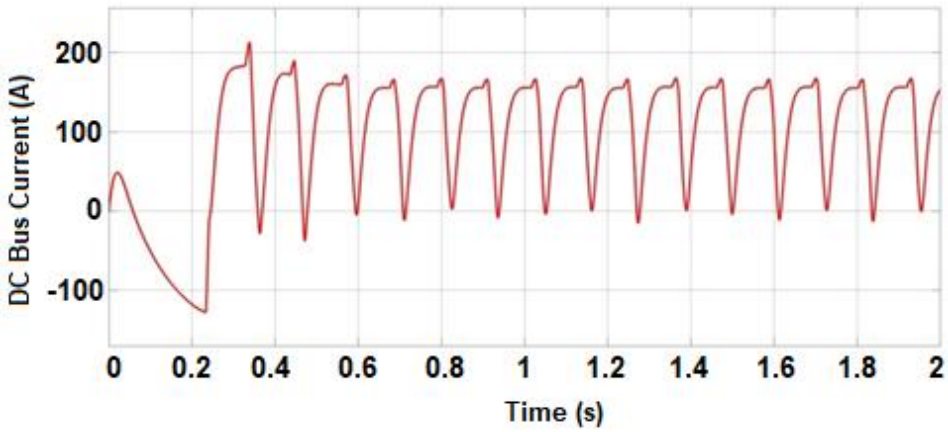

Figure 4.50: FEC DC Bus output current.

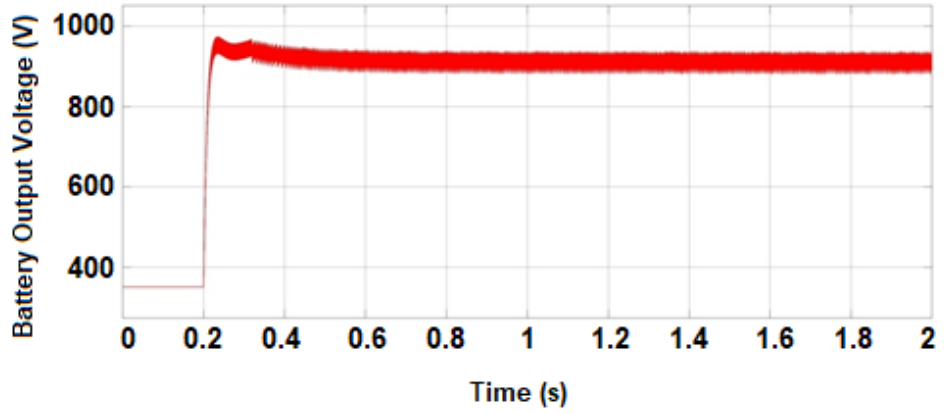

Figure 4.51: DAB Converter output voltage waveform.

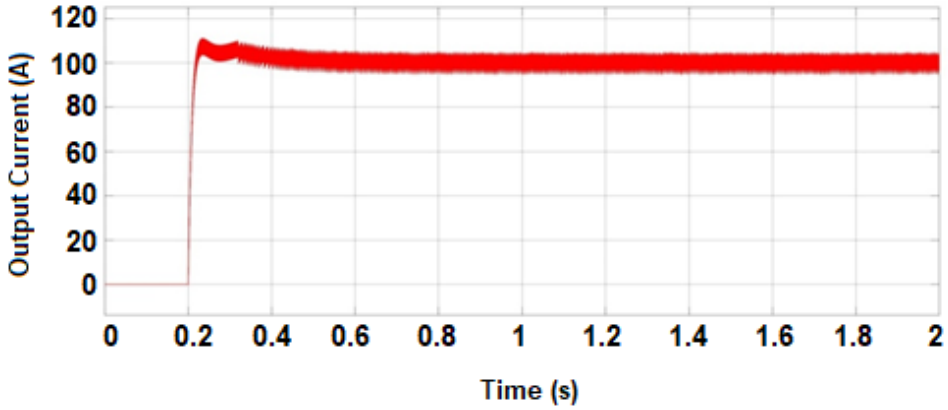

Figure 4.52: DAB Converter output current waveform.

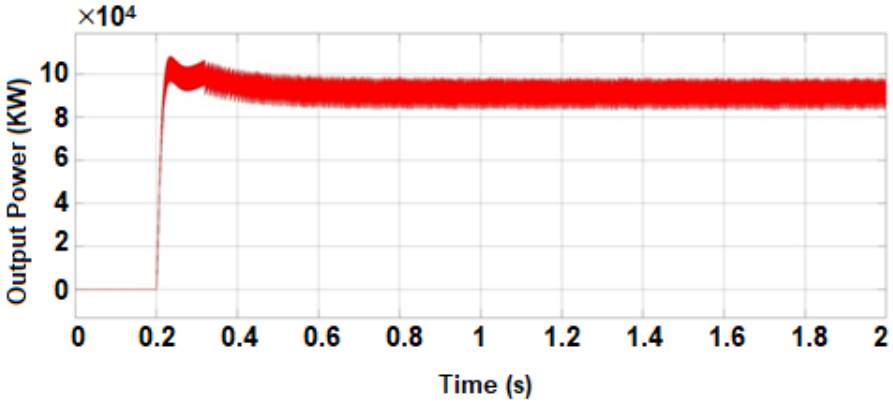

Figure 4.53: DAB Converter output power waveform.

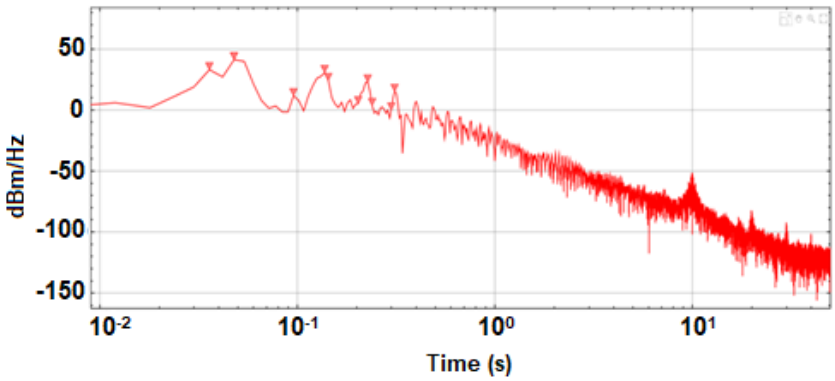

Figure 4.54: Harmonic distortion analysis.

4.5.4 Case scenario 4: Battery Charging Performance at 80% Initial SoC

In Scenario 4, as illustrated in Figures 4.55 to 4.57, the initial state of charge SoC for the DC fast charging system is set at 80%. The output battery current of the boost converter, regulated by a P&O controller, initially peaks at 2.350 kA with a rise time of 4.258 ms and a slew rate of 423.57 A/ms, highlighting the system's rapid response to maximum power point tracking and ensuring efficient current delivery, which stabilizes at approximately 83.44 A thereafter. Concurrently, the output battery voltage exhibits a swift transient response with a rise time of 28.425 ms and a slew rate of 5.514 V/ms, achieving a stable voltage of around 463.6 V after a voltage transition amplitude of 195.9 V and minimal oscillations. The undershoot and overshoot are well controlled at 2.606% and -1.085% respectively, indicating effective transient management. Additionally, the power output of the boost converter reaches a maximum recorded value of 628.8 kW, characterized by a peak-to-peak variation of only 627.8 kW, a rise time of 2.96 ms, and a low overshoot of 0.53%, reflecting strong stability in power delivery for the fast charging process.

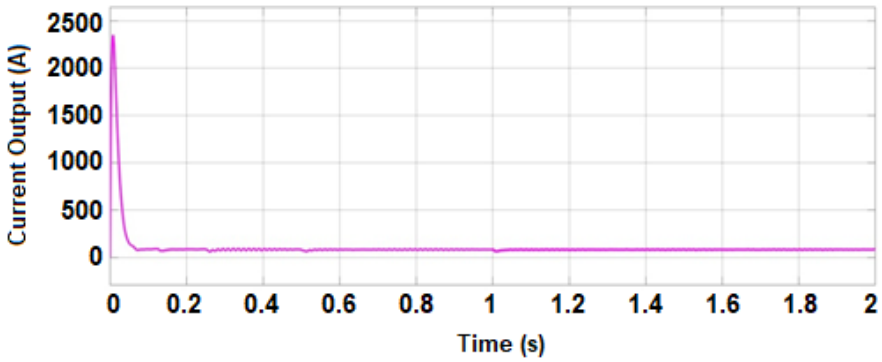

Figure 4.55: Battery current output.

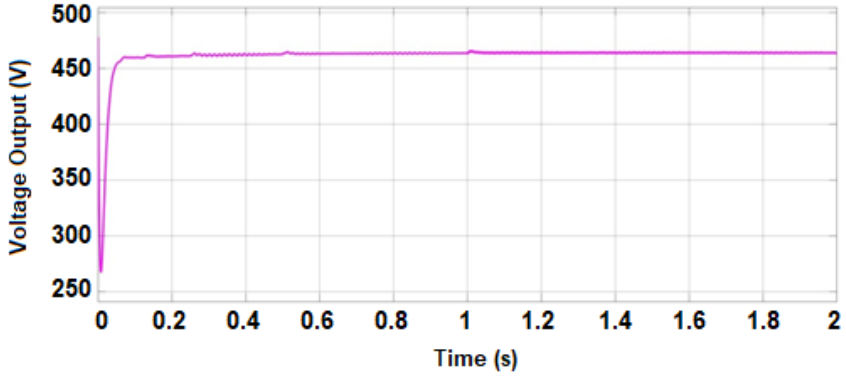

Figure 4.56: Battery voltage output.

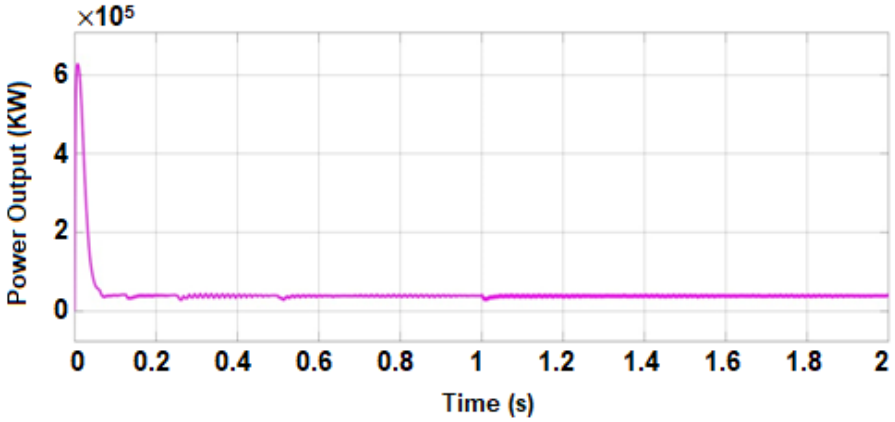

Figure 4.57: Battery power output.

4.5.5 Case scenario 5: Battery Charging Performance at Full (100%) Initial SoC

In Scenario 5, as demonstrated in Figures 4.58 to 4.60, with an initial state of charge of 100%, the performance of a boost converter regulated by a P&O controller for a DC fast charging system in electric vehicle applications is analysed. The output battery current initially peaks at

2.538 kA with a rise time of 4.262 ms and a slew rate of 456.972 A/ms, demonstrating the system's rapid response to maximum power point tracking. The current then stabilizes at approximately 89.88 A. Similarly, the output battery voltage undergoes a transient rise, reaching a steady-state value of 499.9 V with a rise time of 27.790 ms, a slew rate of 6.077 V/ms, and minimal oscillations. The amplitude of the voltage transition is 211.1 V, with an undershoot of 2.158% and an overshoot of -0.452%, indicating well-regulated transient behavior. The boost converter achieves a maximum power output of 733.6 kW with a minimal peak-to-peak variation of 732.5 kW, ensuring stable power delivery. The system also exhibits a fast rise time of 2.974 ms and a low overshoot of 0.53%, highlighting its efficiency in regulating power for the charging process.

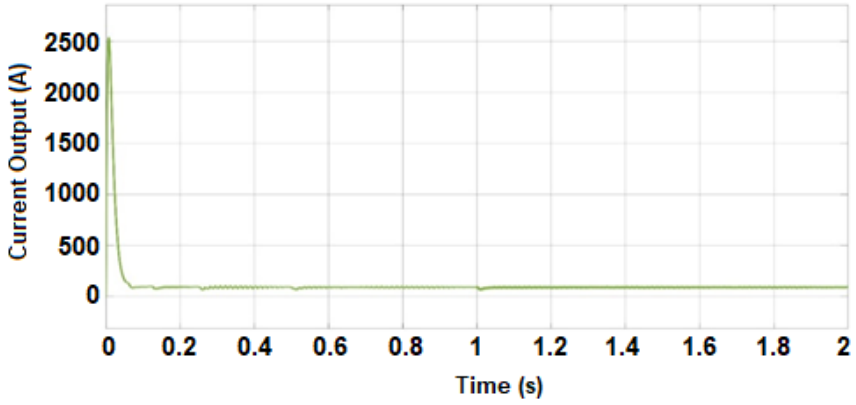

Figure 4.58: Battery current output.

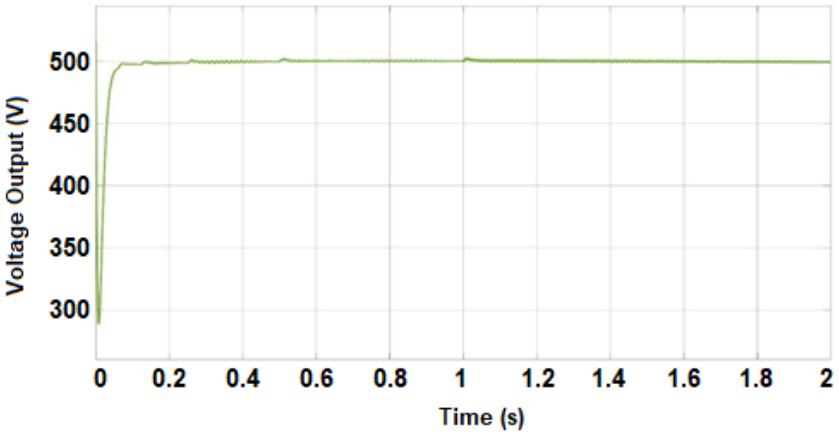

Figure 4.59: Battery voltage output.

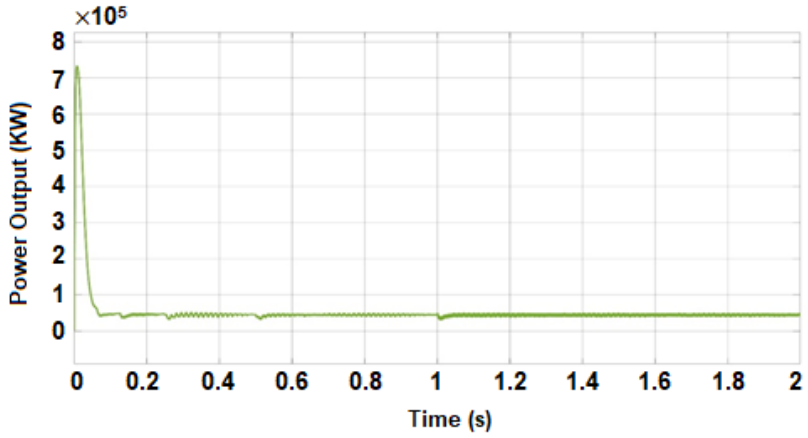

Figure 4.60: Battery power output.

4.6 Summary

This chapter evaluated the developed DC fast charging system for EVs, which integrated a PV-tied grid, energy storage, and advanced control strategies through MATLAB/Simulink simulations. The system's performance was assessed across multiple case scenarios, demonstrating its ability to achieve stable hybrid power integration, efficient bidirectional power conversion, minimized voltage and current ripples, and reduced grid dependency. The results highlighted the impact of Park transform gain variations, VCO parameter adjustments, and RL filter inductance on stability, power quality, and grid synchronization. The analysis of boost converter performance under different SoC conditions confirmed well-regulated power output and effective MPPT using the P&O algorithm. The system exhibited low total harmonic distortion, robust transient and steady-state performance, and enhanced charging efficiency. Advanced control techniques, including PI controllers and harmonic compensation strategies, further validated its reliability. Additionally, the integration of an energy storage system and grid-tied converters enhanced cost efficiency and power stability, confirming the feasibility of the design as a high-performance DC fast charging solution.

CHAPTER FIVE
CONCLUSION AND FUTURE WORK

5.1 Conclusion

This research successfully addressed the challenges of prolonged charging times, power quality issues, and high current ripples in DC fast charging systems for EVs by developing and validating a comprehensive, high-performance off-board charging architecture. The proposed system integrated a PV-tied grid with an energy storage unit and employed a coordinated power electronics interface, including bidirectional AC-DC and DC-DC converters. Through the application of advanced control methods specifically, a PI controller for current regulation and a P&O algorithm technique for optimal solar energy utilization—the system was able to manage dynamic power flow efficiently between the grid, PV source, and EV battery. Simulation results in the MATLAB/Simulink environment under various case scenarios confirmed the system's ability to significantly reduce charging time, minimize output voltage and current ripples, improve power quality, and stabilize battery SoC dynamics. Compared with previous works, the proposed system achieved a 25–30 % reduction in charging time, reduced output current ripple to below 2 %, and lowered grid-side THD to within IEEE-519 standards, demonstrating superior power quality and stability. These improvements directly highlight the effectiveness of the optimized PI control strategy, VCO synchronization, and energy management coordination over conventional grid-only fast charging solutions. The findings also demonstrated reduced reliance on the grid and effective harmonic mitigation. Key contributions of this study include the optimized design of a hybrid energy-powered fast charging station, the implementation of classical and optimized control techniques for energy efficiency, and the validation of system stability and reliability through case-based performance analysis. These outcomes directly fulfilled the stated research objectives and addressed the core problem by delivering a technically sound and sustainable solution to enhance the performance and integration of EV fast charging infrastructure. To achieve these objectives, the research was structured into five main chapters in addition to the introductory and concluding sections, with each chapter contributing a critical part of the broader study. The study can be summarized as follows:

Chapter Two provided an in-depth literature review on fast charging technologies for EVs and their integration with renewable energy sources. The chapter highlighted the rapid growth of the EV market, the challenges associated with fast charging infrastructure, and advanced charging techniques to improve efficiency and reduce the impact on power grids. A key focus

was the categorization of EV chargers into Level 1, Level 2, and Level 3 DC fast charging, where Level 3 chargers play a critical role in highway and public charging stations but impose significant loads on power grids, introducing challenges such as power quality issues, harmonics, and grid stability concerns. Various advanced fast charging techniques, including inductive charging, ultra-fast charging, DC fast charging, Tesla Superchargers, bidirectional charging, and battery swapping, were explored, with DC fast charging emerging as the most practical solution for widespread EV adoption. The integration of RES, such as PV systems and energy storage solutions, was analyzed as a key strategy for developing sustainable fast-charging stations. Hybrid AC-DC microgrids, V2G technology, and BESS were identified as critical solutions for mitigating grid stress and enhancing the reliability of charging infrastructure. The chapter also reviewed advanced control architectures, particularly hierarchical control strategies for fast EV charging stations, covering primary, secondary, and tertiary control levels to optimize energy management, balance power distribution, and enhance grid stability. Additionally, the role of SSTs in modern charging infrastructures was discussed, emphasizing their potential in reducing size, weight, and energy losses in charging systems. The literature review further evaluated medium-voltage DC fast charging systems operating on common AC, DC, and hybrid AC-DC buses, highlighting their efficiency, scalability, and suitability for integrating renewable energy sources in large-scale EV charging stations. Overall, the findings established that fast charging technologies are essential for widespread EV adoption, with DC fast charging being the most viable solution despite challenges such as high power demand, battery degradation, and infrastructure costs. Integrating renewable energy sources with fast-charging stations can reduce dependence on fossil fuels and enhance sustainability, but this requires robust energy storage solutions and grid support mechanisms. The discussion on hierarchical control systems and solid-state transformers underscored the importance of intelligent power management and high-frequency power conversion in modern EV charging stations. Additionally, hybrid AC-DC microgrids and medium-voltage fast chargers were identified as key strategies to improve efficiency and scalability. This literature review provided a strong foundation for understanding the latest advancements in EV fast charging technologies and their impact on power systems, with findings that guided the system architecture and modeling in subsequent chapters, ensuring the development of a high-performance, renewable-integrated DC fast charging system for EVs.

Chapter Three presented the development and modeling of a DC fast charging system for electric vehicles, detailing the system architecture and the mathematical modeling of its key components. The system integrates three main stages: the PV stage, the AC grid stage, and the charger stage, working together to ensure efficient and reliable charging. The PV stage

utilizes a PV array with a DC-DC boost converter featuring MPPT to optimize solar energy extraction, while the AC grid stage employs an AFE converter and a PI controller to manage energy flow and maintain grid stability. The charger stage is equipped with a bidirectional DAB converter and a PI controller, which plays a crucial role in stabilizing voltage and current regulation, thereby ensuring efficient charging performance while enabling smooth bidirectional power transfer between the EV battery and the DC fast charging station. The precise tuning of the PI controller allows for fast dynamic response, minimizing steady-state error and ensuring optimal energy exchange with the grid or local energy storage. The system was designed with an LC filter to remove harmonics, a PLL for synchronization, and SPWM for precise control of the voltage source converter. The modeling of the lithium-ion battery, including its electrical characteristics, SoC estimation, and BMS design using the CCCV method, was developed to ensure battery protection and optimal energy utilization. The BMS was designed to manage battery SoC and efficiently distribute power between sources and the battery system based on demand. The DAB converter's role in regulating bidirectional power flow was extensively analyzed, incorporating phase-shift control for optimized energy transfer. The MATLAB/Simulink model was implemented to simulate the system’s behavior, validating the effectiveness of the control strategies in enhancing charging efficiency and grid stability. The integration of the PV system and the DC fast charging architecture ensures a sustainable approach to EV charging by leveraging renewable energy while mitigating grid stress. This chapter provided a comprehensive foundation for the system’s modeling and control, forming the basis for further optimization and real-world application in high-performance DC fast charging systems.

Chapter four chapter provided a detailed performance evaluation of the developed DC fast charging system for EVs. The simulation results confirmed the system’s capability to achieve stable hybrid power integration, efficient bidirectional power conversion, and reduced voltage and current ripples. The impact of Park transform gain variations, VCO parameter adjustments, and RL filter inductance on stability, power quality, and grid synchronization was thoroughly analyzed. The boost converter’s performance under varying SoC conditions demonstrated well-regulated power output with effective MPPT using the P&O algorithm. The system exhibited low total harmonic distortion, robust transient and steady-state performance, and high charging efficiency. The integration of advanced control strategies, including PI controllers and harmonic compensation techniques, validated the system’s reliability. Furthermore, the incorporation of energy storage and grid-tied converters significantly improved cost efficiency and power stability, reinforcing the feasibility of the proposed design as a high-performance DC fast charging solution for electric vehicles.

Chapter five concludes the study by summarizing key findings from previous chapters: Chapter 2 reviewed fast charging technologies, emphasizing DC fast charging as the most viable solution despite grid challenges, while highlighting the benefits of renewable energy integration, hybrid microgrids, and advanced control strategies. Chapter 3 detailed the modeling of a DC fast charging system, integrating PV, grid, and charger stages with optimized control mechanisms like MPPT, bidirectional DAB converters, and PI controllers to ensure efficiency and stability. Chapter 4 validated the system's performance through simulations, demonstrating stable power integration, low harmonic distortion, and high charging efficiency, supported by robust energy storage and grid-tied converters. Overall, the study establishes that renewable-integrated DC fast charging, combined with advanced control and energy management, offers a sustainable and high-performance solution for EV adoption, addressing grid challenges while enhancing efficiency and reliability.

5.2 Recommendation and Future Work

The findings of this dissertation highlight the viability of renewable-integrated DC fast charging systems for EVs while identifying areas for further improvement and research. Based on the challenges and limitations encountered, the following recommendations and future work are proposed:

Recommendations

1. Enhanced Grid Integration Strategies – Future deployments of fast-charging stations should incorporate advanced grid-support mechanisms, such as dynamic load management and demand response systems, to mitigate power quality issues and grid instability caused by high-power charging demands.
2. Optimization of Hybrid Energy Systems – The integration of multiple renewable energy sources (e.g., wind and solar) with battery energy storage systems (BESS) should be further optimized to ensure uninterrupted power supply, especially in off-grid or weak-grid scenarios.
3. Improved Battery Management Systems (BMS) – Future BMS designs should incorporate artificial intelligence (AI) and machine learning (ML) techniques for more accurate state-of-charge (SoC) estimation, thermal management, and predictive maintenance to extend battery lifespan.
4. Standardization of Charging Protocols – Policymakers and industry stakeholders should work toward standardizing fast-charging protocols, including bidirectional (V2G/V2H) capabilities, to ensure interoperability and scalability across different EV models and charging networks.

5. Cost Reduction and Scalability – Research should focus on reducing the capital and operational costs of fast-charging infrastructure, particularly in solid-state transformers (SSTs) and high-power converters, to accelerate large-scale adoption.

Future Work

1. AI-Based Energy Management Systems – Future studies could explore AI-driven energy management systems for dynamic power allocation between renewable sources, grid power, and energy storage to maximize efficiency and minimize costs.
2. Ultra-Fast Charging with Next-Gen Batteries – Research should investigate ultra-fast charging (350 kW+) compatibility with emerging battery technologies (e.g., solid-state batteries) to reduce charging times while mitigating degradation effects.
3. Cybersecurity for Smart Charging Networks – As EV charging infrastructure becomes more interconnected, cybersecurity frameworks must be developed to protect against potential cyber threats in grid-connected and V2G-enabled systems.
4. Economic and Environmental Impact Analysis – Further studies should evaluate the long-term economic feasibility and carbon footprint reduction of renewable-powered fast-charging stations compared to conventional grid-dependent systems.

REFERENCES:

[1] M. M. Mahfouz and M. R. Iravani, “Grid-Integration of Battery-Enabled DC Fast Charging Station for Electric Vehicles,” *IEEE Trans. ENERGY Convers.*, vol. 35, no. 1, pp. 375–385, 2020.

[2] G. Bramerdorfer *et al.*, “More Robust and Reliable Optimized Energy Conversion Facilitated through Electric Machines , Power Electronics and Drives , and Their Control : State-of-the-Art and Trends,” *IEEE Trans. Energy Convers.*, vol. 35, no. 4, pp. 1997–2012, 2020.

[3] S. Islam, S. Member, N. Mithulananthan, and K. Y. Lee, “Suitability of PV and Battery Storage in EV Charging at Business Premises,” *IEEE Trans. POWER Syst.*, vol. 33, no. 4, pp. 4382–4396, 2018.

[4] E. Ucer, S. Member, M. C. Kisacikoglu, M. Yavuz, A. Meintz, and C. Rames, “Modeling and Analysis of a Fast Charging Station and Evaluation of Service Quality for Electric Vehicles,” *ieee Trans. Transp. Electrif.*, vol. 5, no. 1, pp. 215–225, 2019.

[5] M. Al-saadi, J. Olmos, A. Saez-de-ibarra, J. Van Mierlo, and M. Berecibar, “Fast Charging Impact on the Lithium-Ion Batteries’ Lifetime and Cost-Effective Battery Sizing in Heavy-Duty Electric Vehicles Applications,” *Energies*, vol. 15, no. 4, pp. 2–24, 2022, doi: 10.3390/en15041278.

[6] W. Khan, F. Ahmad, and M. S. Alam, “Fast EV charging station integration with grid ensuring optimal and quality power exchange,” *Eng. Sci. Technol. an Int. J.*, vol. 22, no. 1, pp. 143–152, 2019, doi: 10.1016/j.jestch.2018.08.005.

[7] M. S. Mastoi *et al.*, “A study of charging-dispatch strategies and vehicle-to-grid technologies for electric vehicles in distribution networks,” *Energy Reports*, vol. 9, pp. 1777–1806, 2023, doi: 10.1016/j.egyr.2022.12.139.

[8] M. S. Mastoi *et al.*, “An in-depth analysis of electric vehicle charging station infrastructure, policy implications, and future trends,” *Energy Reports*, vol. 8, pp. 11504–11529, 2022, doi: 10.1016/j.egyr.2022.09.011.

[9] A. Benmouna, L. Borderiou, and M. Becherif, “Charging Stations for Large-Scale Deployment of Electric Vehicles,” *Batteries*, vol. 10, no. 1, 2024, doi: 10.3390/batteries10010033.

[10] M. Safayatullah, M. T. Elrais, S. Ghosh, R. Rezaii, and I. Batarseh, “A Comprehensive Review of Power Converter Topologies and Control Methods for Electric Vehicle Fast Charging Applications,” *IEEE Access*, vol. 10, pp. 40753–40793, 2022, doi: 10.1109/ACCESS.2022.3166935.

[11] B. Al-Hanahi, I. Ahmad, D. Habibi, and M. A. S. Masoum, “Charging Infrastructure for Commercial Electric Vehicles: Challenges and Future Works,” *IEEE Access*, vol. 9, pp. 121476–121492, 2021, doi: 10.1109/ACCESS.2021.3108817.

[12] S. Atanalian, K. Al-Haddad, R. Zgheib, and H. Y. Kanaan, “A Review on Electric Vehicles Battery Chargers and AC/DC Converters for Fast Charging Stations,” *2021 IEEE 3rd Int. Multidiscip. Conf. Eng. Technol. IMCET 2021*, pp. 43–48, 2021, doi: 10.1109/IMCET53404.2021.9665577.

[13] F. Nasr Esfahani, A. Darwish, and X. Ma, “Design and Control of a Modular Integrated On-Board Battery Charger for EV Applications with Cell Balancing,” *Batteries*, vol. 10, no. 1, 2024, doi: 10.3390/batteries10010017.

[14] S. Panchanathan *et al.*, “A Comprehensive Review of the Bidirectional Converter Topologies for the Vehicle-to-Grid System,” *Energies*, vol. 16, no. 5, 2023, doi: 10.3390/en16052503.

[15] M. I. Juma, B. M. M. Mwinyiwiwa, C. J. Msigwa, and A. T. Mushi, “Design of a hybrid energy system with energy storage for standalone DC microgrid application,” *Energies*, vol. 14, no. 18, pp. 1–15, 2021, doi: 10.3390/en14185994.

[16] S. Saelee and T. Horanont, “Optimal Placement of EV Charging Station Considering the Road Traffic Volume and EV Running Distance,” *J. Traffic Logist. Eng.*, 2016, doi: 10.18178/jtle.4.1.19-23.

[17] O. Elma, “A dynamic charging strategy with hybrid fast charging station for electric vehicles,” *Energy*, vol. 202, 2020, doi: 10.1016/j.energy.2020.117680.

[18] H. Arya and M. Das, “Solar Powered EV Fast Charging Station to Support Distribution Grid,” *ICPS 2021 - 9th IEEE Int. Conf. Power Syst. Dev. Towar. Incl. Growth Sustain. Resilient Grid*, 2021, doi: 10.1109/ICPS52420.2021.9670361.

[19] M. Ahmadi, H. J. Kaleybar, M. Brenna, F. Castelli-Dezza, and M. S. Carmeli, “Implementation of DC Micro Grid Tied PV-Storage Based EV Fast Charging Station,” *21st IEEE Int. Conf. Environ. Electr. Eng. 2021 5th IEEE Ind. Commer. Power Syst. Eur. EEEIC / I CPS Eur. 2021 - Proc.*, 2021, doi: 10.1109/EEEIC/ICPSEurope51590.2021.9584631.

[20] A. Tomaszewska *et al.*, “Lithium-ion battery fast charging: A review,” *eTransportation*, vol. 1, p. 100011, 2019, doi: 10.1016/j.etran.2019.100011.

[21] A. Zentani, A. Almaktoof, and M. T. Kahn, “A Comprehensive Review of Developments in Electric Vehicles Fast Charging Technology,” *Appl. Sci.*, vol. 14, no. 11, 2024, doi: 10.3390/app14114728.

[22] B. B. Gicha, L. T. Tufa, and J. Lee, “The electric vehicle revolution in Sub-Saharan Africa: Trends, challenges, and opportunities,” *Energy Strateg. Rev.*, vol. 53, no. February, p. 101384, 2024, doi: 10.1016/j.esr.2024.101384.

[23] A. Razmjoo *et al.*, “A Comprehensive Study on the Expansion of Electric Vehicles in Europe,” *Appl. Sci.*, vol. 12, no. 22, 2022, doi: 10.3390/app122211656.

[24] K. M. Janasak, “Challenges Faced In Electric Vehicle Adoption,” *Proc. - Annu. Reliab.*

Maintainab. Symp., no. November 2021, pp. 1–6, 2024, doi: 10.1109/RAMS51492.2024.10457699.

[25] S. LaMonaca and L. Ryan, “The state of play in electric vehicle charging services – A review of infrastructure provision, players, and policies,” *Renew. Sustain. Energy Rev.*, vol. 154, no. August 2021, p. 111733, 2022, doi: 10.1016/j.rser.2021.111733.

[26] B. A. Rayan, U. Subramaniam, and S. Balamurugan, “Wireless Power Transfer in Electric Vehicles: A Review on Compensation Topologies, Coil Structures, and Safety Aspects,” *Energies*, vol. 16, no. 7, 2023, doi: 10.3390/en16073084.

[27] N. Tesla, “Nikola Tesla U.S. Patent Apparatus for Transmitting Electrical Energy | Tesla Universe.” 1914. [Online]. Available: https://teslauniverse.com/nikola-tesla/patents/us-patent-1119732-apparatus-transmitting-electrical-energy

[28] V. M. Macharia, V. K. Garg, and D. Kumar, “A review of electric vehicle technology: Architectures, battery technology and its management system, relevant standards, application of artificial intelligence, cyber security, and interoperability challenges,” *IET Electr. Syst. Transp.*, vol. 13, no. 2, 2023, doi: 10.1049/els2.12083.

[29] H. Wen *et al.*, “Improving the Misalignment Tolerance of Wireless Power Transfer System for AUV with Solenoid-Dual Combined Planar Magnetic Coupler,” *J. Mar. Sci. Eng.*, vol. 11, no. 8, 2023, doi: 10.3390/jmse11081571.

[30] M. Amjad, M. Farooq-i-Azam, Q. Ni, M. Dong, and E. A. Ansari, “Wireless charging systems for electric vehicles,” *Renew. Sustain. Energy Rev.*, vol. 167, no. May 2021, 2022, doi: 10.1016/j.rser.2022.112730.

[31] A. Ahmad, M. S. Alam, Y. Rafat, and S. Shariff, “Designing and demonstration of misalignment reduction for wireless charging of autonomous electric vehicle,” *eTransportation*, vol. 4, p. 100052, 2020, doi: 10.1016/j.etran.2020.100052.

[32] G. Palani, U. Sengamalai, P. Vishnuram, and B. Nastasi, “Challenges and Barriers of Wireless Charging Technologies for Electric Vehicles,” *Energies*, vol. 16, no. 5, 2023, doi: 10.3390/en16052138.

[33] C. Panchal, S. Stegen, and J. Lu, “Review of static and dynamic wireless electric vehicle charging system,” *Eng. Sci. Technol. an Int. J.*, vol. 21, no. 5, pp. 922–937, 2018, doi: 10.1016/j.jestch.2018.06.015.

[34] R. Bosshard and J. W. Kolar, “Inductive Power Transfer for Electric Vehicle Charging: Technical challenges and tradeoffs,” *IEEE Power Electron. Mag.*, vol. 3, no. 3, pp. 22–30, 2016, doi: 10.1109/MPEL.2016.2583839.

[35] D. Meyer and J. Wang, “Integrating ultra-fast charging stations within the power grids of smart cities: A review,” *IET Smart Grid*, vol. 1, no. 1, pp. 3–10, 2018, doi: 10.1049/iet-stg.2018.0006.

[36] C. Leone, M. Longo, and L. M. Fernández-Ramírez, “Optimal size of a smart ultra-fast

charging station," *Electron.*, vol. 10, no. 23, 2021, doi: 10.3390/electronics10232887.

[37] P. Franzese *et al.*, "Fast DC Charging Infrastructures for Electric Vehicles: Overview of Technologies, Standards, and Challenges," *IEEE Trans. Transp. Electrif.*, vol. PP, no. 3, pp. 1–1, 2023, doi: 10.1109/tte.2023.3239224.

[38] G. Rajendran, C. A. Vaithilingam, N. Misron, K. Naidu, and M. R. Ahmed, "A comprehensive review on system architecture and international standards for electric vehicle charging stations," *J. Energy Storage*, vol. 42, no. August, p. 103099, 2021, doi: 10.1016/j.est.2021.103099.

[39] R. H. Ashique, Z. Salam, M. J. Bin Abdul Aziz, and A. R. Bhatti, "Integrated photovoltaic-grid dc fast charging system for electric vehicle: A review of the architecture and control," *Renew. Sustain. Energy Rev.*, vol. 69, no. May 2016, pp. 1243–1257, 2017, doi: 10.1016/j.rser.2016.11.245.

[40] F. M. Shakeel and O. P. Malik, "Vehicle-To-Grid Technology in a Micro-grid Using DC Fast Charging Architecture," *2019 IEEE Can. Conf. Electr. Comput. Eng. CCECE 2019*, pp. 1–4, 2019, doi: 10.1109/CCECE.2019.8861592.

[41] A. Saadaoui, M. Ouassaid, and M. Maaroufi, "Overview of Integration of Power Electronic Topologies and Advanced Control Techniques of Ultra-Fast EV Charging Stations in Standalone Microgrids," *Energies*, vol. 16, no. 3, 2023, doi: 10.3390/en16031031.

[42] H. Yu, S. Niu, Y. Shang, Z. Shao, Y. Jia, and L. Jian, "Electric vehicles integration and vehicle-to-grid operation in active distribution grids: A comprehensive review on power architectures, grid connection standards and typical applications," *Renew. Sustain. Energy Rev.*, vol. 168, no. April, p. 112812, 2022, doi: 10.1016/j.rser.2022.112812.

[43] K. L. Lim, S. Speidel, and T. Bräunl, "A comparative study of AC and DC public electric vehicle charging station usage in Western Australia," *Renew. Sustain. Energy Transit.*, vol. 2, no. April, p. 100021, 2022, doi: 10.1016/j.rset.2022.100021.

[44] A. Ahmad, Z. Qin, T. Wijekoon, and P. Bauer, "An Overview on Medium Voltage Grid Integration of Ultra-Fast Charging Stations: Current Status and Future Trends," *IEEE Open J. Ind. Electron. Soc.*, vol. 3, no. June, pp. 420–447, 2022, doi: 10.1109/OJIES.2022.3179743.

[45] S. Sachan, S. Deb, P. P. Singh, M. S. Alam, and S. M. Shariff, "A comprehensive review of standards and best practices for utility grid integration with electric vehicle charging stations," *Wiley Interdiscip. Rev. Energy Environ.*, vol. 11, no. 3, 2022, doi: 10.1002/wene.424.

[46] A. Meintz *et al.*, "Enabling fast charging – Vehicle considerations," *J. Power Sources*, vol. 367, pp. 216–227, 2017, doi: 10.1016/j.jpowsour.2017.07.093.

[47] A. Burnham *et al.*, "Enabling fast charging – Infrastructure and economic

considerations," *J. Power Sources*, vol. 367, pp. 237–249, 2017, doi: 10.1016/j.jpowsour.2017.06.079.

[48] A. Mahdy, H. M. Hasanien, R. A. Turky, and S. H. E. Abdel Aleem, "Modeling and optimal operation of hybrid wave energy and PV system feeding supercharging stations based on golden jackal optimal control strategy," *Energy*, vol. 263, no. August 2022, 2023, doi: 10.1016/j.energy.2022.125932.

[49] J. A. Sanguesa, V. Torres-Sanz, P. Garrido, F. J. Martinez, and J. M. Marquez-Barja, "A Review on Electric Vehicles: Technologies and Challenges," *Smart Cities*, vol. 4, no. 1, pp. 372–404, 2021.

[50] S. Hemavathi and A. Shinisha, "A study on trends and developments in electric vehicle charging technologies," *J. Energy Storage*, vol. 52, no. January, p. 105013, 2022, doi: 10.1016/j.est.2022.105013.

[51] S. Kim *et al.*, "Projecting Recent Advancements in Battery Technology to Next-Generation Electric Vehicles," *Energy Technol.*, vol. 10, no. 8, pp. 1–12, 2022, doi: 10.1002/ente.202200303.

[52] K. Taghizad-Tavana, A. Alizadeh, M. Ghanbari-Ghalehjoughi, and S. Nojavan, "A Comprehensive Review of Electric Vehicles in Energy Systems: Integration with Renewable Energy Sources, Charging Levels, Different Types, and Standards," *Energies*, vol. 16, no. 2, 2023, doi: 10.3390/en16020630.

[53] Z. Huang, Z. Guo, P. Ma, M. Wang, Y. Long, and M. Zhang, "Economic-environmental scheduling of microgrid considering V2G-enabled electric vehicles integration," *Sustain. Energy, Grids Networks*, vol. 32, p. 100872, 2022, doi: 10.1016/j.segan.2022.100872.

[54] M. O. Tarar, N. U. Hassan, I. H. Naqvi, and M. Pecht, "Techno-Economic Framework for Electric Vehicle Battery Swapping Stations," *IEEE Trans. Transp. Electrif.*, vol. 9, no. 3, pp. 4458–4473, 2023, doi: 10.1109/TTE.2023.3252169.

[55] G. Benedetto *et al.*, "Impact of bidirectional EV charging stations on a distribution network: a Power Hardware-In-the-Loop implementation," *Sustain. Energy, Grids Networks*, vol. 35, p. 101106, 2023, doi: 10.1016/j.segan.2023.101106.

[56] H. R. Sayarshad, V. Mahmoodian, and H. O. Gao, "Non-myopic dynamic routing of electric taxis with battery swapping stations," *Sustain. Cities Soc.*, vol. 57, no. September 2019, 2020, doi: 10.1016/j.scs.2020.102113.

[57] S. Schmidt, "Use of battery swapping for improving environmental balance and price-performance ratio of electric vehicles," *eTransportation*, vol. 9, p. 100128, 2021, doi: 10.1016/j.etran.2021.100128.

[58] X. Sun, Z. Li, X. Wang, and C. Li, "Technology development of electric vehicles: A review," *Energies*, vol. 13, no. 1, pp. 1–29, 2019, doi: 10.3390/en13010090.

[59] M. Y. Metwly, M. S. Abdel-Majeed, A. S. Abdel-Khalik, R. A. Hamdy, M. S. Hamad, and

S. Ahmed, “A Review of Integrated On-Board EV Battery Chargers: Advanced Topologies, Recent Developments and Optimal Selection of FSCW Slot/Pole Combination,” *IEEE Access*, vol. 8, pp. 85216–85242, 2020, doi: 10.1109/ACCESS.2020.2992741.

[60] A. Khaligh and M. Dantonio, “Global Trends in High-Power On-Board Chargers for Electric Vehicles,” *IEEE Trans. Veh. Technol.*, vol. 68, no. 4, pp. 3306–3324, 2019, doi: 10.1109/TVT.2019.2897050.

[61] M. Brenna, F. Foiadelli, C. Leone, and M. Longo, “Electric Vehicles Charging Technology Review and Optimal Size Estimation,” *J. Electr. Eng. Technol.*, vol. 15, no. 6, pp. 2539–2552, 2020, doi: 10.1007/s42835-020-00547-x.

[62] S. A. Q. Mohammed and J. W. Jung, “A Comprehensive State-of-the-Art Review of Wired/Wireless Charging Technologies for Battery Electric Vehicles: Classification/Common Topologies/Future Research Issues,” *IEEE Access*, vol. 9, pp. 19572–19585, 2021, doi: 10.1109/ACCESS.2021.3055027.

[63] F. N. Esfahani, A. Darwish, and B. W. Williams, “Power Converter Topologies for Grid-Tied Solar Photovoltaic (PV) Powered Electric Vehicles (EVs)—A Comprehensive Review,” *Energies*, vol. 15, no. 13, 2022, doi: 10.3390/en15134648.

[64] D. K. Mishra *et al.*, “A review on solid-state transformer: A breakthrough technology for future smart distribution grids,” *Int. J. Electr. Power Energy Syst.*, vol. 133, no. April, 2021, doi: 10.1016/j.ijepes.2021.107255.

[65] A. F. Moghaddam and A. Van den Bossche, “Forward converter current fed equalizer for lithium based batteries in ultralight electrical vehicles,” *Electron.*, vol. 8, no. 4, 2019, doi: 10.3390/electronics8040408.

[66] H. He *et al.*, “China’s battery electric vehicles lead the world: achievements in technology system architecture and technological breakthroughs,” *Green Energy Intell. Transp.*, vol. 1, no. 1, 2022, doi: 10.1016/j.geits.2022.100020.

[67] D. Ronanki, A. Kelkar, and S. S. Williamson, “Extreme fast charging technology—prospects to enhance sustainable electric transportation,” *Energies*, vol. 12, no. 19, pp. 1–17, 2019, doi: 10.3390/en12193721.

[68] M. Genovese, V. Cigolotti, E. Jannelli, and P. Fragiacomo, “Current standards and configurations for the permitting and operation of hydrogen refueling stations,” *Int. J. Hydrogen Energy*, vol. 48, no. 51, pp. 19357–19371, 2023, doi: 10.1016/j.ijhydene.2023.01.324.

[69] W. Xie *et al.*, “Challenges and opportunities toward fast-charging of lithium-ion batteries,” *J. Energy Storage*, vol. 32, no. July, p. 101837, 2020, doi: 10.1016/j.est.2020.101837.

[70] H. S. Das, M. M. Rahman, S. Li, and C. W. Tan, “Electric vehicles standards, charging

infrastructure, and impact on grid integration: A technological review," *Renew. Sustain. Energy Rev.*, vol. 120, no. November 2019, 2020, doi: 10.1016/j.rser.2019.109618.

[71] K. Dimitriadou, N. Rigogiannis, S. Fountoukidis, F. Kotarela, A. Kyritsis, and N. Papanikolaou, "Current Trends in Electric Vehicle Charging Infrastructure Opportunities and Challenges in Wireless Charging Integration," *Energies*, vol. 16, no. 4. MDPI, Feb. 01, 2023. doi: 10.3390/en16042057.

[72] L. Rubino, C. Capasso, and O. Veneri, "Review on plug-in electric vehicle charging architectures integrated with distributed energy sources for sustainable mobility," *Appl. Energy*, vol. 207, pp. 438–464, 2017, doi: 10.1016/j.apenergy.2017.06.097.

[73] A. Draz, A. M. Othman, and A. A. El-fergany, "State-of-the-Art with numerical analysis on electric fast charging stations : infrastructures , standards , techniques , and challenges Electric vehicle Supply Equipment Point of Common Coupling," *Renew. Energy Focus J.*, vol. 47, no. September, 2023.

[74] S. Jaman *et al.*, "Development and Validation of V2G Technology for Electric Vehicle Chargers Using Combo CCS Type 2 Connector Standards," *Energies*, vol. 15, no. 19, 2022, doi: 10.3390/en15197364.

[75] M. Neaimeh and P. B. Andersen, "Mind the gap- open communication protocols for vehicle grid integration," *Energy Informatics*, vol. 3, no. 1, pp. 1–17, 2020, doi: 10.1186/s42162-020-0103-1.

[76] F. Xie, C. Liu, S. Li, Z. Lin, and Y. Huang, "Long-term strategic planning of inter-city fast charging infrastructure for battery electric vehicles," *Transp. Res. Part E Logist. Transp. Rev.*, vol. 109, no. June 2017, pp. 261–276, 2018, doi: 10.1016/j.tre.2017.11.014.

[77] I. Aretxabaleta, I. M. De Alegria, J. Andreu, I. Kortabarria, and E. Robles, "High-Voltage Stations for Electric Vehicle Fast-Charging: Trends, Standards, Charging Modes and Comparison of Unity Power-Factor Rectifiers," *IEEE Access*, vol. 9, pp. 102177–102194, 2021, doi: 10.1109/ACCESS.2021.3093696.

[78] L. Jiang *et al.*, "Hybrid charging strategy with adaptive current control of lithium-ion battery for electric vehicles," *Renew. Energy*, vol. 160, pp. 1385–1395, 2020, doi: 10.1016/j.renene.2020.07.018.

[79] O. M. F. Camacho and L. Mihet-Popa, "Fast Charging and Smart Charging Tests for Electric Vehicles Batteries Using Renewable Energy," *Oil Gas Sci. Technol. - Rev. IFP Energies Nouv.*, vol. 71, no. 1, 2014, doi: 10.2516/ogst/2014001.

[80] H. Ben Sassi, C. Alaoui, F. Errahimi, and N. Es-Sbai, "Vehicle-to-grid technology and its suitability for the Moroccan national grid," *J. Energy Storage*, vol. 33, no. October 2020, p. 102023, 2021, doi: 10.1016/j.est.2020.102023.

[81] A. Sharma and S. Sharma, "Review of power electronics in vehicle-to-grid systems," *J. Energy Storage*, vol. 21, no. August 2018, pp. 337–361, 2019, doi:

10.1016/j.est.2018.11.022.

[82] M. Subashini and S. Vijayan, “Smart Charging for Zero Emission Vehicles – A Comprehensive Review,” *Renew. Energy Focus*, vol. 46, pp. 57–67, 2023, doi: 10.1016/j.ref.2023.05.005.

[83] N. Dharavat *et al.*, “Impact of plug-in electric vehicles on grid integration with distributed energy resources: A review,” *Front. Energy Res.*, vol. 10, no. January, pp. 1–13, 2023, doi: 10.3389/fenrg.2022.1099890.

[84] N. Wassiliadis *et al.*, “Review of fast charging strategies for lithium-ion battery systems and their applicability for battery electric vehicles,” *J. Energy Storage*, vol. 44, no. July, 2021, doi: 10.1016/j.est.2021.103306.

[85] M. S. Hossain Lipu *et al.*, “Intelligent algorithms and control strategies for battery management system in electric vehicles: Progress, challenges and future outlook,” *J. Clean. Prod.*, vol. 292, 2021, doi: 10.1016/j.jclepro.2021.126044.

[86] M. Wu, L. Qin, and G. Wu, “State of charge estimation of Power lithium-ion battery based on an Affine Iterative Adaptive Extended Kalman Filter,” *J. Energy Storage*, vol. 51, no. September 2020, 2022, doi: 10.1016/j.est.2022.104472.

[87] Z. Zhang, L. Jiang, L. Zhang, and C. Huang, “State-of-charge estimation of lithium-ion battery pack by using an adaptive extended Kalman filter for electric vehicles,” *J. Energy Storage*, vol. 37, no. June 2020, 2021, doi: 10.1016/j.est.2021.102457.

[88] S. Aggarwal, A. Kumar Singh, R. Singh Rathore, M. Bajaj, and D. Gupta, “Revolutionizing load management: A novel technique to diminish the impact of electric vehicle charging stations on the electricity grid,” *Sustain. Energy Technol. Assessments*, vol. 65, no. April, p. 103784, 2024, doi: 10.1016/j.seta.2024.103784.

[89] Emmanuel Augustine Etukudoh, Ahmad Hamdan, Valentine Ikenna Ilojianya, Cosmas Dominic Daudu, and Adefunke Fabuyide, “Electric Vehicle Charging Infrastructure: a Comparative Review in Canada, Usa, and Africa,” *Eng. Sci. Technol. J.*, vol. 5, no. 1, pp. 245–258, 2024, doi: 10.51594/estj.v5i1.747.

[90] A. Pal, A. Bhattacharya, and A. K. Chakraborty, “Allocation of electric vehicle charging station considering uncertainties,” *Sustain. Energy, Grids Networks*, vol. 25, p. 100422, 2021, doi: 10.1016/j.segan.2020.100422.

[91] S. Dawn *et al.*, “Integration of Renewable Energy in Microgrids and Smart Grids in Deregulated Power Systems: A Comparative Exploration,” *Adv. Energy Sustain. Res.*, vol. 2400088, 2024, doi: 10.1002/aesr.202400088.

[92] A. Kumar, S. Kumar, U. K. Sinha, B. K. Saw, and A. K. Bohre, “Integration of Green Renewable DG based EV Charging Stations Planning in Unbalanced Distribution Network,” *2023 IEEE Int. Conf. Power Electron. Smart Grid, Renew. Energy Power Electron. Smart Grid, Renew. Energy Sustain. Dev. PESGRE 2023*, no. December, pp.

1–6, 2023, doi: 10.1109/PESGRE58662.2023.10405050.

[93] A. R. Singh *et al.*, “Electric vehicle charging technologies, infrastructure expansion, grid integration strategies, and their role in promoting sustainable e-mobility,” *Alexandria Eng. J.*, vol. 105, no. June, pp. 300–330, 2024, doi: 10.1016/j.aej.2024.06.093.

[94] J. Suvvala, S. K. K, C. Dhananjayulu, H. Kotb, and A. Elrashidi, “Integration of renewable energy sources using multiport converters for ultra-fast charging stations for electric vehicles: An overview,” *Heliyon*, vol. 10, no. 15, p. e35782, 2024, doi: 10.1016/j.heliyon.2024.e35782.

[95] Q. Hassan, S. Algburi, A. Z. Sameen, H. M. Salman, and M. Jaszczur, “A review of hybrid renewable energy systems: Solar and wind-powered solutions: Challenges, opportunities, and policy implications,” *Results Eng.*, vol. 20, no. November, p. 101621, 2023, doi: 10.1016/j.rineng.2023.101621.

[96] O. E. Olabode, I. K. Okakwu, D. O. Akinyele, T. O. Ajewole, S. Oyelami, and O. V. Olisa, “Effect of Ambient Temperature and Solar Irradiance on Photovoltaic Modules’ Performance,” *Iran. J. Energy Environ.*, vol. 15, no. 4, pp. 402–420, 2024, doi: 10.5829/ijee.2024.15.04.08.

[97] A. Ahmad, Z. Qin, T. Wijekoon, and P. Bauer, “An Overview on Medium Voltage Grid Integration of Ultra-Fast Charging Stations: Current Status and Future Trends,” *IEEE Open J. Ind. Electron. Soc.*, vol. 3, no. March, pp. 420–447, 2022, doi: 10.1109/OJIES.2022.3179743.

[98] J. Hmad, A. Houari, A. E. M. Bouzid, A. Saim, and H. Trabelsi, “A Review on Mode Transition Strategies between Grid-Connected and Standalone Operation of Voltage Source Inverters-Based Microgrids,” *Energies*, vol. 16, no. 13, 2023, doi: 10.3390/en16135062.

[99] O. Ardakanian, C. Rosenberg, and S. Keshav, “Distributed control of electric vehicle charging,” *e-Energy 2013 - Proc. 4th ACM Int. Conf. Futur. Energy Syst.*, pp. 101–112, 2013, doi: 10.1145/2487166.2487178.

[100] Y. Wu, Z. Wang, Y. Huangfu, A. Ravey, D. Chrenko, and F. Gao, “Hierarchical Operation of Electric Vehicle Charging Station in Smart Grid Integration Applications — An Overview,” *Int. J. Electr. Power Energy Syst.*, vol. 139, 2022, doi: 10.1016/j.ijepes.2022.108005.

[101] Y. Dan, S. Liu, Y. Zhu, and H. Xie, “Tertiary Control for Energy Management of EV Charging Station Integrated With PV and Energy Storage,” *Front. Energy Res.*, vol. 9, no. January, pp. 1–16, 2022, doi: 10.3389/fenrg.2021.793553.

[102] P. Vishnuram and S. Alagarsamy, “Grid Integration for Electric Vehicles: A Realistic Strategy for Environmentally Friendly Mobility and Renewable Power,” *World Electr. Veh. J.*, vol. 15, no. 2, 2024, doi: 10.3390/wevj15020070.

[103] A. G. Olabi *et al.*, “Battery electric vehicles: Progress, power electronic converters, strength (S), weakness (W), opportunity (O), and threats (T),” *Int. J. Thermofluids*, vol. 16, no. September, p. 100212, 2022, doi: 10.1016/j.ijft.2022.100212.

[104] I. Aghabali, J. Bauman, P. J. Kollmeyer, Y. Wang, B. Bilgin, and A. Emadi, “800-V Electric Vehicle Powertrains: Review and Analysis of Benefits, Challenges, and Future Trends,” *IEEE Trans. Transp. Electrif.*, vol. 7, no. 3, pp. 927–948, 2021, doi: 10.1109/TTE.2020.3044938.

[105] A. Ahmad, Z. Qin, T. Wijekoon, and P. Bauer, “An Overview on Medium Voltage Grid Integration of Ultra-Fast Charging Stations: Current Status and Future Trends,” *IEEE Open J. Ind. Electron. Soc.*, vol. 3, no. May, pp. 420–447, 2022, doi: 10.1109/OJIES.2022.3179743.

[106] J. Kumar K, S. Kumar, and N. V.S, “Standards for electric vehicle charging stations in India: A review,” *Energy Storage*, vol. 4, no. 1, pp. 1–19, 2022, doi: 10.1002/est2.261.

[107] A. A. S. Mohamed, A. A. Shaier, H. Metwally, and S. I. Selem, “An Overview of Dynamic Inductive Charging for Electric Vehicles,” *Energies*, vol. 15, no. 15, 2022, doi: 10.3390/en15155613.

[108] S. S. G. Acharige, M. E. Haque, M. T. Arif, N. Hosseinzadeh, K. N. Hasan, and A. M. T. Oo, “Review of Electric Vehicle Charging Technologies, Standards, Architectures, and Converter Configurations,” *IEEE Access*, 2023, doi: 10.1109/ACCESS.2023.3267164.

[109] M. A. H. Rafi and J. Bauman, “A Comprehensive Review of DC Fast-Charging Stations with Energy Storage: Architectures, Power Converters, and Analysis,” *IEEE Trans. Transp. Electrif.*, vol. 7, no. 2, pp. 345–368, 2021, doi: 10.1109/TTE.2020.3015743.

[110] K. V. Singh, H. O. Bansal, and D. Singh, “A comprehensive review on hybrid electric vehicles: architectures and components,” *J. Mod. Transp.*, vol. 27, no. 2, pp. 77–107, 2019, doi: 10.1007/s40534-019-0184-3.

[111] C. Vanlalchhuanawmi, S. Deb, A. Onen, and T. S. Ustun, “Energy management strategies in distribution system integrating electric vehicle and battery energy storage system A review,” *Energy Storage*, vol. 6, no. 5, pp. 1–22, 2024, doi: 10.1002/est2.682.

[112] J. Li and A. Li, “Optimizing Electric Vehicle Integration with Vehicle-to-Grid Technology: The Influence of Price Difference and Battery Costs on Adoption, Profits, and Green Energy Utilization,” *Sustain.*, vol. 16, no. 3, 2024, doi: 10.3390/su16031118.

[113] A. Rehman, H. M. Khalid, and S. M. Muyeen, “Grid-integrated solutions for sustainable EV charging a comparative study of renewable energy and battery storage systems,” *Front. Energy Res.*, no. September, pp. 1–15, 2024, doi: 10.3389/fenrg.2024.1403883.

[114] M. Ntombela, K. Musasa, and K. Moloi, “A Comprehensive Review of the Incorporation of Electric Vehicles and Renewable Energy Distributed Generation Regarding Smart Grids,” *World Electr. Veh. Journal, MDPI*, vol. 14, no. 176, pp. 1–28, 2023.

[115] M. Gjelaj, C. Træholt, S. Hashemi, and P. B. Andersen, “Optimal design of DC fast-charging stations for EVs in low voltage grids,” *2017 IEEE Transp. Electrif. Conf. Expo, ITEC 2017*, pp. 684–689, 2017, doi: 10.1109/ITEC.2017.7993352.

[116] A. K. M. Yousuf, Z. Wang, R. Paranjape, and Y. Tang, “An In-Depth Exploration of Electric Vehicle Charging Station Infrastructure: A Comprehensive Review of Challenges, Mitigation Approaches, and Optimization Strategies,” *IEEE Access*, vol. 12, no. March, pp. 51570–51589, 2024, doi: 10.1109/ACCESS.2024.3385731.

[117] H. R. Sayarshad, “Optimization of electric charging infrastructure: integrated model for routing and charging coordination with power-aware operations,” *npj Sustain. Mobil. Transp.*, vol. 1, no. 1, 2024, doi: 10.1038/s44333-024-00004-6.

[118] J. N. Sabhahit, S. S. Solanke, V. K. Jadoun, H. Malik, F. P. G. Márquez, and J. M. Pinar-Pérez, “Contingency Analysis of a Grid of Connected EVs for Primary Frequency Control of an Industrial Microgrid Using Efficient Control Scheme,” *Energies*, vol. 15, no. 9, 2022, doi: 10.3390/en15093102.

[119] S. Charadi, Y. Chaibi, A. Redouane, A. Allouhi, A. El Hasnaoui, and H. Mahmoudi, “Efficiency and energy-loss analysis for hybrid AC/DC distribution systems and microgrids: A review,” *Int. Trans. Electr. Energy Syst.*, vol. 31, no. 12, pp. 1–30, 2021, doi: 10.1002/2050-7038.13203.

[120] M. ElMenshawy and A. Massoud, “Medium-Voltage DC-DC Converter Topologies for Electric Bus Fast Charging Stations: State-of-the-Art Review,” *Energies*, vol. 15, no. 15, 2022, doi: 10.3390/en15155487.

[121] F. Baumgarte, *Technologies for Digitalization and Decarbonization of Individual Mobility*. 2022. [Online]. Available: https://www.researchgate.net/publication/363210509_Technologies_for_Digitalization_and_Decarbonization_of_Individual_Mobility

[122] L. F. Grisales-Noreña, O. D. Montoya, and C. A. Ramos-Paja, “An energy management system for optimal operation of BSS in DC distributed generation environments based on a parallel PSO algorithm,” *J. Energy Storage*, vol. 29, no. May, p. 101488, 2020, doi: 10.1016/j.est.2020.101488.

[123] A. Ashok Kumar and N. Amutha Prabha, “A comprehensive review of DC microgrid in market segments and control technique,” *Heliyon*, vol. 8, no. 11, p. e11694, 2022, doi: 10.1016/j.heliyon.2022.e11694.

[124] J. Huber, P. Wallmeier, R. Pieper, F. Schafmeister, and J. W. Kolar, “Comparative Evaluation of MVAC-LVDC SST and Hybrid Transformer Concepts for Future Datacenters,” *2022 Int. Power Electron. Conf. IPEC-Himeji 2022-ECCE Asia*, vol. 2022, pp. 2027–2034, 2022, doi: 10.23919/IPEC-Himeji2022-ECCE53331.2022.9807028.

[125] D. S. Abraham *et al.*, “Electric vehicles charging stations’ architectures, criteria, power

converters, and control strategies in microgrids," *Electron.*, vol. 10, no. 16, 2021, doi: 10.3390/electronics10161895.

[126] M. A. Ravindran *et al.*, "A Novel Technological Review on Fast Charging Infrastructure for Electrical Vehicles: Challenges, Solutions, and Future Research Directions," *Alexandria Eng. J.*, vol. 82, no. September, pp. 260–290, 2023, doi: 10.1016/j.aej.2023.10.009.

[127] M. Kisacikoglu *et al.*, "High-Power Electric Vehicle Charging Hub Integration Platform (eCHIP): Design Guidelines and Specifications for DC Distribution-Based Charging Hub," *U.S. Dep. ENERGY*, no. April, 2024.

[128] J. Thoma, D. Chilachava, and D. Kranzer, "A highly efficient DC-DC-converter for medium-voltage applications," *ENERGYCON 2014 - IEEE Int. Energy Conf.*, pp. 127–131, 2014, doi: 10.1109/ENERGYCON.2014.6850417.

[129] Z. Liu, S. Miao, W. Wang, and D. Sun, "Comprehensive control scheme for an interlinking converter in a hybrid AC/DC microgrid," *CSEE J. Power Energy Syst.*, vol. 7, no. 4, pp. 719–729, 2020, doi: 10.17775/CSEEJPES.2020.00970.

[130] T. Dragičević *et al.*, "DC Microgrids - Part II: A Review of Power Architectures, Applications, and Standardization Issues," *IEEE Trans. Power Electron.*, vol. 31, no. 5, pp. 3528–3549, 2016, doi: 10.1109/TPEL.2015.2464277.

[131] A. Abu-Siada, J. Budiri, and A. F. Abdou, "Solid state transformers topologies, controllers, and applications State-of-the-art literature review," *Electron.*, vol. 7, no. 11, 2018, doi: 10.3390/electronics7110298.

[132] J. Suvvala, S. K. K, C. Dhananjayulu, H. Kotb, and A. Elrashidi, "Integration of renewable energy sources using multiport converters for ultra-fast charging stations for electric vehicles: An overview," *Heliyon*, vol. 10, no. 15, p. e35782, 2024, doi: 10.1016/j.heliyon.2024.e35782.

[133] M. A. Shamshuddin, F. Rojas, R. Cardenas, J. Pereda, M. Diaz, and R. Kennel, "Solid state transformers: Concepts, classification, and control," *Energies*, vol. 13, no. 9, pp. 1–35, 2020, doi: 10.3390/en13092319.

[134] A. H. Okilly and J. Baek, "Design and Fabrication of an Isolated Two-Stage AC–DC Power Supply with a 99.50% PF and ZVS for High-Power Density Industrial Applications," *Electron.*, vol. 11, no. 12, 2022, doi: 10.3390/electronics11121898.

[135] C. Saber, D. Labrousse, B. Revol, and A. Gascher, "Challenges Facing PFC of a Single-Phase On-Board Charger for Electric Vehicles Based on a Current Source Active Rectifier Input Stage," *IEEE Trans. Power Electron.*, vol. 31, no. 9, pp. 6192–6202, 2016, doi: 10.1109/TPEL.2015.2500958.

[136] I. Alhurayyis, A. Elkhateb, and J. Morrow, "Isolated and Nonisolated DC-to-DC Converters for Medium-Voltage DC Networks: A Review," *IEEE J. Emerg. Sel. Top.*

Power Electron., vol. 9, no. 6, pp. 7486–7500, 2021, doi: 10.1109/JESTPE.2020.3028057.

[137] P. Dini, S. Saponara, and A. Colicelli, “Overview on Battery Charging Systems for Electric Vehicles,” *Electron.*, vol. 12, no. 20, 2023, doi: 10.3390/electronics12204295.

[138] K. M. Muttaqi, E. Isac, A. Mandal, D. Sutanto, and S. Akter, “Fast and random charging of electric vehicles and its impacts: State-of-the-art technologies and case studies,” *Electr. Power Syst. Res.*, vol. 226, no. February 2023, p. 109899, 2024, doi: 10.1016/j.epsr.2023.109899.

[139] H. Tu, H. Feng, S. Srdic, and S. Lukic, “Extreme Fast Charging of Electric Vehicles: A Technology Overview,” *IEEE Trans. Transp. Electrif.*, vol. 5, no. 4, pp. 861–878, 2019, doi: 10.1109/TTE.2019.2958709.

[140] A. Ali *et al.*, “A Comprehensive Review on Charging Topologies and Power Electronic Converter Solutions for Electric Vehicles,” *J. Mod. POWER Syst. CLEAN ENERGY*, vol. XX, no. Xx, 2023, doi: 10.35833/MPCE.2023.000107.

[141] H. Kilicoglu and P. Tricoli, “Technical Review and Survey of Future Trends of Power Converters for Fast-Charging Stations of Electric Vehicles,” *Energies*, vol. 16, no. 13, 2023, doi: 10.3390/en16135204.

[142] A. Erat and A. M. Vural, “DC / DC Modular Multilevel Converters for HVDC Interconnection A Comprehensive Review,” *Int. Trans. Electr. Energy Syst.*, vol. 2022, 2022, doi: 10.1155/2022/2687243.

[143] H. S. Khan, M. Aamir, M. Ali, A. Waqar, S. Umaid Ali, and J. Imtiaz, “Finite control set model predictive control for parallel connected online UPS system under unbalanced and nonlinear loads,” *Energies*, vol. 12, no. 4, 2019, doi: 10.3390/en12040581.

[144] Y. Wang, Y. Guan, O. B. Fosso, M. Molinas, S. Z. Chen, and Y. Zhang, “An Input-Voltage-Sharing Control Strategy of Input-Series-Output-Parallel Isolated Bidirectional DC/DC Converter for DC Distribution Network,” *IEEE Trans. Power Electron.*, vol. 37, no. 2, pp. 1592–1604, 2022, doi: 10.1109/TPEL.2021.3107355.

[145] B. Zhao, Q. Song, W. Liu, and Y. Sun, “Overview of dual-active-bridge isolated bidirectional DC-DC converter for high-frequency-link power-conversion system,” *IEEE Trans. Power Electron.*, vol. 29, no. 8, pp. 4091–4106, 2014, doi: 10.1109/TPEL.2013.2289913.

[146] A. Maitra, “Utility Direct Medium Voltage DC Fast Charger Update: DC Fast Charger Characterization,” 2012.

[147] S.Sainadh, “EXTREME FAST CHARGING OF ELECTRIC VEHICLE BY USING SOLID STATE TRANFORMER,” *Int. J. Recent Dev. Sci. Technol.*, vol. 06, no. 01, pp. 53–68, 2022.

[148] J. S. Lai, W. H. Lai, S. R. Moon, L. Zhang, and A. Maitra, “A 15-kV class intelligent

universal transformer for utility applications," *Conf. Proc. - IEEE Appl. Power Electron. Conf. Expo. - APEC*, vol. 2016-May, pp. 1974–1981, 2016, doi: 10.1109/APEC.2016.7468139.

[149] S. Srdic, X. Liang, C. Zhang, W. Yu, and S. Lukic, "A SiC-based high-performance medium-voltage fast charger for plug-in electric vehicles," *ECCE 2016 - IEEE Energy Convers. Congr. Expo. Proc.*, pp. 1–6, 2016, doi: 10.1109/ECCE.2016.7854777.

[150] O. S. Chaudhary, M. Denaï, S. S. Refaat, and G. Pissanidis, "Technology and Applications of Wide Bandgap Semiconductor Materials: Current State and Future Trends," *Energies*, vol. 16, no. 18, 2023, doi: 10.3390/en16186689.

[151] L. Gill, T. Ikari, T. Kai, B. Li, K. Ngo, and D. Dong, "Medium voltage dual active bridge using 3.3 kV SiC MOSFETs for EV charging application," *2019 IEEE Energy Convers. Congr. Expo. ECCE 2019*, pp. 1237–1244, 2019, doi: 10.1109/ECCE.2019.8912874.

[152] X. Liang, S. Srdic, J. Won, E. Aponte, K. Booth, and S. Lukic, "A 12.47 kV medium voltage input 350 kW EV fast charger using 10 kV SiC MOSFET," *Conf. Proc. - IEEE Appl. Power Electron. Conf. Expo. - APEC*, vol. 2019-March, pp. 581–587, 2019, doi: 10.1109/APEC.2019.8722239.

[153] Y. Tahir *et al.*, "A state-of-the-art review on topologies and control techniques of solid-state transformers for electric vehicle extreme fast charging," *IET Power Electron.*, vol. 14, no. 9, pp. 1560–1576, 2021, doi: 10.1049/pel2.12141.

[154] D. Rothmund, T. Guillod, D. Bortis, and J. W. Kolar, "99.1% Efficient 10 kV SiC-Based Medium-Voltage ZVS Bidirectional Single-Phase PFC AC/DC Stage," *IEEE J. Emerg. Sel. Top. Power Electron.*, vol. 7, no. 2, pp. 779–797, 2019, doi: 10.1109/JESTPE.2018.2886140.

[155] F. Wang, G. Wang, A. Huang, W. Yu, and X. Ni, "Design and operation of A 3.6kV high performance solid state transformer based on 13kV SiC MOSFET and JBS diode," *2014 IEEE Energy Convers. Congr. Expo. ECCE 2014*, pp. 4553–4560, 2014, doi: 10.1109/ECCE.2014.6954024.

[156] A. Edpuganti and A. K. Rathore, "A Survey of Low Switching Frequency Modulation Techniques for Medium-Voltage Multilevel Converters," *IEEE Trans. Ind. Appl.*, vol. 51, no. 5, pp. 4212–4228, 2015, doi: 10.1109/TIA.2015.2437351.

[157] M. Hosseinpour, A. Dastgiri, and M. Shahparasti, "Design and Analysis of a Power Quality Improvement System for Photovoltaic Generation Based on LCL-Type Grid Connected Inverter," *Int. J. Eng. Trans. A Basics*, vol. 37, no. 2, pp. 252–267, 2024, doi: 10.5829/ije.2024.37.02b.04.

[158] Y. Tong, F. Tang, Y. Chen, F. Zhou, and X. Jin, "Design algorithm of grid-side LCL-filter for three-phase voltage source PWM rectifier," *IEEE Power Energy Soc. 2008 Gen. Meet. Convers. Deliv. Electr. Energy 21st Century, PES*, pp. 1–6, 2008, doi:

10.1109/PES.2008.4596088.

[159] S. Sadeghi, “Classifying FPGA Technology in Digital Signal Processing : A review Classifying FPGA Technology in Digital Signal Processing : A review,” *Int. J. Eng. Technol. Sci.*, vol. 2024, no. September, 2024.

[160] A. Ventosa-Cutillas, P. Montero-Robina, F. Umbría, F. Cuesta, and F. Gordillo, “Integrated control and modulation for three-level NPC rectifiers,” *Energies*, vol. 12, no. 9, pp. 1–15, 2019, doi: 10.3390/en12091641.

[161] F. Wang, Q. Ge, and Y. Zhang, “A new control strategy for neutral-point-clamped active rectifier based on DSP-FPGA,” *Proc. - 12th Int. Conf. Electr. Mach. Syst. ICEMS 2009*, vol. 1, no. 2, pp. 1–4, 2009, doi: 10.1109/ICEMS.2009.5382946.

[162] I. M. O. Mohammed, M. N. Gitau, R. C. Bansal, and K. Musasa, “Modelling and Control of a VIENNA Smart Rectifier-I for Wind Power Systems Integrated Under Transient Conditions,” *Technol. Econ. Smart Grids Sustain. Energy*, vol. 4, no. 1, pp. 1–24, 2019, doi: 10.1007/s40866-018-0057-6.

[163] B. Kavya Santhoshi, D. Ravi Kishore, K. Sailakshmi, G. D. S. L. Sravani, and A. Durga Prasanna, “Near Unity Power Factor Correction Vienna Rectifier for Plug-In Type Three Phase EV Charging Station,” *IOP Conf. Ser. Earth Environ. Sci.*, vol. 1375, no. 1, 2024, doi: 10.1088/1755-1315/1375/1/012024.

[164] R. Islam, S. M. S. H. Rafin, and O. A. Mohammed, “Comprehensive Review of Power Electronic Converters in Electric Vehicle Applications,” *Forecasting*, vol. 5, no. 1, pp. 22–80, 2023, doi: 10.3390/forecast5010002.

[165] A. Zhaksylyk *et al.*, “Review of Active Front-End Rectifiers in EV DC Charging Applications,” *Batteries*, vol. 9, no. 3, pp. 1–35, 2023, doi: 10.3390/batteries9030150.

[166] J. Gao, T. Q. Zheng, and F. Lin, “Improved deadbeat current controller with a repetitive-control-based observer for PWM rectifiers,” *J. Power Electron.*, vol. 11, no. 1, pp. 64–73, 2011, doi: 10.6113/JPE.2011.11.1.064.

[167] A. Saadaoui, M. Ouassaid, and M. Maaroufi, “Backstepping Control of a Phase Shifted Full Bridge DC/DC Converter for EV Fast Chargers,” *2023 18th Conf. Electr. Mach. Drives Power Syst. ELMA 2023 - Proc.*, no. May, 2023, doi: 10.1109/ELMA58392.2023.10202300.

[168] S. Habib *et al.*, “Contemporary trends in power electronics converters for charging solutions of electric vehicles,” *CSEE J. Power Energy Syst.*, vol. 6, no. 4, pp. 911–929, 2020, doi: 10.17775/CSEEJPES.2019.02700.

[169] O. Ibrahim, N. Z. Yahaya, N. Saad, and K. Y. Ahmed, “Design and simulation of phase-shifted full bridge converter for hybrid energy systems,” *Int. Conf. Intell. Adv. Syst. ICIAS 2016*, pp. 1–6, 2017, doi: 10.1109/ICIAS.2016.7824043.

[170] C. C. Hua, Y. H. Fang, and C. W. Lin, “LLC resonant converter for electric vehicle battery

chargers," *IET Power Electron.*, vol. 9, no. 12, pp. 2369–2376, 2016, doi: 10.1049/iet-pel.2016.0066.

[171] J. Shahsevani and R. Beiranvand, "Application-Oriented Review of the LLC-Based Resonant Converters," *IEEE Access*, vol. 12, no. April, pp. 52687–52726, 2024, doi: 10.1109/ACCESS.2024.3386430.

[172] M. C. Annamalai and N. Amutha prabha, "A comprehensive review on isolated and non-isolated converter configuration and fast charging technology: For battery and plug in hybrid electric vehicle," *Heliyon*, vol. 9, no. 8, p. e18808, 2023, doi: 10.1016/j.heliyon.2023.e18808.

[173] Y. Wei, Q. Luo, Z. Wang, and A. Mantooth, "Wide voltage gain range application for full-bridge LLC resonant converter with narrow switching frequency range," *IET Power Electron.*, vol. 13, no. 15, pp. 3283–3293, 2020, doi: 10.1049/iet-pel.2020.0443.

[174] P. Costa, P. Lobler, L. Roggia, and L. Schuch, "Modeling and Control of DAB Converter Applied to Batteries Charging," *IEEE Trans. Energy Convers.*, vol. 37, no. 1, pp. 175–184, 2022, doi: 10.1109/TEC.2021.3082468.

[175] G. G. Oggier and M. Ordonez, "High-efficiency DAB converter using switching sequences and burst mode," *IEEE Trans. Power Electron.*, vol. 31, no. 3, pp. 2069–2082, 2016, doi: 10.1109/TPEL.2015.2440753.

[176] A. R. Alonso, J. Sebastian, D. G. Lamar, M. M. Hernando, and A. Vazquez, "An overall study of a Dual Active Bridge for bidirectional DC/DC conversion," *2010 IEEE Energy Convers. Congr. Expo. ECCE 2010 - Proc.*, pp. 1129–1135, 2010, doi: 10.1109/ECCE.2010.5617847.

[177] P. Muthukumar, M. Venkateshkumar, and C. S. Chin, "A Comparative Study of Cutting-Edge Bi-Directional Power Converters and Intelligent Control Methodologies for Advanced Electric Mobility," *IEEE Access*, vol. 12, no. January, pp. 28710–28752, 2024, doi: 10.1109/ACCESS.2024.3360267.

[178] Z. Shi, Y. Guo, P. Li, and H. Sun, "A Boost CLLC Converter Controlled by PWM and PFM Hybrid Modulation for Photovoltaic Power Generation," *IEEE Access*, vol. 8, pp. 112015–112026, 2020, doi: 10.1109/ACCESS.2020.3002334.

[179] M. Bartecka, M. Kłos, and J. Paska, "Effective Design Methodology of CLLC Resonant Converter Based on the Minimal Area Product of High-Frequency Transformer," *Energies*, vol. 17, no. 1, pp. 1–24, 2024, doi: 10.3390/en17010055.

[180] Y. Liu, S. Liu, C. Wang, J. Jiang, J. Li, and S. Ye, "An Improved Space Vector Modulation with Capacitor Voltage Control for T-Type Five-Level Nested Neutral Point Piloted Converter," *IEEE Trans. Power Electron.*, vol. 36, no. 5, pp. 5262–5277, 2021, doi: 10.1109/TPEL.2020.3025976.

[181] F. Sebaaly, H. Vahedi, H. Y. Kanaan, N. Moubayed, and K. Al-Haddad, "Design and

Implementation of Space Vector Modulation-Based Sliding Mode Control for Grid-Connected 3L-NPC Inverter," *IEEE Trans. Ind. Electron.*, vol. 63, no. 12, pp. 7854–7863, 2016, doi: 10.1109/TIE.2016.2563381.

[182] M. Tetik and F. Parlak, "Velocity Vector Controlled S-Curve Motion Profile in Permanent Magnet Synchronous Machine (Pmsm)," *NWSA Acad. Journals*, vol. 12, no. 4, pp. 203–217, 2017, doi: 10.12739/nwsa.2017.12.4.2a0128.

[183] P. Najafi, A. H. Viki, M. Shahparasti, S. Sajjad Seyedalipour, and E. Pouresmaeil, "A novel space vector modulation scheme for a 10-switch converter," *Energies*, vol. 13, no. 7, 2020, doi: 10.3390/en13071855.

[184] M. Pastor and D. Gordan, "Phase-Shifted Full-Bridge Converter With High Efficiency," *15th Int. Conf. Elektro 2024, ELEKTRO 2024 - Proc.*, 2024, doi: 10.1109/ELEKTRO60337.2024.10556882.

[185] P. Dini and S. Saponara, "Electro-thermal model-based design of bidirectional on-board chargers in hybrid and full electric vehicles," *Electron.*, vol. 11, no. 1, 2022, doi: 10.3390/electronics11010112.

[186] T. Q. Duong and S. J. Choi, "Moving Discretized Control Set Model Predictive Control with Dominant Parameter Identification Strategy for Dual Active Bridge Converters," *Mathematics*, vol. 12, no. 4, 2024, doi: 10.3390/math12040563.

[187] D. Baocang, *Modern Predictive Control*, 1st Editio. Boca Raton, CRC Press, 2018. doi: doi.org/10.1201/9781315222585.

[188] I. Sami, W. Alhosaini, D. Khan, and E. M. Ahmed, "Advancing Dual-Active-Bridge DC–DC Converters with a New Control Strategy Based on a Double Integral Super Twisting Sliding Mode Control," *World Electr. Veh. J.*, vol. 15, no. 8, pp. 1–22, 2024, doi: 10.3390/wevj15080348.

[189] K. Zhou, Y. Wu, X. Wu, Y. Sun, D. Teng, and Y. Liu, "Research and Development Review of Power Converter Topologies and Control Technology for Electric Vehicle Fast-Charging Systems," *Electron.*, vol. 12, no. 7, 2023, doi: 10.3390/electronics12071581.

[190] S. A. Gorji, H. G. Sahebi, M. Ektesabi, and A. B. Rad, "Topologies and control schemes of bidirectional DC–DC power converters: An overview," *IEEE Access*, vol. 7, pp. 117997–118019, 2019, doi: 10.1109/ACCESS.2019.2937239.

[191] J. H. Jung, H. S. Kim, M. H. Ryu, and J. W. Baek, "Design methodology of bidirectional CLLC resonant converter for high-frequency isolation of DC distribution systems," *IEEE Trans. Power Electron.*, vol. 28, no. 4, pp. 1741–1755, 2013, doi: 10.1109/TPEL.2012.2213346.

[192] A. Babazadeh and D. Maksimović, "Hybrid digital adaptive control for fast transient response in synchronous buck DC-DC converters," *IEEE Trans. Power Electron.*, vol.

24, no. 11, pp. 2625–2638, 2009, doi: 10.1109/TPEL.2009.2033065.

[193] M. A. Elgendy, B. Zahawi, and D. J. Atkinson, “Operating characteristics of the P&O algorithm at high perturbation frequencies for standalone PV systems,” *IEEE Trans. Energy Convers.*, vol. 30, no. 1, pp. 189–198, 2015, doi: 10.1109/TEC.2014.2331391.

[194] A. Zentani, A. Almaktoof, M. T. E. Kahn, and M. K. Elmezughi, “An Effectual Control Technique for Islanded Operation of a Step-Up Power Converter Fed by Small Wind Turbine System,” *2022 Int. Conf. Electr. Eng. Sustain. Technol. ICEEST 2022 - Proc.*, pp. 1–6, 2022, doi: 10.1109/ICEEST56292.2022.10077860.

[195] L. Badreddine, S. Zouggar, M. L. Elhafyani, and F. Z. Kadda, “Experimental Modeling and Control of a Small Wind PMSG Turbine,” *IEEE*, 2014.

[196] V. Salas, E. Olías, A. Barrado, and A. Lázaro, “Review of the maximum power point tracking algorithms for stand-alone photovoltaic systems,” *Sol. Energy Mater. Sol. Cells*, vol. 90, no. 11, pp. 1555–1578, 2006, doi: 10.1016/j.solmat.2005.10.023.

[197] B. Masood, M. S. Siddique, R. M. Asif, and M. Zia-Ul-Haq, “Maximum power point tracking using hybrid perturb & observe and incremental conductance techniques,” *Int. Conf. Eng. Technol. Technopreneuship, ICE2T 2014*, vol. 2014-Augus, no. August, pp. 354–359, 2015, doi: 10.1109/ICE2T.2014.7006277.

[198] M. Ahmadi, M. Abrari, M. Ghanaatshoar, and A. Khalafi, “A novel algorithm for maximum power point tracking using computer vision (CVMPPT),” *PLoS One*, vol. 19, no. 4 April, pp. 1–16, 2024, doi: 10.1371/journal.pone.0301363.

[199] A. W. Leedy, L. Guo, and K. A. Aganah, “A constant voltage MPPT method for a solar powered boost converter with DC motor load,” *Conf. Proc. - IEEE SOUTHEASTCON*, 2012, doi: 10.1109/SECon.2012.6196885.

[200] C. L. Liu, J. H. Chen, Y. H. Liu, and Z. Z. Yang, “An asymmetrical fuzzy-logic-control-based MPPT algorithm for photovoltaic systems,” *Energies*, vol. 7, no. 4, pp. 2177–2193, 2014, doi: 10.3390/en7042177.

[201] N. Kumar Pandey, R. Kumar Pachauri, S. Choudhury, and R. Kumar Sahu, “Asymmetrical interval Type-2 Fuzzy logic controller based MPPT for PV system under sudden irradiance changes,” *Mater. Today Proc.*, vol. 80, pp. 710–716, 2023, doi: 10.1016/j.matpr.2022.11.074.

[202] A. H. Ahmed, A. E. S. B. Kotb, and A. M. Ali, “Comparison between fuzzy logic and PI control for the speed of BLDC motor,” *Int. J. Power Electron. Drive Syst.*, vol. 9, no. 3, pp. 1116–1123, 2018, doi: 10.11591/ijpeds.v9.i3.pp1116-1123.

[203] B. Salma, J. Tarik, B. Mohamed Khalifa, N. Elmehdi, and L. Roa, “Improving photovoltaic system performance with artificial neural network control,” *Data Metadata*, vol. 2, 2023, doi: 10.56294/dm2023144.

[204] S. Zheng, M. Shahzad, H. M. Asif, J. Gao, and H. A. Muqeet, “Advanced optimizer for

maximum power point tracking of photovoltaic systems in smart grid: A roadmap towards clean energy technologies," *Renew. Energy*, vol. 206, no. October 2022, pp. 1326–1335, 2023, doi: 10.1016/j.renene.2023.01.023.

[205] N. Van Nguyen, K. S. Jeon, J. W. Lee, and Y. H. Byun, "Development of Repetitively Enhanced Neural Networks (RENN) for efficient missile design and optimization," *3rd Int. Jt. Conf. Comput. Sci. Optim. CSO 2010 Theor. Dev. Eng. Pract.*, vol. 1, pp. 431–435, 2010, doi: 10.1109/CSO.2010.150.

[206] A. K. Asundi, A. L. H. P. Shaik, S. Mohiuddin, Naseeruddin, and F. B. Kalburgi, "Electric vehicle with smart grid integration using a hybrid honey badger algorithm and artificial neural network," *Int. J. Adv. Technol. Eng. Explor.*, vol. 11, no. 116, pp. 979–991, 2024, doi: 10.19101/IJATEE.2023.10102555.

[207] K. Tang and C. Meng, "Particle Swarm Optimization Algorithm Using Velocity Pausing and Adaptive Strategy," *Symmetry (Basel).*, vol. 16, no. 661, 2024, doi: doi.org/10.3390/sym16060661.

[208] J. C. Bansal;, P. K. Singh, and N. R. Pal, *Evolutionary and Swarm Intelligence Algorithms*, vol. 779. 2019. [Online]. Available: http://link.springer.com/10.1007/978-3-319-91341-4

[209] R. Sabzehgar, Y. M. Roshan, and P. Fajri, "Modeling and control of a multifunctional three-phase converter for bidirectional power flow in plug-in electric vehicles," *Energies*, vol. 13, no. 10, 2020, doi: 10.3390/en13102591.

[210] Isdawimah, N. Nadhiroh, A. D. Aji, and Ismujianto, "Real-Time Monitoring of Power Quality for Web Based Electrical Power Panel Using LabVIEW," *ICECOS 2019 - 3rd Int. Conf. Electr. Eng. Comput. Sci. Proceeding*, pp. 217–221, 2019, doi: 10.1109/ICECOS47637.2019.8984441.

[211] C. Fjellstedt, J. Forslund, and K. Thomas, "Experimental Investigation of the Frequency Response of an LC-Filter and Power Transformer for Grid Connection," *Energies*, vol. 16, no. 15, 2023, doi: 10.3390/en16155784.

[212] I. Colak, E. Kabalci, R. Bayindir, and G. Bal, "Modeling of a three phase SPWM multilevel VSI with low THD using Matlab/Simulink," *2009 13th Eur. Conf. Power Electron. Appl. EPE '09*, 2009.

[213] A. Mehrizi-Sani and S. Filizadeh, "Harmonic and loss analysis of space-vector modulated converters," *Proc. Int.*, 2007, [Online]. Available: http://individual.utoronto.ca/mehrizi/downloads/MehriziSani_2007_SVMHarmonicAndLoss.pdf

[214] C. J. O'Rourke, M. M. Qasim, M. R. Overlin, and J. L. Kirtley, "A Geometric Interpretation of Reference Frames and Transformations: Dq0, Clarke, and Park," *IEEE Trans. Energy Convers.*, vol. 34, no. 4, pp. 2070–2083, 2019, doi: 10.1109/TEC.2019.2941175.

[215] A. Nicastri and A. Nagliero, “Comparison and evaluation of the PLL techniques for the design of the grid-connected inverter systems,” *IEEE Int. Symp. Ind. Electron.*, pp. 3865–3870, 2010, doi: 10.1109/ISIE.2010.5637778.

[216] Q. Zhong, K. Wu, N. Luo, Z. Chen, and J. Shi, “Inverse Park Transformation PLL for VSC-HVDC under Unbalanced Voltage Condition,” *2022 6th Int. Conf. Smart Grid Smart Cities, ICSGSC 2022*, no. 1, pp. 98–102, 2022, doi: 10.1109/ICSGSC56353.2022.9963020.

[217] Dipraj, A. Singh, R. K. Singh, and S. Sharma, “Analogous Research of Classical PI Controller and Fuzzy Logic Controller to Control the Speed of D.C. Servo Motor,” *J. Phys. Conf. Ser.*, vol. 2007, no. 1, 2021, doi: 10.1088/1742-6596/2007/1/012044.

[218] J. Selvaraj and N. A. Rahim, “Multilevel Inverter For Grid-Connected PV System Employing Digital PI Controller,” *IEEE Trans. Ind. Electron.*, vol. 56, no. 1, pp. 149–158, 2009, doi: 10.1109/TIE.2008.928116.

[219] M. S. Tavazoei, “From traditional to fractional PI control: A key for generalization,” *IEEE Ind. Electron. Mag.*, vol. 6, no. 3, pp. 41–51, 2012, doi: 10.1109/MIE.2012.2207818.

[220] S. Cole, *Steady-State and Dynamic Modelling of VSC HVDC Systems for Power System Simulation*, no. September. 2010.

[221] A. Ortega and F. Milano, “Generalized model of vsc-based energy storage systems for transient stability analysis,” *IEEE Trans. Power Syst.*, vol. 31, no. 5, pp. 3369–3380, 2016, doi: 10.1109/TPWRS.2015.2496217.

[222] Y. Astudillo-baza, M. Torres-sabino, and M. Águila-muñoz, “PI control of a phase tracking loop,” *Int. J. Eng. Sci.*, vol. 11, no. 11, pp. 16–21, 2022, doi: 10.9790/1813-11111621.

[223] B. K. Naick, M. Das, T. K. Chatterjee, and K. Chatterjee, “Study and implementation of synchronization algorithm in three phase grid connected PV system,” *2016 3rd Int. Conf. Recent Adv. Inf. Technol. RAIT 2016*, pp. 304–309, 2016, doi: 10.1109/RAIT.2016.7507921.

[224] V. V. Babu, J. P. Roselyn, and P. Sundaravadivel, “Coordination of SRF-PLL and Grid Forming Inverter Control in Microgrid with Solar PV and Energy Storage,” *J. Low Power Electron. Appl.*, vol. 14, no. 2, 2024, doi: 10.3390/jlpea14020029.

[225] P. K. Dhakal, A. M. S. Mendes, and P. G. Pereirinha, “Analysis of Active Front End Rectifier with LLC Resonant Converter for EV Charging Application,” *2022 IEEE Veh. Power Propuls. Conf. VPPC 2022 - Proc.*, pp. 0–5, 2022, doi: 10.1109/VPPC55846.2022.10003354.

[226] C. Adragna, A. Bianco, G. Gritti, and M. Sucameli, “State-of-the-Art Power Factor Correction : An Industry Perspective,” pp. 1324–1354, 2024.

[227] N. Mohan, T. M. Undeland, and W. P. Robbins, *Power Electronics, Converter,*

Application, and Design, Second Edi. Minneapolis, Trondheim: John Wiley & Sons, 1989. [Online]. Available: https://uodiyala.edu.iq/uploads/PDF ELIBRARY UODIYALA/EL23/Mohan_-_Power_Electronics.pdf

[228] A. Rodríguez, A. Vázquez, D. G. Lamar, M. M. Hernando, and J. Sebastián, "Different purpose design strategies and techniques to improve the performance of a dual active bridge with phase-shift control," *IEEE Trans. Power Electron.*, vol. 30, no. 2, pp. 790–804, 2015, doi: 10.1109/TPEL.2014.2309853.

[229] F. Krismer and J. W. Kolar, "Accurate power loss model derivation of a high-current dual active bridge converter for an automotive application," *IEEE Trans. Ind. Electron.*, vol. 57, no. 3, pp. 881–891, 2010, doi: 10.1109/TIE.2009.2025284.

[230] R. C. Dorf and R. H. Bishop, *Modern Control Systems*, vol. 11, no. 1. 2016. [Online]. Available: http://scioteca.caf.com/bitstream/handle/123456789/1091/RED2017-Eng-8ene.pdf?sequence=12&isAllowed=y%0Ahttp://dx.doi.org/10.1016/j.regsciurbeco.2008.06.005%0Ahttps://www.researchgate.net/publication/305320484_SISTEM_PEMBETUNGAN_TERPUSAT_STRATEGI_MELESTARI

[231] B. Friedland, *Control system design*, vol. 11, no. 1. 1986. [Online]. Available: http://scioteca.caf.com/bitstream/handle/123456789/1091/RED2017-Eng-8ene.pdf?sequence=12&isAllowed=y%0Ahttp://dx.doi.org/10.1016/j.regsciurbeco.2008.06.005%0Ahttps://www.researchgate.net/publication/305320484_SISTEM_PEMBETUNGAN_TERPUSAT_STRATEGI_MELESTARI

[232] K. I. Baradieh *et al.*, "A Study on the Impact of Different PV Model Parameters and Various DC Faults on the Characteristics and Performance of the Photovoltaic Arrays," *Inventions*, vol. 9, no. 5, p. 93, 2024, doi: 10.3390/inventions9050093.

[233] C. Qi and Z. Ming, "Photovoltaic Module Simulink Model for a Stand-alone PV System," *Phys. Procedia*, vol. 24, pp. 94–100, 2012, doi: 10.1016/j.phpro.2012.02.015.

[234] A. Trejos, D. Gonzalez, and C. A. Ramos-Paja, "Modeling of step-up grid-connected photovoltaic systems for control purposes," *Energies*, vol. 5, no. 6, pp. 1900–1926, 2012, doi: 10.3390/en5061900.

[235] A. Saxena, R. Kumar, M. Amir, and S. M. Muyeen, "Maximum power extraction from solar PV systems using intelligent based soft computing strategies: A critical review and comprehensive performance analysis," *Heliyon*, vol. 10, no. 2, p. e22417, 2024, doi: 10.1016/j.heliyon.2023.e22417.

[236] S. Sholapur, K. R. Mohan, and T. R. Narsimhegowda, "Boost Converter Topology for PV System with Perturb And Observe MPPT Algorithm," *IOSR J. Electr. Electron. Eng.*, vol. 9, no. 4, pp. 50–56, 2014, doi: 10.9790/1676-09425056.

[237] M. A. Chewale, V. B. Savakhande, and V. R. Sagar, "MPPT Based Boost Converter for Photovoltaic Application," *13th Int. Conf. Recent Innov. Sci. Eng. Manag.*, no. 18, pp.

322–334, 2018.

[238] W. Hart Danial, *Power Electronics*. Indiana: McGraw-Hill, 2011.

[239] K. Kumar, N. Ramesh Babu, and K. R. Prabhu, “Design and analysis of modified single P&O MPPT control algorithm for a standalone hybrid solar and wind energy conversion system,” *Gazi Univ. J. Sci.*, vol. 30, no. 4, pp. 296–312, 2017.

[240] D. Torres Lobera and S. Valkealahti, “Dynamic thermal model of solar PV systems under varying climatic conditions,” *Sol. Energy*, vol. 93, pp. 183–194, 2013, doi: 10.1016/j.solener.2013.03.028.

[241] M. Kamran, M. Mudassar, M. R. Fazal, M. U. Asghar, M. Bilal, and R. Asghar, “Implementation of improved Perturb & Observe MPPT technique with confined search space for standalone photovoltaic system,” *J. King Saud Univ. - Eng. Sci.*, 2018, doi: 10.1016/j.jksues.2018.04.006.

[242] D. D’Amato, M. Lorito, V. G. Monopoli, R. Consoletti, G. Maiellaro, and F. C. 1, “Design Procedure and Testing for the Electrification of a Maintenance Railway Vehicle,” *Energies*, vol. 16, no. 5, p. 21, 2023.

[243] O. Tremblay, L. A. Dessaint, and A. I. Dekkiche, “A generic battery model for the dynamic simulation of hybrid electric vehicles,” *VPPC 2007 - Proc. 2007 IEEE Veh. Power Propuls. Conf.*, no. V, pp. 284–289, 2007, doi: 10.1109/VPPC.2007.4544139.

[244] O. Tremblay and L. A. Dessaint, “Experimental validation of a battery dynamic model for EV applications,” *24th Int. Batter. Hybrid Fuel Cell Electr. Veh. Symp. Exhib. 2009, EVS 24*, vol. 2, pp. 930–939, 2009.

APPENDICES

Appendix 1: Battery management system

Appendix 2: P&O MATLAB Code

Appendix 1: Battery management system

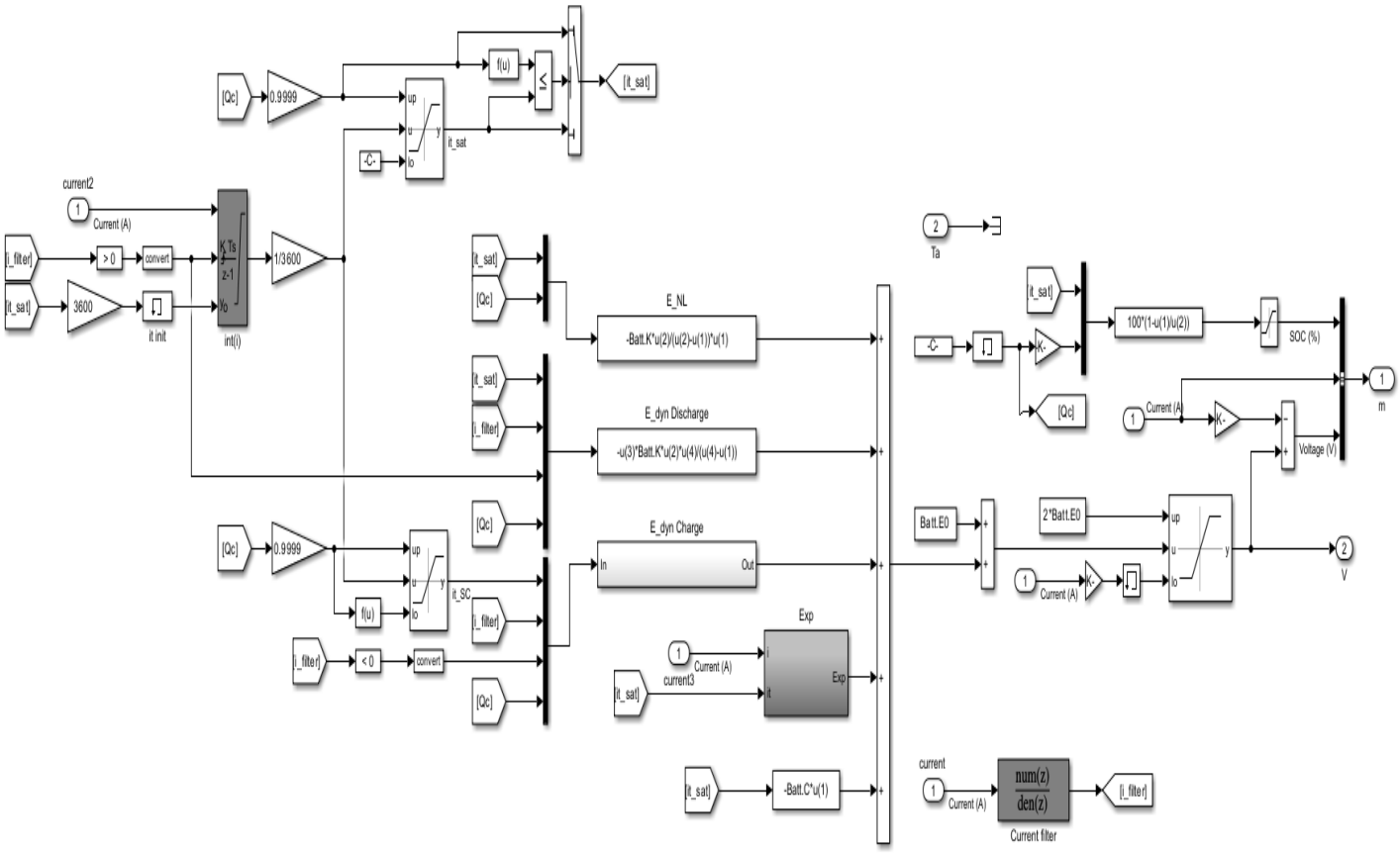

Appendix 2: P&O MATLAB Code

A MATLAB program software for the gradual process to extract maximum power by using the proposed P&O MPPT control algorithm from the small wind source is presented.

Step-1: Start the procedure

Step-2: Calculates change in power ΔP and change in voltage ΔV

For i=k (Maximum number of repetitions)

If change in power, ΔP is positive;

If change in voltage, ΔV is positive;

Decreases the V_{ref}, D =D_{init}, $-D_{del}$,

Else

if change in voltage, ΔV is negative;

Increase the V_{ref}, D =D_{init}, + D_{del}

End

Else

If change in voltage, ΔV < 0;

Increase the V_{ref}, D =D_{init}, + D_{del}

Else

If change in voltage, ΔV is negative;

Decreases the V_{ref}, D =D_{init}, $-D_{del}$

End

End

Step-3: else D= D_{init}

End

If D > V_{up} I D < = V_{low}

D = D_{init}

End

Step-4: Stop the process